

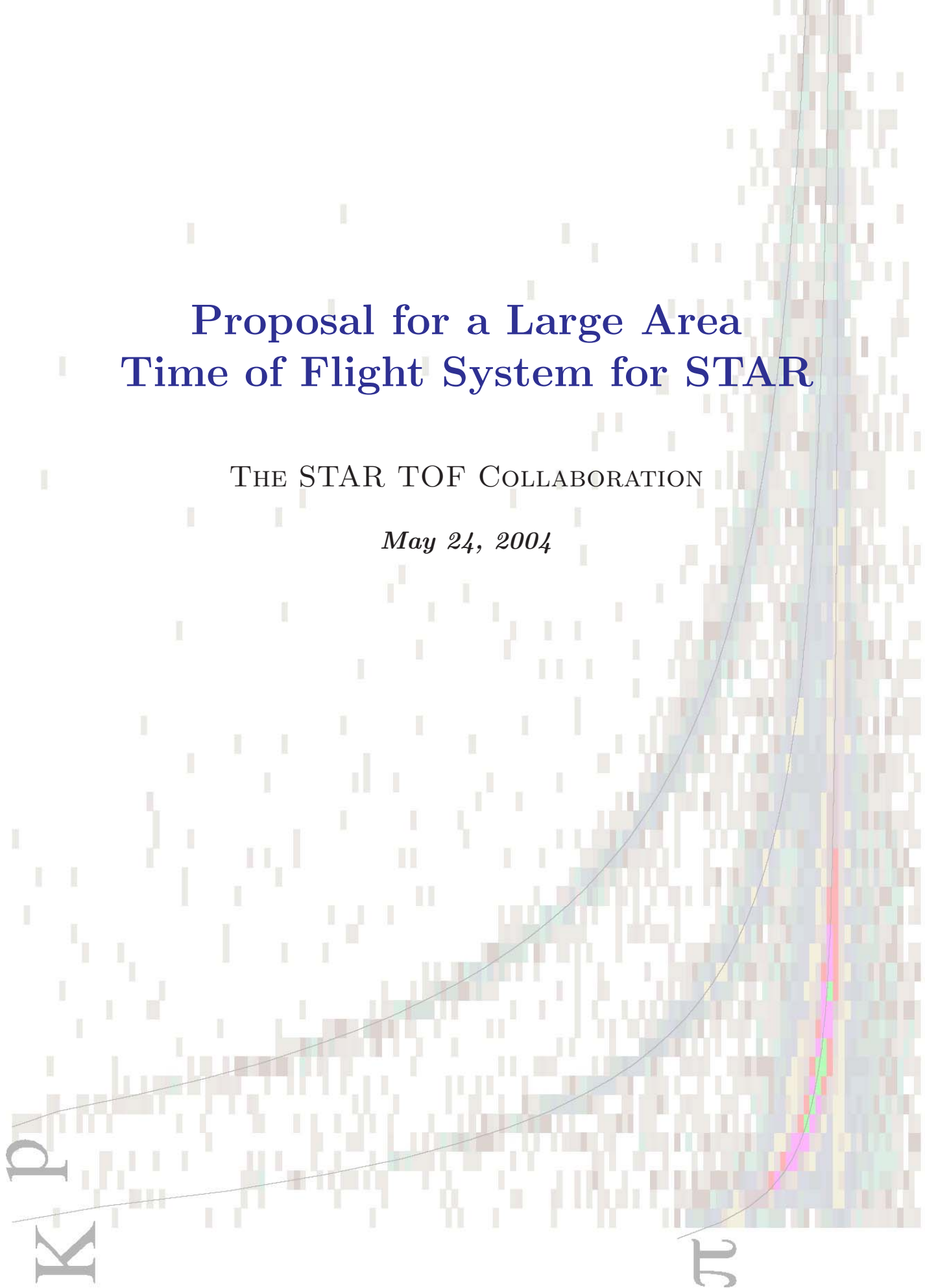
# Proposal for a Large Area Time of Flight System for STAR

THE STAR TOF COLLABORATION

*May 24, 2004*

K  
p

$\pi$





# Proposal for a Large Area Time of Flight System for STAR

## STAR-TOF

(The STAR TOF Collaboration)

P. Fachini, Zhangbu Xu

*Brookhaven National Laboratory, Upton, NY 11973*

Feng Liu, Lianshou Liu, Zhixu Liu, Jinghua Fu,  
Yuan Hu, Zhiming Li, Yuanfang Wu, Yan Lu  
*HuaZhong Normal University, Wuhan, China*

Jin Li, Junguang Lu, Bingyun Zhang

*Institute of High Energy Physics (IHEP), Beijing, China*

Wenlong Zhan, Zhiyu Sun

*Institute of Modern Physics (IMP), Lanzhou, China*

D. Hardtke, F. Retiere, N. Xu

*Lawrence Berkeley National Laboratory, Berkeley, CA 94720*

L. Kotchenda

*Moscow Engineering Physics Institute, Moscow, Russia*

J.W. Mitchell

*NASA - Goddard Space Flight Center, Greenbelt, MD 20771*

G. Paic, E. Cuautle, A. Martinez, G. Calderon  
*UNAM & CINVESTAV, Mexico City, Mexico*

B. Bonner, G. Eppley, F. Geurts, W.J. Llope,  
G. Mutchler, T. Nussbaum, J. Roberts, P. Yepes  
*Rice University, Houston, TX 77005*

Wenging Shen, Yugang Ma, Xiangzhou Cai

*Shanghai Institute of Nuclear Research (SINR), Shanghai, China*

Kejun Kang, Jianping Cheng, Yuanjing Li, Yulan Li, Yi Wang  
*Tsinghua University, Beijing, China*

C. Whitten, H. Huang, G. Igo, V. Ghazikhanian,  
S. Trentalange, A. Tai, H. Long

*University of California - Los Angeles, Los Angeles, CA 90095*

Hongfang Chen, Xin Dong, Xiaolian Wang, Ziping Zhang, Cheng Li,  
Lijuan Ruan, Shuwei Ye, Jian Wu, Ming Shao, Shengli Huang  
*University of Science and Technology of China (USTC), Hefei, China*

G. Hoffmann, A. Ishihara, C.F. Moore, L. Ray, J. Schambach, H. Ward,  
M. Daugherty, K. Kajimoto, M. McCain  
*University of Texas, Austin, TX 78712*

T. Trainor

*University of Washington, Seattle, WA 98195*

C. Markert

*Yale University, New Haven, CT 06520*

## **Acknowledgement**

The STAR Collaboration gratefully acknowledges the pioneering research and development work performed by the LAA project, and especially C. Williams, under A. Zichichi on MRPC Time Of Flight Technology.

# Contents

<b>1</b>	<b>Executive Summary</b>	<b>2</b>		
<b>2</b>	<b>Overview</b>	<b>4</b>		
2.1	Introduction . . . . .	4		
2.2	STAR Heavy Ion Physics and the TOF Upgrade . . . . .	5		
2.3	TOF MRPC Detector Technology	11		
2.4	Project Cost-Schedule and Resources	12		
2.5	Summary . . . . .	13		
<b>3</b>	<b>TOF Physics Discussion</b>	<b>14</b>		
3.1	Introduction . . . . .	14		
3.2	Partonic Collective Dynamics at RHIC	15		
3.2.1	Transverse anisotropic flow	16		
3.2.2	Transverse radial flow . . . . .	17		
3.2.3	Simulation Results . . . . .	19		
3.3	Event-by-Event Fluctuations and the Correlation Structure of Heavy Ion Collision Events . . . . .	21		
3.3.1	Particle Flavor Dependent Fragmentation at Moderate PT . . . . .	27		
3.4	Charm Meson Measurement . . . . .	36		
3.4.1	Simulation Results . . . . .	38		
3.5	Physics of Resonances at RHIC . . . . .	42		
3.6	Searches for Exotic Dibaryons . . . . .	48		
3.7	Additional Important Physics Benefits . . . . .	51		
3.7.1	Identical and Non-identical Two-Particle Correlations . . . . .	51		
3.7.2	Nucleus & Antinucleus production . . . . .	52		
<b>4</b>	<b>Detector Design</b>	<b>53</b>		
4.1	The STAR Approach to Time Of Flight . . . . .	53		
4.2	Requirements . . . . .	54		
4.3	Design . . . . .	55		
4.4	Mechanical Design . . . . .	61		
4.5	Gas System Design . . . . .	67		
4.5.1	Pressure Control . . . . .	69		
4.5.2	Mixture Control & Temperature Measurement . . . . .	70		
4.5.3	Gas Sampling & Purification	70		
4.5.4	Computer Control & Data Acquisition . . . . .	72		
4.6	Electronics Design . . . . .	73		
4.6.1	TFEE . . . . .	78		
4.6.2	TDIG . . . . .	79		
4.6.3	TTST . . . . .	82		
4.6.4	TCPU . . . . .	82		
4.6.5	TMIT . . . . .	83		
4.6.6	TDRC . . . . .	83		
4.7	Power Systems . . . . .	85		
4.8	Test & Monitoring Software . . . . .	86		
4.9	Start Detector Design . . . . .	86		
<b>5</b>	<b>The Full-Size STAR Prototypes: TOFr &amp; TOFr'</b>	<b>91</b>		
5.1	TOFr Construction . . . . .	91		
5.2	TOFr Testing at the AGS . . . . .	96		
5.3	TOFr in STAR in RHIC Run-3 . . . . .	99		
5.4	TOFr' in STAR in RHIC Run-4 . . . . .	102		
<b>6</b>	<b>Construction</b>	<b>106</b>		
6.1	Module Construction & QA . . . . .	106		
6.2	Tray Construction & QA . . . . .	108		
6.3	Electronics Construction & QA . . . . .	109		
6.4	Integration Issues . . . . .	110		
	<b>List Of Figures</b>	<b>112</b>		
	<b>List Of Tables</b>	<b>117</b>		
	<b>Bibliography</b>	<b>118</b>		
<b>A</b>	<b>Appendix – Simulation Codes used in Section 3.3</b>	<b>126</b>		
<b>B</b>	<b>Appendix – The STAR TOFp and pVPD Systems</b>	<b>128</b>		
B.1	TOFp Production and Matching Software . . . . .	129		
B.2	TOFp Systems Calibrations and Performance . . . . .	133		
<b>C</b>	<b>Appendix – STAR TOF Project Preliminary Management Plan</b>	<b>138</b>		
<b>D</b>	<b>Appendix – Response to the BNL Detector Advisory Committee</b>	<b>170</b>		

# 1 Executive Summary

The STAR Collaboration proposes to build a barrel Time of Flight (TOF) detector based on recently developed Multi-gap Resistive Plate Chamber (MRPC) technology. This detector will significantly extend the reach of the STAR scientific program, doubling the percentage of kaons and protons for which particle identification is possible to more than 95% of all those produced within the MRPC-TOF acceptance. Combined with existing STAR detectors, the barrel TOF detector will allow STAR to extract the maximum amount of information available from soft physics measures on an event-by-event basis. It will:

- allow the detailed unfolding of large and small scale correlations and fluctuations, mapping, in detail, the dynamics and evolution of the produced matter;
- reduce significantly the integrated luminosity needed for key measures such as multiply-strange baryon ( $\Omega$ ) elliptic flow ( $v_2$ ); such measures are needed to identify possible partonic collectivity and to explore in detail the early time bulk physics properties of the produced matter;
- extend the  $p_T$  reach for accurate measurement of the mass and width of resonances to  $\sim 1\text{-}2$  GeV/c, affording a precision tool for model comparison and providing essential information concerning the importance of re-scattering versus regeneration during the period between chemical and thermal freeze-out.

When combined with a possible future vertex detector upgrade, the proposed TOF detector will also reduce the integrated luminosity needed to measure a statistically robust sample of  $D^0$ ,  $D^+$ ,  $D_s^+$  mesons by approximately an order of magnitude, enabling STAR to make systematic studies of charm thermalization and  $D^0$  meson flow.

The development of new, low-cost MRPC technology for the ALICE experiment combined with the parallel development of new high precision TDC chips at CERN provides a cost effective means to fulfill the physics-driven requirements of this proposal: to extract the maximum information available from soft (up to  $\sim 2\text{-}3$  GeV/c) hadronic spectra. After extensive testing of MRPC technology at CERN and BNL and its successful implementation in the HARP experiment, this technology is mature. A 168 channel MRPC prototype tray was installed in STAR for in-situ testing during the d+Au RHIC Run-3. It demonstrated stable performance, meeting all key performance requirements and producing important physics results (not possible with particle identification from the TPC alone) on the Cronin effect for identified particles. This result was submitted to the Physical Review Letters on September 15, 2003 (nucl-ex/0309012) demonstrating the ability and importance of this new technology for producing new physics results in STAR. A 180-channel tray with the next generation of front-end electronics and mechanical design was operated in STAR during the Au+Au Run-4 and also performed well.

By providing nearly complete particle identification within the large solid angle acceptance subtended by the STAR Time Projection Chamber (TPC), Silicon Vertex

Tracker (SVT), and Barrel Electromagnetic Calorimeter (BEMC), the proposed barrel Time of Flight detector will uniquely position STAR to provide definitive measures, unavailable otherwise without extremely large amounts of beam time, to establish whether or not the relevant degrees of freedom for the new matter being produced at RHIC are equilibrated and partonic in nature.

The research and development of the electronic components of this detector is expected to continue in FY2004 and FY2005. The construction project is proposed to begin in mid-FY2005, and to continue through FY2007. The cost of the U.S. contribution to this construction is projected to be \$4.7M in FY2004 dollars, adjusted for inflation over the life of the project. Subject to approval by the Chinese funding agencies, the Chinese institutions involved in this project are committed to the construction and testing of  $\sim 4000$  MRPC chambers, the full amount required for this detector. This represents a projected in-kind contribution of approximately \$2.3M by the participating Chinese institutions.

## 2 Overview

### 2.1 Introduction

A unique strength of the STAR detector at RHIC is its large, uniform acceptance capable of measuring and identifying a substantial fraction of the particles produced in heavy ion collisions. This large acceptance is central to STAR's scientific capability and has already resulted in new and intriguing physics results such as the recent measurement of the suppression of back-to-back jets in central Au+Au collisions. Large acceptance detectors central to the STAR heavy ion physics program are the Silicon Vertex Tracker (SVT), the Time-Projection Chamber (TPC), and the Barrel Electromagnetic Calorimeter (BEMC) all having an acceptance covering  $2\pi$  in azimuthal angle and  $|\eta| \lesssim 1.5$  in pseudo-rapidity. We propose a barrel Time-of-Flight (TOF) detector matching the acceptance of these detectors. This upgrade will provide essential particle identification capability. Specifically, it will double the percentage of kaons and protons for which particle identification is possible to more than 95% of all those produced within the acceptance of the TOF barrel ( $|\eta| \lesssim 1$ ), greatly enhancing the discovery potential of STAR. This increase in particle identification efficiency over a large solid angle is especially important for measurements of multi-particle correlations since the feasibility of such measurements depends on the single particle efficiency raised to the power of the number of particles used in the correlation. The extended momentum range for particle identified spectra provided by the MRPC barrel TOF detector is crucial to understand the information contained in the large scale correlations and fluctuations being observed in Au+Au collisions at RHIC.

Large acceptance TOF coverage is integral to the STAR detector design. The importance of the capability provided by large acceptance TOF was underscored in the 1996 review by NSAC of STAR's proposal for Additional Experimental Equipment. At that time, the TOF detector technology proposed was based on mesh-dynode phototubes and was deemed to be too expensive. In its conclusions, the NSAC [9] subcommittee noted:

“STAR should aim at a [TOF] coverage which is sufficient for event-by-event kaon (and possibly proton) identification, which in other observables is the prominent feature and strength of STAR. If fiscal constraints are such that this cannot be realized, ...further R&D should be encouraged to search for a viable solution for large area coverage.”

STAR has found a viable solution. The proposed TOF detector is based on a new detector technology called the Multi-gap Resistive Plate Chamber (MRPC), which has been developed at CERN for the LHC. In particular, the LHC heavy ion experiment, ALICE, has adopted MRPC technology for its TOF detector [6]. This technology has also been used successfully in the HARP experiment at CERN for a period of approximately 2 years. It has now been used successfully in the STAR experiment for two years. The sections of this chapter which follow will provide an overview of



the physics justification, technical construction, and installation plan for a proposed STAR Barrel MRPC TOF detector.

## 2.2 STAR Heavy Ion Physics and the TOF Upgrade

The main goal of the relativistic heavy ion program at RHIC is to produce a new form of matter, the Quark-Gluon Plasma (QGP), and to study Quantum Chromodynamics (QCD) at high temperature. Initial experimental measurements of particle multiplicity and transverse momentum (energy) distributions indicate that the high energy density being reached in nucleus-nucleus collisions at RHIC is unprecedented. Recent RHIC results have offered a new view into nucleus-nucleus collisions with respect to studying the gluon dominated initial phase, partonic and hadronic evolution dynamics, and hadronic freeze-out scenarios. The following is a selected list of key physics topics in STAR where the proposed barrel TOF detector will have a major impact on enhancing STAR's future physics capability. The large acceptance of the proposed STAR TOF is essential for these physics achievements.

The proposed barrel TOF detector will significantly extend STAR's physics reach for the following topics:

1. Unfolding the origin of non-statistical fluctuations and correlations as well as the conditions at the phase boundary for hadronization through measurement of event-by-event pion, kaon and proton mean transverse momentum,  $\langle p_T \rangle$ , multiplicity fluctuations, and two particle correlations in  $\eta$ - $\phi$ . The proposed TOF detector is essential to provide the required  $p_T$  coverage and overall particle identification (PID) acceptance necessary for such measurements.
2. Determining the nature of the strongly interacting dense matter produced in the early stage of nucleus-nucleus collisions at RHIC and whether the relevant degrees of freedom are partonic; studying parton dynamics in the early stage of the collision and searching for possible partonic collectivity; placing constraints on the initial conditions in terms of the parton structure function of the colliding nuclei. These topics will be studied by measuring the yields and  $p_T$  spectra of  $\Omega$  baryons and  $D$  mesons to determine important constraints on the initial parton flux and the magnitude of the elliptic flow and transverse radial flow of heavy quarks. Elliptic flow of the  $\Omega$  is of particular importance to search for partonic collectivity. The added capability of the barrel TOF detector is essential to increase the efficiency for detection of these particles so that precision measurements are possible within the beam time projected to be available.
3. Exploring possible new physics domains at RHIC such as a possible critical point in the QCD phase diagram and searches for exotic di-Omega particles. Recent theoretical conjecture has raised the possibility of a critical point in the phase diagram relating temperature and baryon density. If a critical point

exists, one way it might be observed is through QCD critical phenomenon manifest through unusually large fluctuations of particle ratios such as  $K/\pi$  and  $K/p$ . With respect to possible exotic states, the Di-Omega is predicted to be one of the most stable di-baryon candidates based on recent QCD inspired chiral  $SU(3)$  phenomenological calculations. RHIC is the first accelerator where multiple Omegas are produced per collision with sufficiently high probability that a sensitive search for a possible di-Omega particle is possible. Without the PID capability of the full TOF these studies are not possible since the detection efficiency for a possible Di-Omega particle is too low.

### Fluctuations and Large Scale Correlations

With the proposed barrel TOF detector, STAR will investigate the nature of non-statistical fluctuations and will study medium induced modification of multiparticle correlations. Specifically, by using the TOF to measure particle identified spectra in the full range of  $p_T$  relevant for soft physics measures, STAR will investigate the transport and possible correlation of quantum numbers such as strangeness and baryon number in various regions of phase space. Possible fluctuations in these distributions as a function of centrality will be studied as well. Such fluctuations are expected to be sensitive to important underlying physics like the possible existence of a critical point and/or the order of the quark-hadron phase transition. Possible modification of the correlation length due to the presence of a strongly interacting QCD medium will probe the nature of the medium over a time scale long compared to that for the initial non-equilibrium phase probed by high  $p_T$  particles, providing important complementary information. The proposed full TOF detector is essential to provide detailed information on flavor composition and particle dynamics in order to search for and study these types of fluctuations and correlations.

In the analysis of event-wise  $\langle p_T \rangle$  fluctuations from the top 15% most central Au+Au collisions at 130 GeV, STAR has already observed fluctuations significantly beyond what can be accounted for by statistics [27]. Figure 1 shows a distribution of event-wise mean- $p_T$  with respect to  $\hat{p}_T$  in units of  $\sigma_{\hat{p}_T}/\sqrt{n}$ . This distribution is compared to a gamma distribution which is the reference appropriate in the absence of non-statistical fluctuations ( $\hat{p}_T$  and  $\sigma_{\hat{p}_T}^2$  are the mean and variance of the inclusive  $p_T$  distribution respectively.) To match the gamma distribution with the data, an increase in the *rms* width by  $\sim 14\%$  is required which is attributed to dynamical (non-statistical) fluctuations.

This observation is just one example of why a large acceptance TOF detector is necessary. This effect results from a large scale fluctuation over the full STAR acceptance ( $|\eta| \lesssim 1.0$ ,  $2\pi$  in  $\phi$ ). Its origin can not be unambiguously determined without additional particle identification. Possible divergent origins of the excess fluctuations in Fig.1 include large event-by-event temperature variations for the selected centrality class and/or large fluctuations in the relative numbers of pions, kaons, and protons since the observed mean  $p_T$  is known to be strongly particle dependent. In order to disentangle different dynamical explanations and understand the underlying physics leading to these fluctuations it is essential to measure event-by-event mean  $p_T$  and

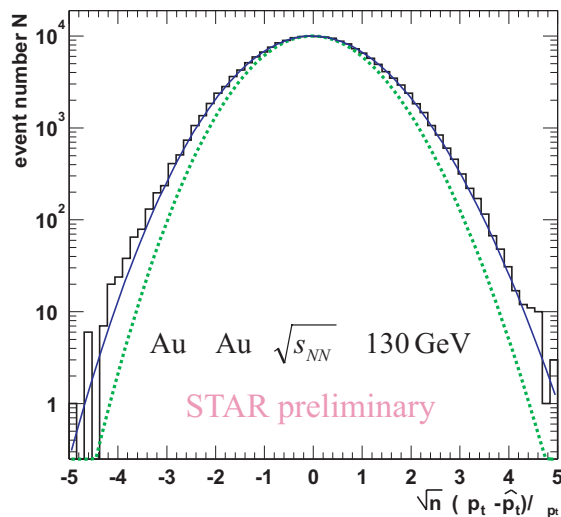


Figure 1: Distributions of  $\sqrt{n}(\langle p_T \rangle - \hat{p}_T) / \sigma_{\hat{p}_T}$  for all primary hadrons from central (top 15%) events (upper histogram) compared to two gamma distributions: reference in the absence of non-statistical fluctuations (dotted line) and with a 14% increased *rms* width (solid curve).

particle number fluctuations for pions, kaons and protons, respectively. The limited PID capability in the low  $p_T$  region from the TPC+SVT alone does not provide adequate coverage in acceptance or transverse momentum to determine the mean  $p_T$  for identified particles event by event. For example, the average  $p_T$  of protons is approximately 0.9 GeV/c, while the PID from TPC  $dE/dx$  covers only up to  $p_T < 1.0$  GeV/c. The extended  $p_T$  coverage of proton PID above 2.0 GeV/c from the barrel TOF system is essential to determine the event mean  $p_T$  for protons in this instance.

First observations of large-scale charge correlations in Au+Au collisions at RHIC already show strong variation with collision centrality, exhibiting features similar to those expected from correlations in p-p interactions in peripheral heavy ion collisions, but very different structure for the most central heavy ion events. This suggests the correlations observed in central collisions may be influenced by strong medium effects; the study of possible medium-induced modifications to local quantum number conservation at hadronization is just beginning.

Conserved quantum numbers such as electric charge, baryon number, and strangeness are expected to be locally conserved in pair production in nuclear collisions. An interesting possibility is that local quantum number conservation could be modified due to the presence of a strongly interacting QCD medium surrounding the produced particle pair. While a first observation of charge correlations of particles in large  $\Delta\eta$  and  $\Delta\phi$  appears to exhibit gross features qualitatively similar to those observed in elementary p-p collisions, the study of possible medium induced modifications is just beginning. The large acceptance of the TPC ( $|\eta| \lesssim 1.5$  and  $2\pi$  in  $\phi$ ) will be essential to achieve the necessary sensitivity to large-scale structure of the expected correlations.

In addition, the proposed barrel TOF detector is essential to measure the correlation length for local baryon number and strangeness conservation, to search for possible medium effects, and to extend the  $p_T$  acceptance to cover the transition region between soft and semi-hard particle production. Baryon number and strangeness are generally considered more sensitive probes of the QCD medium than charge conservation, which may be heavily influenced by the decays of resonances in the final state.

Event-by-event fluctuation analysis in heavy ion collisions has been advocated as a unique tool in searches for a phase transition and possible critical phenomena near the QCD phase boundary. Strong dependence of non-statistical fluctuations on centrality, beam energy, and nucleus size could provide direct indication of a phase transition to a quark-gluon plasma [25, 26]. The large acceptance of the TPC combined with the proposed barrel TOF detector will reduce the statistical error to 10-15% for the measurement of event-by-event kaon and proton yields in central Au+Au collisions. With the addition the proposed barrel TOF detector, STAR will have unprecedented sensitivity to explore event-by-event physics in this domain.

### Collective Flow Observables

Collective flow measurements have been very important for studying relativistic nucleus-nucleus collisions at all beam energies [18, 19] because the magnitude and pattern of the collective motion is closely related to the equation of state (EOS) of the produced matter. Assuming local equilibrium, the EOS will be driven by the degrees of freedom relevant for the basic constituents which make up the matter. It is therefore possible by studying collective flow to determine important information about the nature of the matter when it is produced, *e.g.* whether it is partonic or hadronic in nature.

STAR has measured both elliptic and transverse radial flow observables systematically for several particle species up to the moderate-to-high  $p_T$  region. These measurements have already yielded important information as shown in Figure 2(a) which shows an example of the STAR measurement for the anisotropy parameter (elliptic flow)  $v_2 = \langle \cos(2\psi) \rangle$  vs. transverse momentum for  $K_S^0$  and  $\Lambda$  from 200 GeV Au + Au minimum bias collisions. Two intriguing features are noted: (i) in the low  $p_T$  region, the predictions of a hydrodynamic calculation [20] match the data rather well in contrast to results at the SPS where the calculation over-predicted the observed anisotropy significantly; (ii) in the region  $p_T \geq 2$  GeV/c, the magnitude of the elliptic flow reaches saturation, the amount of elliptic flow ( $v_2$ ) at saturation being mass dependent. The saturation seems constant up to  $p_T \sim 6$  GeV/c.

Figure 2 (b) shows the  $\langle p_T \rangle$  versus particle mass for central Au+Au and minimum bias p+p collisions. Thermal fit results are shown as curves. Two important observations are noted: (i) for Au+Au collisions, the bulk of the particles fall along the curve with the freeze-out temperature and velocity parameters  $[T_{fo}, \beta]_{AuAu} = [110 \text{ (MeV)}, 0.55 \text{ (c)}]$  indicating a substantial degree of transverse radial flow. The results for p+p collisions indicate a behavior closer to the curve for  $[T_{fo}, \beta]_{pp} = [170 \text{ (MeV)}, 0.0 \text{ (c)}]$ . The apparent conclusion is that particles freeze-out at hadronization

in p+p collisions when the temperature is very close to that of the chemical freeze-out temperature [23, 24]. In Au+Au collisions, the multi-strange baryons  $\Xi$  and  $\Omega$  clearly deviate from the bulk freeze-out curve showing somewhat smaller collective velocity and a higher temperature.

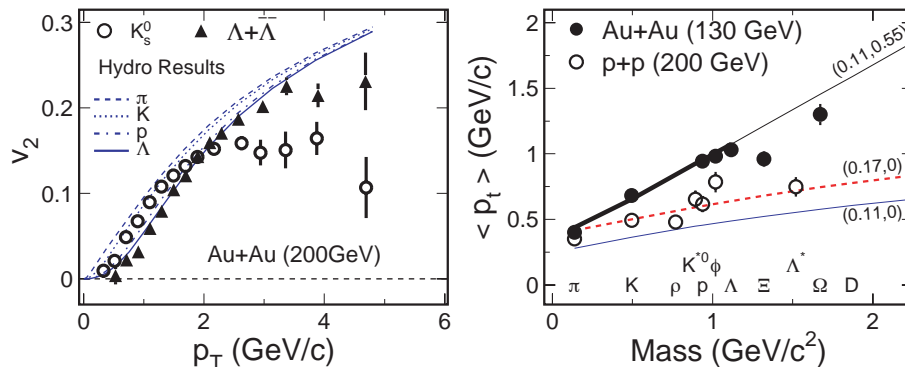


Figure 2: (Left) Azimuthal anisotropy parameters  $v_2$  as a function of  $p_T$  for strange particles  $K_S^0$  (open circle) and  $\bar{\Lambda}/\Lambda$  (closed triangles) from minimum bias 200 GeV Au+Au collisions. Lines are from hydrodynamic model calculations [20] for (from top to bottom) pions, kaons, protons, and  $\bar{\Lambda}/\Lambda$ . (Right) The  $\langle p_T \rangle$  vs. particle mass. The lines represent the thermal results with given temperature and velocity  $(T_{fo}, \beta)$ .

These studies, carried out for particles for which topological identification is possible, demonstrate the importance of studying elliptic flow as a function of particle species. They also point to a potentially definitive signature of partonic collectivity in relativistic nucleus-nucleus collisions.

Due to the fact that at late times, the expansion of the produced matter tends to reduce the effects of spatial anisotropy in the initial collision, elliptic flow is expected to be self-quenching. If observed, elliptic flow is therefore likely developed in the early stage of the collision when partonic degrees of freedom are most relevant. Due to the small elastic hadronic cross sections for multi-strange baryons ( $\Xi$ ,  $\Omega$ ) and charm hadrons ( $D$ ,  $J/\Psi$ ), those particles are expected to couple weakly to hadronic matter in the later stages of the collision (as evidenced by the departure of the behavior of the omega and cascade baryons from the trend for lighter particles). A finite value of  $v_2$  for those particles should therefore carry partonic information. A non-zero value of  $v_2$  and possible  $v_2$  saturation for those particles would serve as a very strong signature of partonic collectivity in nuclear collisions at RHIC.

The barrel TOF detector will allow measurement of the elliptic flow for  $\Omega$  baryons up to moderately high  $p_T$ , well into the region of possible saturation. Specifically, it will increase the  $\Omega$  detection efficiency over the existing TPC+SVT configuration in STAR by a factor of 3 to 8 for the  $p_T$  region from 1.5 GeV/c to  $>4$  GeV/c. Such an enhancement in the detection efficiency is necessary in order to unambiguously

establish possible collective phenomenon for the  $\Omega$  within reasonable amount of running time. Without the proposed barrel TOF system, due to the reduced detection efficiency and increased combinatorial background, the beam time needed to make this measurement is prohibitive. A precise measurement of the  $\Omega$  yield at moderately high  $p_T$  as a function of collision centrality and beam species will also allow STAR to study possible suppression of the  $\Omega$  baryon yield relative to the yield in p+p interactions scaled appropriately. This intriguing phenomenon has already been studied in STAR for unidentified charged hadrons,  $K_s^0$ , and  $\Lambda^0$ . The transverse momentum at which the yield saturates and decreases relative to p+p is mass-dependent. The  $\Omega$  baryon is particularly interesting because it is a three-strange quark cluster.

### D Meson Production

For  $D$  mesons at moderate  $p_T$ , particle identification of the daughter kaon and pion is possible, although these are separated by large gaps in rapidity and  $\phi$  angle. Therefore, the large acceptance of the proposed barrel TOF is essential to measure the  $D$  meson spectrum from the  $D \rightarrow K + \pi$  decay, where the decay kinematics of the  $D$  meson decay can be fully reconstructed.

With the proposed barrel TOF detector, the combinatorial background for  $D \rightarrow K + \pi$  candidates can be reduced by a factor of 3 due to the identification of the decay daughters. This will allow STAR to make a  $D$  meson yield measurement with an error approximately 15% for central Au+Au collisions with one-year of data-taking. Without the barrel TOF, a multi-year run and analysis period would be required for a single beam energy and species, and a systematic study of the yield and spectra of open charm would thus not be feasible. The determination of the  $D$  meson yield and the shape of the  $p_T$  distribution will provide constraints on the incoming gluon flux in the colliding nuclei and provide important information on the magnitude of the transverse radial flow of charm quarks. In order to further reduce the background and extend the  $p_T$  reach, a STAR micro-vertex detector upgrade will be required to precisely measure the displaced  $D$  meson decay vertices. Both the barrel TOF and the micro-vertex detector upgrades are required in order to complete the STAR  $D$  meson physics program aimed at constraining the gluon structure function of the nuclei, determining open charm yields for the normalization of charmonium measurements, studying the energy loss of charm quark jets in the QCD medium, and searching for possible charm quark thermalization. Together, the barrel TOF detector and future micro-vertex detector will reduce the amount of beam time required for charm measurements by more than an order of magnitude.

### Hadronic Dynamics

In order to develop transport models to describe nucleus-nucleus collisions, it is imperative that the hadronic evolution and dynamics be understood. These play a dominant role in determining the total charged particle yield, momentum correlations and space-time geometry of the final state. The precise measurement of resonances with a range of lifetimes can trace the evolution between the hadron formation stage and the final decoupling of the system, since resonances continue to decay, scatter, and regenerate during this period, and their yield is therefore sensitive to the

medium. Short lived resonances such as the  $\rho$ ,  $\Delta$ , and  $\Lambda(1520)$  are particularly interesting in-medium probes because of their short lifetime. However, the large width of these resonances makes their measurement very susceptible to large combinatorial backgrounds and distortion of the background invariant mass distribution due to particle misidentification. This is precisely the reason there are difficulties measuring the yield of  $\rho$  and  $\Lambda(1520)$  from the central Au+Au collisions in the ongoing STAR scientific program. As most charged particles are believed to come from resonance decays, a precise determination of resonance contributions will constrain models of hadronization such as thermal/statistical models and string fragmentation models.

STAR has already observed a list of resonances including the  $\rho$ ,  $K^*(892)$ ,  $f^0(980)$ ,  $\phi(1020)$ ,  $\Delta$ ,  $\Sigma(1385)$ , and  $\Lambda(1520)$ , some of which have been observed for the first time in heavy ion collisions. Despite this exciting development, the crucial information which could be provided by these studies is not fully available. This is because the signal to noise and  $p_T$  range accessible using the TPC alone are not adequate for resonance studies to be a precision tool. In STAR, the proposed TOF upgrade will 1) significantly reduce the combinatorial background by identifying the decay daughters so that precise yields can be measured up to moderately high  $p_T$  ( $\sim 2$  GeV), and 2) remove the residual background structure underneath the resonance peaks due to misidentification of particles from the decays of other resonances. Precise measurements of resonances are important to determine the evolution dynamics during the time interval from hadron formation to kinetic freeze-out.

The barrel TOF detector will also allow us to measure non-identical two-particle correlations. Non-identical two-particle correlations are sensitive to the temporal emission pattern of different particles at the kinetic freeze-out stage. These correlation functions are constructed at the same velocity for different particle species. Because of their different masses, these particles have different momenta in the correlation function. Presently STAR does not have sufficient  $p_T$  coverage to allow non-identical particle correlations to place significant constraints on models of hadronic evolution. A large area TOF detector is necessary to extend the  $p_T$  reach and provide sufficient data rate.

### 2.3 TOF MRPC Detector Technology

The Multi-gap Resistive Plate Chamber (MRPC) is a new detector capable of sub-one hundred picosecond time resolution and high detection efficiency ( $>95\%$ ) for minimum ionizing particles. The mechanical and electric structure of the MRPC is different from that of previous Resistive Plate Chambers (RPC). The STAR MRPC TOF proposal is based on a successful MRPC R&D program involving collaborators from Rice University and the Chinese institutions in STAR in collaboration with the ALICE TOF group at CERN. This team has constructed a number of MRPC detectors and tested them in the CERN T10 beam line during the period from 2000 - 2001. The MRPC detectors tested have demonstrated the timing resolution, detection efficiency, and operational stability necessary to meet STAR's requirements. In addition, a full scale STAR MRPC prototype tray (1/120 of the full barrel TOF

detector) has been tested at the AGS, installed in the STAR detector during the fall of 2002, and operated successfully in RHIC Run-3 (FY2003). A second-generation prototype was operated successfully in RHIC Run-4. Details of the prototype results are presented in section 5. As a brief summary, the MRPC TOF prototype tray installed in STAR for Run-3 demonstrated stable performance, meeting all key performance parameters and producing important physics results. The conclusion from these studies is that MRPC technology is mature for use in large scale detector applications. Further evidence for this fact is provided by the HARP experiment at CERN which successfully operated a  $\sim 400$  channel system for approximately two years.

The proposed detector is a full-acceptance time-of-flight system matching the acceptance of the SVT, TPC, and BEMC. Coverage of the entire sixty square meter area of STAR will be accomplished by placing approximately 3800 MRPC modules in an overlapping geometry within 120 aluminum trays that fit inside the integration envelope of the present STAR Central Trigger Barrel (CTB). Each MRPC module has 6 pairs of copper pick-up pads, thus the envisioned detector would comprise approximately 23,000 channels, each having an active area of  $3.3 \text{ cm} \times 6.1 \text{ cm}$ . With this degree of granularity, the expected occupancy and multiple hit percentage is approximately 12% and 1% respectively for a central Au+Au collision at  $\sqrt{s_{\text{NN}}}=200 \text{ GeV}$ . The full barrel TOF detector will extend STAR's present capability for kaon separation from  $\sim 0.6$  to  $\sim 1.7 \text{ GeV}/c$ ; the range for proton separation would be increased from approximately  $\sim 1 \text{ GeV}/c$  to  $\sim 3.0 \text{ GeV}/c$ . This extension of the momentum range for particle identification is crucial to enable a number of key measurements that can not be achieved otherwise.

Prototypes of the proposed electronics for front end signal amplification and discrimination have been in use for three years. The digitization is based on a time-to-digital integrated circuit now in final development at CERN.

## 2.4 Project Cost-Schedule and Resources

The cost of the MRPC TOF barrel construction is proposed to be shared jointly by the U.S. and Chinese institutions collaborating on the project. The U.S. part of the construction project is projected to be \$4.7M in FY2004 dollars, adjusted for inflation over the life of the project. The proposed Chinese contribution in equivalent U.S. dollars is valued at \$2.3M dollars. The average level of contingency for all project components is 27%.

The project schedule (also see Appendix C) anticipates that research and development of the electronic components will continue until the third quarter of FY2005. The construction schedule begins in the second quarter of FY2005. MRPC module construction in China would begin at this time and continue until the end of FY2007. The construction of the mechanical and electronic components would also begin in mid-FY2005, allowing for installation of a 4-tray system in time for the run beginning in the fall of 2005. Detector construction and commissioning would be completed by the end of FY2007.

The team within STAR proposing to construct and integrate this detector system



consists of 47 scientists, engineers, and students from 10 institutions in the United States (4) and China (6).

In addition to contributing to the scientific measurements afforded by this detector system, the Chinese institutions will be responsible for providing high quality MRPC modules, built and tested in China, for integration into the barrel TOF system. These groups have extensive experience with this technology from test beam work at CERN, as well as module construction and testing in China. Twenty MRPC modules constructed in China were installed in the prototype TOF tray and were tested at the AGS in the spring of 2002, and operated successfully in STAR in RHIC Run-3. The results of these tests indicate the MRPC TOF detectors tested meet all STAR specifications.

The U.S. institutions participating in this project are responsible for the design, fabrication, testing, and integration of the front end and readout electronics as well as the mechanical assemblies required for this detector. They are responsible as well for overall project management and coordination.

The proposed TOF upgrade is a major STAR construction project involving international cooperation, with the STAR groups from China contributing significantly to the project both financially and technically. This project has been discussed in concept with the Directorate of the National Natural Science Foundation of China, which looks forward to reviewing a corresponding Chinese proposal once the review process for this proposal is begun by the U.S. Department of Energy. The team proposing to construct this detector has considerable experience in TOF techniques, and MRPC construction and testing as well as in high energy and nuclear physics experimentation in general.

## 2.5 Summary

A full acceptance time of flight system based on multi-gap resistive plate chamber technology is proposed. This detector is essential to upgrade STAR's particle identification capabilities. It will allow precision soft physics studies out to transverse momenta of approximately 2-3 GeV/c (depending on particle species) to help address the question of whether the relevant degrees of freedom in the initial stage of heavy ion collisions at RHIC are partonic, and whether they are equilibrated. With the proposed MRPC TOF barrel, essential information on the evolution of the produced matter will be afforded by examining, in detail, large-scale correlation structures, non-identical two-particle correlations, and short-lived hadronic resonances. Without a full acceptance TOF barrel, these studies are significantly compromised or impossible. In addition, the proposed TOF barrel upgrade will reduce the time required for data acquisition and analysis of D mesons and the elliptic flow of multiply-strange baryons (e.g. the  $\Omega$ ). With the TOF system, these studies will become possible without multiple RHIC runs and production analysis runs extending more than 1 year. These studies are essential to measure the degree of thermalization of the produced matter and to search for possible partonic collectivity. A search for a possible di-Omega di-baryon state is also made possible with the addition of the proposed system.

### 3 TOF Physics Discussion

#### 3.1 Introduction

Figure 3 shows a schematic description of a central nucleus-nucleus collision as a function of time. Two Lorentz contracted nuclei collide, presumably creating non-equilibrated partonic matter which is initially comprised mainly of gluons. The high density partonic matter evolves towards equilibrium and expands under high pressure. During the later stages of the evolution, hadrons are formed until chemical freeze-out. The resulting high density hadronic system continues to expand until the particle density is sufficiently dilute that elastic collisions stop and kinetic freeze-out is reached.

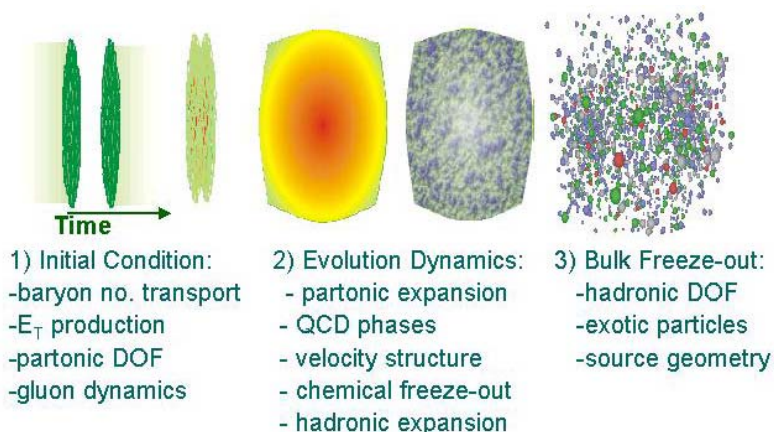


Figure 3: A schematic description of nucleus-nucleus collisions at RHIC from Ref. [12].

The proposed MRPC barrel TOF detector will provide crucial information, unavailable otherwise, to determine whether this type of physical picture is fundamentally correct. For the earliest gluon dominated stage, the barrel TOF will enable a systematic study of open charm to place important constraints on the gluon structure function of the colliding nuclei and establish a baseline for studies of quarkonium ( $J/\psi$ ) suppression (enhancement) in a deconfined color medium. It will allow STAR to make definitive measurements of elliptic flow for multiply-strange baryons and heavy mesons ( $\Omega$ ,  $D$  mesons and possibly  $J/\psi$ ) to study the pressure in the early stage of the collision and to search for possible partonic collectivity. Concerning the later stages of the collision, the proposed barrel TOF detector will provide detailed information on particle production in the hadronic stage as well as the evolution of the matter between chemical and kinetic freeze-out through systematic studies of large scale correlation structures, resonance production, and non-identical particle correlations. It will also enable sensitive searches for rare and exotic particles, which will test the boundaries of what is presently known about possible stable multi-quark (antiquark) configurations.

Key scientific measurements that will be made possible or will be significantly enhanced by the proposed barrel TOF detector are discussed in the sections which follow.

### 3.2 Partonic Collective Dynamics at RHIC

The proposed barrel TOF detector will enhance or make available a number of observables that are sensitive to collective dynamics in nucleus-nucleus collisions at RHIC, both in the early stage of the evolution when the degrees of freedom are presumed to be partonic (quarks and gluons), and in the later stage when they are hadronic.

Collective flow measurements have been very important for studying relativistic nucleus-nucleus collisions at all beam energies [18, 19] because the magnitude and pattern of the collective motion is closely related to the equation of state (EOS) of the produced matter. Assuming, local equilibrium, the EOS will be driven by the degrees of freedom relevant for the basic constituents which make up the matter. It is therefore possible by studying collective flow to determine important information about the nature of the matter when it is produced, *e.g.* whether it is partonic or hadronic in nature.

In order to access information about the early partonic stage, one possibility is to make measurements using particles that have small interaction cross sections during the hadronic stage, such as the  $\phi$ ,  $\Xi$ ,  $\Omega$ ,  $D$ ,  $J/\psi$ , and  $\psi'$ . For these particles, collective behavior observed in the lab is expected to be strongly correlated with pressure, equation of state, etc. in the early partonic stage of the evolution. An example of such an observable is the azimuthal anisotropy parameter  $v_2$  (where  $v_2 = \langle \cos[2(\phi - \psi_{RP})] \rangle$ , and  $\phi$  is the azimuthal angle of the particle of interest and  $\psi_{RP}$  is the azimuthal angle of the reaction plane). By measuring  $v_2$  for these particles, important information can be accessed about the early stage evolution. A specific example discussed below is the information afforded by measurements of transverse anisotropic flow (elliptic flow) and transverse radial flow for the  $\Omega$ .

The focus of the STAR physics measurements of collective dynamics includes:

1. measurement of collective flow for rarely produced particles;
2. studying collective flow as a function of centrality;
3. systematic investigations of collective flow as a function of the colliding beam species.

The additional PID capability provided by the proposed barrel TOF detector is essential for these studies. Specifically, it will:

- increase the detection efficiencies for rarely produced particles such as the  $\Omega$  and  $D$  meson making it possible to measure flow observables for these particles with an amount of beam time and analysis time that is not prohibitive;

- extend the range for  $p_T$  spectra to 5-6 GeV/c for these particles where the transition between soft physics and hard scattering becomes important and must be studied;
- allow STAR to make a systematic investigation of collective flow as a function of centrality and colliding system (A)

### 3.2.1 Transverse anisotropic flow

The transverse momentum distribution of particles produced in relativistic heavy ion collisions can be described by the following relation:

$$\frac{d^3N}{dp_T^2 d\phi dy} = \frac{dN}{2\pi dp_T^2 dy} \left[ 1 + 2 \sum_n v_n \cos(n\phi) \right]. \quad (1)$$

In this expression,  $p_T$  is the transverse momentum of a given particle,  $\phi$  is its azimuthal angle with respect to the reaction plane (the plane containing the impact parameter and the z axis) [29, 30], and  $y$  is the particle's rapidity. The  $v_n$  harmonic coefficients in this decomposition are termed anisotropy parameters. The coefficients  $v_1$  and  $v_2$  are called *directed flow* and *elliptic flow*, respectively. Here the word "flow" is used to denote collective behavior in general, without necessarily implying a hydrodynamic description. Directed flow  $v_1$  and elliptic flow  $v_2$  are sensitive to the initial gluon density, the degree of thermalization of the constituents, and the conditions of the system at freeze-out. They are therefore important indicators of the properties of the matter during various stages of its evolution.

First experimental results from RHIC [18] included measurements of  $v_2$  as a function of collision centrality for charged hadrons, and  $v_2$  as a function of  $p_T$  for charged hadrons, as well as identified charged pions, charged kaons, and protons ( $p_T < 0.9$  GeV/c). These initial results were of great interest because the degree to which the initial geometrical anisotropy of the nuclear matter mutually swept out by the colliding nuclei is converted to an anisotropy in the momentum distribution of produced particles is indicative of the density of the system and the mean free path for scattering of particles (parton and/or hadron). These properties are related to the equation of state of the matter.

Further results [18, 33] from RHIC have shown that in the low momentum region,  $p_T \leq 2$  GeV/c, hydrodynamic model calculations provide a good description of  $v_2$  as a function of  $p_T$  for  $\pi, K, p, \Lambda$  [34, 35, 20]. Alternatively, in the region where  $p_T \geq 2.5$  GeV/c, the hard scattering of partons becomes prominent and the hydrodynamic model predictions fail. Recent theoretical work has attempted to explain these observations by assuming various values for the initial gluon density (and energy loss) in an early partonic stage [31], and by assuming an equation of state described by a hydrodynamic model [20, 32]. In general, flow that is observed may be hadronic or partonic in origin [31, 37, 38].

These studies have been very important in their own right and have yielded very important clues as to the condition of the matter produced in Au+Au collisions at

RHIC in the early stages of the collision. More importantly however, they have shown that, combined with observations of transverse radial flow, the measurement of elliptic flow for multiply strange baryons may provide a key and potentially definitive insight into the state of the matter and possible partonic collectivity in the early stage of the collision. Specifically, significant elliptic flow observed for the  $\Xi$  and  $\Omega$ , would be a strong indication of partonic collectivity in the initial stages of the collision.

Based on analysis of TPC only Au+Au data at 200 GeV in the nucleon-nucleon center of mass system, approximately 2000  $\Omega$ 's were reconstructed from 3.5 million central collisions. For flow studies, min bias data is required, which reduces the yield per event of  $\Omega$ 's by approximately a factor of 5. A simple scaling based on the number of  $\Omega$ 's needed for flow studies ( $\sim 40,000$ ) indicates a data sample of approximately 350 million events would be required using data from the TPC alone. The additional information provided by the STAR SVT is expected to improve the reconstruction efficiency by a factor of 2-3. However, without the proposed barrel TOF detector, the number of minimum bias Au+Au collisions needed to obtain a statistically significant sample of  $\Omega$ 's for flow studies is still 100 million. Given that the time to analyze  $\sim 3$  million events from the RHIC Run-1 took 2.5 months, this study is beyond the realm of feasibility for the present STAR detector without the additional PID capability provided by the proposed barrel TOF detector. With the proposed TOF upgrade, the additional particle identification capability for detecting the decay daughters increases the reconstruction efficiency for  $\Omega$ 's by a factor of 3-8, making this measurement possible.

### 3.2.2 Transverse radial flow

At the SPS, it has been observed that multi-strange baryons like  $\Xi$  and  $\Omega$  [45] do not follow the common flow pattern shown by lighter hadrons  $\pi$ , K, and p [46] (See the open circles in Fig. 4 left plot). This observation was interpreted as a result of the earlier freeze-out of the multi-strange baryons due to their smaller elastic cross sections in a hadron gas [47]. This effect provides a unique possibility for studying the collision properties at the early stage of the collision.

The data in Fig. 4 provide an important insight as to how information on the early stage of the collision can be accessed. Due to the fact that at late times, the expansion of the produced matter tends to reduce the effects of spatial anisotropy in the initial collision, elliptic flow is expected to be self-quenching. If observed, elliptic flow is therefore likely developed in the early stage of the collision when partonic degrees of freedom are most relevant. Due to the small elastic hadronic cross sections for multi-strange baryons ( $\Xi, \Omega$ ) and charm hadrons ( $D, J/\Psi$ ), those particles are expected to couple weakly to hadronic matter in the later stages of the collision (as evidenced by the departure of the behavior of the inverse slope for the omega and cascade from the trend for lighter particles). A finite value of  $v_2$  for those particles therefore should carry partonic information. A non-zero value of  $v_2$  and possible  $v_2$  saturation for those particles would serve as a strong signature of partonic collectivity in nuclear collisions at RHIC.

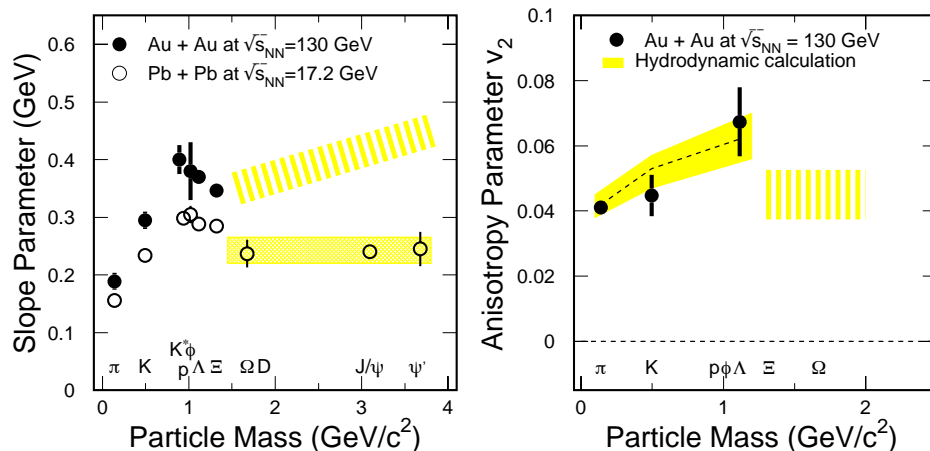


Figure 4: (Left) Measured slope parameter as a function of particle mass. Open symbols are for results from Pb+Pb central collisions at the SPS ( $\sqrt{s_{NN}} = 17.2$  GeV); filled symbols are for central Au+Au collisions at RHIC ( $\sqrt{s_{NN}} = 130$  GeV). (Right) Integrated azimuthal anisotropy parameters  $v_2$  as a function of particle mass. Data points are from minimum bias Au+Au collisions at RHIC ( $\sqrt{s_{NN}} = 130$  GeV). The gray band indicates the predictions of a hydrodynamic model [20]. The expected range if there is significant partonic collectivity is indicated by the dashed band in both plots.

The barrel TOF detector will allow measurement of the elliptic flow for  $\Omega$  baryons up to moderately high  $p_T$ , well into the region of possible saturation. Specifically, as shown in the following section, the  $\Omega$  detection efficiency is increased over that for the existing TPC+SVT configuration in STAR by a factor of 3 to 8 for the  $p_T$  region from 1.5 GeV/c to  $>4$  GeV/c. Such an enhancement in the detection efficiency is essential to make this measurement in order to unambiguously establish possible collective phenomenon for the  $\Omega$  within a reasonable amount of running time. Without the proposed barrel TOF system, due to the reduced detection efficiency and increased combinatorial background, the beam time needed to make this measurement is prohibitive.

An increase of the slope parameter for the  $\Omega$ ,  $D$ ,  $J/\Psi$ ,  $\Psi'$ , as shown in the dashed band of the left panel of Fig. 4 combined with a non-zero  $v_2$  for those particles as indicated in the dashed band of the right panel would provide a strong signature of partonic collectivity in nucleus-nucleus collisions at RHIC. Due to the acceptance and  $p_T$  range needed, only STAR can make this measurement at RHIC. STAR can only make this measurement with the addition of the particle identification capability provided by the proposed barrel TOF detector.

### 3.2.3 Simulation Results

A TOF detector matching the TPC acceptance in the mid-rapidity region will significantly enhance STAR's hyperon detection efficiency. Figure 5 illustrates the increase in detection efficiencies for the  $\Omega$  using the PID capability that will be provided by the proposed barrel TOF detector. Compared to the particle identification capability with the TPC only, the addition of the proposed barrel TOF detector results in a dramatic improvement for  $p_T > 2.0$  GeV/c; at 4.0 GeV/c it enhances the efficiency by a factor of 8.

The analysis was performed by embedding  $\Omega$ 's having a  $p_T$  spectrum similar to that observed in the STAR Au+Au collision data. The increase in the detection efficiency from the proposed TOF barrel is most significant for the higher  $p_T$   $\Omega$ s, which have daughter kaons ( $p_T > 0.5$  GeV/c) and  $\Lambda$  decay protons ( $p_T > 0.9$  GeV/c) beyond the PID capability of the present TPC + SVT.

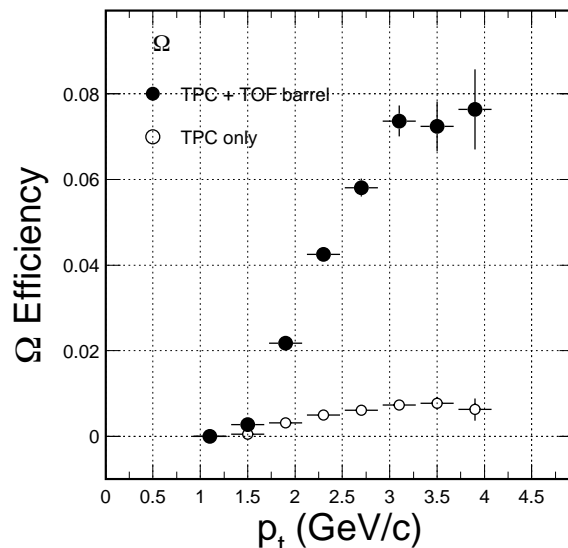


Figure 5: Detection efficiencies with and without TOF PID for  $\Omega$  decays.

Using the  $\Omega$  detection efficiency from these simulations, the spectra and corresponding statistical errors were estimated assuming event samples of varying size for 10% central 200 GeV Au+Au collisions. The results are shown in Figure 6. The figure shows the simulated  $p_T$  distribution for  $\Omega + \bar{\Omega}$  in central collisions (left two frames) and minimum bias collisions (right two frames). What would be measured by the STAR detector assuming TPC PID only (squares) and with the addition of the proposed barrel TOF detector (circles) is also indicated. The right hand panels show the relative statistical error in the spectra assuming event samples of up to 30 million events. These results reflect a value of  $dN/dy = 0.64$  for the  $\Omega + \bar{\Omega}$  and an inverse slope parameter of  $T=450$  MeV.

The results in the right panel are for minimum bias Au+Au collisions. For this simulation, the capability of the SVT has also been included in the comparison (TPC

+ SVT versus TPC + SVT + TOF in the upper left panel). The  $\Omega$  yield per event for minimum bias events is approximately a factor of 10 less than in central collisions. Thus the  $\Omega$  yield from a sample of 8M central events has roughly same statistical precision as a function of  $p_T$  as a sample of 80M minimum bias events. For elliptic flow studies, minimum bias data is needed, since the magnitude of  $v_2$  depends on the initial coordinate space anisotropy of the overlap region, and this is larger for more peripheral collisions.

The lower left panel for minimum bias events (panel b) shows the statistical precision needed for a robust measurement of elliptic flow for  $\Omega + \bar{\Omega}$ . The statistical errors are plotted on a presumed distribution of  $v_2$  vs  $p_T$  to indicate the estimated level of statistical precision with respect to the estimated magnitude of  $v_2$  as a function of  $p_T$ . The resolution in determining the reaction plane was taken to be 0.75, consistent with the resolution that has been observed in minimum bias Au+Au collisions in STAR.

This level of statistical precision requires approximately 30 million minimum bias collisions assuming the increased efficiency provided by the particle identification capability of the proposed barrel TOF detector. It requires 5-10 times more events if TPC PID only is assumed. With the barrel TOF detector, this measurement is challenging but feasible. Without the barrel TOF detector it is not possible given the resources and time required to acquire and analyze several hundred million events.

The importance of achieving this level of statistical precision is illustrated by the following example. STAR preliminary results have shown that  $v_2$  for the  $\Lambda$  is approximately 17% at a  $p_T$  of 3 GeV/c. Comparing the  $v_2$  expected for the  $\Lambda$  and the  $\Omega$ , if the relevant degrees of freedom in the early (partonic) stage are those of the constituent quark masses then  $v_2$  would be expected to be proportional to the mass and the  $v_2$  of the  $\Omega$  would be expected to be  $\sim 25\%$ . However, if the relevant degrees of freedom when the collective flow is generated are those of massless quarks/gluons, the partonic  $v_2$  of  $\Omega$  and the  $\Lambda$  would be expected to be approximately the same. To differentiate these scenarios it is necessary that  $v_2$  for the  $\Omega$  is measured with a relative uncertainty of less than 10%.

The conclusion is that with the additional PID capability provided by the barrel TOF detector, it will be possible to make a definitive measurement of  $v_2$  as a function of  $p_T$  for the  $\Omega$  as well as other multiply-strange baryons and heavy mesons. These measurements will provide crucial information on the relevant degrees of freedom in the early (partonic) stage of the collision and on possible partonic collectivity. Without the proposed barrel TOF detector, these measurements are not possible given the amount of beam time and analysis resources that would be necessary to process the hundreds of millions of events that would be required.



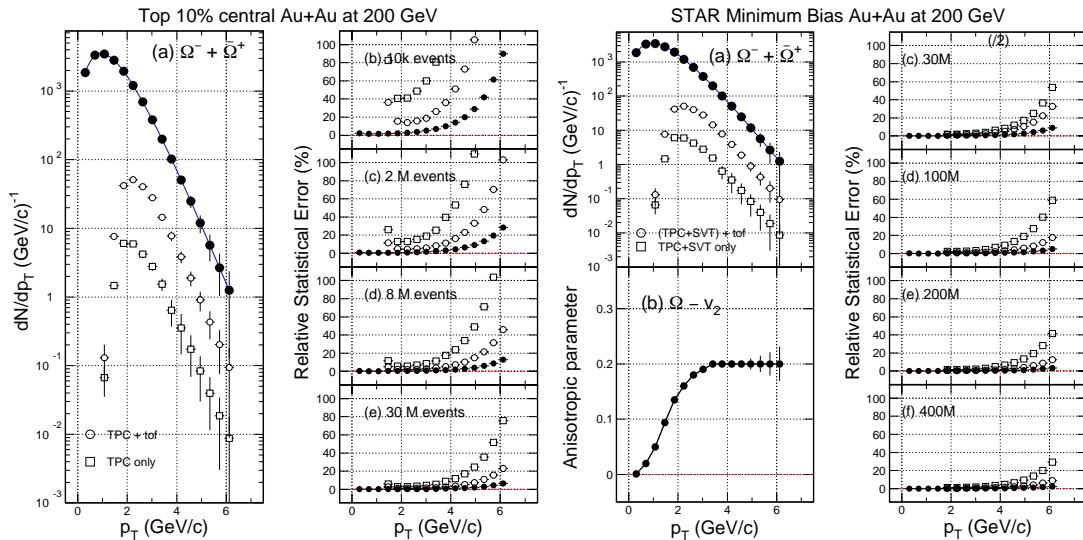


Figure 6: **Left:** Estimate for spectra and statistical errors from 200 GeV Au+Au top 10% central collisions. The value of  $dN/dy = 0.64$  and an inverse slope parameter  $T = 450$  MeV are used, for the sum of  $\Omega$  and  $\bar{\Omega}$ . The resulting  $p_T$  spectrum, as well as what would be measured in STAR using TPC PID only, and TPC+TOF PID are indicated in left panel (a) and TPC + SVT versus TPC+SVT+TOF in the right panel (a). **Right:** An estimate of the statistical precision needed relative to the projected anisotropy  $v_2$  from minimum bias Au+Au collisions at 200 GeV is shown in panel b. The reaction plane resolution is taken to be 0.75 consistent with previous STAR measurements. This level of statistical precision can be achieved with 30 million minimum bias events with the proposed TOF upgrade. Without the proposed TOF barrel, the number of events needed is 5-10 times greater, and this measurement is not feasible.

### 3.3 Event-by-Event Fluctuations and the Correlation Structure of Heavy Ion Collision Events

#### Introduction

Event-by-event analyses of fluctuations and correlations in heavy ion collisions are predicted to provide significant new information on the hot, dense system produced in relativistic heavy ion collisions and the search for color-deconfined matter. Theoretical studies [51]-[61] have concluded that large non-statistical event-wise fluctuations displaying non-monotonic dependence on collision parameters (*e.g.*, energy, ion species, centrality, rapidity range) should be observed if the evolving collision system passes through a QCD phase transition [51] or near a critical endpoint [57]-[59] or evolves hadronizing QGP droplets [51]-[56]. Some recent studies [62] have focused on the time interval from hadronization to kinetic decoupling and its effect on large-scale charge-dependent pseudorapidity correlations.

How are event-by-event fluctuations and correlations in RHIC events related to

collision dynamics and QCD? The system comprised of the two colliding nuclei prior to interaction is initially highly correlated (the entropy is extremely low). The collision process is one of correlation modification and reduction, or equivalently entropy increase. Correlations present during the earliest partonic interactions are expected to be transported from early to late-stage degrees of freedom by several mechanisms, including hydrodynamic response to early pressure in a glue-dominated medium, initial-state multiple scattering, dynamical interactions between the soft, prehadronic medium and hard scattered partons, color string fragmentation and modification by the prehadronic medium, critical correlations associated with a QCD phase transition, and hadronic processes later in the collision. Observation of structure in the hadronic final state depends in part on survival through dissipative processes during system evolution which include nonperturbative-QCD dynamics, the hadronization process itself, and final-state hadronic interactions.

It is precisely because of this that the correlations and fluctuations observed in the final state are important: they carry information on the various stages in the evolution of the matter. This information can be extracted in detail only with particle-identified spectra, since some dynamical/dissipative processes produce final state effects which scale with particle mass, and some do not. The mass dependence of the observed correlations and fluctuations provides clues as to which processes produced them. Based on correlation structures already observed in Au+Au collisions in STAR, large acceptance particle identification capability extending beyond the  $p_T$  range covered by  $dE/dx$  in the TPC + SVT is crucial for understanding this important and unique source of information.

### The QCD medium, velocity fields and dissipation

To unfold correlations and extract the information they carry, it is necessary to separate the effects of various underlying dynamical/ dissipative processes which may result in large scale collective motion (global "structure" in the overall "velocity field" of all the produced particles) or more localized effects such as local temperature (thermal) fluctuations which may affect the motion of smaller groups of particles. These concepts are familiar from heavy ion phenomenology [67]. Examples of large scale velocity fields include radial flow, elliptic flow, and Bjorken expansion. These are specific examples of a more general concept. The structure of the velocity field observed in the final state (the "velocity structure") is expected in general to be complex, since it contains contributions from the entire history of the collision.

Thermal and velocity correlation structures show up in heavy ion collisions as non-statistical fluctuations in event-wise averaged global quantities (*e.g.*, event-wise mean  $p_T$ ) and in two-particle momentum-space correlations [65]. Little is known at present about the detailed velocity structure of RHIC events. Distinguishing velocity structure and thermal fluctuations from equilibrated thermal energy in the hadron system requires particle identification (mass measurement) of pions, kaons, and protons for transverse momentum substantially beyond  $\sim 1$  GeV/c. In STAR, this can only be accomplished with the addition of the proposed barrel TOF detector.

Separate determination of velocity and thermal structures in RHIC events is essential because the velocity structure represents an otherwise unknown, fundamental degree of freedom of the collision system and because velocity and temperature fluctuations are affected differently by QCD dynamics. For example, localized energy perturbations (*e.g.* QGP droplets) could produce ‘hot spots’ which would be manifest in the data as local temperature fluctuations with respect to a characteristic scale in pseudorapidity and azimuth. Dynamics which produce structured pressure gradients in the early collision should produce event-wise (large scale) fluctuations in the velocity field. Minijets are expected to produce both local temperature and velocity fluctuations. Whether QCD dynamical processes result in thermal or velocity structure, both lead to momentum-space fluctuations and correlations in the unidentified hadron momentum distribution. Unambiguous interpretation of the resulting fluctuation and correlation structure with nonidentified particles simply is not possible.

Analysis of first RHIC data by STAR has revealed that Au+Au collisions have a complex correlation structure, including large-scale two-particle correlations in  $p_T$ ,  $\eta$ , and  $\phi$ , which provide direct access to a range of QCD phenomena available from no other experimental source. Charge-independent (isoscalar) and charge-dependent (isovector) correlation structures already being observed [64, 68] in distributions of relative two-particle transverse momentum ( $m_{t1} \otimes m_{t2}$  up to  $\sim 2$  GeV/c), pseudo-rapidity ( $\eta_1 \otimes \eta_2$  up to 2 units), and azimuthal angle ( $\phi_1 \otimes \phi_2$  up to  $\pi$  radians) are comparable in size to the STAR TPC acceptance. To fully extract the information these correlations carry and use it to understand the role of nonperturbative QCD in Au+Au collisions at RHIC requires particle identification ( $\pi$ , K, p) over the full STAR TPC acceptance, over a momentum range substantially exceeding that for dE/dx PID in the TPC+SVT. This can only be accomplished with the addition of the proposed barrel TOF detector.

### Correlations and fluctuations of transverse momentum

Under certain assumptions expected to be valid for central Au+Au collisions at RHIC (validity of the central limit theorem (CLT) [65], absence of internal correlations and fixed parent distribution), the mean and *rms* width of the event-wise  $\langle p_T \rangle$  distribution should be equal to  $\hat{p}_T$  and  $\sigma_{\hat{p}_T}/\sqrt{\bar{N}}$ , respectively, where  $\hat{p}_T$  and  $\sigma_{\hat{p}_T}^2$  are the mean and variance of the inclusive  $p_T$  distribution, and  $\bar{N}$  is the mean event multiplicity [65, 75]. The frequency distribution of event-wise  $\langle p_T \rangle$  for the 15% most central Au+Au collisions at  $\sqrt{s_{NN}} = 130$  GeV from STAR displays a  $13.7 \pm 0.1(\text{stat}) \pm 1.3(\text{sys})\%$  increased width compared to a gamma-distribution reference, which is the appropriate reference assuming finite-number statistics in the absence of non-statistical fluctuations [64, 74, 75]. This reference distribution is indicated as a dotted line in Fig. 7. The distribution in the variable  $(\langle p_T \rangle - \hat{p}_T)/(\sigma_{\hat{p}_T}/\sqrt{\bar{N}})$  minimizes systematic contributions from multiplicity fluctuations and variations of inclusive parameters with centrality.

It is possible to quantify the excess variance of  $\langle p_T \rangle$  observed in Fig. 7 using several

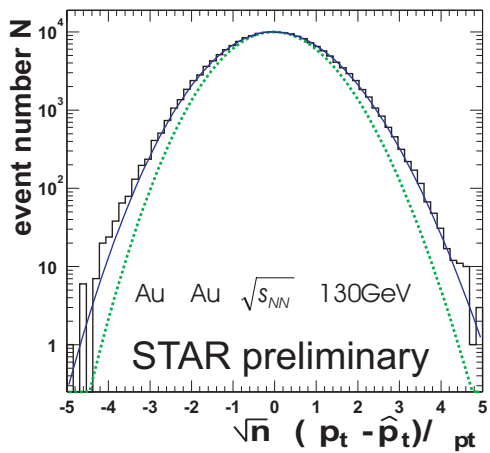


Figure 7: Mean- $p_T$  distribution for  $\sqrt{s_{NN}} = 130$  GeV Au+Au central collisions with respect to  $\hat{p}_T$  in units of  $\sigma_{\hat{p}_T}/\sqrt{N}$  compared to a gamma distribution reference expected in the absence of non-statistical fluctuations (dotted curve) and a gamma distribution calculated with an *rms* width increased by 14% (solid curve).

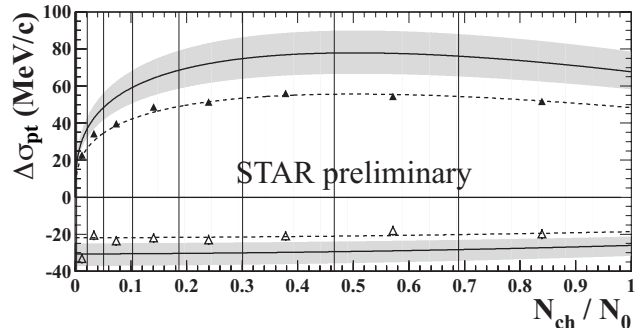


Figure 8: Centrality dependence for Charge Independent (CI) (solid triangles) and Charge Dependent (CD) (open triangles) fluctuation measure  $\Delta\sigma_{p_T}$  for 130 GeV minimum bias Au+Au events. The CD values are multiplied by 3 for clarity. The dashed lines are curve fits. Solid lines and bands reflect an extrapolation to 100% for primary charged hadrons in the detector acceptance and include a  $\pm 15\%$  systematic error.

quantities [63, 70], for example:

$$\Delta\sigma_{p_T}^2 \equiv \frac{1}{\varepsilon} \sum_{j=1}^{\varepsilon} N_j (\langle p_T \rangle_j - \hat{p}_T)^2 - \sigma_{\hat{p}_T}^2 \equiv 2\sigma_{\hat{p}_T} \Delta\sigma_{p_T}, \quad (2)$$

defines the difference variable  $\Delta\sigma_{p_T}$ . A closely-related differential measure is [70]

$$\Phi_{p_T} \equiv \left[ \frac{1}{\varepsilon} \sum_{j=1}^{\varepsilon} \frac{N_j^2}{\bar{N}} (\langle p_T \rangle_j - \hat{p}_T)^2 \right]^{1/2} - \sigma_{\hat{p}_T}, \quad (3)$$

where  $\varepsilon$  is the number of events,  $j$  is the event index,  $N_j$  is the event multiplicity, and  $\bar{N}$  is the ensemble-mean multiplicity. For small fractional variations of  $N_j$  within the event ensemble  $\Delta\sigma_{p_T} \cong \Phi_{p_T}$ .

The centrality dependence of  $\Delta\sigma_{p_T}$  is shown in Fig. 8 for 205k  $\sqrt{s_{NN}}=130$  GeV Au+Au minimum bias events. The number of charged particles measured per event over the maximum number observed in the sample  $N_{ch}/N_o$  is used as a relative measure of event centrality. These data were derived using 70% of all the primary charged particles (this is less than 100% due to tracking inefficiency and track quality requirements) for charge independent and charge dependent fluctuations [64, 74]. Statistical

errors are  $\pm 0.5$  MeV/c. The dashed lines are polynomial fits to the data, the solid lines are estimated extrapolations to 100% of the primary particles in the acceptance, and the shaded bands indicate a  $\pm 15\%$  systematic error.

This analysis provides a quantitative measure of the non-statistical fluctuations visually apparent in Fig. 7 and reveals an intriguing non-monotonic dependence on centrality which may be related to the growing influence of a dissipative (opaque) medium produced in the overlap region in central Au+Au collisions at RHIC. If true, this would represent important independent confirmation of results observed in back-to-back jet studies in STAR. However, to distinguish between thermal fluctuations and velocity structure –to really understand the origin of this newly observed behavior and what it is indicating–requires application of this analysis to identified hadrons. The particle identification capability of the proposed barrel TOF detector is needed to unambiguously interpret the meaning of this potentially definitive result.

### Event-wise fluctuations versus two-particle correlations

The enhanced event-wise fluctuations seen in Figs. 7 and 8 result in fact from projections of more general two-particle correlations. An example of the rich structure apparent simply by examining the two-particle correlation in relative transverse mass ( $m_{t1} \otimes m_{t2}$ ) is shown in Figs. 9 and 10. These distributions are simply plots of the ratio of the number of real to mixed-event particle pairs observed in a particular bin of  $(m_{t1}, m_{t2})$ . To have more or less uniform statistics in all bins, a transformation has been made which "flattens" the single particle  $p_T$  distribution and maps the  $m_t$  interval  $[m_0, \infty]$  onto the  $X$  interval  $[0, 1]$ . This minimizes statistical "noise" and allows correlation structure to be clearly seen. Most of the visible structure falls within the  $m_t - m_0$  interval  $[0.1, 2.0]$  GeV/c<sup>2</sup>. Fig. 9 provides a perspective view and Figure 10 a projection onto the  $X_{pT1} \otimes X_{pT2}$  plane with bin-by-bin intensity (occupation) indicated by color.<sup>1</sup>

These plots exhibit remarkable richness in the two-particle correlation structure in  $m_{t1} \otimes m_{t2}$ . The interpretation given the dominant features in the perspective view include quantum-interference (HBT) and Coulomb-interaction correlations which contribute to the diagonal ridge at low  $m_t$ . The peak at high  $m_t$  is presumably due to hard-QCD processes. The large-scale saddle shape which dominates the distribution is consistent with fluctuations in the effective temperature. All these features have similar amplitudes and represent non-statistical correlations (absence of correlation would be indicated by statistical fluctuations about unity). The event-wise analyses of excess  $\langle p_T \rangle$  fluctuations shown in Fig. 7 and Fig. 8 integrate over all sources of two-particle correlations seen in Fig. 9.

Several conclusions are drawn from these figures. First, two-particle distributions being observed in STAR are rich in structure, and therefore carry a wealth of information on various dynamical/dissipative processes that are important through the evolution of the collision. Secondly, the observed structure is coherent over a large

---

<sup>1</sup>Measured  $P_T$  was mapped to  $X(m_t)$ , where  $X(m_t) \equiv 1 - [(1 + m_t/T) \exp(-m_t/T)] / [(1 + m_0/T) \exp(-m_0/T)]$ ,  $m_t = \sqrt{P_T^2 + m_0^2}$ , and  $m_0$  was assumed equal to the pion mass.

scale. Examining one corner of the phase space in Fig. 9 would provide a very limited perspective on the global features of the full correlation. Third, to fully interpret the information carried by these correlations, particle identification is needed beyond the  $p_T$  range afforded by  $dE/dx$  in the TPC+SVT. One of the most interesting features is near  $m_t \sim 1 \text{ GeV}/c^2$ . This is in a range where the underlying particle composition producing this correlation structure is not known and can not be determined with the existing PID capability of STAR. This structure could be a result of an increasing two-particle correlation in the range of  $m_{t1} \otimes m_{t2}$  for a given species, or, it could be due to a change in the relative number of underlying particle species ( $\pi$ ,  $k$ ,  $p$ ), or both, or neither. If the speculation above is correct that this region is dominated by hard QCD processes, rough charge ordering should be observed, the correlation strength for pairs of same species and opposite sign should be strongest, and a reasonably well-known ratio of meson to baryon pairs would be expected. With the existing PID capability of the STAR TPC + SVT, this information is not available. To realize the full scientific potential of STAR for a robust study of QCD in relativistic heavy ion collisions, it is important to utilize every bit of information available. This is a clear and important example of a major source of unique information that will be lost without the additional PID capability provided by the proposed barrel TOF detector.

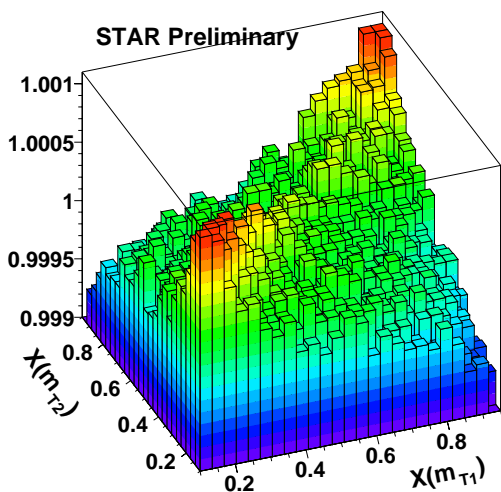


Figure 9: Perspective view of the two-dimensional  $X(m_{t1}) \otimes X(m_{t2})$  correlations for all charge independent correlations for  $\sqrt{s_{NN}}=130 \text{ GeV}$  Au+Au collision data.

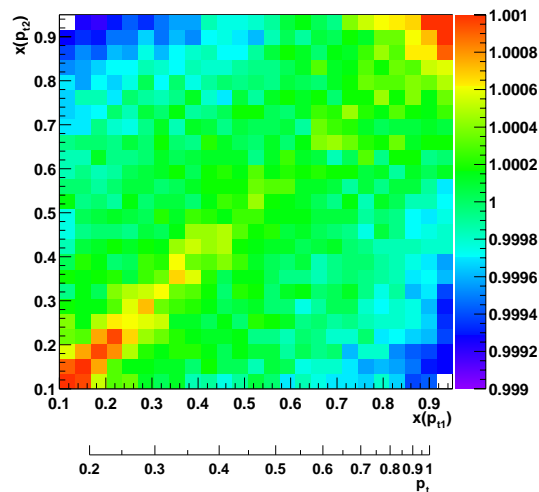


Figure 10: Transverse-mass two-particle  $X(p_{t1}) \otimes X(p_{t2})$  correlations for all charged hadrons in the top 15% most central collision events. Corresponding  $p_T$  values in  $\text{GeV}/c$  are shown in the lower horizontal scale.

The conclusions from this section are clear: there is a wealth of correlation structure being observed (some for the first time) in Au+Au collisions at RHIC in several two-particle phase space distributions. These correlation structures are capable of providing crucial information, unavailable otherwise, on important dynamical

cal/dissipative processes central to the evolution of heavy ion collisions at RHIC. Examples include hydrodynamic response to early pressure in a glue-dominated medium, initial-state multiple scattering, critical correlations associated with a possible QCD phase transition, nonperturbative-QCD dynamics, hadronization, and final-state hadronic interactions. To understand these processes, it is necessary to utilize the observed correlations and fluctuations to the fullest. This can not be done in STAR without the addition of the large acceptance particle identification capability that will be provided by the proposed barrel TOF detector. Without this upgrade, STAR will not have access to an important, and perhaps defining source of information to understand the new matter being created at RHIC.

### 3.3.1 Particle Flavor Dependent Fragmentation at Moderate $p_T$

At intermediate  $p_T$  ( $>2$  GeV/c), a description of the observed correlation structures in terms of jets and mini-jets becomes appropriate. In central heavy-ion collisions, it is impossible to fully reconstruct jets due to the large underlying soft particle production and finite probability of multiple hard interactions in a single Au+Au event. The presence of jets, however, can be inferred by measuring two-particle azimuthal and rapidity correlations [48]. These jet-like correlations are spread over a large region of phase-space ( $\Delta\phi \otimes \Delta\eta \approx 0.7$ ). STAR has observed such correlations for charged hadrons [49]. Correlations due to dijets occur over the full available phase-space of the collision. Thus, a large acceptance is vital for studying possible medium induced modifications of jet fragmentation in heavy-ion collisions.

The proposed barrel TOF would allow for two-particle azimuthal correlation studies for several particle species over a large phase-space. Specifically, it would be possible to identify for protons up to 3 GeV/c, and to measure the relative strengths of meson-meson, meson-baryon, and baryon-baryon azimuthal and rapidity correlations. These measurements would allow for a further understanding of particle flavor dependent fragmentation at RHIC energies and a deeper understanding of jet quenching phenomena in heavy-ion collisions.

The particle production mechanism(s) at moderate  $p_T$  are poorly understood in central Au+Au collisions. STAR has reported that hadrons above  $p_T=3$  GeV/c show azimuthal correlations characteristic of jet fragmentation [68]. In Figure 11, the analysis described in Ref. [68] is repeated for a trigger particle threshold of 2 GeV/c, which is accessible using the full TOF. The relative strengths of jet-like (squares) and dijet-like (circles) azimuthal correlations are plotted as a function of the number of participants. The jet-like correlations are slightly suppressed in the most peripheral collisions, and show an enhancement above the expectation from proton-proton collisions for the more central collisions.

PHENIX, on the other hand, reports a proton-to-pion ratio near unity in central Au+Au collisions, which is in contrast to the measured value of  $\approx 0.2$  in p+p collisions. This enhancement in the proton-to-pion ratio can have several explanations. One possibility is that protons at moderate  $p_T$  ( $\approx 2-3$  GeV/c) come primarily from soft processes such as hydrodynamical collective flow. In this case, there will

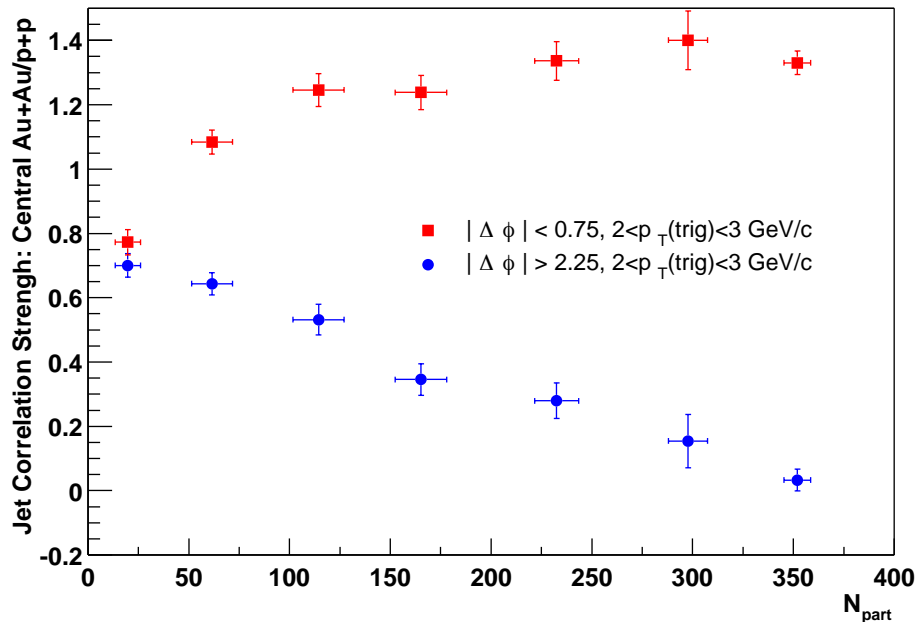


Figure 11: Relative azimuthal correlations for central Au+Au and minimum bias p+p collisions. The squares show the small-angle correlation strength, and the circles show the back-to-back correlation strength.

be no localized jet-like correlations between moderate  $p_T$  protons and other hadrons in the event. An alternative explanation for the proton-to-pion ratio is that initial state nuclear effects, including multiple nucleon-nucleon soft interactions, boost the proton-to-pion ratio in jet fragmentation. Identified particle azimuthal correlations can be used to distinguish between these two possibilities. If there is a large contribution to the proton yield from soft processes, azimuthal correlations triggered on a leading proton should show a large suppression. Alternatively, a medium induced particle flavor dependent jet fragmentation would lead to relative enhancements in the azimuthal correlations for leading protons over leading mesons. A systematic comparison between nucleus-nucleus and p+p collisions is also necessary to establish the possible flavor modification of jet fragmentation.

These measurements require large acceptance and the ability to distinguish mesons from baryons into the hard scattering regime. The full TOF coupled with the BEMC, EEMC and possible topological identification will lead to a thorough understanding of the mechanisms of particle production in the moderate  $p_T$  region where the transition from soft to hard processes is expected to occur.

### Particle identification, correlations and velocity structure

The previous material represents a partial summary of the correlation structures revealed from RHIC data. It is clear that a wealth of structure has emerged and that RHIC collisions may not be viewed as simple equilibrated systems. What role does



large-acceptance particle identification play in this analysis?

In the broadest terms, some of the questions being addressed at RHIC are:

- What evidence is there of hydrodynamic response to pressure gradients?
- Is correlation structure developing in a prehadronic medium with partial transmission through hadronization, or is all the structure observed a consequence of hadronic dynamics?

These types of questions cannot be answered by examining a limited part of the observed correlation structure using unidentified hadrons [66]. Ambiguous and conflicting interpretations can only be resolved by performing a general correlation analysis over a broader  $p_T$  interval than is currently accessible to TPC PID, so that detailed information on correlations and fluctuations of identified particles is available in the full acceptance of STAR. This requires the additional PID capability provided by the proposed barrel TOF detector.

An example of how the barrel TOF detector would provide information crucial for deciding between two possible interpretations of observed correlation structure is the following. Analysis of STAR p+p and Au+Au minimum-bias  $p_T$  distributions indicates that inclusive mean- $p_T$  ( $\hat{p}_T$ ) is approximately independent of particle mass (pions, kaons, protons) for p+p and peripheral Au+Au collisions and increases monotonically with centrality in proportion to particle mass [83]. Assuming the increase in  $\hat{p}_T$  with centrality is caused by increasing transverse expansion it is straightforward to conclude that for more central A+A collisions

- ‘temperature’ fluctuations in a locally-equilibrated system should produce mass-independent event-wise  $\langle p_T \rangle$  fluctuations, and
- transverse-expansion-velocity fluctuations should produce event-wise  $\langle p_T \rangle$  fluctuations which increase monotonically with particle mass.

Thus, mass dependence of  $\langle p_T \rangle$  fluctuations coupled with centrality dependence would provide a key test of the production mechanism for these fluctuations, the structure of the velocity field, the extent of local equilibration, and the nature of the medium. The observed CD correlation structures for nonidentified hadrons (mainly pions) should thus have counterparts for identified protons/antiprotons and kaons, structures depending on local baryon-number and strangeness conservation. The correlation lengths and amplitudes of these structures are presently unknown. Do different hadron types experience different medium properties, possibly at different times in the collision? Large-acceptance MRPC-TOF is required to answer these questions.

Simulations were done which demonstrate the particle mass dependence of the mean- $p_T$  fluctuation measure,  $\Delta\sigma_{p_T}(CI)$ . This was done for Monte Carlo events which included arbitrary mixtures of random, event-to-event fluctuations in both the temperature and the transverse flow. The events were generated by random sampling a Maxwell-Boltzmann parent distribution with temperature  $T$ . In addition to this

random, thermal motion an overall transverse expansion flow field was added to each particle’s velocity. This was done by assigning a random coordinate space position to each particle and computing a transverse flow velocity,  $\beta_t(r)=\tanh[\eta_t(r)]$ , where  $\eta_t(r)=\eta_f(r/R_{max})$ . This transverse boost velocity was added relativistically to the particle’s random thermal velocity to arrive at the total, final state particle velocity. The present model is consistent with other parametrizations of transverse expansion used in so-called “blast-wave” models to describe the  $p_T$  distributions and HBT radii in relativistic heavy-ion collision sources.

Twenty thousand (20K) events were generated in this manner for a number of cases in which the particle content consisted entirely of either charged pions (equal numbers of  $\pi^+$  and  $\pi^-$ ), charged kaons (equal numbers of  $K^+$  and  $K^-$ ), or protons and antiprotons. The local temperature average was  $T=100$  MeV, and the average transverse expansion boost parameter,  $\eta_f$ , was 0.9. The radial density distribution was assumed uniform (a box-like distribution) from  $r=0$  to  $R_{max}=9.0$  fm. The pseudorapidity and azimuthal distributions were assumed to be flat. These parameters are typical of those which describe the measured spectra shape and HBT radii at RHIC. Kinematic acceptances were  $p_T$  from 0.1 to 2.0 GeV/c,  $|\eta|\leq 1.0$ , and full  $2\pi$  azimuthal angle. Results for  $\Delta\sigma_{p_T}(CI)$  were scaled to an average multiplicity per event of 772 which is typical for charged pions in this acceptance in central Au+Au collisions at  $\sqrt{s_{NN}} = 200$  GeV.

Temperature fluctuations were simulated by randomly sampling a Gaussian distribution for the temperature parameter  $T$  where the sigma of the distribution was  $\sigma_T=0.0032$  GeV. Transverse flow fluctuations were similarly studied by event-to-event random sampling of a Gaussian distribution for the boost parameter  $\eta_f$  where  $\sigma_{\eta_f}=0.03$ . Combined temperature and transverse flow fluctuations were also studied where  $\sigma_T=0.0023$  GeV and  $\sigma_{\eta_f}=0.021$ . Each of these three cases results in similar values for  $\Delta\sigma_{p_T}(CI)$  for charged pions which approximate the measured results for STAR Au+Au collisions at 130 GeV.

Table I: Particle mass dependence of  $\Delta\sigma_{p_T}(CI)$  for pions, kaons, and protons assuming random event-to-event fluctuations in temperature, transverse flow velocity, or a mixture of both types of fluctuations. Units are in MeV/c.

Particle	$\sigma_T=0.0032$ GeV	$\sigma_T=0.0$	$\sigma_T=0.0023$ GeV
	$\sigma_{\eta_f}=0.0$	$\sigma_{\eta_f}=0.03$	$\sigma_{\eta_f}=0.021$
Pions	96	79	91
Kaons	67	167	123
Protons	27	196	104

The results are listed in Table I and shown in Figure 12 where it is seen that pure temperature fluctuations result in mean- $p_T$  fluctuations which decrease monotonically with particle mass due to the combined effects of fixed temperature fluctuation and

increasing effective temperature, whereas transverse flow velocity fluctuations cause  $\Delta\sigma_{p_T}$  (CI) to monotonically increase with particle mass. A mixture of both kinds of fluctuations produces intermediate results.

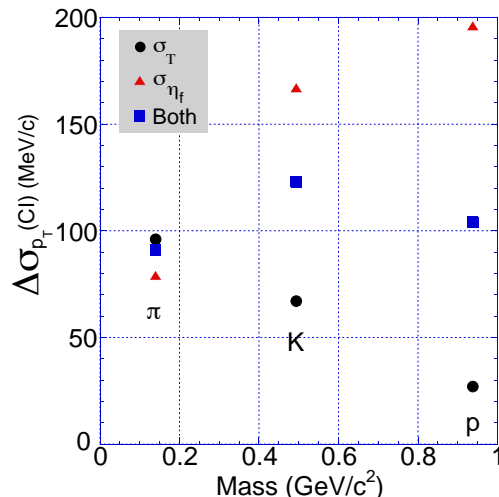


Figure 12: The expected behavior of  $\Delta\sigma_{p_T}$  (CI) as a function of particle mass assuming the dominant contribution to it is due to temperature fluctuations (black circles), fluctuations in the transverse flow velocity (red triangles), or a combination of both types of fluctuations (blue squares). Without the additional PID provided by the barrel TOF detector, measurement of  $\Delta\sigma_{p_T}$  as a function mass (this plot) *is not possible* over much of the  $p_T$  range of interest and essential information to interpret the origin of the observed  $\Delta\sigma_{p_T}$  is simply lost.

The simulations reported here were done for transverse velocity fluctuations. Similar studies could also be done for velocity fluctuations along the axial (longitudinal and azimuthal) directions. Mass dependent fluctuation/correlation analyses combined with spectra and HBT radii measurements would enable separate determination of the thermal and velocity fluctuation structure of RHIC events.

This is a clear demonstration of how the additional particle identification capability that would be provided by the barrel TOF detector is absolutely critical to understand the large scale correlations being observed and unambiguously unfold the importance of various essential dynamical/dissipative processes which affect the particle production observed in the final state. Without the proposed barrel TOF detector, these studies will be limited at best, and will serve mainly as a reminder that large acceptance PID up to intermediate  $p_T$  is essential to fully understand the history and evolution of the new matter being produced at RHIC.

### The two-arm spectrometer

It can be argued that the required reach in momentum difference variables could

be achieved with small acceptance coverage (and cost) by use of a ‘two-armed spectrometer’ to scan two-particle momentum space in small segments. The two-arm spectrometer alternative does not satisfy the stringent precision requirements for correlation analysis of nucleus-nucleus collisions. In elementary collisions (*e.g.*, e+e, p+p) two-particle correlations have amplitudes of order unity; a two-arm spectrometer may thus suffice for large-scale correlation analysis. The same physics in A+A collisions leads to observed correlations diluted by the event multiplicity which are therefore typically one *permil* in relative amplitude. For STAR’s large coverage the reduction of systematic errors below the permil level was achieved with powerful common-mode rejection techniques applied to the entire acceptance [72, 73, 84].

A+A event multiplicities with large-acceptance detectors provide the necessary statistical power to detect these small (permil) effects. Practical considerations of systematic error in precision measurements of large-scale correlations require that the entire acceptance be observed in each event to insure adequate common-mode rejection of systematic ‘noise.’

### Present and proposed particle identification capabilities

The study of large-scale fluctuations and correlations presented in the preceding sections would not be possible with identified particles using PID based on the present TPC and SVT  $dE/dx$  capabilities. Figs. 13 and 14 show simulated transverse momentum and pseudorapidity distributions for accepted and reconstructed protons and kaons respectively for existing methods and full-coverage ToF. The dramatic improvement in coverage on  $p_T$  for protons and kaons is evident. Significant improvement is even seen with pions (see Fig. 15). These simulations incorporate distribution parameters from a recent STAR analysis of 200 GeV Au-Au central-collision data, as well as total acceptance and efficiencies from detailed analyses of year-2000 130 GeV Au+Au central and minimum-bias data.

Simulations included fiducial acceptances, particle-decay loss, tracking inefficiencies, two-track merging, and particle-identification efficiencies for the present TPC  $dE/dx$  plus kink analysis<sup>2</sup> [85] PID (B - blue), PID with full TOF as proposed here (G - green), and perfect PID (R - red). From these figures we see that  $\langle p_T \rangle$  fluctuation studies following the trends described above, especially the requirement to connect the soft part of the two-particle  $p_T$  distribution to hard processes through the medium, are not meaningful for identified protons, kaons, and even pions without substantial ToF coverage, since the observed large-scale correlation structure in Figs. 9 and 10 at moderate and higher  $p_T$  is not then accessed.

This is more clearly illustrated in Fig. 16 which shows simulated  $X(m_t)$  distributions corresponding to Figs. 15 - 13. The values of  $T$  for approximately flat  $X(m_t)$  distributions for pions, kaons and protons are 175, 310 and 340 MeV, respectively. In Figure 16, the  $p_T$  distributions shown previously (Figs. 15, 14, and 13) are replotted

---

<sup>2</sup>This is a TPC tracking analysis method for charged-kaon identification in which single-prong decays or ‘kinks’ are identified in the TPC, where kinematic correlations between the parent particle momentum and the decay angle are used to select with minimal background  $K \rightarrow \mu + \nu$  and  $K \rightarrow \pi + \pi^0$  decays.

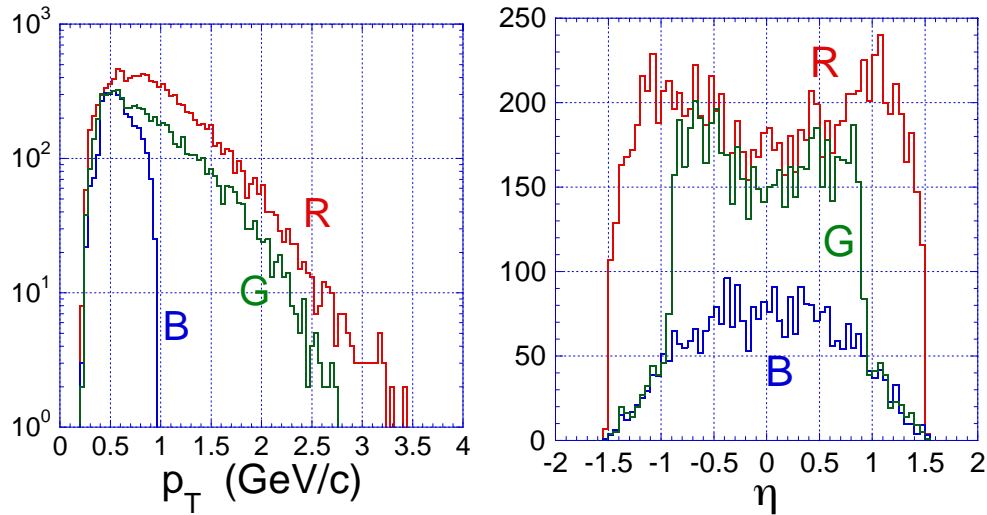


Figure 13: Simulated proton spectra versus transverse momentum (left) and pseudorapidity (right) for 200 GeV Au+Au central collisions for all accepted and reconstructed tracks (R - red), those identified using the TPC only (B - blue), and those identified using both TPC and full TOF (G - green).

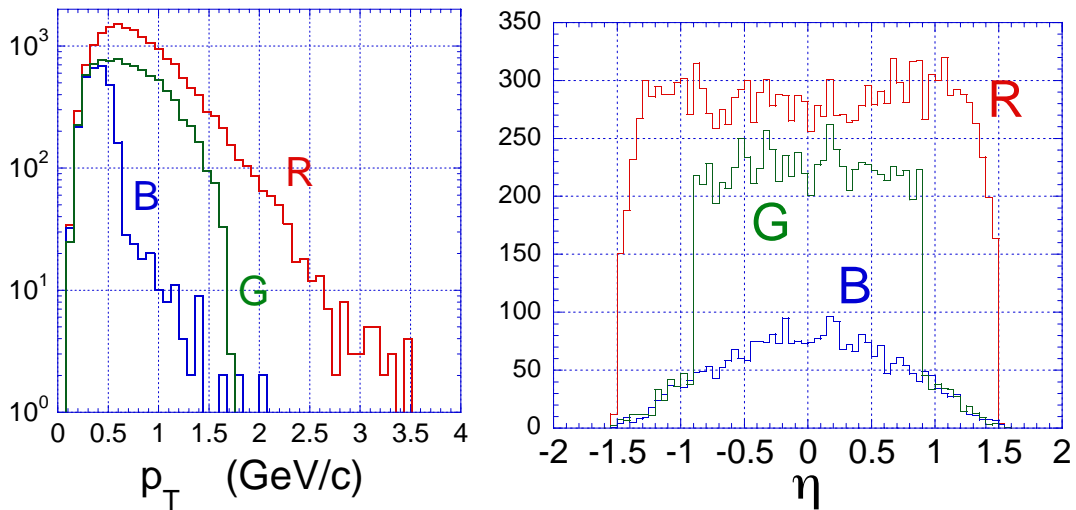


Figure 14: Simulated kaon spectra versus transverse momentum (left) and pseudorapidity (right) for 200 GeV Au+Au central collisions for all accepted and reconstructed tracks (R - red), those identified using the TPC only (B - blue), and those identified using both TPC and full TOF (G - green).

on  $X(m_t)$ . Shown in Figure 16 are the spectra for pions (left panel), kaons (center panel), and protons (right panel). The red (R), blue (B), and green (G) lines indicate the perfect PID (total reconstructed), TPC  $dE/dx$  and kink-analysis PID, and TPC plus full MRPC-TOF PID yields respectively. In the critical region  $X(m_t) > 0.7$  which contains the interplay between partially-damped hard-QCD processes and the

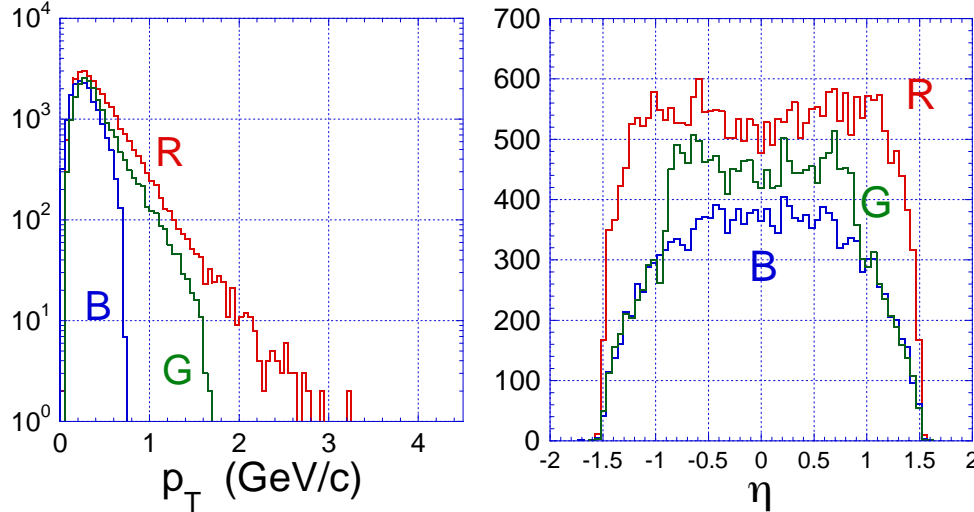


Figure 15: Simulated pion spectra versus transverse momentum (left) and pseudorapidity (right) for 200 GeV Au+Au central collisions for all accepted and reconstructed tracks (R - red), those identified using the TPC only (B - blue), and those identified using both TPC and full TOF (G - green).

structured dissipative medium the identified particle yield from TPC PID alone is virtually non-existent, while a reasonable yield (roughly 50%) of all three particle types is achievable with full MRPC-TOF. These arguments carry over to all aspects of large-scale correlation structure, including number as well as  $p_T$  correlations. The basic  $p_T$  continuity argument depends on the connection between hard processes at higher  $p_T$  and the results of dissipation in the soft  $p_T$  spectrum through the intermediary of the QCD medium, which is a primary goal of the STAR program.

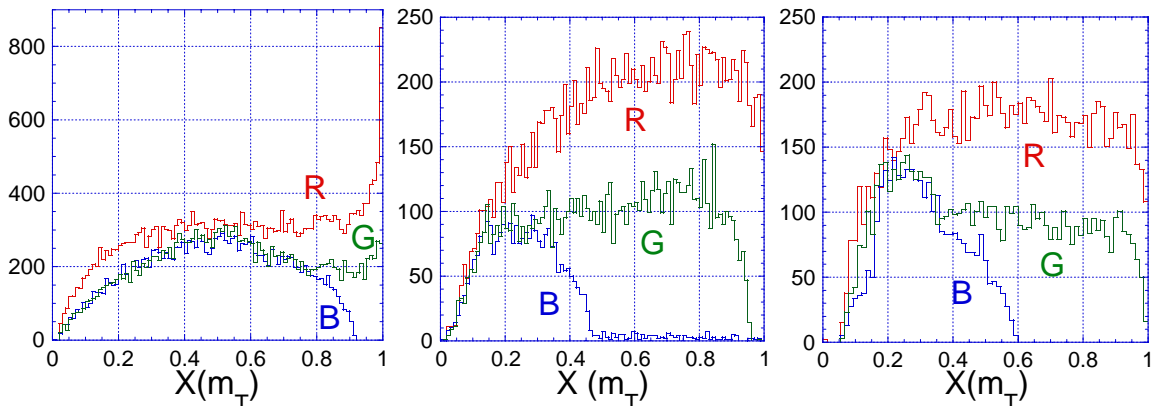


Figure 16: Simulated pion (left), kaon (center), and proton (right) spectra versus  $X(m_T)$  for 200 GeV Au+Au central collisions for all accepted and reconstructed tracks (R - red), those identified using the TPC only (B - blue), and those identified using both TPC and full TOF (G - green).

## Required data volumes

Unlike a number of the other physics topics discussed in the proposal, the studies discussed here in general do not require extraordinarily large samples of events. Event samples that number in the millions are adequate for most studies, although a systematic study as a function of beam energy, colliding species, *etc.* will require a number of such samples.

The important point for these physics studies is that *they are not possible at all without the addition of the proposed barrel TOF detector.*

That is because *without the extended reach in  $p_T$  for particle identification over the large acceptance of the proposed TOF upgrade detector, it is simply not possible to unambiguously relate the structure of the observed correlations and fluctuations to the underlying dynamical/dissipative/QCD processes which have produced them. A crucial source of unique information will simply be lost.*

## Summary

An initial survey of correlations and fluctuations in first-year RHIC events at  $\sqrt{s_{NN}} = 130$  GeV has revealed particle correlations rich in structure, including isoscalar and isovector correlations of hadron number and mean  $p_T$  on the variables  $(\eta, \phi)$ . Some of the physical mechanisms revealed were previously known in heavy ion collisions, some are familiar from elementary collisions but newly observed in heavy ion collisions, and some features are unique to RHIC collisions, giving us the first comprehensive look at the properties of a dynamically evolving QCD medium.

An initial survey has been completed with unidentified hadrons in the STAR TPC acceptance. Some of the novel physical mechanisms which produce these structures are suggested already by studies on collision centrality. Detailed study of thermal and velocity correlation structures can be pursued effectively with STAR using the scale-dependent fluctuation/correlation analyses described here, provided the most abundant hadron masses ( $\pi$ ,  $k$ ,  $p$ ) are measured. Full interpretation of revealed structure, for instance discrimination between thermal and velocity structures, relies on determination of mass dependence.

A common property of the newly-observed structures is their large characteristic scale relative to the STAR TPC acceptance, which is the largest available at RHIC for precision studies of identified particle momenta. The correlation lengths observed on pseudorapidity (2 units) and azimuthal angle (2 *rad*) in Au+Au collisions with STAR, together with the large range in transverse momentum (up to 1 - 2 GeV/c) required to span the interval from soft-QCD physics to perturbative-QCD hard scattering require the large coverage of a full-barrel MRPC-TOF detector in STAR. No other detector combination at RHIC can access this comprehensive and essential physics program.

### 3.4 Charm Meson Measurement

RHIC is the first heavy ion facility with a sufficiently high center-of-mass energy that the low Bjorken  $x$  behavior of the parton structure functions of the nucleon are directly relevant to the initial collisions of the colliding nuclei. At low Bjorken  $x$  the gluon distribution is dominant, and it is therefore expected that gluon dynamics will dominate the initial stage of the collision. An interesting conjecture is that at some scale of  $x$  and  $Q^2$ , the gluon distribution in the incoming nuclei is saturated, and that this may be reflected in the observed multiplicity [95].

Charm quark production in relativistic heavy ion collisions is particularly sensitive to the early gluon dominated stages of the collision. It can occur during initial parton-parton collisions, during the subsequent secondary parton cascade, and during the thermal expansion and rescattering processes which happen later [96, 97]. Most  $c\bar{c}$  production is expected to occur during the early partonic stages, much of it via hard gluon fusion,  $gg \rightarrow c\bar{c}$  production during the initial stage. The cross section for this process is known. During the later stage of the hot partonic system  $c\bar{c}$  production is also expected to occur, but the amount of such production depends strongly upon the initial temperature, thermalization time scale, and longitudinal space-momentum correlations [96]-[98]. Because the yield of charm is sensitive to the details of the early stages, the measurement of the charm production rate is very important for determining a proper description the initial conditions and the early stages of relativistic nucleus-nucleus collisions.

The information afforded by the measurement of charm production, and specifically by  $D$  mesons, is particularly robust since the yield of mesons with open charm is affected only weakly by final state interactions within the medium; charm quarks are produced during the initial stages; subsequently they are not created or annihilated; during final state rescattering they emerge from the collision, primarily as mesons or baryons with open charm. Studies of open charm differ in this respect from studies of the  $J/\psi$ , since the observed yield for charmonium is sensitive to screening in a color deconfined medium and final state hadronic scattering (medium) effects. The measurement of open charm is indeed an important "calibration" for the study of  $J/\psi$  suppression [99] or enhancement (the latter has been conjectured to be possible due to the coalescence of open charm [100]).

Studying the energy loss of partons in QCD matter is an exciting new possibility afforded for the first time by the high energy of the RHIC machine. Recently, the measurement of the suppression of high  $p_T$  particle production [101, 96], the identification of jet fragmentation, and the possible disappearance of "away-side" jets have generated considerable interest[49]. When a parton propagates through QCD matter, it loses energy by gluon bremsstrahlung. For a heavy quark, the amount of energy loss in the medium is expected to be lower than for a light quark due to suppression of gluon radiation at small angles (the "dead cone" phenomenon)[103]. This is expected to result in charm enhancement at moderate  $p_T$ . A calculation by Ref.[103] shows a factor of 2 enhancement of  $D/\pi$  ratio at 5 GeV in hot QGP matter compared to the yield expected in p+p collisions. The enhancement is about a factor of 1.2 in cold



nuclear matter.

For the reasons stated above, measurement of the yield and spectra of particles with open charm (in particular,  $D$  mesons) is particularly important to fully understand the nature and evolution of the new matter being produced at RHIC. Within STAR, the beam time and analysis effort required to perform a systematic study of open charm yields and spectra are prohibitive without the additional particle identification capability provided by the proposed large acceptance MRPC barrel TOF detector.

With the proposed barrel TOF, a systematic study of open charm is possible. It will focus on:

1. placing important constraints on the gluon structure function of the colliding nuclei through comparison of measured yields and spectra of  $D$  mesons with pQCD calculations of open charm quark production via gluon-gluon fusion
2. establishing a baseline for studying possible quarkonium ( $J/\psi$ ) suppression in a deconfined color medium by determining the amount of open charm being produced
3. probing charm quark dynamics in the partonic state through the measurement of transverse radial flow and possibly elliptic flow of mesons with open charm;
4. measuring possible energy loss of charm quark jets in the dense medium at intermediate  $p_T$ .

Without the proposed MRPC barrel TOF detector, the beam time and analysis effort required to achieve these goals are prohibitive. For example, with the present STAR detector (without TOF), to make a significant measurement of the yield of  $D$  mesons (integrated over  $p_T$ ) at the  $3\sigma$  level of significance requires  $\sim 12$  million events. (Measuring  $D$  meson spectra out to 4-6 GeV/c requires  $\sim 85$  million.) Based on previous experience, the time necessary to analyze 12 million events is  $\sim 10$  months. With the full barrel TOF detector, the number of events (and the time needed) are reduced by a factor of  $\sim 5$  (2.6M events). Since measurements with several beam species will need to be studied as a function of centrality, for a full systematic study, the measurement of open charm quickly becomes problematic without the additional PID capability provided by the proposed barrel TOF detector.

In STAR,  $D$  mesons will be measured by reconstructing their invariant mass through the  $K-\pi$  decay channel. Two approaches will be used: the event-mixing technique, subtracting combinatorial background from the invariant mass distribution for all possible  $D$  meson ( $K-\pi$ ) candidates, and direct reconstruction of  $D$  mesons by detecting a displaced decay vertex. To fully utilize the second technique a new STAR micro vertex detector will be needed. Currently this detector is in the R&D stage.

The proposed barrel TOF upgrade is absolutely essential to make a systematic study of the yield and spectra of open charm in STAR. Specifically, this upgrade will:

- allow the identification of a significantly greater percentage of the kaons and pions from the  $D^0 \rightarrow K^-\pi^+$  and  $\bar{D}^0 \rightarrow K^+\pi^-$  two-body decay channel, greatly improving the signal to background ratio in the reconstructed  $D^0$  invariant mass distribution. The centroid of the  $p_T$  distribution for kaons that survive STAR's acceptance and efficiency cuts is about 1 GeV/c. For kaons, PID based on  $dE/dx$  in the STAR TPC cuts off at  $\sim 0.6$  GeV/c. The proposed barrel TOF will extend PID for kaons to 1.7 GeV/c. As a consequence,  $5\times$  more kaons will be identified, and a better sampling of the kaon  $p_T$  distribution will be possible, greatly increasing the efficiency for  $D$  meson detection and reconstruction. The improvement will mainly be due to the reduction of combinatoric background. This reduction could be even greater in the future with the addition of a possible microVertex detector.
- significantly reduce the time and resources needed to perform a systematic study of open charm. Without the additional PID capability provided by the barrel TOF detector, the beam and analysis time required to utilize the large acceptance of STAR to systematically investigate the dependence of open charm production on beam energy, centrality, and beam species are prohibitive.

### 3.4.1 Simulation Results

This section presents results from simulation studies made to estimate STAR's capabilities for detecting neutral  $D$  mesons. These studies used TPC tracking and  $dE/dx$ -based particle identification (PID). Varying amounts of TOF coverage were then added. The event-mixing technique was used to extract an open charm signal by subtracting a combinatorial background. The resulting simulated invariant mass distribution was used to draw conclusions about STAR's ability to determine  $D$  meson yields and spectra. This technique will be used for real data as well, and is expected for a sufficiently large number of events to yield a peak at the  $D$  meson mass. It has been used successfully in STAR already to measure the yield of the  $K^{*0}$ . The effects of flow and nearby resonances are manageable.

The expected yield and spectra of  $D$  mesons is uncertain at RHIC. Recent PHENIX results [104], using single leptons at high  $p_T$  from the Au+Au  $\sqrt{s_{NN}} = 130$  GeV data, report  $dN_{c\bar{c}}/dy = 2.1$  with large statistical and systematic errors. Assuming most  $c\bar{c}$  production goes into  $D$  mesons and that 1/2 are neutral ( $c\bar{u}$  and  $\bar{c}u$ ), the estimated relative yield of  $(D^0 + \bar{D}^0)/h^-$  is 0.007. The slope parameter for the neutral  $D$  mesons'  $m_t$  spectrum is assumed to be approximately 300 MeV based on a general extrapolation of inverse slope versus mass [106] and extrapolations of the  $J/\psi$  slope versus energy density [107]. A Gaussian rapidity distribution with  $\sigma_y=2.0$  (typical for mesons produced at RHIC) is assumed.

Given these assumptions, the two-body decay channels  $D^0 \rightarrow K^-\pi^+$  and  $\bar{D}^0 \rightarrow K^+\pi^-$  were simulated; their branching fractions were taken to be 3.8%. The resulting  $D^0$  peak in the reconstructed  $K^-\pi^+$  invariant mass spectrum (pure decays only, no background) using all  $K^-$  and  $\pi^+$  particles which survive acceptance cuts, decay

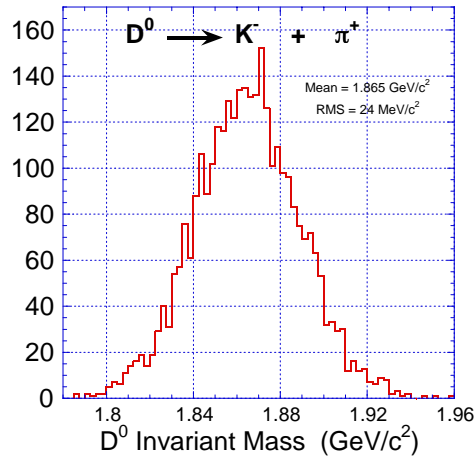


Figure 17: The resulting  $D^0$  peak in the reconstructed  $K^-\pi^+$  invariant mass spectrum (pure decays only, no background) using all  $K^-, \pi^+$  particles which survive the acceptance (including decay losses) and tracking inefficiency.

losses and tracking inefficiencies is shown in Figure 17. The observed width of 24 MeV/c<sup>2</sup> is mainly due to momentum resolution (typically 2-3%).

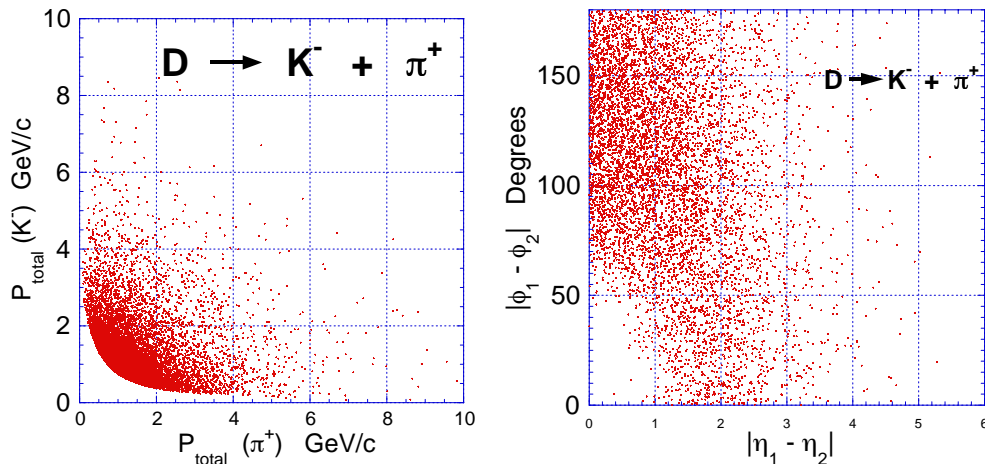


Figure 18: (left) Scatter plot of the total momenta of the daughter kaon versus the pion, and (right) the azimuthal angle – pseudorapidity correlation ( $\Delta\phi - \Delta\eta$ ) between the kaon and pion daughters from  $D^0$  decay.

Particle identification is most important for correctly identifying the charged kaon daughters from the  $D^0$  and  $\bar{D}^0$  two-body  $K\pi$  decay branches. This mainly serves to reduce the large combinatorial background in the invariant mass distribution. Precise measurement of the momentum of the daughter kaon is also necessary for good  $D$  meson invariant mass reconstruction. A scatter plot of the total momenta of the daughter kaon versus the pion from  $D^0$  decay is shown on the left in Figure 18. From

this figure it is seen that if TPC dE/dx PID were required for both decay daughters there would be *no D meson signal*, as TPC PID is only effective for momenta  $p < 600$  MeV/c. However, the TPC is capable of some limited identification of the daughter kaons. The azimuthal angle - pseudorapidity correlation ( $\Delta\phi - \Delta\eta$ ) between the kaon and pion daughters shown on the right in Figure 18 demonstrates the necessity of having a large acceptance TOF detector for efficient  $D$  meson measurement.

Table II: Statistical significance of  $D$  meson signal for a variety of particle ID options as a function of  $p_T$ . The last two columns are the number of events  $N_{events}$  required for a  $3\sigma$  signal in the invariant mass distribution for  $D^0 + \bar{D}^0$  mesons under different assumptions. HIJING was used as the basis for simulating the effect of TOF PID to provide data on backgrounds and charm production.

Description	$S(D^0)$	mass width	TPC PID	100% TOF
All $p_T$	0.066	23(MeV)	12M	2.6M
$4 > p_T > 2$ GeV	0.011	25(MeV)	59M	23M
$6 > p_T > 4$ GeV	0.0012	37(MeV)	85M	42M
$p_T > 6$ GeV	0.0002	45(MeV)	115M	115M

Background simulation and subtraction were performed for various assumed configurations using the  $p_T, \eta$  distributions of charged pions, kaons, protons, and antiprotons from the year 2000 STAR and PHENIX Au+Au top centrality data. An overall multiplicity rescaling factor (1.14) was used for 200 GeV data as well as the  $K^-/K^+$  and  $p/\bar{p}$  ratios for 200 GeV. The monte carlo generator MEVSIM was used to generate events, without  $D$  mesons, from which the background  $K+\pi$  invariant mass histogram was formed. Using the expected width of the  $D^0$  peak (assuming  $\pm 2\sigma$ ) the rate of background pairs was obtained for a variety of PID options. Using the same analysis approach, the  $D$  signal from simulations of pure  $D^0$ s was obtained. The signal-to-background ratio was determined by scaling the simulated signal to the assumed production rate for  $D^0$  (assumed to be 1.1 per unit rapidity) with the branching ratio, normalized to the rate of background pairs. With this information, the statistical significance of the signal was determined as a function of the number of events. The signal is obtained from  $S=Y-B$ , where  $Y$  is the total yield and  $B$  is the background under the peak. For this analysis the statistical error of the mixed event background was assumed to be much smaller than the signal sample so that the statistical error in the signal was dominant,  $\sqrt{Y} \approx \sqrt{B}$ . The statistical significance of the  $D^0$  signal is then,

$$\frac{S}{\Delta S} |_{D^0} = \frac{\bar{S}(D^0)}{\sqrt{\bar{B}}} \sqrt{N_{events}} \quad (4)$$

where  $\bar{S}(D^0)$  and  $\bar{B}$  are the number of true reconstructed  $D^0$ s per event and the number of background pairs under the peak per event, respectively. The statistical

significance of the combined  $D^0$  and  $\bar{D}^0$  signal was determined by multiplying this amount by  $\sqrt{2}$  assuming equal yields for  $D^0$  and  $\bar{D}^0$ .

Table II shows the sensitivity of  $D^0$  reconstruction to particle identification as function of  $p_T$ . With the addition of the full TOF detector, the measurement of the  $D^0/\pi$  ratio with 20% error at  $p_T \simeq 5$  GeV requires  $\sim 40$  million events. This measurement will directly test theoretical predictions about the energy loss of heavy (charmed) quarks in the early gluon-dominated stage of the collision, providing essential information about the properties of the produced matter. This measurement is challenging but feasible. Without the barrel TOF it is not possible.

In summary, with the present configuration of STAR the observation simply of the  $D$  meson yield requires  $\sim 12$  million events based on the statistical calculations presented here. With the proposed barrel TOF detector the number of events required is reduced by a factor of  $\sim 5$ . Using the barrel TOF detector the statistical significance of the  $D$  meson signal is maximized by requiring particle identification of (at least) the daughter kaon. In this scenario a robust measurement of the yield of neutral  $D$  mesons should be possible in a single (nominal) RHIC year of running. This measurement will provide an essential baseline on charm production to help "calibrate"  $J/\psi$  suppression (enhancement) studies. It will also provide a first measurement of the spectra ( $p_T$  dependence) for  $D$  meson production, providing important initial results concerning the  $D/\pi$  ratio as a function of  $p_T$  to study heavy quark energy loss and suppression of gluon bremsstrahlung due to the "dead cone" effect in hot partonic matter. These studies are not possible with the projected amount of running time and analysis capability available without the additional particle identification provided by the proposed barrel TOF detector.

### 3.5 Physics of Resonances at RHIC

In a thermal statistical description of nucleus-nucleus collisions the dynamical evolution is thought to be marked by two epochs: chemical freeze-out when particle production stops and kinetic freeze-out when particle interactions cease and stable particles free-stream to the experimental detectors. Between these times, particles continue to interact through elastic collisions without changing particle flavor. In this picture, the chemical freeze-out stage separates the partonic (early) stage from later hadronic evolution.

In order to understand the evolution of the produced matter after hadronization, it is necessary to understand the properties of the system between chemical and kinetic freeze-out. This can be accomplished using resonance production to probe dynamics between these stages. After their initial formation, the number and kinematic distribution of resonances continues to evolve through decay, rescattering, and re-generation. By systematically measuring a number of different resonances with a range of lifetimes (from a few to several tens of fm/c) it is possible to map out the dynamical evolution of nucleus-nucleus collisions between chemical and kinetic freeze-out.

Within STAR the resonances studied thus far include the  $\rho$ ,  $\Delta$ ,  $f_0$ ,  $K^*$ ,  $\Sigma(1385)$ ,  $\Lambda(1520)$ , and the  $\phi$ . The physics goals of these resonance measurements are:

1. to provide stringent constraints on theoretical models of particle production at RHIC. Resonances contribute significantly to the production of stable particles in the final state and the contribution from various resonances must be accounted for in detail by models of particle production.
2. to study the effect of the dense medium on resonance properties. In particular, properties such as the mass and width of short-lived resonances such as the  $\rho$  meson (which contributes to the dilepton mass spectrum) have been predicted to be sensitive to the properties of the medium in which they are formed.
3. to provide an important probe of the time evolution of the system from chemical to kinetic freeze-out. Since the lifetime of short lived resonances is comparable to that between chemical and kinetic freeze-out, their survival probability depends strongly on the time duration of the evolution and the density of the local medium.
4. to provide a measurement of flavor dependence of particle production at intermediate  $p_T$  ( $\gtrsim 2$ -3 GeV/c) for studying the transition between the soft physics and hard scattering regimes.

The study of resonances provides essential information unavailable otherwise about the evolution of the later stages of the collision from hadronization to the final state. Without the proposed barrel TOF detector, this study is seriously compromised due to the amount of combinatoric background and the limited range of  $p_T$  over which resonances can be studied. The proposed barrel TOF detector will:

- provide PID for the decay products of resonances. Since the  $K/\pi$  ratio is  $\sim 15\%$  and the  $p/\pi$  ratio is  $\sim 10\%$ , the combinatoric background in the present STAR setup for decays containing a kaon or a proton is very large. The additional PID capability from the barrel TOF will significantly reduce this background.
- reduce significantly the background from correlated pairs (decays of real particles) from the same event that lie underneath the resonance mass distribution of interest so that reliable information on the invariant mass, width, and branching ratio can be extracted for a given resonance. This is particularly important for resonances with very short life-times, such as the  $\rho$ ,  $\Delta$ , and  $\Lambda(1520)$ , which have irregular underlying background shapes. ( $K^*$  decays, for example, form a significant background under the  $\rho$  mass peak.)
- allow the measurement of rare and wide resonances such as  $\Lambda(1520) \rightarrow p+K$ , which cannot be measured well in central Au+Au collisions with the current STAR configuration due to background.
- extend the measurement for many resonances to the intermediate  $p_T$  region, which is essential to disentangle collective expansion dynamics from hard-scattering contributions. Collective expansion results in a  $p_T$  dependent modification of the primordial production of resonances which depends on the resonance lifetime.
- allow STAR to fully detail final state hadron (in particular resonance) production at RHIC as a function of beam energy, collision centrality and colliding species. This can only be achieved with the proposed barrel TOF detector with an acceptance matching that of the existing SVT, TPC and barrel EMC.

### Resonance Production in Heavy Ion Collisions:

In order to understand collision dynamics in nucleus-nucleus interactions it is imperative to make precise measurements of resonance production because it is a key process dominating the yield of most stable particles in the final state. In order to fully characterize properties of a possible new form of matter at RHIC, the features of resonance matter must be understood. Because of its large acceptance STAR is uniquely positioned at RHIC to make a comprehensive study of the full spectrum of produced resonances, provided it has the additional particle identification capability provided by the barrel TOF detector. Without the proposed barrel TOF system large combinatoric backgrounds and the limited range of  $p_T$  accessible for identified particles with the existing STAR setup are a limiting factor.

The proposed barrel TOF detector upgrade will significantly extend STAR's ability to make a comprehensive study of resonances. Specifically, precision measurements of the  $\rho$ ,  $\Delta$ , and  $\Lambda(1520)$  resonances over a wide  $p_T$  range will be made to extract their yield and  $p_T$  spectra in central heavy ion collisions. The measurement of the  $p_T$  spectra in particular is problematic with the present SVT+TPC only. In addition,

the barrel TOF upgrade will significantly improve the measurement of the  $\phi$  and the  $K^*$  compared to what is possible using the STAR TPC alone. With the improved signal to background afforded by the barrel TOF, important measures such as elliptic flow will be determined with precision over a broad range of  $p_T$ .

The precise measurement of resonance production possible with the barrel TOF detector will also provide essential information needed to constrain models of particle production. The soft processes of QCD (e.g., hadronization) are not calculable using a perturbative approach. Progress in understanding such processes relies instead on testing the predictions of phenomenological models of particle production. In  $e^+e^-$  collisions, string fragmentation has been successfully used in Monte Carlo Models in an empirical approach to describe the data [116]. In nucleus-nucleus collisions, thermal statistical models of particle production have been used with success to fit experimental data and extract thermal parameters such as temperature and chemical potential at the AGS, SPS, and RHIC [118]. Important questions remain as to whether thermal models truly provide a fundamental description of the collision. An important factor in understanding the extent to which these models fully describe heavy ion collisions will be to understand in detail the yield of stable particles coming from the feed-down of resonance decays. This will provide stringent constraints on thermal statistical models, as well as transport models such as UrQMD and AMPT [119]. The comprehensive study needed to acquire information for a large number of resonances over a range of  $p_T$  can only be accomplished with the additional particle identification capability provided by the proposed barrel TOF detector.

### Medium Effects in Hot and Dense Matter:

In heavy ion collisions, one of the most interesting predictions about the hot, dense medium produced at RHIC is that it may result in a modification of hadron mass, width, and branching ratios (see [110, 114] and references therein). To study this effect in detail, precise measurements are necessary. Recent RHIC results [115] indicate that resonances with large width can have a different mass from the nominal one due to the phase space population of the particles which create the resonance (e.g.  $\pi^+\pi^-\rightarrow\rho$ ). Rescattering can also modify the resonance mass and width.

Fig. 19 shows the invariant mass distribution of  $\pi^+\pi^-$  from Au+Au and p+p collisions. These measurements represent the first direct observation of  $\rho$  decays into the  $\pi\pi$  channel in relativistic heavy ion collisions. Despite this important achievement, the most important information potentially available from this measurement is significantly compromised, since the  $\rho$  mass distribution, particularly for  $p_T > 1$  GeV/c, contains a sizeable contamination from misidentified particles. The contamination is mainly due to misidentifying the  $K^*\rightarrow K+\pi$  daughters as a  $\pi^+\pi^-$  pair. This is a prime example of how contamination poses a fundamental limitation in extracting crucial information about possible in-medium modification of the resonance mass and width (in this case the  $\rho$  as a function of  $p_T$ ). With the proposed barrel TOF, the  $\rho$  would be cleanly identified up to a  $p_T$  of  $\sim 3$  GeV/c. This is an example of why the barrel TOF detector is essential. With the additional PID capability afforded by this detector, STAR will be able to extract essential information on the characteristics of



the medium in which resonances are produced and the effect of the medium on their hadronic decay channels.

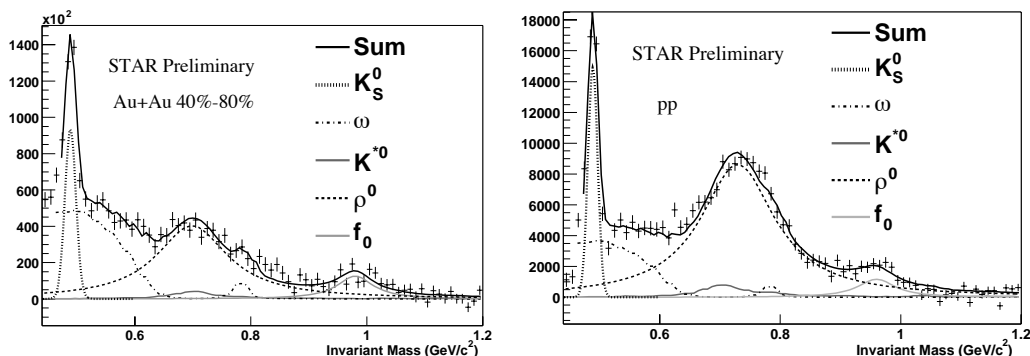


Figure 19: The  $\pi^+\pi^-$  invariant mass distribution after background subtraction from 40%-80% Au+Au (left) and p+p (right) collisions.

## Simulation Results

STAR's enhanced capabilities for resonance studies with the TOF are illustrated here using the  $K^{*0}$ ,  $\phi$ , and  $\Lambda(1520)$  resonances. Both the  $K^{*0}$  and  $\phi$  were observed in STAR's first run [105, 121], with spectra measured out to about  $p_T \sim 2$  GeV/c. The yields for these resonances were obtained from invariant mass distributions after subtracting a mixed event background. In principle, particle identification is not required to simply observe these short lived resonances. However, precise measurement requires the PID capability of the proposed barrel TOF detector to reduce the combinatorial background, and increase the ratio of signal-to- $\sqrt{\text{background}}$  per event. A further improvement afforded by the barrel TOF would be to remove other residual backgrounds and peaks which remain after mixed event background subtraction due to nearby resonances, misidentified decay daughters, and particle correlations from other dynamical sources. These residual backgrounds are clearly seen in the  $K^{*0}$  analysis [105] and other preliminary resonance analyses of STAR data. A significant reduction in the combinatorial background will reduce this background as well, further enhancing the signal to background ratio.

Simulations were performed for the  $K^{*0}$  and  $\phi$  resonances using a mixed-event background for Au+Au  $\sqrt{s_{NN}}=200$  GeV collisions similar to the one described in the preceding section for  $D$  mesons. The statistical significance per event,  $\bar{S}/\sqrt{\bar{B}}$ , was determined with and without the proposed TOF upgrade. The quantity  $(\bar{S}/\sqrt{\bar{B}})^2$  indicates the reduction in the number of events required for the same level of significance on the signal. This is taken to be a figure of merit for the improvement possible with the proposed barrel TOF. The results are shown in Table III.

Fig. 20 (left panel) shows the contamination in the  $K^* \rightarrow K + \pi$  invariant mass spectrum due to the misidentification of pions as kaons. The uncertainty in the determination of the  $K^*$  signal is about 20%. It is strongly dependent on the detailed shape of the background. The barrel TOF detector will remove this contamination

Table III: For the  $K^{*0}$ ,  $\phi$ , and  $\Lambda(1520)$ , the ratio as a function of  $p_T$  of the figure of merit  $(\bar{S}/\sqrt{\bar{B}})^2$  obtained with full TOF + TPC to that for the TPC only. The inverse of these numbers equals the reduction factor in the required number of events while still achieving the same statistical significance of the signal.

Resonance	Parent $p_T$ (GeV/c)	TPC+TOF
$K^{*0}$	0 - 1	2.0
$K^{*0}$	1 - 2	1.85
$K^{*0}$	2 - 3	1.74
$K^{*0}$	3 - 5	1.39
$\phi(1020)$	0 - 2	5.0
$\phi(1020)$	2 - 5	3.42
$\Lambda(1520)$	0 - 1.6	11.4

and significantly reduce this uncertainty. A full GEANT simulation with the present STAR detector and the inclusion of the barrel TOF detector was performed to study the background, detector response, occupancy and efficiency of the TOF. Fig. 20 (right panel) shows the dramatic improvement possible in reducing the residual background with the addition of the barrel TOF detector. In this case the background is essentially gone.

The proposed barrel TOF detector will significantly reduce the combinatorial background for the entire spectrum of resonances of interest in STAR. A further example of particular interest is the  $\Lambda(1520)$ . The proposed barrel TOF will cleanly identify both its decay products (proton and kaon), removing the large combinatorial background from pions. This background reduction is particularly important for the higher  $p_T$  region where both the proton and kaon are beyond the PID capability of the existing TPC+SVT.

The simulation performed here was for decay daughters with  $p_T$  up to 1.6 GeV/c. HIJING was used to simulate the background. The yield of  $\Lambda(1520)$  per central Au+Au collision was estimated to be 0.6 using Au+Au data from RHIC. With the proposed barrel TOF detector, the level of significance of the  $\Lambda(1520)$ , *i.e.* the signal divided by the square root of the background, increases relative to that for the TPC alone (2.1) to 7.1. This corresponds to a factor of  $\sim 3.4$  resulting in a reduction in the number of events required to achieve the same level of significance by a factor of  $\sim 11.4$ .

Figure 21 shows the expected  $\Lambda(1520)$  signal from approximately 1.7M central Au+Au events. With the proposed barrel TOF detector, precision measurement of the  $\Lambda(1520)$   $p_T$  spectrum is possible from several million events. Without it, measurement of the  $p_T$  spectrum would require approximately an order of magnitude more.

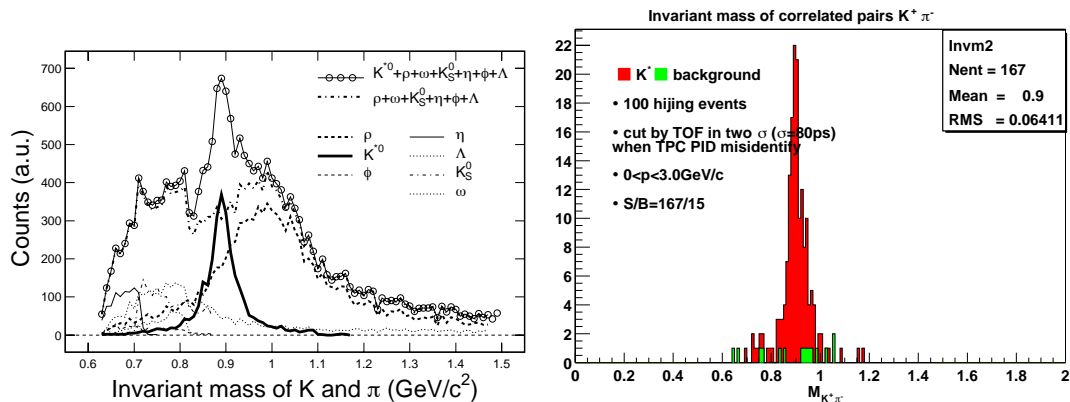


Figure 20: Left: Correlated  $K+\pi$  pairs from  $K^{*0}$  decay (open symbols). For  $K_S^0$  (thin dot-dashed line),  $\rho$  (thick dashed line),  $\omega$  (thin dotted line), and  $\eta$  (thin solid line), assuming of their decay pions is misidentified as a kaon. For the  $\phi$  (thin dashed line), one of its decay kaons is presumed to be misidentified as a pion. For the  $\Lambda$  (thin short-dashed line), the decay proton is misidentified as a kaon. These are realistic assumptions given the limitations of particle identification in the STAR TPC. The total background for  $K^{*0}$  is shown as thick dot-dashed line. The  $K^{*0}$  signal is shown as thick solid-line. Simple PID from specific ionization ( $dE/dx$ ) in the TPC was used for this simulation. The events are HIJING Au+Au collision at 130 GeV. Right: Correlated  $K+\pi$  pairs from  $K^{*0}$  after applying the PID cuts from the proposed barrel TOF detector.

In summary, a comprehensive systematic study of resonance production is crucial to fully understand particle production at RHIC, and details of the later stages of Au+Au collisions. Due to its large uniform acceptance, STAR is uniquely positioned to carry out this study, provided it has the additional PID capability afforded by the the proposed barrel TOF detector.

Without the proposed upgrade, the measurements discussed here will require many tens of millions of events throughout the lifetime of the experiment. With the proposed barrel TOF detector the required amount of data for precision studies of the  $K^*$ ,  $\phi$ , and  $\Lambda(1520)$  is reduced by factors of 2, 5 and 11.4, respectively.

The savings in the required data volume makes the difference in determining whether a comprehensive study of resonance production and a full understanding of particle production at RHIC are possible or not. Without the additional PID capability from the proposed TOF barrel, correlations from particle misidentification result in considerably larger systematic uncertainty in resonance measurements. This will prevent detailed conclusions to constrain models of particle production and to study in-medium modification of hadron properties. The proposed barrel TOF is essential to increase the statistical significance of the signal available for resonance studies and decrease systematic uncertainties. Precision measurement of resonances is an important step to disentangle conventional hadronic dynamics from properties of the new matter created in nucleus-nucleus collisions at RHIC.

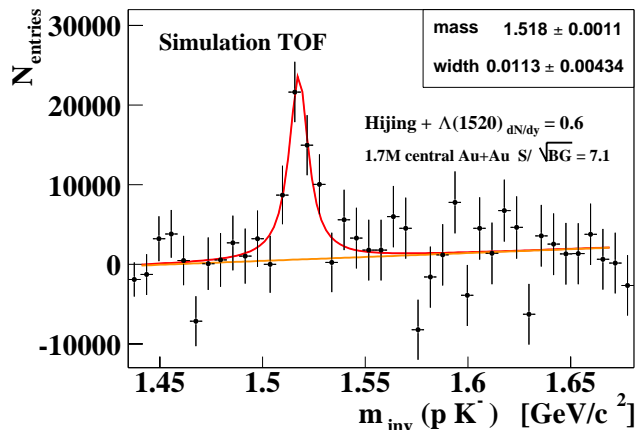


Figure 21: Expected  $\Lambda(1520)$  signal from 1.7M central Au+Au collisions with the proposed TOF detector. Without the barrel TOF detector the significance of the  $\Lambda(1520)$  is only 2.1 for  $p_T$  up to 1.6 GeV/c. The proposed barrel TOF upgrade increases the significance of the signal by a factor of  $\sim 3.4$ , resulting in a reduction of 11.4 in the number of events required to achieve the same level of significance. With the proposed barrel TOF detector, precision measurement of the  $\Lambda(1520)$   $p_T$  spectrum is possible from several million events. Without it, measurement of the  $p_T$  spectrum would require approximately an order of magnitude more.

### 3.6 Searches for Exotic Dibaryons

Nucleus-nucleus collisions provide a unique environment for possible production of multiply strange dibaryons, which could be formed through coalescence of hyperons in the final state or hadronization of the quark-gluon plasma. Initial STAR measurements of anti-deuterons at RHIC indicate that the coalescence probability is not significantly reduced at RHIC compared with that at lower energies [136]. There are several advantages for formation of strange dibaryons by coalescence at RHIC energies. First, the absolute yield of hyperons at RHIC is significantly higher than that in nucleus-nucleus collisions at lower energies, which compensates for a possible reduction in the coalescence probability. Second, at RHIC energy the production of anti-baryons is comparable with that of baryons. This allows a systematic study of particles and anti-particles, which have different backgrounds. Third, searches for certain exotic particles such as a  $[\Omega-\Omega]$ , are feasible at RHIC energy since there are enough  $\Omega$ 's produced per collision that coalescence formation for the  $[\Omega-\Omega]$  dibaryon is possible.

Three dibaryon candidates are of particular interest: the H or  $[\Lambda-\Lambda]$ , the  $[\Xi-p]$  (J), and the  $[\Omega-\Omega]$ . The H particle was the original dibaryon (uuddss) state proposed by Jaffe over two decades ago [138] (sometimes denoted  $[\Lambda-\Lambda]$  if very weakly bound). The decay channel suitable for the STAR detector system is  $H \rightarrow \Lambda + p + \pi^-$ , where the  $\Lambda$  further decays to  $p + \pi^-$ . The  $[\Xi^0-p]$  dibaryon [139] is above the  $\Lambda\Lambda$  threshold. It cannot decay to two  $\Lambda$  hyperons because of charge conservation. The  $[\Xi^0-p]$  can decay

weakly into a  $\Lambda+p$  in the final state, which could be detected in the STAR TPC.

The proposed TOF detector will add two important capabilities which are critical for a sensitive search for exotic dibaryons: 1) the time-of-flight measurement provides crucial particle identification (PID) needed for the decay daughters to reduce the background level. This is particularly significant when the decay daughters are protons or kaons; 2) with the reduction in background afforded by TOF PID, geometrical cuts in decay topology such as the cut on the distance of closest approach of the decay daughters and the decay vertex of the parent can be modified to increase the detection efficiency while keeping similar signal to background ratios. This increase in the detection efficiency is critical for searches of exotic particles, in particular for the  $[\Omega-\Omega]$  dibaryon.

Recent theoretical calculations based on a chiral SU(3) quark model and analyses of the symmetry properties of two-baryon systems indicate that the  $[\Omega-\Omega]_{0+}$  is the most interesting possibility for a dibaryon state [140, 141, 142]. It is predicted to be deeply bound, with a binding energy close to 100 MeV; it is also a very compact object with the mean-squared distance between the two  $\Omega$ 's being approximately 0.63 fm, much smaller than the size of the deuteron. It is possible that a tightly bound di-Omega state may even be a six strange quark state, rather than a dibaryon configuration. The  $[\Omega-\Omega]$  is a charge two state. The Coulomb interaction was included in the estimate of the mass. Both two-body and three-body decay channels are available: the three body decay modes are,

$$\begin{aligned} [\Omega - \Omega]_{0+} &\rightarrow \Omega^- + \Xi^- + \pi^0, \\ [\Omega - \Omega]_{0+} &\rightarrow \Omega^- + \Xi^0 + \pi^-, \\ [\Omega - \Omega]_{0+} &\rightarrow \Omega^- + \Lambda + K^-, \end{aligned}$$

The two body decay mode is,

$$[\Omega - \Omega]_{0+} \rightarrow \Omega^- + \Xi^-.$$

These are all weak decay modes with an expected mean lifetime time on the order of  $10^{-10}$  sec. Although these predictions are from a chiral SU(3) quark model, it is noted that the symmetry property of  $[\Omega-\Omega]_{0+}$ , and in particular the quark exchange effect between the two  $\Omega$ s, plays an important role in forming the  $[\Omega-\Omega]_{0+}$  as a deeply bound state. The qualitative physical picture for the  $[\Omega-\Omega]$  does not depend sensitively on details of the theoretical model.

There is no solid theoretical framework which can be used to reliably estimate the production rate of a possible  $[\Omega-\Omega]$  dibaryon in nucleus-nucleus collisions at RHIC. A comprehensive experimental program to search for these dibaryons is the only approach to deepen our understanding of the possibility for its production. Phenomenological estimates based on coalescence and/or statistical production predict an  $[\Omega-\Omega]$  yield ranging from  $10^{-4}$  to  $10^{-7}$  per central Au+Au collision [143, 144]. For example, in a thermal statistical hadronization model, the particle yield is proportional to  $m^{3/2}e^{-m/T}$ . Assuming a  $T \sim 170$  MeV at chemical freeze-out, the ratio of

$[\Omega\text{-}\Omega]$  to  $\Omega$  yield is found to be approximately  $1.5 \times 10^{-4}$ , corresponding to a rapidity density of  $[\Omega\text{-}\Omega]$  in central Au+Au collisions at 200 GeV of  $\sim 5 \times 10^{-5}$ . In order to reach a meaningful sensitivity for the  $[\Omega\text{-}\Omega]$  search, it is essential to use a large acceptance detector with high detection efficiency for hyperon decays.

The proposed barrel TOF detector, which matches the TPC acceptance in the mid-rapidity region, will significantly enhance the hyperon detection efficiency. Figure 5 shows the detection efficiency of  $\Omega$  with and without the PID capability afforded by the proposed barrel TOF. The increase in the  $\Omega$  detection efficiency due to the TOF PID over that of TPC+SVT is  $p_T$  dependent. For  $\Omega$   $p_T \sim 2$  GeV/c, where most of the reconstructed  $\Omega$ 's yield is, the enhancement in the detection efficiency is between a factor of 5 and 10.

It is estimated that a sensitive  $[\Omega\text{-}\Omega]$  search program can be carried out using the barrel TOF system with a data sample of  $\sim 100$  million central Au+Au collisions. The measurement will challenge the limits of STAR's present capability but it is feasible. Without the proposed barrel TOF system, it is not possible.

In conclusion, it is emphasized that experimental searches for dibaryons at RHIC will potentially provide a major scientific advance in the understanding of multi-hyperon systems based on a QCD inspired physical picture. In spite of the many theoretical and experimental uncertainties which must always be confronted when entering a new regime, the experimental search for dibaryons is a worthwhile scientific endeavor at RHIC. The STAR TOF upgrade will greatly aid in the search for a possible di-Omega state.

### 3.7 Additional Important Physics Benefits

In addition to the science measurements described in the preceding sections, there are additional studies in STAR where the PID capability provided by the proposed TOF upgrade results in a quantitative improvement. Two such studies are momentum/space-time correlations of identical and non-identical particles, and production of anti-nuclei.

#### 3.7.1 Identical and Non-identical Two-Particle Correlations

The measurement of momentum/space-time correlations for identical and non-identical particles in nucleus-nucleus collisions can provide important information on particle production regarding the source geometry, temporal emission pattern, and geometrical correlations with the reaction plane. Initial measurements in STAR of Hanbury-Brown Twist (HBT) correlations of pions indicate that  $R_{out} \sim R_{side}$ , where  $R_{out}$  and  $R_{side}$  are the radii of the pion emission source projected to the outward and sideward directions respectively. This observation is in clear contradiction to predictions from hydrodynamic descriptions of nucleus-nucleus collisions, particularly in the instance of a long-lived mixed phase [125].

This result was a surprise, given the success of hydrodynamic models in predicting the magnitude and  $p_T$  dependence of elliptic flow for light mesons and baryons having  $p_T \leq 1-2$  GeV/c. It continues to be an important unsolved problem in attempting to understand the hadronic evolution of nucleus-nucleus collisions. Further analysis with identical and non-identical particles is needed to understand this result as well as the hadronic evolution of the collision in general. The proposed barrel TOF will contribute significantly to these studies by extending the  $p_T$  range in which particles can be cleanly identified.

Specifically, the proposed barrel TOF upgrade will:

- allow for systematic investigation of non-identical particle correlations to disentangle particle flavor dependence of temporal emission and flow patterns;
- extend the  $p_T$  coverage of the HBT measurement

The ability to study identical and non-identical particle correlations, and, in particular, to extend the  $p_T$  range over which these studies can be made to  $\sim 2-3$  GeV/c is very important to place significant constraints on models proposed to describe the evolution of the hadronic matter in the collision. A prime example is the Blast-Wave parameterization Ref [127]. It is capable of predictions consistent with the observed ratio of  $R_{out}/R_{side}$ , but only if the duration for particle emission is exceedingly fast ( $\sim 1.5$  fm/c). If this picture is correct, it is interesting and important, and quite different from the behavior expected for a long-lived mixed phase.

The Blast Wave model makes specific predictions for non-identical particle HBT as a function of  $p_T$ , but these predictions are only definitive in a range of  $p_T$  for pions, kaons, and protons that is above that where these particles can be identified by  $dE/dx$  in the present TPC + SVT. Above some transverse momentum in the few GeV

range, the dominant source of particle production must switch from soft (expanding fireball) to hard (prompt production from the collision of incoming partons) processes. The space-time emission pattern of soft and hard processes is completely different. Particles arising from hard processes are emitted after  $\sim 1$  fm/c, while particles from soft processes which participate in the transverse expansion are emitted after  $\sim 10$  fm/c. Since  $\pi$ -p, and  $\pi$ -K correlation functions are sensitive to the relative emission times of pions, kaons, and protons, they can be used to study the transition from soft to hard processes, provided particle identification is possible in a high enough range of transverse momentum. It is in this intermediate  $p_T$  range – the transition region between soft physics and hard scattering—that models are significantly constrained by their predictions. Without the barrel TOF upgrade, HBT studies of identical and non-identical particle correlations will be compromised and will be limited in their ability to place significant constraints on models of particle production. Important information will be lost.

### 3.7.2 Nucleus & Antinucleus production

The addition of a full TOF system affords STAR the possibility of extending its measurement of nuclei and anti-nuclei significantly.

First, the proposed barrel TOF detector will give STAR the ability to measure deuterons in a range of transverse momentum where beam pipe related backgrounds are no longer dominant (this is presently a limiting factor for this measurement). This will allow first measurements of the  $\bar{d}/d$  ratio at RHIC in addition to accurate measurements of the inverse slope parameters for ant-deuterons and deuterons. This is not possible using TPC  $dE/dx$  identification alone. The same comment is true for tritons and anti-tritons. In this case, the additional particle identification capability provided by the proposed barrel TOF upgrade will result in the first measurement of the  $\bar{t}/{}^3\bar{\text{He}}$  ratio at RHIC. The barrel TOF detector will also significantly enhance STAR's chances to make a discovery observation of  ${}^4\bar{\text{He}}$  due to the improved particle identification capability and candidate separation possible at high  $p_T$ .

With the additional capability afforded by the barrel TOF, thorough searches for nucleus and anti-nucleus production will be made. This will result in significant constraints on the models of the sources for nucleon and anti-nucleon production and upon the factors influencing nucleon (anti-nucleon) coalescence such as nucleon and anti-nucleon number density and radial flow profiles in heavy ion collisions.



## 4 Detector Design

To meet the physics objectives outlined in the previous section, the TOF system must measure time intervals with a specific precision using information on the track momenta and positions determined by a separate system (the TPC). In section 4.1, the measurement approach in this environment is related to the necessary precision for the time interval measurements to particle identification requirements. The requirements on the design of the TOF system driven by the physics objectives are then outlined in section 4.2. This is followed by detailed descriptions of the resulting design of the MRPC detectors (section 4.3), the mechanical components (section 4.4), the gas system (section 4.5), and the electronics (section 4.6).

### 4.1 The STAR Approach to Time Of Flight

The TOF system measures time intervals with two detectors – an event “start” detector near the beam pipe (see section 4.9) and a charged particle “stop detector” (the barrel of MRPCs), each of which has a specific resolution on particle arrival times. Following offline corrections, the difference of these times is the sole quantity of interest provided by this system. These time intervals,  $\Delta t$ , are associated with reconstructed tracks in the STAR TPC by track extrapolation to the TOF detectors. The TPC thus provides the momentum,  $p$ , and total path length,  $s$ , and so allows the calculation of the inverse velocity,  $1/\beta$ , for each TPC track via,

$$1/\beta = c\Delta t/s, \quad (5)$$

where  $c$  is the speed of light. It is this inverse velocity versus the particle momentum that provides the basis for the particle identification (PID) capabilities of the system. That is, the track momentum and the associated inverse velocity give the particle mass,  $M$ , via,

$$M = p\sqrt{(1/\beta)^2 - 1}. \quad (6)$$

The TPC is a large cylinder with an outer(inner) diameter of 4(1) m which extends  $\pm 2.1$  m on either side of the beam intersection region, or approximately two units of pseudorapidity from -1 to 1. Its track momentum resolution,  $\Delta p/p$ , is 1-2% in the momentum range of interest for this TOF system, and its resolution on track total path lengths is less than 0.5cm. This makes the TPC an extremely powerful particle tracker for use in combination with the TOF system.

A TOF system in STAR at the cylindrical radius of the TPC with a total time interval resolution of 100 ps thus has the PID capabilities indicated in Figure 22. Shown in this figure is the particle mass via TOF for each of four charged hadrons of interest - pions, Kaons, protons, and deuterons, as labelled, versus the particle momentum for the STAR geometry and for the momentum and path length resolutions of the STAR TPC. Plotted for each particle are a pair of lines indicating the dependence of  $M+\Delta M$  (upper line in pair) and  $M-\Delta M$  (lower line in pair) versus the momentum. The solid pairs of lines correspond to tracks in STAR near pseudorapidity  $\eta \sim 0$  (the center of the

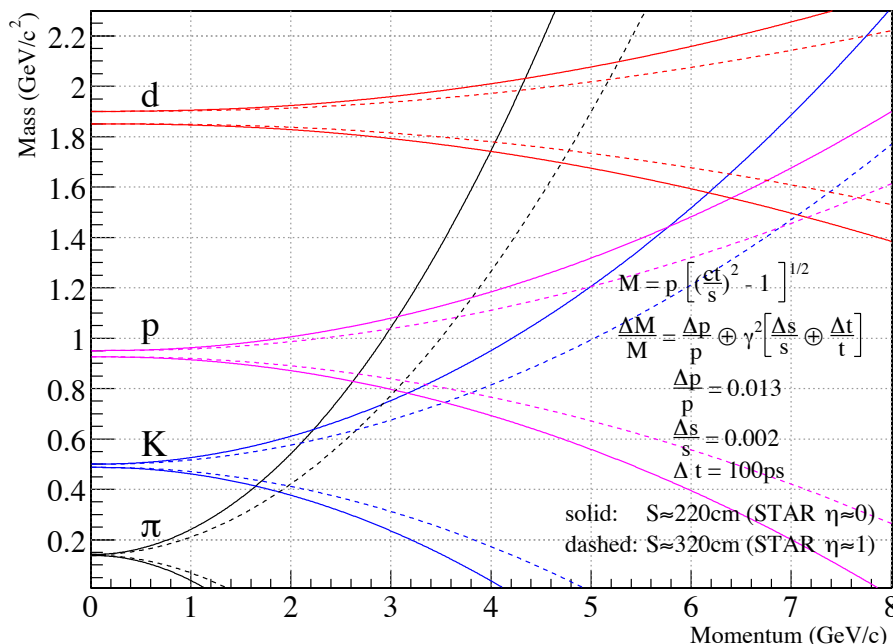


Figure 22: The momentum dependence of the particle mass resolution for a 100ps total resolution TOF system in the STAR environment. In regions where the lines are non-overlapping, the corresponding particle can be identified by the proposed system.

TPC), while the dashed pairs of lines correspond to tracks near pseudorapidity  $\eta \sim 1$ , which have a  $\sim 50\%$  longer path length. The lowest momenta at which an upper line for a particular particle touches the lower line for another particle is the maximum momentum for which “ $2\sigma$ ” PID is possible via a STAR TOF system with a 100 ps total time interval resolution after corrections. From the figure, such a system would provide direct  $\pi/K/p$  identification up to momenta of  $\sim 1.7(1.9)$  GeV/c, and direct  $p$  vs.  $(\pi+K)$  identification up to  $\sim 2.6(3.1)$  GeV/c, for tracks near  $\eta \sim 0(1)$ . Deuterons can be directly identified out to  $\sim 4(4.7)$  GeV/c. It is also interesting to note from this figure that, with increasing momentum, pions, not Kaons, are the first particles to lead to a significant background in the proton identification, and similarly pions, not protons, are also the first background to deuteron identification.

## 4.2 Requirements

The primary requirement for the system to meet the physics objectives is on the total time interval resolution of the TOF system. Other constraints must also be considered.

- The total resolution after all corrections must be 100 ps. For a start resolution of  $\sim 50$  ps (attained by the existing start detector called the pVPD used in Runs 2, 3, and 4), and a 30 ps contribution from the timing corrections, this dictates

a pure stop resolution of less than  $\sim 80$  ps. The detectors developed for this project have demonstrated pure stop resolutions in the range from 50-70 ps, satisfying this requirement. For high-multiplicity heavy ion collisions, the start time can be determined to negligible error event by event using the stop timing, so the total time resolution will be less than 80 ps in these events.

- The detector segmentation must be such that the occupancy per channel is below 10-15%, in order to retain this timing performance even for the highest multiplicity events.
- The system must fit into the integration envelope for the present CTB system, which it would replace.
- The system must be able to operate inside the 0.5T STAR magnetic field, and not be negatively impacted by a possible future upgrade of the STAR magnet to reach higher fields.
- The system must be able to operate at particle fluxes up to  $\sim 200$  Hz/cm<sup>2</sup>. The particle flux in Au+Au collisions at the 1500 Hz maximum interaction rate seen in RHIC Run-1 was 2.2 Hz/cm<sup>2</sup>. The RHIC-2 era will see the maximum rate increase by a factor of 16. The interaction rate in p+p collisions at  $2 \times 10^{32}$  cm<sup>-2</sup>s<sup>-1</sup> will be 8 MHz, with a resulting flux of 175 Hz/cm<sup>2</sup>.
- The system must be inexpensive.
- The system must be safe.
- The system must not impair the performance of other STAR detectors. This concerns the effects of the total interaction and radiation lengths of the detectors on the EMC performance, as well as the effects on the TPC and FTPC performance if the MRPC gas containment is incomplete.

To address these design requirements, it is proposed to use a new technology developed at CERN and approved for use in the ALICE experiment [6]. This design has a high timing resolution, a high granularity, is impervious to magnetic fields, is inexpensive, reliable, and relatively easy to construct. A number of authors of the present proposal participated directly in the development of this technology at CERN. In November 1999, members of the STAR collaboration who participated in the development efforts at CERN submitted a Letter of Intent to STAR management and DOE for an MRPC-based TOF system for STAR [7]. Since that time we have pursued an extensive testing program on TOF modules constructed as prototypes for a STAR TOF system [8], leading finally to the present proposal.

### 4.3 Design

The multi-gap resistive plate chamber (MRPC) technology was first developed by the CERN ALICE group [145]. It has proved to be inexpensive and capable of the necessary timing resolution.

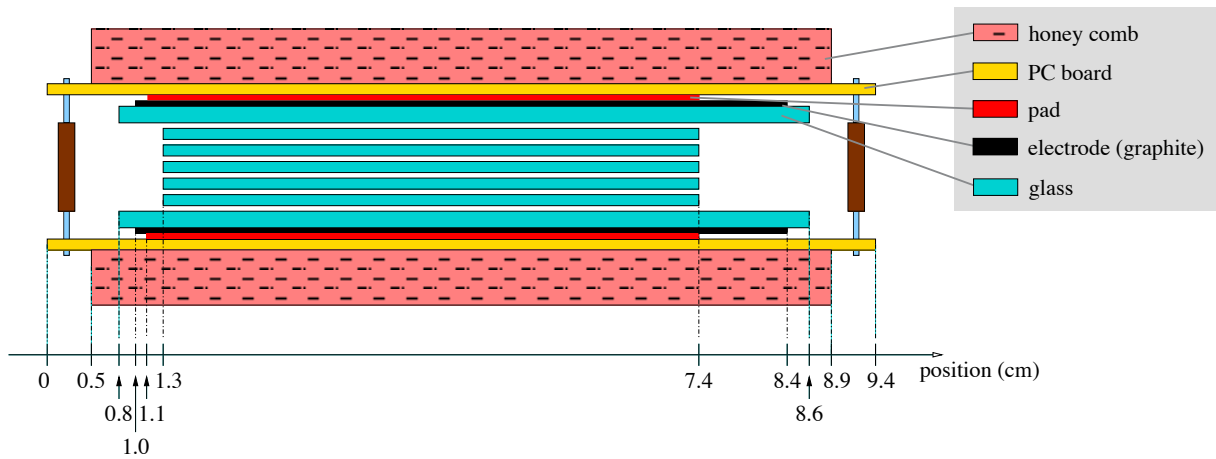
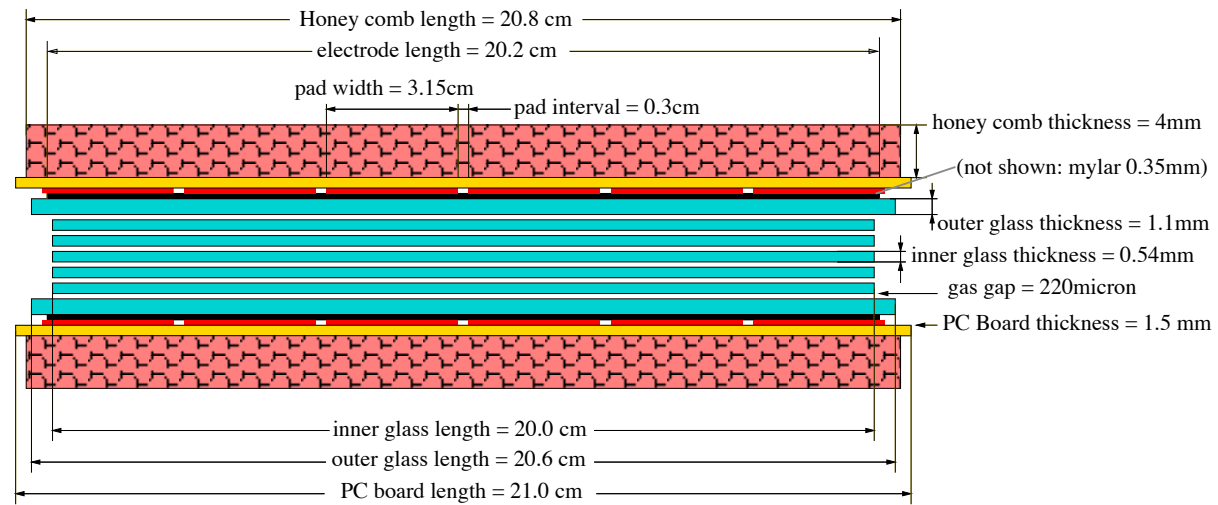


Figure 23: Two side views of the structure of an MRPC module. The upper(lower) view shows the long(short) edge. The two views are not shown at the same scale.

Figure 23 shows two side views of an MRPC module appropriate for STAR. The upper(lower) view in this figure shows the long(short) edge of a module. The two views are not shown at the same scale. An MRPC is basically a stack of resistive plates with a series of uniform gas gaps. Electrodes are applied to the outer surface of the outer plates. A strong electric field is generated in each sub-gap by applying a high voltage across these external electrodes. All the internal plates are electrically floating. A charged particle going through the chamber generates avalanches in the gas gaps. Because the glass plates are resistive, they are transparent to charge induction from avalanches in the gaps. Typical resistivity for the glass plates is on the order of  $10^{13}$   $\Omega/\text{cm}$ . Thus the induced signal on the pads is the sum of possible avalanches from all gas gaps. The electrodes are made of resistive graphite tape and are also transparent to charge. Copper pickup pads are used to read out the signals. A view of these pads for the present MRPCs is shown in Figure 24.

The graphite electrodes have a surface resistivity of  $10^5$   $\Omega$  and cover the entire active area. The glass plates are 0.54 mm thick. They are kept parallel by using 0.22 mm diameter nylon fishing line as a spacer. The signal is read out by an array of copper pickup pads. The pickup pad layers are separated from the outer electrodes by 0.35 mm of Mylar.

Figures 25-27 show beam test results from a module produced by the China TOF group with six 0.25 mm gas gaps, 0.7 mm inner glass, and a  $2 \times 6$  array of  $3\text{cm} \times 3\text{cm}$  pickup pads. For these tests, the signal from the pads is amplified by Maxim 3760 fast current amplifier connected to a discriminator which is based on the AD96685 comparator. The output from the amplifier and discriminator is connected to CAMAC ADC (LeCroy 2248) and TDC (LeCroy 2228) modules, respectively.

The prototype MRPCs were tested at the CERN PS T10 beam line with a 7 GeV/c pion beam. The gas mixture used is 90% C<sub>2</sub>H<sub>2</sub>F<sub>4</sub>, 5% iso-Butane and 5% SF<sub>6</sub>.

The upper left frame of Figure 25 shows the raw time distribution for the 7 GeV/c test beam. In the lower frame is the Time *vs.* Amplitude correlation, or “slewing.” The upper right frame of Figure 25 shows the time resolution after the slewing correction and the subtraction (in quadrature) of the start time resolution, which was measured independently. In both of the upper frames and on the ordinate of the lower frame, the time distributions are shown in units of TDC channels, each of which are  $\sim 50$  ps wide.

The sigma of the raw time distribution (before the slewing correction) is approximately 120 ps. After slewing and start corrections, the stop resolution is 1.33 TDC ch, or  $\sim 67$  ps. For a number of chambers we observed stop resolutions of 50-60 ps.

Figure 26 shows the efficiency (left frame), the corrected time resolution (middle frame), and the time walk (right frame) as a function of the high voltage. The detection efficiency exceeds 97% for a wide range of high voltage settings from 15.5 to 17 kV. In this region of high voltage, the stop resolution is always less than 65 ps, decreasing to 60 ps at the highest voltage settings. The time walk decreases linearly with increasing high voltage with a slope of  $\sim 30$  ps/kV.

Figure 27 shows the corrected TOF distribution for a 3 GeV/c test beam. The

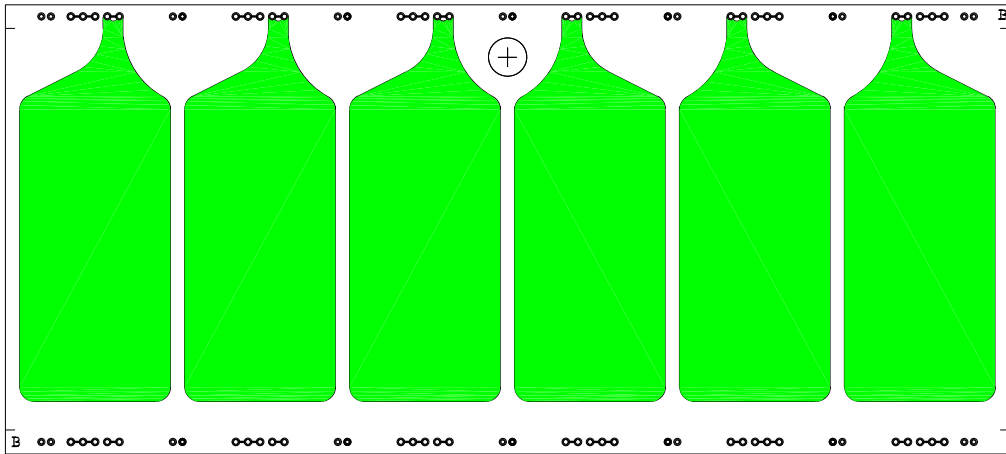


Figure 24: The circuit board with the copper read-out pads for the present MRPC detectors.

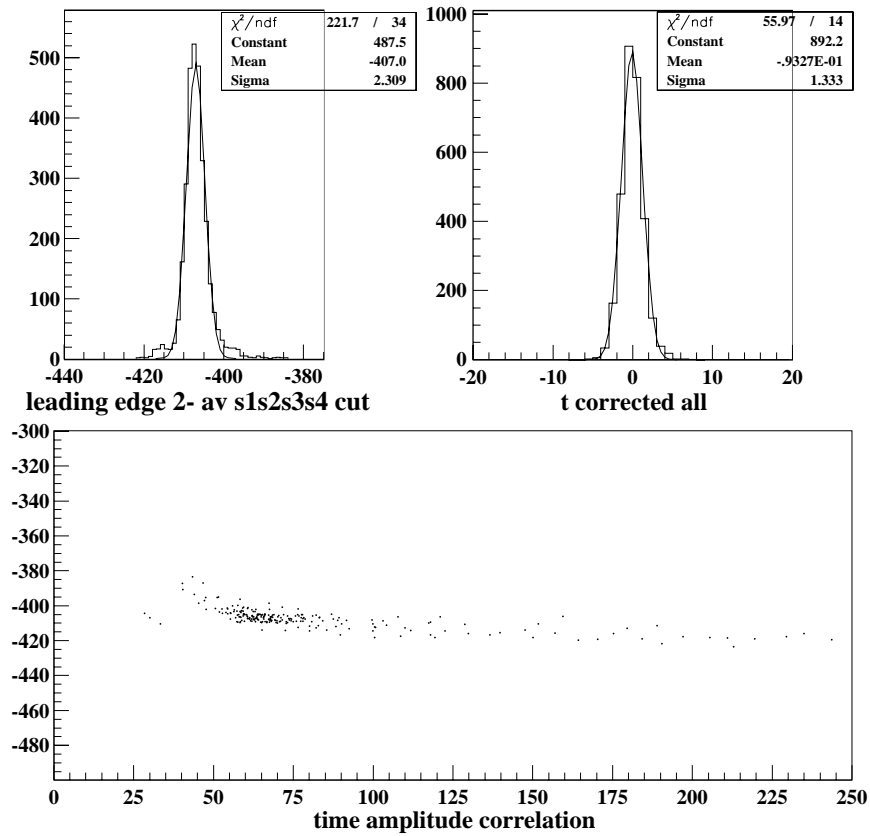


Figure 25: The raw time distribution (upper left), the time-amplitude (“slewing”) correlation (lower), and the pure stop time resolution after the slewing and start resolution corrections (upper right).

flight path for these data was 2.8 m, which is comparable to that in STAR. The start time resolution was also comparable to that expected in STAR. The  $\pi/p$  separation is about  $4\sigma$  under these conditions. It is clear that this system will satisfy the requirements set by the physics goals in STAR. In the following section, we describe the mechanical design of the system.

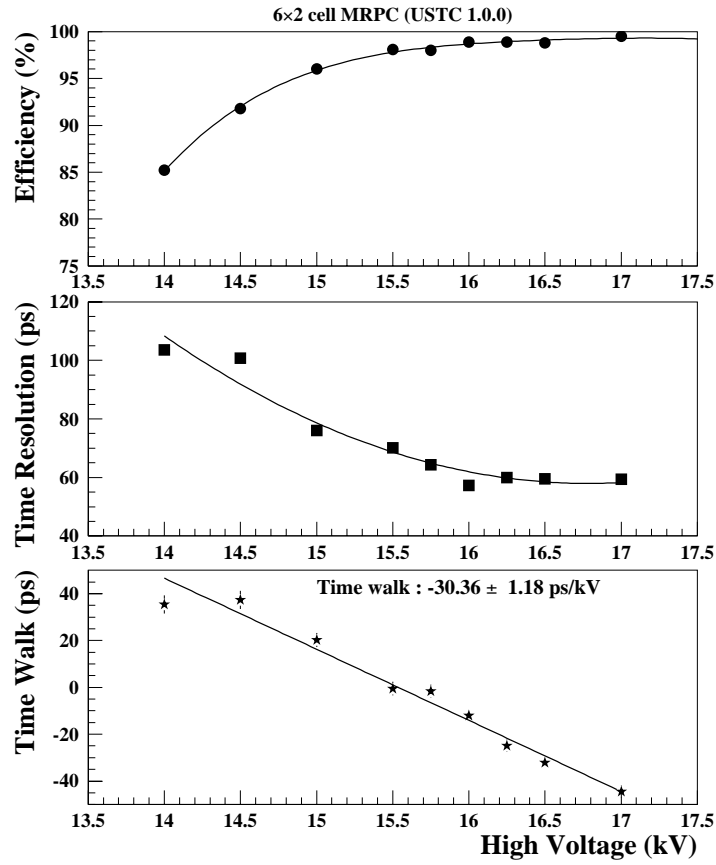


Figure 26: The detection efficiency (upper frame), slewing-corrected time resolution (middle frame), and time walk (lower frame), as a function of high voltage for the 6 gap MRPC.

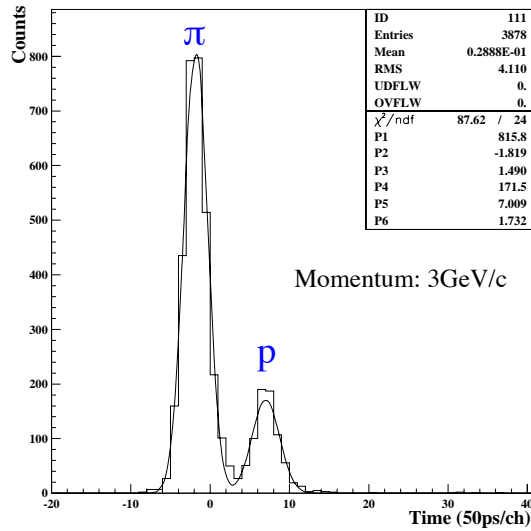


Figure 27: The corrected time-of-flight distribution of pions and protons in a beam of 3 GeV/c momentum. The flight path is 2.8 m.



## 4.4 Mechanical Design

The primary mechanical structure on the stop side of the system is a “tray.” These hold the detectors in three dimensions at specific positions and angles, support the on-detector electronics, and form all but one wall of the gas volume. The trays for the proposed system are similar to those we have used successfully in the CTB (125 trays), TOFp (1 tray), and TOFr (1 tray) systems. (The TOF patch, “TOFp,” is a 41-channel conventional scintillator-based TOF system that was installed before RHIC Run-2, see Appendix B or Ref. [4].) In these systems, a tray is a welded 50 mil-thick aluminum box that slides onto rails attached to the TPC outer field cage. Additional requirements for the proposed system are that the MRPC trays must reside in a gas-tight volume, and that  $\sim 200$  signal cables must be passed out of this volume to the on-board electronics. This necessitated modifications to the basic tray design. The design is such that no part of the proposed system exceeds the assigned maximum “integration” radius of 219.5 cm. The welded-aluminum tray appropriate for the present system, as well other mechanical aspects such as the detector and electronics positioning inside this tray, are described in this section.

In this discussion, it will often be convenient to refer to photographs shown in section 5, which describe the two full-size STAR prototypes, called “TOFr” and “TOFr’.” The construction of the large-area system will use many of the same techniques and materials that were used in the TOFr’ tray (see section 5.4).

A tray is an aluminum box with 50 mil (0.13 cm) wall thickness and welded corners. A CTB, TOFp, or TOFr tray is 95” (241.3 cm) long, 8.5” (21.6 cm) wide, and  $\sim 3.5$ ” (8.9 cm) high. It takes 120 trays to cover the cylindrical outer radius of the TPC, which are arranged as two adjoining cylindrical shells of 60 trays each. Each cylindrical shell subtends approximately 1 unit of pseudorapidity. Unlike the CTB and TOFp trays, these trays must be gas-tight. The detectors inside the gas volume are standard MRPC “modules,” 6 channels each, with detector channel dimensions of 3.3cm $\times$ 6.1cm. Each tray contains 32 MRPC modules, or 192 MRPC channels total.

The “top” of the tray 90mil-thick Aluminum which is machined in one piece. Large holes in this top are covered by the TAMP boards, which close the gas volume and allow the MRPC signal freed-through from inside to outside this volume. Mounted above the TAMP layer is another layer of boards, TDIG, that perform the digitization. At the high- $|Z|$  end of the tray is another board, called TCPU, which performs the communication of the digital data produced by TDIG. The total height of the complete tray must not exceed a maximum height determined by the STAR integration envelope for this detector. The length of the tray likewise must not exceed a specified maximum length.

Shown in Figure 28 is an end view of the STAR geometry near the radius of interest. The radius of the bottom of the tray, at the centerline of the tray, when installed is 209.91 cm and is shown by the lower black arc. The maximum radius allowed is 219.5 cm, which is shown as the upper black arc. The new trays will be the same width as in the STAR CTB and TOFp systems. This thus defines the maximum total height of each tray (including electronics) to be 9.32 cm.

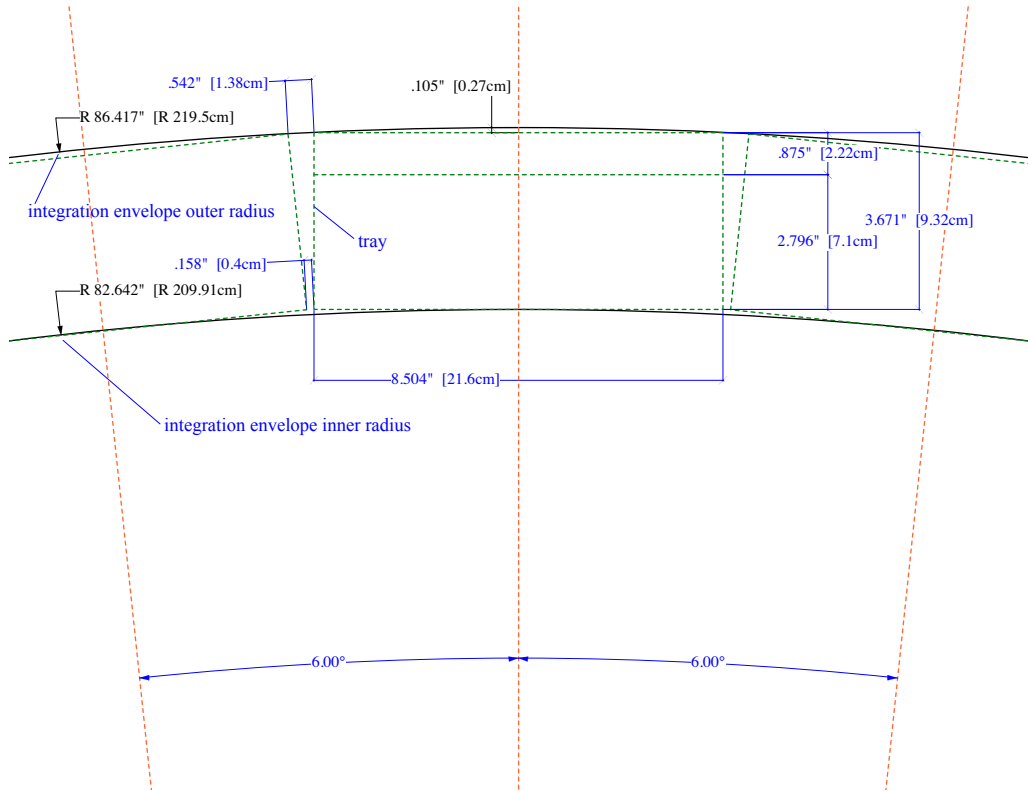


Figure 28: An end view of STAR showing the dimensions of the integration envelope allocated for this system.

This distance specifies the rest of the design. It is estimated that  $7/8''$  (2.22cm) of space at the top of this volume is needed for the two layers of electronics (TAMP and TDIG, see section 4.6 below). The height of the upper edge of the side walls of the tray is thus set at  $9.32\text{ cm} - 2.22\text{ cm} = 7.1\text{ cm}$ . The rails take up  $0.5'' + 0.05''$  contingency (1.27 cm + .13 cm) of space just under this height. This space is also a convenient place to put the interior gas piping and HV cabling. With the thickness of the tray bottom of 50 mil (0.13 cm), the height of the space left for holding detectors is thus 5.7 cm.

Shown in Figure 29 is the side view of the tray for this system. Several different arrangements of detectors were studied in Autocad. While they all allowed the 32 detectors to fit into this 5.7 cm height, the arrangement shown in Figure 29 has the detectors placed most projectively to the average primary vertex location at  $z=0$ .

The left side of the figure is near STAR  $z \sim \eta \sim 0$ , and the right side is near  $\eta \sim 1$ . The dashed red lines denote the boundary of the integration volume. The STAR  $z$ -axis is located 209.91 cm below the lower left corner of this red dashed box. The integration volume extends to  $z=246\text{ cm}$ . The tray length for the proposed system is 91", slightly shorter than the 95" length of the trays used in the CTB, TOFp, and TOFr systems.

In the present design there are 32 modules in each tray (192 detector channels).

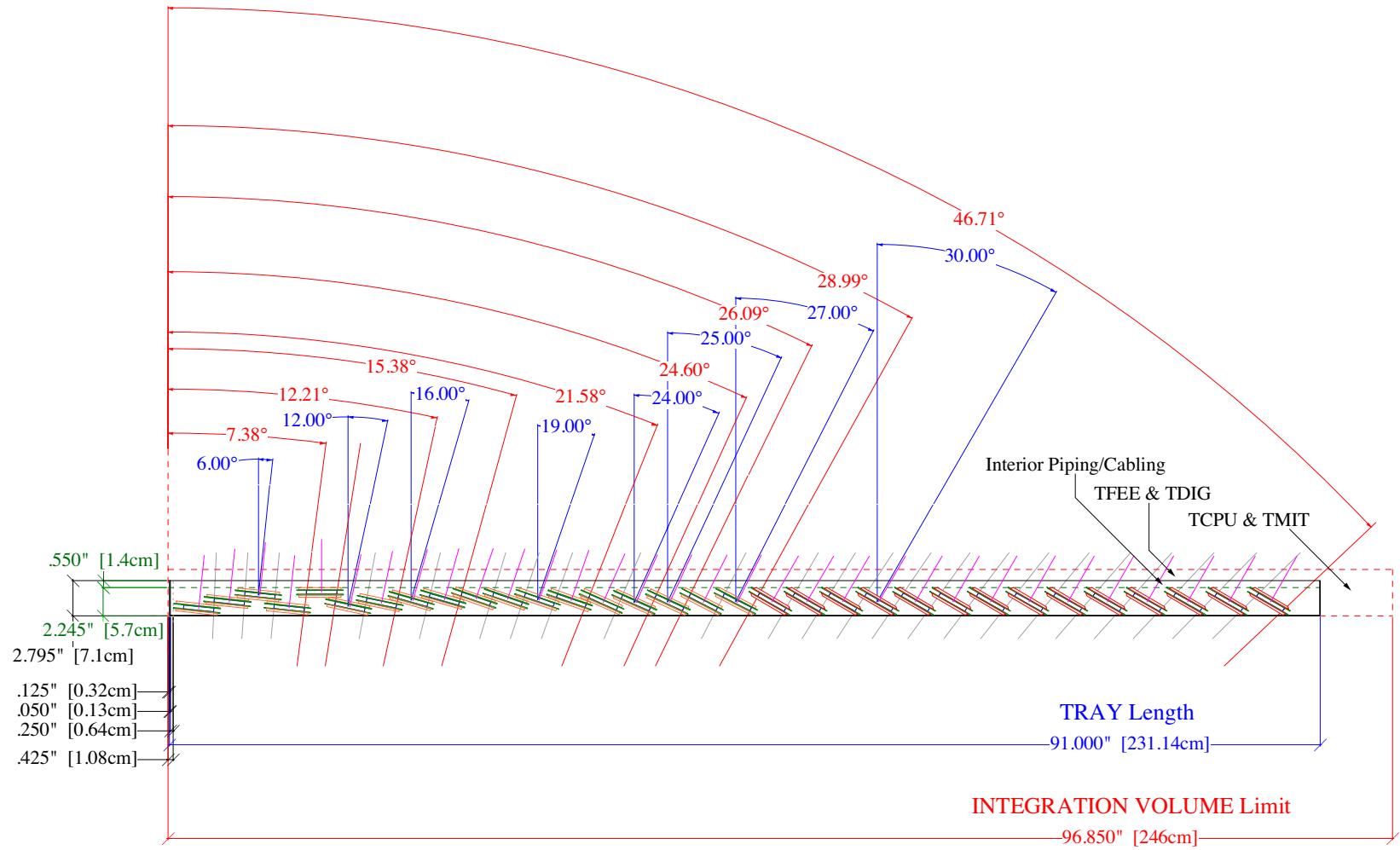


Figure 29: A dimensioned side view of the tray indicating the detector positioning.

Although in a standard 95" (241.3 cm) long tray, there would be room for another module or two, depending on the module arrangement, a 91" (231.4 cm) length has several positive impacts. First, a channel count of 192 is divisible both by 24 and 32, allowing useful simplifications in the design of the DAQ interface and efficient deployment of the CERN HPTDC chips. The shorter-length tray also allows plenty of space for the electronic board TCPU which is mounted at the end of each tray as part of the DAQ interface, and for the facilities (gas and HV feedthroughs, as well as connector and cable strain relief).

The support for the MRPC modules in the two full-sized STAR prototypes, TOFr and TOFr', was based on so-called "sawtooths," while a different technique is envisioned for the next full-sized prototype, "TOFr5," for RHIC Run-5 (FY2005), and for the full system.

In the sawtooth approach (see Figures 38 and 39), phenolic-impregnated Kraft paper honeycomb ("hexcell", which is 1/4" (0.64 cm) thick, light, workable and extremely rigid) panels was machined into specific shapes. These shapes are glued to the inner walls of the tray going from the bottom of the tray up to the top, and the detectors are placed in the precisely oriented voids in the hexcell along the way. Thus all detectors are held up/down and in/out by the four sides of hexcell at their edges, and left/right by the walls of the tray itself. A small gap is left between the modules and the tray wall. The sides of the modules which are adjacent with the tray side walls are covered with two layers of Kapton tape before the modules are inserted. The interior bottom of the tray is also covered with a Kapton layer before the sawtooths and detectors are installed.

An alternative approach for mounting the MRPCs inside the tray is presently being explored and will be used in the next prototype tray to be built for STAR for RHIC Run-5 (FY2005). Two long thin strips of acrylic are attached to the underside of the tray top and run the length of the tray along each long vertical side. Mirror image reveals are machined into these two "Inner Sides," and an MRPC will sit in each reveal. This approach has several important advantages. First, the tolerances on the detector positioning with respect to the tray body over all 120+ trays in the system are dramatically reduced. Second, it mounts the detectors to the tray top, not the tray bottom, which allows one to drop into the tray (or remove) all the active elements (MRPCs, HV and signal cabling, and FEE) as one piece. Third, as these inner sides are produced on a computer controlled milling machine ("Hurco" machines at UT-Austin), the fabrication of the MRPC supports is much less labor-intensive compared to the sawtooth approach.

After the detectors are mounted, the interior HV cabling and then the interior gas piping is installed. The mechanical support for the TFEE cards is the tray top. This is a single piece of aluminum, which fits exactly over the tray bottom in a "shoe-box" design. The TAMP plates bolt vertically onto the top side of the tray top via PEM studs embedded into the tray top. Dow Corning 730 Freon-resistant sealant is used to gas-seal the TAMP boards onto the tray top.

The 192 short twisted pair cables that carry the detector signals off the MRPCs are connected to the pins on the underside of the TAMP plates. The top assembly

(tray top, TAMP boards, inner sides, and MRPCs) is dropped into the tray bottom in one piece. The same sealant is used where the tray top assembly meets the tray bottom. After leak checking, gas is flowed through the tray. Then, the low voltage power and threshold distribution to the TFEE boards are attached. After gas has been flowing for  $\sim 1/2$  day, all tray systems can then be powered up and tested.

GEANT simulations were performed to evaluate the integrated thickness of the tray and detectors in interaction and radiation lengths. The results are shown in Figures 30. The gaps in azimuth between trays are at an angle of  $\pm 0.052$  radians in this figure. In each frame, the three lines correspond to the CTB trays and detectors, the scintillator-based TOFp tray and detectors, and the presently proposed TOF trays with MRPC detectors, as labeled in each frame. In the two views versus the pseudorapidity, one notices 32 peaks for the present TOF system - these tracks are those passing through two MRPC modules. The two views versus the azimuthal angle give a clearer indication of the relative thicknesses of these three detector systems. The CTB is generally always the thinnest in terms of both interaction and radiation lengths. In terms of interaction lengths, TOFp is thicker than TOF, but in terms of radiation lengths, TOF is thicker than TOFp. This is because the thickest component of TOFp is the 2 cm-thick plastic slats, while glass and FR4 printed circuit boards in the MRPCs are the thickest components of TOF. The total interaction(radiation) length of the TOF trays is 21%(26%) more than that for the CTB.

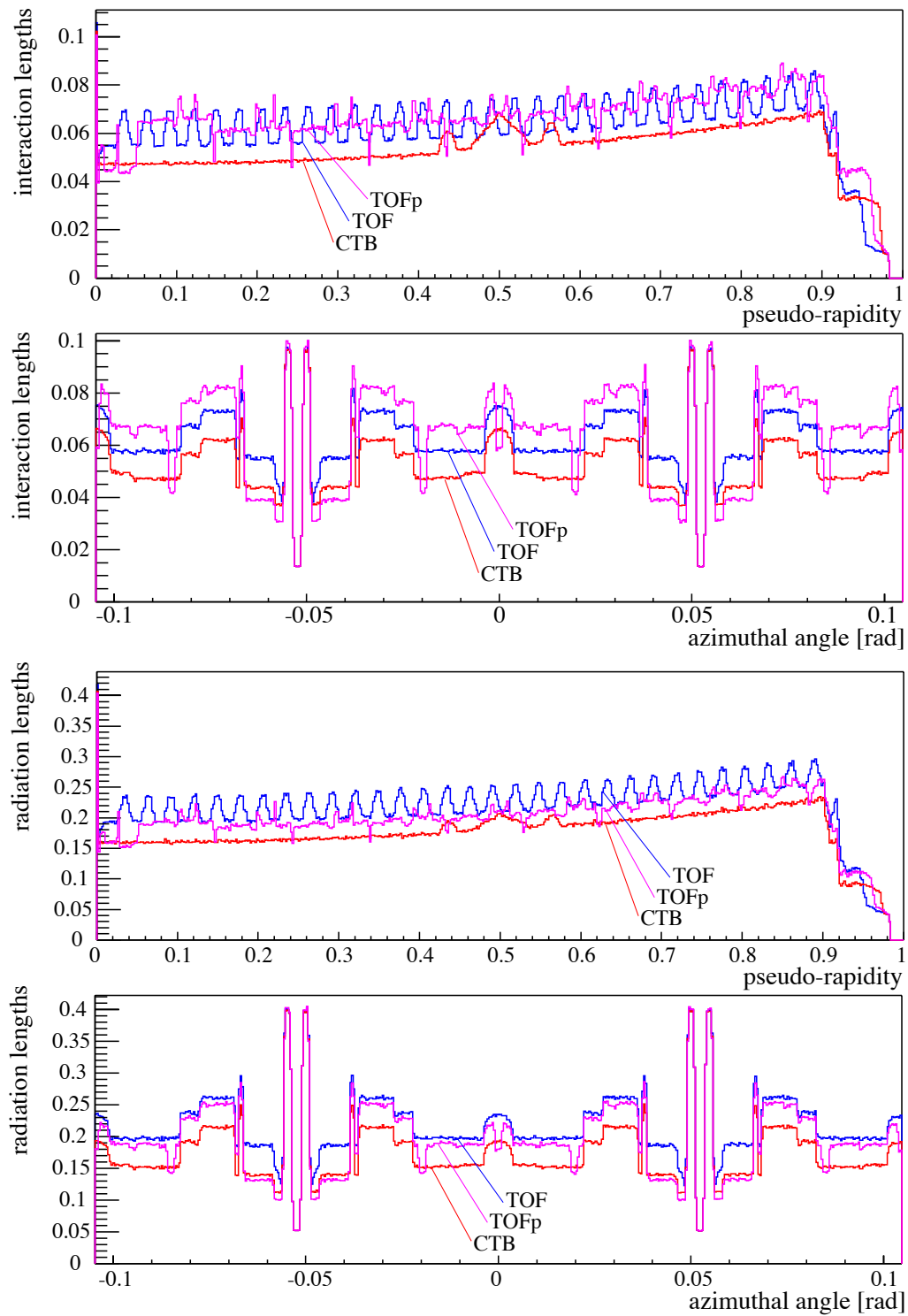


Figure 30: The integrated thickness of the tray and detectors in interaction lengths (upper two frames) and radiation lengths (lower two frames), versus the pseudorapidity and azimuthal angle, as labeled.

### 4.5 Gas System Design

We have operated prototype trays in STAR for two RHIC runs using a mixture of 95% Freon R134a and 5% iso-butane. The performance of these trays with this gas mixture meets STAR’s design requirement for timing resolution. However, we reserve the use of SF6 as a backup option if we encounter difficulty producing MRPC modules that do not “streamer” excessively at the normal operating voltage.

The primary purpose of the TOF Gas System is to provide a mixture of 90% R134a, 5% iso-butane, and 5% SF6 to the TOF chambers at the correct pressure. This system can regulate the flow rate of the mixture while monitoring mixture temperature, flammable gas content, oxygen and moisture. A computer control/data acquisition system collects and logs the gas system operating parameters while providing a means of remotely controlling system valves. Shown in Figure 31 is the schematic, and Table IV lists the parameters, of the proposed gas system.

The TOFr system was successfully operated for several weeks during the AGS test without SF6, see 5.2. This test will be continued with the TOFr tray installed in STAR. If we continue successful operation, without SF6, we will plan to operate the full TOF system with a 2-component gas system.

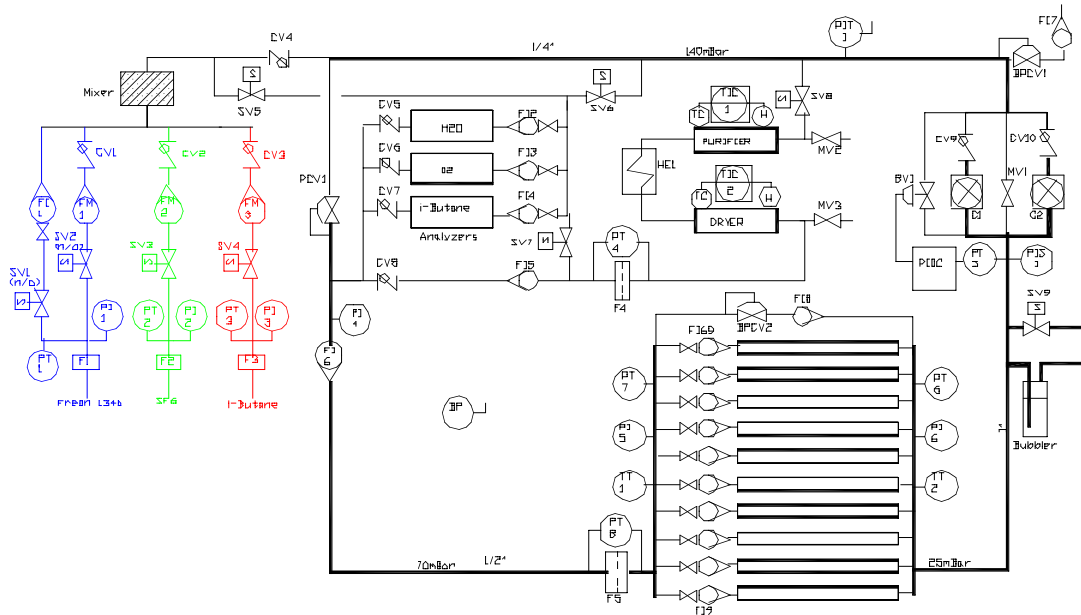


Figure 31: The schematic of the proposed gas system.

The system operates nominally as a closed circuit gas system with the majority of the mixture re-circulating through the TOF chambers and delivery system. During normal operation a small amount of fresh mixture is added and equivalent quantity of the existing mixture is vented. The gas system can be operated in an open system configuration for purging.

The mixture circulation rate through the small membrane compressor is 15 LPM at 140 mbar. The gas system contains two compressors (C1,C2), one active and one

Table IV: The design parameters of the gas system.

Mixture	90% R134a, 5% i-C <sub>4</sub> H <sub>10</sub> , 5% SF <sub>6</sub>
Compressor pressure	100-150 mbar
Supply pressure	70±0.1 mbar
Return pressure	2.5±0.1 mbar
Re-circulation flow	700 liter/hr
Mixture flow through TOF chambers	300-600 liter/hr
Purge flow	600 liter/hr
Make-up mixture flow	0.2-2 liter/min
Oxygen content	<30 ppm
Water content	<20 ppm

spare. The mixture from the compressors goes to the supply line through the check valves CV9 or CV10. The 140 mbar output pressure from the compressor is reduced to 70 mbar by the pressure regulator (PCV1) and this pressure level is maintained with the back pressure regulator (BPCV2).

The return gas manifold is maintained at 2.5 mbar above atmospheric pressure by a differential pressure transmitter (PT5) and electro-pneumatic PID Controller (PIDC) that operates bypass valve (BV1). The bypass shunts flow from the compressor discharge line directly back to the compressor's inlet. A second manual bypass valve (MV1) is adjusted to enable the automatic control loop to be used within its optimum range.

The bypass line including the back pressure control valve (BPCV2) allows smoothing the gas system start and rapid response to increased or reduced iso-butane content measured with the iso-butane analyzer upstream of the compressor. Also, it permits *e.g.* the preparation of the mixture with a homogeneous iso-butane content.

Two flow indicators (FI6 and FI8) will measure the re-circulating flows: main and bypass. A difference between them is the flow through the TOF chambers. The measurements of the fresh mixture (FM1, FM2 and FM3) and flow through the flow indicator (FI7) provides an estimation of the tray leakage.

The purity and composition of the mixture is monitored using oxygen, iso-butane and humidity analyzers. A fraction of the re-circulating mixture can be passed through a purifier and dryer to remove moisture and contaminants as needed.

A computer driven data acquisition/control system monitors all of the process variables. The computer system flags quantities which fall outside of predefined limits and initiates corrective action.

It is imperative that the TOF chambers inside pressure accurately track barometric pressure. A rapid change in atmospheric pressure is typical preceding storms and hurricanes. To assure that the TOF chambers follow a fast rise in atmospheric pressure, a relatively large flow of inert gas will be admitted into the TOF chambers in the event that normal pressure controls fail to keep up with falling relative internal



pressure. The vent lines and associated valves are sized to allow for rapid venting of the TOF chamber mixture to prevent a high internal pressure in the case of a rapid decline in barometric pressure.

#### 4.5.1 Pressure Control

There are two sources of pressure in the system: the first is the compressors located at the exit of the TOF chambers. The second is the flow of fresh mixture through the mixing manifold. Nominally the pressure within the TOF chambers is controlled by maintaining a constant pressure upstream of the DC and PC via the pressure reducing regulator (PCV1) plus back pressure regulator (BPCV2) and varying the pressure downstream of the TOF chambers by regulating the amount of mixture shunted from the compressor output to inlet. On a longer time scale, the flow of fresh mixture is constant.

The output from the compressor is 700 liter/hr at 140 mbar. A back pressure regulator (BPCV1) in the outlet line is set to 140 mbar thus maintaining a maximum delivery pressure independent of the compressor output. This pressure is reduced to 70 mbar by the pressure regulator (PCV1) and supported with the back pressure regulator (BPCV2) upstream of the TOF chambers. The TOF chambers exhaust pressure, measured at the return gas manifold is maintained at 2.5 mbar by a TESCOM ER3000 electro-pneumatic PID controller. A 0-5 mbar differential pressure transmitter (PT5) on the return manifold produces a 4-20 mA output that the PID controller compares to a set-point value. If the transmitter signal is different from the set point, the controller sends a pneumatic output signal to the bypass control valve (BV1). The bypass shunts flow from the compressor discharge line directly back to the compressor's inlet. Opening the bypass valve causes the TOF chambers exhaust pressure to rise and closing the valve makes the pressure fall. A second bypass valve (MV1), manually adjusted during the initial system set-up, enables this automatic control loop to be used within its optimum range.

The fresh mixture is admitted between the pressure regulator (PVC1) and back pressure regulator (BPCV1). The quantity of fresh mixture is changeable in the range of 0.2-3 liter/min with the mass flow controllers FM1, FM2 and FM3. To purge the detectors with up to 10 liter/min of inert gas, the flow indicator (FI1) is used. Simultaneously, gas is removed from the system through the back pressure regulator (BPCV1). To have the stable content of fresh mixture, the Freon R134a mass flow controller (FM1) operates the SF6 and iso-butane controllers (FM2 and FM3). This means that FM1 is a master, and FM2 and FM3 are the slaves. These units are normally locally controlled. The quantity of fresh mixture is monitored by the PC data acquisition/control system.

When the internal TOF chamber's pressure as measured by PT6 is more than 3 mbar above the atmospheric one, the gas control system will close the solenoid valves (SV2, SV3, and SV4) in the fresh mixture supply line and open the vent line valve (SV9) allowing mixture to vent directly to the atmosphere. Also, a pressure indicating switch (PIS1) has a set-point of 3 mbar and it can operate SV2, SV3,

SV4 and SV9 as the computer control. Should the TOF chambers pressure reach 3.5 mbar, the out-going TOF chamber gas mixture will vent to the atmosphere through the bubbler. With this arrangement, the TOF chambers are protected from either flow controller malfunction, a rapid drop in atmospheric pressure, and/or a failure of the back pressure regulator.

In the event of a rapid rise in atmospheric pressure, or effectively a fast drop in the TOF chambers internal pressure (up to 6 mbar/min), a dual set point Dwyer differential pressure transmitter (PT6) in the return manifold will trip as the pressure falls below 0.5 mbar causing an audible and visual alarm. When the pressure at PT6 falls below atmospheric (0.1 mbar gauge) a second set-point trips and the computer control system will stop the compressor, shut-off the flow of iso-butane, shut-off the HV, and pass inert gas by opening the solenoid valve (SV1) to supply an additional 5 liter/min of inert gas.

A pressure indicating switch (PIS1) with dual set points is also installed in the return manifold. This switch is not connected to the computer control system but is hardwired to perform the same functions as the computer in the event of a falling TOF chambers pressure. Thus the system is equipped with two separate means of preventing the TOF chambers from experiencing an external over pressure.

In the event of a power failure, the solenoid valves SV1, SV2, and SV9 will open, or remain open and SV3, SV4 will close, causing 5 liter/min of inert gas to flow through the TOF chambers. This flow rate is adequate to assure that fluctuations in the atmospheric pressure will not result in the creation of over- or negative-pressure inside the TOF chambers.

The computer data acquisition /control system will measure the atmospheric pressure with a barometer (BP) to have available the absolute pressure data.

#### 4.5.2 Mixture Control & Temperature Measurement

Along with automated valve control, the gas system's dedicated computer controlled data acquisition provides constant monitoring of the mixture composition via measuring the mass controllers output signals. The iso-butane analyzer will be used periodically to check iso-butane content in the mixture. The mixture ratio is fixed by the Teledyne mass flow controllers (FM1, FM2 and FM3) with the SF6 and iso-butane flow controllers slaved to the freon controller. The stability of the flow controllers is sufficient to make variation in the mixture negligible.

Two temperature transmitters (TT1 and TT2) are used to measure the mixture temperature within the TOF chambers. The data of measured mixture temperature are logged for later use in data analysis.

#### 4.5.3 Gas Sampling & Purification

The gas system is equipped with oxygen, moisture and iso-butane analyzers plumbed such that each section of the gas system can be selected separately for evaluation. The

Table V: The list of fault conditions in the gas system.

No.	Name	Limit	Action
1	PT-6	<0.1 mbar	Stop Compressor and HV, inert gas purge (open SV1), Alarm (audible, flashing light)
2	PT-6	<0.5 mbar	Alarm (audible, flashing light)
3	PT-6	>3 mbar	Close SV2, SV3 and SV4, Open SV9, Alarm (audible, flashing light)
4	PT-1	<6 PSI	Alarm (audible, flashing light)
5	PT-2	<6 PSI	Alarm (audible, flashing light)
6	PT-3	>5 PSI	Alarm (audible, flashing light)
7	O2&H2O	>100 ppm	Stop HV, Alarm (audible, flashing light)
8	O2&H2O	>90 ppm	Alarm (flashing light)
9	iso-butane	> 7%	Alarm (audible, flashing light)
10	iso-butane	< 4%	Alarm (audible, flashing light)
11	FM1-3	>7% iC4H10	Stop iC4H10 supply and HV. Alarm (audible, flashing light)
12	FM1-3	<4% iC4H10	Alarm (audible, flashing light)
13	PIT-1	<50 mbar	Alarm (audible, flashing light)
14	PT-4	>45 mbar	Alarm (audible, flashing light)
15	PT-8	>10 mbar	Alarm (audible, flashing light)

data from the analyzers is read out and archived by the computer data acquisition system and used to control the gas system.

A mixture dryer and purifier withdraws a portion (about 2 liter/min) of the recirculating flow upstream of the pressure regulator (PCV1) and delivers the conditioned gas to the recirculating flow downstream of PCV1. This loop is used only as needed. The dryer is made from a stainless steel tube containing 1 pound of molecular sieve (zeolite 13X) as adsorbent. This amount permits the removal of about 0.4 lbs of water vapor to a level 2-3 ppm at room temperature. Filters are installed upstream and downstream of the adsorbent to prevent particles from entering to the mixture stream. A heating element is placed inside the dryer. For thermal insulation, a fiber glass insulation is used. The dryer is regenerated by heating to 350-400 °C with purging of the mixture (Nitrogen + 3% H<sub>2</sub>). The purge gas enters at the top of the dryer and exits at the bottom carrying with it the water vapor. A temperature transmitter installed inside the dryer is connected to the temperature controller (TIC2) that supports the dryer temperature on the set-pointed level. A moisture analyzer is used to measure the quantity of the water in the circuit before and after the dryer to determine when the adsorbent is saturated.

The purifier is similar to the dryer except that it is filled with pure copper. The oxidization process takes place at 220 °C that is regulated by the temperature controller (TIC1). A heat exchanger (HE1) is used to reduce the mixture temperature exiting into the dryer. This purifier is regenerated with the same mixture as the dryer. Solenoid valve (SV8) installed at the inlet of the purification loop isolates the unit from the main circuit when it is not in use. If the inside pressure of the purifier/dryer is more than 1/3 PSI, the check valve (CV8) works as the safety valve and prevents the purifier/dryer from damage.

A 10  $\mu\text{m}$  filter is installed after the purifier/dryer to prevent dust from passing into the main mixture supply line. A differential pressure transmitter (PT4) is used to check the plugging of the filters.

#### **4.5.4 Computer Control & Data Acquisition**

The gas system includes a computer driven data acquisition and control system. The controlling computer is a dedicated PC with Intel Pentium processor. It reads the data and operates the gas system via National Instruments SCXI system. This computerized system is programmed to acquire the signals from the various temperature, pressure, flow, and content measuring devices and issue warnings and/or take corrective action in the event that predetermined levels are exceeded. All acquired values can be selected and viewed on the terminal. Gas system parameters may be viewed using the World Wide Web. The interface of the gas system with STAR slow controls will be accomplished by an EPICS interface.

## 4.6 Electronics Design

A Time-of-Flight system measures time intervals, which are defined by independent electronic measurements of one “start time” and some number of “stop times” in each experimental event. While different detectors are used on the start and stop sides, important advantages are gained by performing both the start and stop digitization in the same electronics. This is a common trait of all successful TOF detector systems. In the STAR TOFp [4] and TOFr systems, digitization is performed on the platform using the pVPD signals as direct electronic starts for both the stop detector and the pVPD digitization (see section 4.9 and appendix B). However, for the proposed system, one cannot possibly distribute electronic signals from the start detector to each stop detector (*i.e.* each tray) in time. Also, one could not possibly integrate a system into STAR that digitizes 23k detector channels using long cables and a huge bank of CAMAC or Fastbus electronics. For the proposed system, one must instead digitize versus a clock, and transmit from the detector digital data, instead of logic signals to be digitized elsewhere. The information ultimately needed for timing analyses are still available, as  $(\text{stop-clock}) - (\text{start-clock}) = \text{stop-start}$ , so long as the clocks used on both the start and stop sides are the same to 10-20 ps in every event. Additional comments on the start detector are presented in section 4.9 below.

*The following discussion of the proposed electronics for the large-area TOF system is unchanged from when it was first written in May 2002 except as noted below. It was reviewed by STAR in September 2002 and by the BNL Detector Advisory Committee in December 2002 and November 2003. There are number of small changes that have occurred during two years of R&D that are reflected in the WBS, presented in Appendix C. A top level description of the electronics using the current nomenclature also is available in Appendix C.*

*The following changes have occurred. The fast comparator has been moved from the TFEE card to the TDIG card and the TFEE card is now called TAMP. We are using the Maxim 9601 comparator on TDIG and the Maxim 3664 preamplifier on TAMP. The interface between the start detector PMTs and TDIG is now called TPMT instead of TFEEb. The TMIT card will be mounted outside the pole tip instead of on the tray. There will be only 4 TMIT cards and they will be daughter cards to 4 THUB cards. Each THUB/TMIT will interface 30 or 31 TCPU cards to trigger and DAQ. We plan to use the CERN/ALICE DDL-SIU optical interface cards for the TMIT function. We plan to use the CERN/ALICE RORC (read-out receiver card) for the TDRC function and the description of the DAQ receiver in section 4.6.6 has been updated to reflect this. The description of HPTDC R&D at the end of section 4.6.2 has been updated to reflect the current status.*

Shown in Figure 32 is the top-level diagram of the electronics for the start and stop sides of the present system. The electronics chain on the start side is very similar to that on the stop side by design. The individual electronics boards seen in this figure are discussed in detail in this and the following subsections.

Each tray consists of 192 detector channels and three different types of circuit cards. These types are called TFEE, TDIG, and TCPU, listed in order of the flow

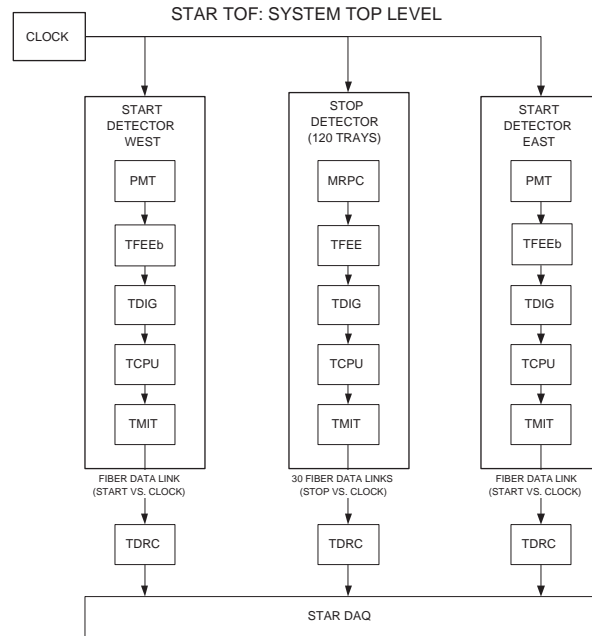


Figure 32: The highest-level diagram of the electronics for the proposed system.

of information from the detector. Every fourth tray also contains a TMIT card that transmits the data to STAR DAQ. The TFEE contains the analog front end electronics and also serves as the top of the gas box and the signal feedthrough. The  $\sim 10''$  long twisted-pair cables from the detector pickup pads are connected to the feed-through. The TFEE pass their output to the TDIG, which digitizes and buffers the detector information. This information is passed to TCPU which formats and buffers the digital detector information. This formatted data is passed to TMIT, which transmits it over an optical fiber to the data receiver TDRC in the STAR DAQ room.

Shown in Figure 33 is the top level electronics diagram at the tray level. The system interfaces include:

- a fiber optic data communication link via the TDRC to the STAR DAQ (TDC data and command echo),
- a high speed differential data link (PECL or LVDS) for multiplicity data to the STAR Level-0 trigger,
- a command link for acquisition commands from the STAR trigger,
- a high speed differential line (1 signal) for the beam crossing timing signal from the STAR trigger, and
- a serial bus for connecting the system's embedded CPUs to the network for configuration and status.

## STAR TOF: TOP LEVEL ELECTRONICS

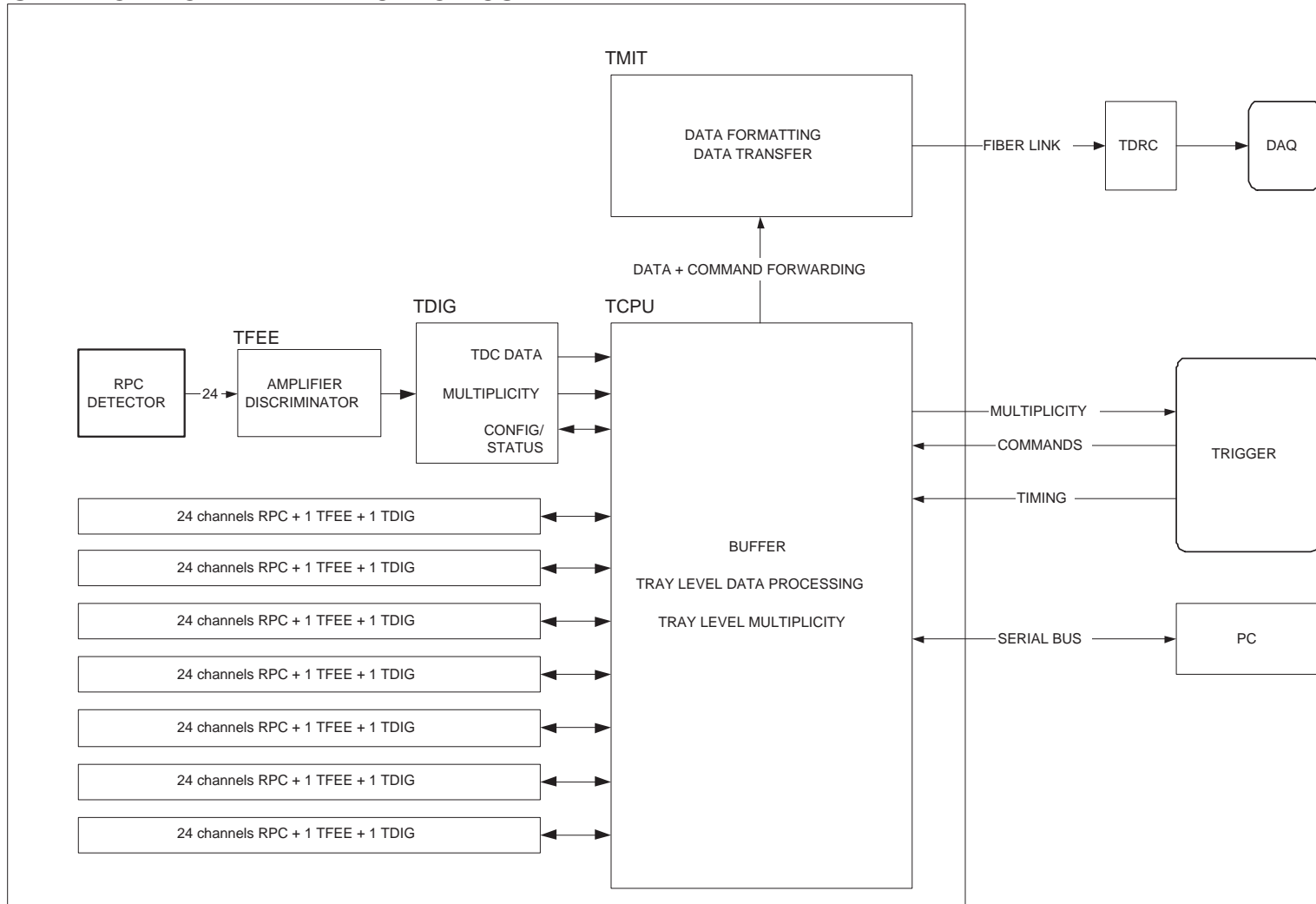


Figure 33: The top level electronics diagram at the tray level.

## STAR TOF: PARTITIONING AND DATA FLOW FOR 1 DETECTOR TRAY

NOTE: CLOCK AND CONTROL NOT SHOWN

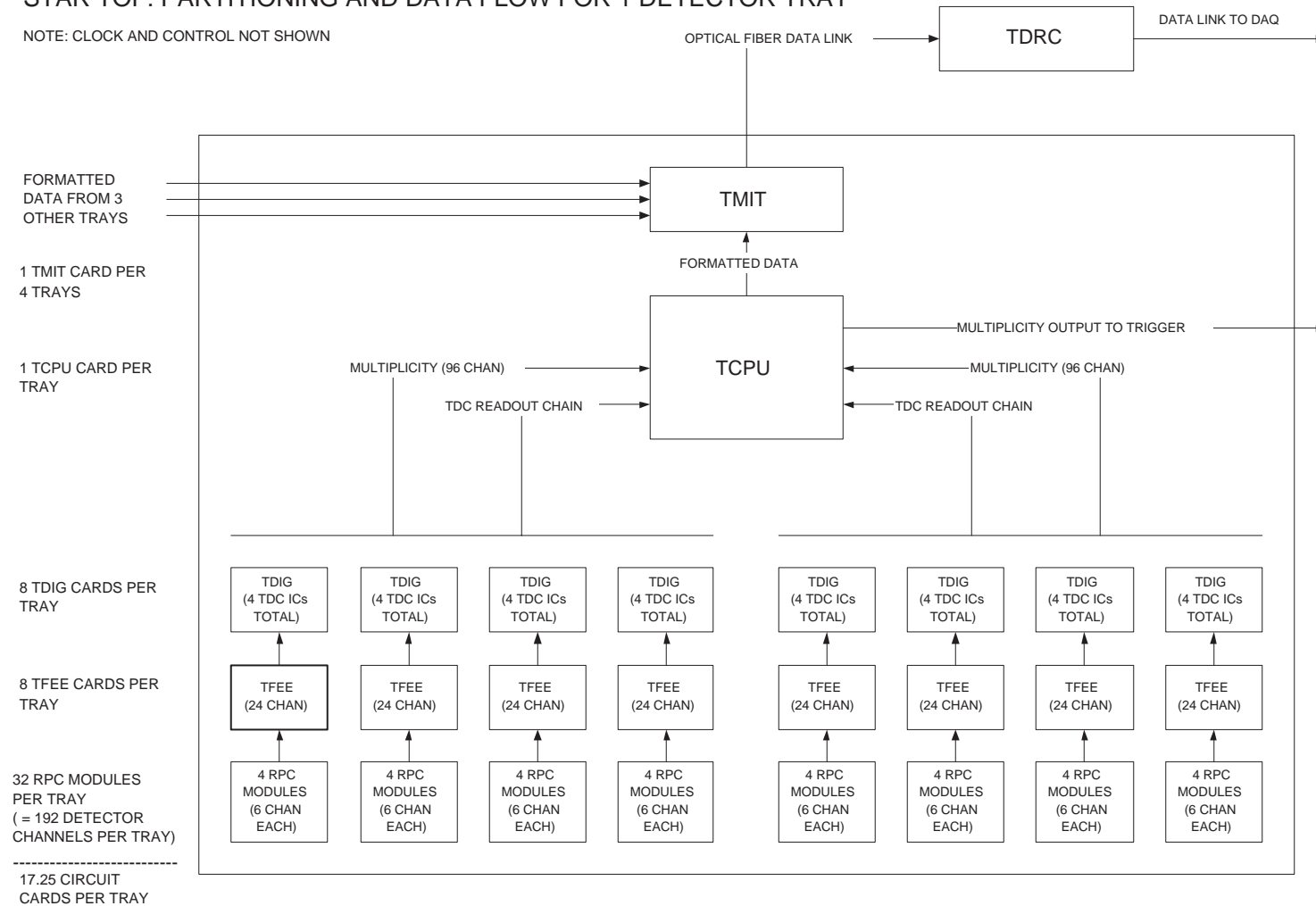


Figure 34: The partitioning of electronics functions between circuit cards.



Each MRPC module contains 6 detector channels. Four modules feed into one TFEE. Each TFEE feeds one TDIG. The 8 TDIG cards in a tray feed into a single TCPU. Data from 4 TCPUs will feed into a single TMIT located as a daughter board on one of the TCPUs. Figure 34 shows the physical partitioning of these different electronics boards and the data flow between them.

Each TFEE card contains the high-bandwidth amplifiers and leading-edge discriminators for 24 detector inputs (4 modules). These two functions are performed by the Maxim 3760 preamplifier and the Analog Devices AD96687 dual comparator. To reduce noise into the low level MRPC output signal, the TFEE is designed as an integral part of the tray mechanical structure. The TFEE will have test inputs and outputs to allow the simulated MRPC signal input and front-end performance measurements using external test equipment (ADCs, TDCs and high performance oscilloscopes) that is independent of the embedded TDC circuitry. This will allow isolated performance measurements of the pre-amplifier, discriminator, and TDC, as well as the comparison of the TDC measurements by TDIG to those when digitizing in CAMAC or in a fast oscilloscope.

Each TDIG card comprises the time-to-digital conversion function for the discriminator outputs from a TFEE, using the HPTDC ASIC under development at CERN for ALICE and CMS. There are eight TDIG cards per tray, and each sees 24 detector channels via one TFEE card. The 4 HPTDC chips on each TDIG card sample rising and falling edges of the discriminated input pulse, giving both leading edge timing and time-over-threshold information (for the slewing correction). The HPTDC chip also contains a buffer for 256 recorded times where stop times are held until read out by the TCPU card. The amplifier/discriminator and TDC functions are physically and electrically separated onto two boards, TFEE and TDIG, to reduce the chance that digital noise from the TDC circuitry will interfere with (i.e. add jitter to) the analog signals in the amplifier/discriminator section.

Each TDIG card also performs the first layer of logic for the multiplicity output, producing the (5-bit) total of active discriminator outputs at each beam crossing interval. This information, aggregated at the tray level by the TCPU card, will be used as an input to the STAR Level-0 trigger. Since the installation of the proposed system implies the removal of the STAR CTB, the system will provide the same kind of multiplicity information for  $|\eta| < 1$  to the Level-0 trigger that the CTB did.

There is one TCPU card per detector tray. The TCPU card configures the eight TDIG and TFEE pairs in the tray and controls data acquisition cycles based on commands from the trigger. The TCPU also receives TDC data from the TDIG cards, formats and buffers the data, and transfers the buffered data to the TMIT daughter board for transmission to the DAQ via the TDRC card.

The TMIT circuit implements a high-speed serial communications protocol at the physical layer. Separating this function into a separate daughter board allows a protocol change to occur transparently to the TCPU hardware - only embedded CPU or PLD firmware changes would be necessary.

The TCPU receives a beam crossing timing signal from the trigger, cleans it up (if necessary) and distributes it to the TDCs on the TDIG boards. In normal operation,

the TCPU will configure itself and operate based on embedded firmware, but the TCPU includes a serial bus connection to a host PC to directly control configuration and obtain status during testing and system integration. This data link will be available for remote diagnostics during final assembly and operation of the system.

The TCPU performs the second layer of logic for the multiplicity output, summing 5-bit inputs from four TDIG cards into a 7-bit multiplicity output for a half-tray (96 channels). The TCPU performs this function for each of the two half-tray signal groups and sends the 7-bit result for each group as a 7-bit differential signal during each beam crossing interval. There are 2 multiplicity outputs for each tray; each is 7 bits in parallel, and each bit is differential (2 signal wires).

In the subsections below, we describe each of the five STAR TOF electronics boards in more detail.

#### 4.6.1 TFEE

This card contains preamplifier and discriminator circuits to accommodate 24 pad signals from 4 MRPC modules. A TOF detector tray will have 8 TFEE cards. Each TFEE card will be 8.4"×10.5". The power dissipation will be about 14 Watts per card, or 110 Watts per tray. The principal functions of the TFEE and TDIG are shown in Figure 35.

The preamp device, a Maxim 3760, is a low noise input trans-impedance integrated circuit whose gain and rise time characteristics are well-defined by internal feedback. This part is commercially available for use as a photodiode receiver preamp in data communication applications. Several designs employing this chip have shown excellent timing performance when connected to actual MRPC pads - the Maxim 3760 has been used extensively for the past two years by both the STAR and ALICE TOF groups.

An ultra-high speed integrated circuit comparator, the AD96685, serves as a simple leading-edge discriminator with externally controlled threshold. This circuit has also been demonstrated successfully in both the TOFp and TOFr systems. The output pulse width, *i.e.* the "Time Over Threshold," will be used to infer the input signal pulse height for the slewing correction.

The TFEE is an integral part of the tray mechanical assembly. This results in the shortest signal path and the maximum shielding. The TDIG cards are stacked above their respective TFEE card to reduce RF cabling. Multiplicity sums have dedicated parallel data paths from each TDIG card to the TCPU. The TDCs on the TDIG cards are read over a dedicated bus in groups of 16 TDCs (four TDIG cards), giving 2 data paths from the TDIG cards to the TCPU. All the TDCs are configured via a JTAG serial bus. The threshold DACs and temperature monitors are configured/read from a separate low speed serial bus.

Provisions will be made during the design of the TFEE cards to optionally bypass the preamp section. This will allow these boards (TFEEb) to operate when the inputs are photomultiplier signals, not MRPC signals. This will allow the identical signal processing chain to be used on the start side with no additional board designs. Access to the preamp outputs will also be included for evaluation of MRPC ADC spectra

during the final testing and QA of fully assembled final trays.

A 6-channel version of TFEE was produced for the prototype TOF tray, TOFr (see section 5). This circuit for TOFr had additional functions that will not be required on TFEE such as an amplified analog output and NIM logic signal output. The pre-amplifier, discriminator, and related circuitry will remain the same, so we have a proven design for this card and experience building and testing production boards.

Table VI shows the bench test results for 41 TOFr FEE cards. The jitter in the pre-amplifier was of order 20 ps or less in all but one channel. This is an outstanding result.

These TOFr FEE cards have proved to be reliable. They have been used for testing MRPC modules at CERN, Rice, and in China and 28 six-channel cards were used for the TOFr tests at the AGS. There was one field failure in a single channel, but this channel proved good when re-tested on the bench, so the failure was likely a poor connection to the interface card.

#### 4.6.2 TDIG

The TDIG card measures leading and trailing edge timing for 4 MRPC modules (24 detector channels). These cards are mounted directly on the TFEE cards - one TDIG card per TFEE card. The discriminator signals, clock, multiplicity gate, and L0 trigger readout commands are primary inputs while the hit edge timing data and 5-bit partial multiplicity sums are outputs. The calculation of the pulse width for the time-over-threshold slewing correction, and any resultant data formatting, will occur downstream of this card.

The multichannel HPTDC ASIC developed at CERN for the ALICE and CMS experiments is our first choice for the TDC measurement. In addition to meeting our time resolution requirements, it has efficient and flexible triggering and readout features. The trigger matching function allows acquired data to be read out from the built-in buffer in an order that accounts for trigger latency. As a backup, we will evaluate a device under development at the University of Oulu in Finland. The Oulu device as specified has adequate timing resolution but does not include readout features of the CERN HPTDC. However, the Oulu TDC is a full custom CMOS ASIC achieving 20 picosecond timing precision with very low power consumption of <5 mW/channel. NASA is currently evaluating chips they have received from Oulu.

Leading edge timing for 24 channels with 25 ps binning will be provided by 3 HPTDC devices operating in 8 channel, Very Hi Res mode. The trailing edge times of all 24 channels will be determined by 1 device operating in 32 channel Hi Res mode with 100 ps time bins. A built in hardware handshake protocol allows 16 HPTDC devices to share a 80 Mbit/sec serial output port so that only 2 data cables are required per CTB tray (4 TDIG boards, 96 MRPC pads each).

Additionally, this card will have slow serial interfaces for TDC and logic configuration, control of discriminator threshold and temperature monitoring. Estimated power consumption is about 10 watts per board or 80 watts per tray.

We have on hand 250 HPTDC chips from the first CERN production run and have

Board	Status	Chan 1	Chan 2	Chan 3	Chan 4	Chan 5	Chan 6
4	OK	16.0	16.0	18.0	16.0	18.0	17.0
5	OK	15.0	16.0	16.0	16.0	16.0	16.0
6	OK	16.2	16.7	15.8	18.8	17.8	16.1
7	OK	16.0	14.0	18.0	18.0	17.0	20.0
8	OK	16.0	19.0	16.0	19.0	16.0	16.0
9	OK	16.7	17.2	15.8	14.8	16.3	16.0
10	OK	16.9	18.6	17.3	18.9	19.7	17.8
11	OK	16.9	18.0	15.0	19.4	16.8	17.3
12	OK	17.4	17.4	20.1	20.5	15.2	16.5
13	OK	17.7	21.0	18.9	17.8	17.8	17.3
14	failed						
15	failed&fixed	14.8	13.9	22.0	15.5	23.2	21.1
16	OK	18.4	18.4	15.8	20.0	19.2	19.7
17	OK	16.5	14.8	20.3	18.5	16.5	20.7
18	OK	15.7	15.0	16.3	19.0	19.2	16.9
19	OK	16.3	16.4	18.0	18.2	17.4	18.8
20	OK	16.2	19.6	17.3	19.7	15.6	18.8
21	OK	16.8	17.0	17.6	17.9	15.3	17.0
22	OK	15.8	15.1	17.1	20.2	20.4	16.9
23	OK	18.3	19.3	15.0	17.6	19.8	16.7
24	don't use	18.2	18.9	33.8	15.5	16.4	17.3
25	OK	15.8	14.5	16.5	15.4	16.7	18.6
26	OK	17.7	18.5	16.2	16.8	17.7	19.2
27	OK	14.7	20.3	20.5	19.3	20.1	18.1
28	OK	18.1	16.8	17.8	16.5	17.5	16.8
29	OK	17.0	16.4	19.2	20.2	18.4	18.2
30	OK	15.8	16.6	18.0	17.3	14.2	17.3
31	OK	19.3	16.8	17.4	17.1	17.9	15.4
32	OK	16.3	17.7	16.2	18.4	19.6	15.4
33	OK	18.1	14.1	18.1	17.7	16.1	16.9
34	OK	13.8	18.0	15.0	15.6	19.3	16.3
35	failed&fixed	16.7	16.1	18.6	23.1	16.9	15.1
36	OK	15.2	14.7	14.1	17.4	17.5	15.1
37	OK	19.8	16.3	16.3	15.6	15.6	15.6
38	OK	14.8	18.1	14.4	16.0	15.4	13.9
39	OK	16.1	17.8	17.3	18.7	15.0	15.7
40	OK	19.3	16.5	19.3	20.3	18.4	14.7
41	OK	17.8	16.7	15.6	15.9	14.6	16.1
43	OK	18.3	17.2	20.2	22.0	21.0	19.2
44	no. not used						
45	bad PCB						
46	OK	15.3	19.1	15.0	24.1	20.1	21.6

Table VI: The bench test results for the TOFr FEE cards. The columns are standard deviations (*i.e.* the resolution) in units of picoseconds. These TOFr FEE cards are very similar to cards proposed for the full system called TFEE.

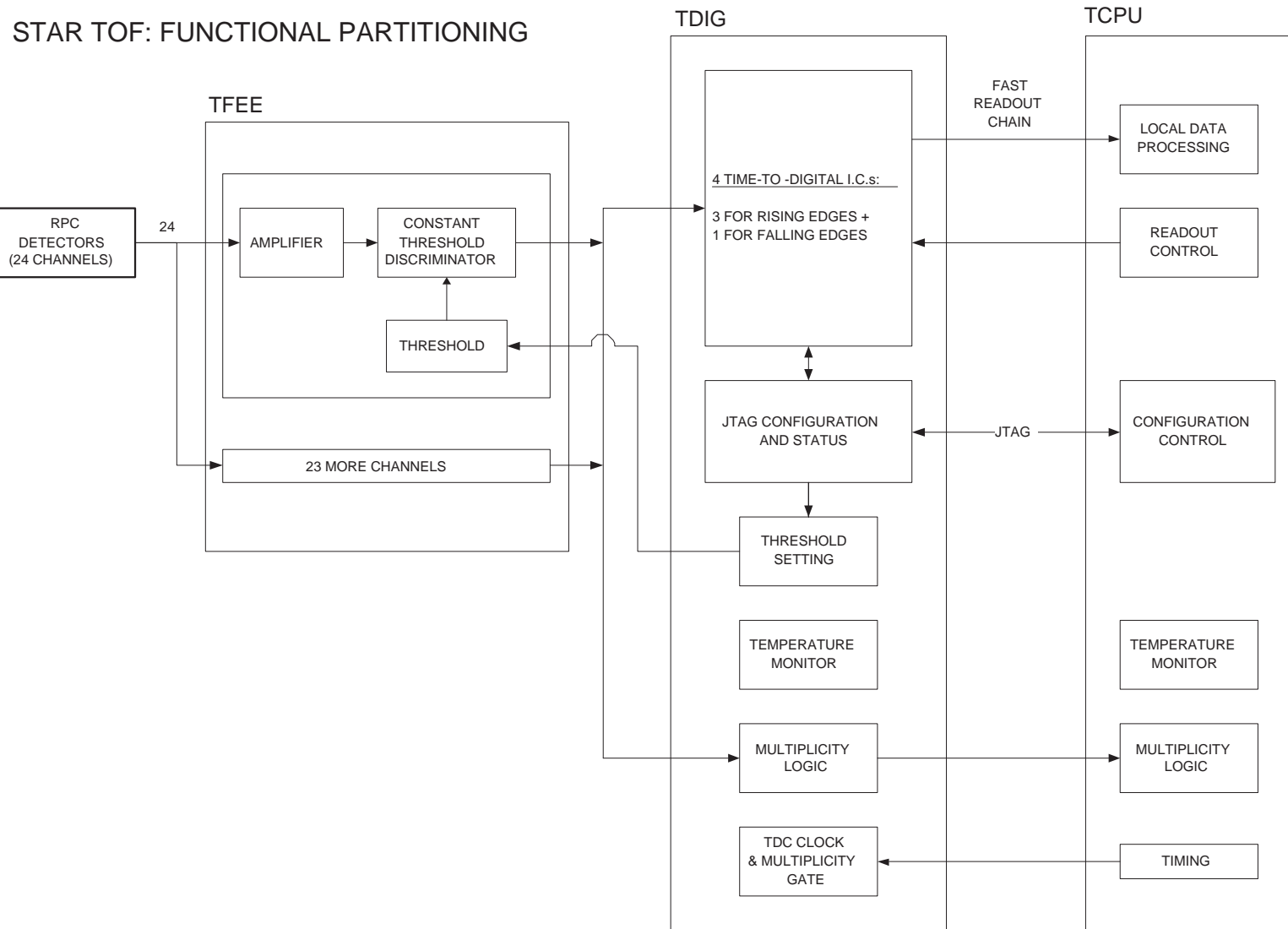


Figure 35: The front end electronics (TFEF) and digital sampling (TDIG) circuit cards.

built a prototype TDIG circuit using the HPTDC. The HPTDCs have been bench tested at CERN and have successfully demonstrated 15 ps timing resolution. The high-resolution mode of the HPTDC is available now in a CAEN VME-based TDC module offering 25 ps resolution (LSB).

### 4.6.3 TTST

The purpose of this card is to serve as an interface to allow convenient testing of the completed trays (MRPC modules plus TFEE) without having to communicate with the full STAR DAQ to get the data out. This board has the same footprint as TDIG and plugs into TFEE in the same way as TDIG. The TTST board contains NIM signal level conditioning circuits to make the TFEE preamp and discriminator outputs compatible with CAMAC TDC & ADC modules. The combination of TFEE and TTST has exactly the same electronic functionality as the TOF FEE boards (see sections 4.6.1 and 5). Only a few of the TTST boards are needed at each location in the project where fully-assembled trays are being tested.

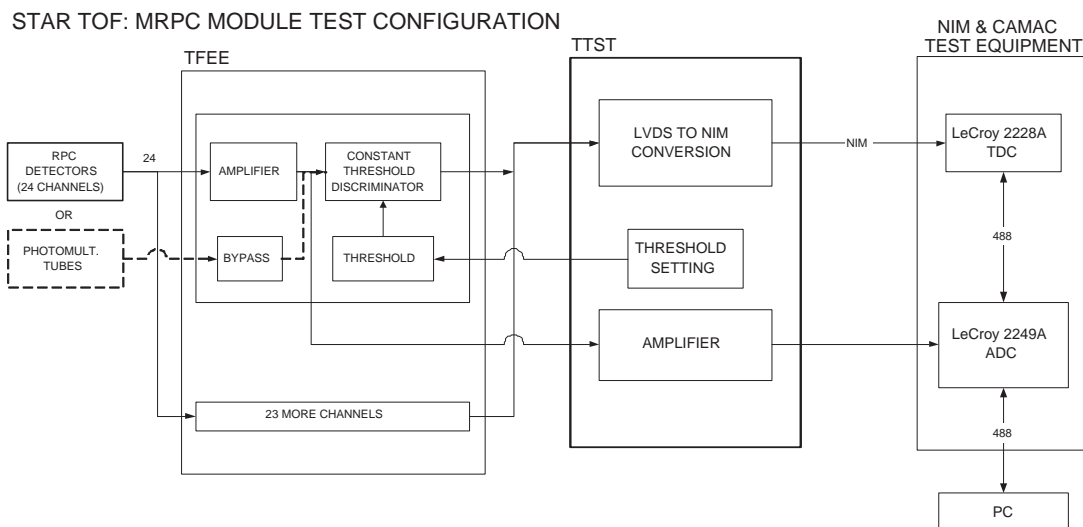


Figure 36: The functional diagram of the construction test electronics chain TFEE to TTST to CAMAC.

### 4.6.4 TCPU

The TCPU circuit card functions as a data concentrator and interface between the external experimental environment and the STAR TOF data acquisition electronics (TFEE and TDIG). The TCPU is implemented as a combination of embedded CPU and programmable logic. The TCPU functions at the detector tray level, and our design has one TCPU per tray. The TCPU concentrates data from 192 detector channels.

The TCPU performs the following functions (see Figure 37):

- **Multiplicity** – Once per beam crossing, the 8 TDIG cards in a tray each provide multiplicity data as a 5-bit value representing from 0 to 24 hits. From these data, the TCPU computes 2 multiplicity sums, each the sum of 4 TDIG inputs, or 96 channels. Each half-tray multiplicity sum is sent to the STAR Level 0 trigger as 7 differential signal pairs, using either PECL or LVDS drivers.
- **TDC readout** – The TCPU will provide readout signals to the 32 TDCs in the tray. It will receive data from the TDCs, buffer the data, format the data, and send it out via the TMIT daughter board. In the process of building data packets from buffered data for transmission via the TMIT board, the TCPU will perform data token management, using tokens received via trigger commands.
- **System configuration** – Prior to data acquisition, the TCPU configures the TDCs, sets the discriminator thresholds, and initializes the trigger command processing and high speed data transmission blocks. Configuration parameters are loaded from on-board EEPROM storage or read from a host PC over the host serial bus. The TCPU sends configuration data to the TDCs over a JTAG daisy chain. The threshold DAC configuration data travels over a separate 2-wire communication path.
- **System status** – System status information includes TDC configuration echo via JTAG, threshold DAC echo via the 2-wire communication path, and temperature monitor information via the 2-wire communication path. We will likely implement limited built-in self-test capabilities in the TDIG and TCPU cards. This information will be included in the system status.
- **System timebase conditioning** – The TCPU will receive a system level beam crossing clock from the RHIC V124 modules. It conditions this signal by PLL frequency multiplication and filtering techniques to produce a TDC sampling clock with acceptably low jitter characteristics.
- **Trigger command processing** – The TCPU will receive and process commands from the trigger. It will also simply pass some commands such as Abort and L2 Accept on to DAQ via the TMIT card.

#### 4.6.5 TMIT

The TMIT takes formatted data from the data/command buffer, serializes it and transmits it over a fiber optic link to the TDRC. The TMIT will be implemented as a PLD (or a communications chip specific to the communications protocol) and an optical transmitter.

#### 4.6.6 TDRC

The TOF data acquisition (DAQ) system, represented by the TDRC block in the preceding figures, has to receive the digitized data from 120 trays and the start

STAR TOF: TCPU FUNCTIONS

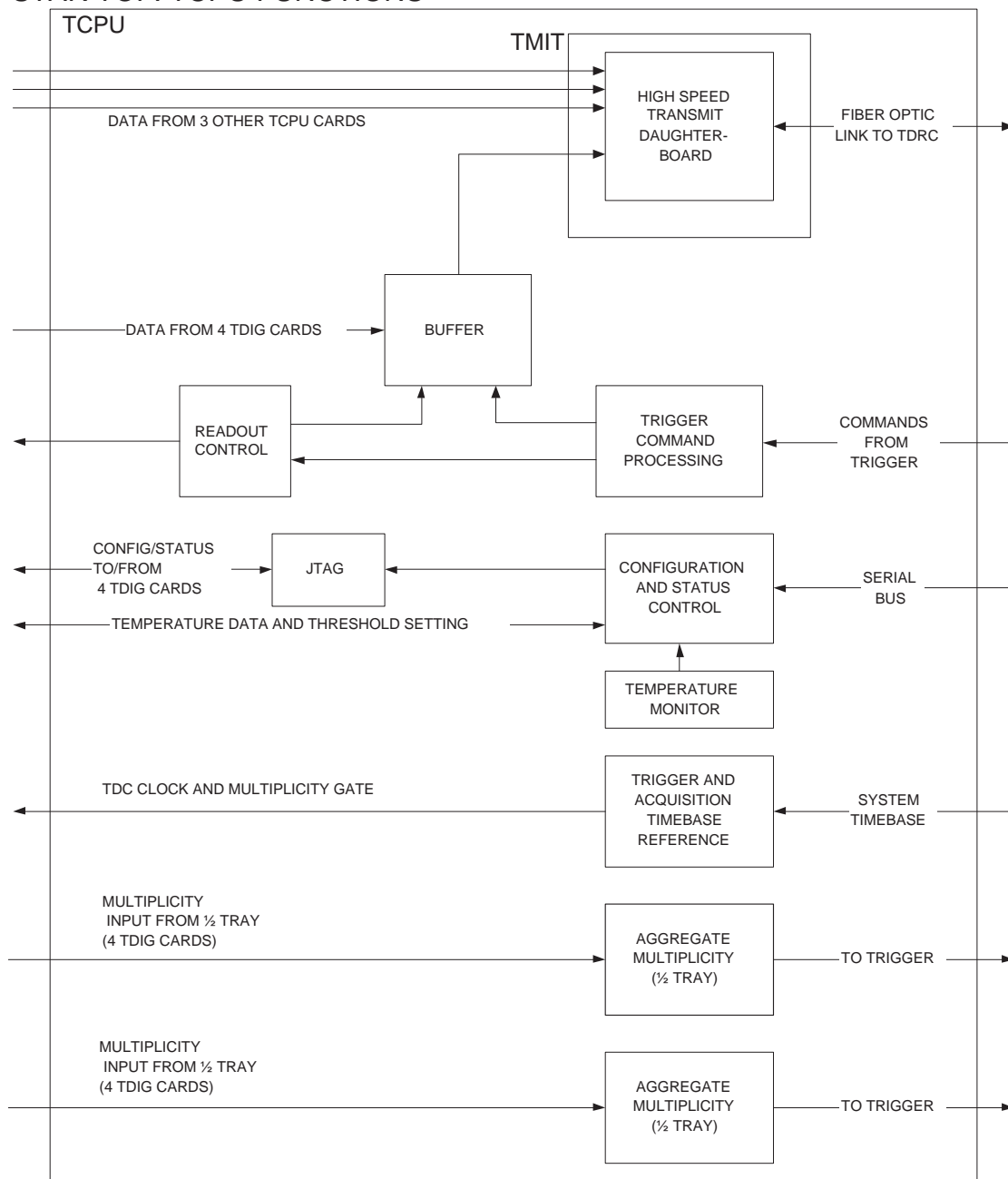


Figure 37: The tray level CPU (TCPU) and high speed data transmit (TMIT) circuit cards.

detectors via optical fiber and present it to the rest of the STAR DAQ system. The data from TOF is provided by 4 fiber links, each carrying the data from 30 trays collected by THUB. The data from TOF to the Level-2 trigger system will be sent over the same fiber to the same receiver.

While most of STAR DAQ is currently implemented in VME, future development



of the STAR DAQ system will be moving into PC based systems running Linux. These systems are ideally suited for the TOF DAQ system as well, so the data needs to be received by an interface that can plug into a PC. Every modern PC has a PCI extension bus, so the most logical choice of a DAQ receiver would be implemented as a fiber receiver that plugs into the PCI bus (or its future extensions like PCI-X).

The CERN experiment ALICE has developed such a system to use in its DAQ system. This system consists of a set of cards that provide the optical link called the Detector Data Link (DDL), one of which is housed on the detector side, the other in the DAQ computer, and a PCI interface card to connect the DDL card to the PCI bus called the Read-Out Receiver Card. (RORC).

The DDL system consists of 2 kinds of cards: the (Source Interface Unit) (SIU) which interfaces to the front-end electronics in the case of ALICE, and the Destination Interface Unit (DIU), which connects to the DAQ front-end processors. Initially, these two cards were implemented as two distinct physical cards, but in their latest implementation in ALICE, these are now the same cards with different firmware running in their programmable logic devices. The two DDL interface units are connected through two multi-mode optical fibers running at 2.5GB/s, so the connection is bi-directional. The DIU is connected to a PCI based RORC in the DAQ computers. The RORC receives data from the detector via the SIU-DIU connection, and provides it to the PC via the PCI bus. At the same time, the RORC can also provide commands to the detector as well as get status information from the detector via the downlink of the fiber connection. The theoretical limit of the 32bit/33MHz version of the PCI bus is 132MB/s, while using the 64bit/66MHz version of PCI one could in principle achieve 528MB/s. The cooperation between the RORC firmware and the PC software allows autonomous data transfer into the PC memory with little CPU assistance. The ALICE DAQ interface is described in [147].

For the PC, we have chosen a dual Intel Xeon system based on a motherboard with 6 PCI-X slots to provide sufficient slots for all four RORCs needed in the TOF DAQ as well as a network card to interface this PC to the rest of STAR DAQ. Currently, the network of choice in STAR DAQ is Myrinet, which exists as an implementation in a PCI-X extension card.

## 4.7 Power Systems

Low voltage supplies on the STAR platforms are needed to power the on-detector electronics which require roughly +4.5V and -8.5V. High voltage of  $\pm 8$  kV is needed to power each MRPC detector. We will evaluate high-channel-density commercial supplies to fill these two roles.

We have used a CAEN SY127 control unit with A631 power modules to provide the high voltage to the TOF prototype trays in the last two RHIC runs (3 and 4). We are comfortable with the performance of this unit and plan to use it in the final system.

## 4.8 Test & Monitoring Software

A small-scale DAQ system has been developed for MRPC testing. The digitization is done using CAMAC TDC and ADC modules. To allow flexibility and possibly further test automation a GPIB-based CAMAC controller was used in these test experiments. Object oriented DAQ software, already successfully used in earlier TOFp tests, allows for optimum flexibility in introducing new or adding additional CAMAC modules, controllers, or online analysis software modules. The CERN HBOOK functionality is wrapped in the C++ code such that the output files are written in the standard ntuple format and therefore directly analyzable on any platform at any institution.

For the AGS tests of the TOFr prototype (discussed in section 5 below), additional scripting software allowed the operation of this DAQ in a daemon-like fashion. The software ran extremely reliably and has collected many millions of test beam events so far.

The main purpose of the online software for this system will be monitoring and control. The STAR Slow Controls system is now mature and well-understood and most if not all operational parameters will be set and monitored through this system. Typically the operations include monitoring of temperatures, controlling and monitoring the high voltage and low voltage, monitoring the comparator thresholds, reading/setting the TDC configuration, and monitoring the parameters of the gas system. Including these parameters in STAR Slow Controls system also means that they are automatically added to the online database. This will be helpful in advanced stages of the data analysis to correct for long term drift such as that related to electronics temperatures or from the gas system parameters.

## 4.9 Start Detector Design

In this section, we present comments on the current start detector, the pVPD, and discuss the advantages of an upgrade to this detector. This detector is described in detail in Ref. [4]. This detector was constructed and commissioned within the contingency of the STAR TOFp construction funding. Its purpose is to provide copies of the raw PMT signals and high-resolution discriminator logic signals to be used in NIM electronics on the platform as the the electronic start for the TOFp and pVPD digitization. The pVPD was installed in STAR in Spring 2001 and ran throughout RHIC Runs 2, 3, and 4. This detector subsystem of STAR TOFp consists of two identical assemblies of three magnetically-shielded Pb+Scintillator+PMT+Linear Base detectors in the “flashlight” design. These detector assemblies are mounted very close to the beam pipe at a STAR  $|Z|$  position of  $\sim 5$  m; one on the East and one on the West. The front-end electronics are single boards of the same TOFp FEE as are used inside the TOFp tray.

In RHIC Run-2’s full-energy Au+Au collisions, we observed that the pVPD is practically 100% efficient for all but perhaps the most peripheral 5% of the (ZDC/CTB triggered) STAR-standard minimum bias events. (The zero degree calorimeter, ZDC, is detects remnant neutrons at zero degrees.) Another observation was that the pVPD

fired in  $\sim 60\%$  of the BBC triggered STAR events taken in Run-2 p+p running. (The beam-beam counter, BBC, coincidence is the minimum bias trigger in p+p running.) After the ZDC, the pVPD is the most forward detector in STAR. There are areas of common acceptance between the pVPD detectors and a few of the most-inner BBC detectors.

In the Au+Au data from that run, we observed sub-50 ps timing resolution of the pVPD. This was achieved by running the pVPD “hot,” meaning we ran the pVPD PMT high voltage to the largest possible values for which the pulse area distributions were still  $>90\%$  on-scale for the LeCroy 2249A ADCs and 8 dB attenuators at each pVPD ADC input. In the Au+Au data, there are numerous hits in each detector channel from very energetic photons which convert in the Pb layer resulting in a large number of prompt photoelectrons. The result is an excellent start time resolution. For the p+p running, the 8 dB attenuators were removed from the TOFp ADC inputs and the pVPD PMT gains were increased by approximately a factor of nine (9) above that used (with ADC attenuators) during the Au+Au running. The data from the p+p run indicate that, when a pVPD channel fires, it is firing on a single particle. The probability that one detector on the east fired and one detector on the west fired in the p+p part of RHIC Run-2 was approximately 12%.

There are immutable penalties to the start time resolution when comparing the operation of such a “small-area” start detector in p+p or d+Au to that in Au+Au. The fact that p+p or d+Au data means single particle start timing in detectors of this size implies a relatively low number of photoelectrons and hence the intrinsic resolution of the detectors are worse compared to Au+Au (which has many 10’s of prompt hits per detector channel per event). Also, the sparse number of final state particles in p+p and d+Au data implies that only rarely can one use the average times of many start detectors in the same event in order to further improve the total start time resolution beyond the intrinsic single channel timing resolution.

The requirements on the performance of the start detector for the proposed large-area TOF system in full energy Au+Au collisions are minimal. In Au+Au with many tens of square meters of TOF coverage, there are many TPC tracks matched to TOF channels. In this case, the start time can be inferred event by event from the stop times with nearly arbitrary precision. According to simulations performed for the TOFp proposal [3], one only needs  $\sim 10$  TPC $\rightarrow$ TOF track matches to be able to infer the event start time solely from the stop times with a resolution of  $\sim 40$  ps. This is sufficient to meet the physics requirements for the whole system (start plus stop plus corrections).

However, for p+p, d+Au, and peripheral light-ion collisions, an increase of the acceptance of the start detector would have a significant positive impact on the system as a whole. Obviously the efficiency per event improves. The resolution of the start detector adds in quadrature to the stop resolution of the large area TOF system. An increased acceptance on the start side also enables multiple independent measurements of the prompt particles in the same event, improving the start resolution. This makes some aspects of the offline analysis, which involves a number of corrections independent of those related to the start detector, easier. Initiating an analysis with an

intrinsically high-resolution start time in a “large” acceptance reduces the magnitude and uncertainty in all other corrections. Examples of stop corrections made considerably easier by better start timing are the hit position correction and the slewing correction.

The pVPD upgrade would involve:

- replacing the 3+3 pVPD shielded PMT assemblies with approximately 20+20 unshielded mesh-dynode PMT assemblies. This number of unshielded mesh-dynode PMTs fits easily into the same volume occupied by the present pVPD. As almost all of weight of the pVPD is in the six steel plus  $\mu$ -metal shield assemblies, the upgraded detector as a whole may be lighter than the present pVPD despite the increased channel count.
- replacing the FEE and CAMAC digitization with the same electronics being developed for the stop side in this proposal (see 4.6). The only modification in the electronics chains on the start and stop sides is in the use of the TPMT board instead of TAMP just after the detectors.
- building two new small light-weight aluminum and Delrin mounting assemblies. Since magnetic shielding is unnecessary for the mesh-dynode PMTs, there are no longer magnetic forces on the mounting structure, which simplifies the design.

The upgraded pVPD would occupy the same integration volume as the present pVPD, which is close to the beam pipe near  $|Z| \sim 5$  m. This volume does not conflict with the PMD, FPD, and BBC detectors in the vicinity. With the pVPD’s magnetic shields gone, the largest source of backgrounds in other detectors from particle interactions in the pVPD is removed. The same FEE plus digitization plus communication electronics chain that is presently proposed for the stop side will be used for this upgraded system. The start side, like the stop side, will be digitized on-detector versus a common clock, and digital data is transmitted off the detector. The economy of using the same basic electronics design for both the start and stop sides of this system requires that the TAMP boards (see section 4.6.1) be modified to include input protection and to accept PMT inputs. This modified board is called TPMT.

The PMTs could be obtained in principle from the STAR CTB, which will have to be decommissioned to make way for the proposed system. However, these PMTs have been damaged by large LED pulses and they afterpulse, a typical problem for Hamamatsu mesh-dynode PMTs as they age. If the TOFp system were decommissioned in the Summer of 2004, there would exist  $\sim 40$  more mesh dynode PMTs which will have higher gains and better resolution than the CTB PMTs (but which may also afterpulse by then). A possible approach would be to decommission both TOFp and the CTB in stages as final TOF trays begin to appear, and then take the best  $\sim 50$  PMTs available. The cost estimate for the pVPD upgrade includes the purchase of new Hamamatsu R5946 PMTs which would be installed when the construction of the TOF barrel is nearly complete.

Twenty detector channels per upgraded PVPD detector is well-matched to the 24 channel TPMT boards. There would be a single TPMT board and a single TDIG

board mounted close to the upgraded pVPD detectors, one on each side of STAR. Power to the PMTs would be provided by a standard LeCroy 1440 mainframe available from HEEP.

This upgraded pVPD system, with a high channel count and crossing-by-crossing clocking of the start timing information, will provide multiplicity information to the STAR Level 0 trigger in the same way as the TOF barrel. Providing Level 0 with the primary vertex location via east/west timing differences event by event requires further design but appears to be feasible using the electronics model described in section 4.6.



## 5 The Full-Size STAR Prototypes: TOFr & TOFr'

The MRPC design incorporating six electrode pads was perfected over several years of testing modules at CERN. The test beam setup and other assistance was provided by the ALICE TOF group. We next proposed a 30-module prototype tray [10] with the requisite on-tray electronics, gas system, and high and low voltage distribution. The shape of this tray is identical to those in the STAR CTB (125 trays) and TOFp (1 tray) subsystems built by the Rice group. The construction of this first prototype, called “TOFr,” was completed in February 2002 and the system was transported to BNL where it was tested in a radiation area near the E949 experiment at the AGS for 70 days in the spring, 2002. It was then installed in STAR and operated throughout RHIC Run-3 (FY2003). Section 5.1 describes the construction of the TOFr tray, section 5.2 discusses the results obtained from the AGS tests, and section 5.3 describes the results obtained in STAR during Run-3.

The second-generation full-sized prototype for STAR, called “TOFr’,” was built in the summer of 2003 and operated in STAR throughout RHIC Run-4. The discussion this second prototype and its operation during RHIC Run-4 is described in section 5.4.

### 5.1 TOFr Construction

The dimensioned side view of the module geometry of the TOFr tray is shown in Figure 38. The  $\eta \sim 0(1)$  end is on the left(right) side. The design supports the insertion of 33 MRPC modules. For TOFr, 28 modules were installed, 24 of these produced by the Chinese groups and 4 produced at CERN. The CERN modules were slightly thicker than the CN modules, which was handled by simple retrofits.

The mechanical support of the MRPC modules in three dimensions was accomplished using so-called “sawtooths”. These are shown at the bottom inset of Figure 38. The sawtooths are 48 differently-shaped pieces of “hexcell” (phenolic-impregnated Kraft paper honeycomb, 1/4” thick) which are glued to the inside walls of the tray. The modules rest inside precisely located voids in the hexcell sawtooths. To fabricate these sawtooths, each pattern was printed to scale on paper. Two layers of hexcell were attached to each other and the pattern by double-sided tape. A band saw was used to cut out the pattern. This resulted in two sawtooth pieces for each shape, one attached to the left side of the tray and the other to the right.

The 96 sawtooths required in total are categorized as “A”, “B”, and “C”. The A sawtooths were glued to the bottom inside walls for the full length of the tray. The TOFr tray after this step is shown in the left side of Figure 39. Next the lower row of modules was installed, resting on the upper edges of the A sawtooths. Then the B sawtooths were glued on the tray inside walls, just above this layer of modules. Then the rest of the modules were installed. Finally, the C sawtooths were glued into position. At this point all modules were mechanically secure inside the tray. The TOFr tray after this step is shown on the right side of Figure 39.

Once the detectors and sawtooths were installed, the interior high voltage and

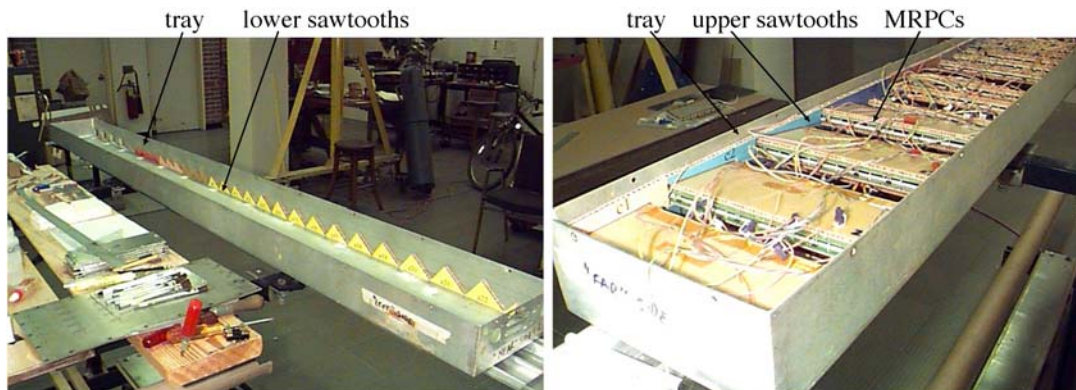


Figure 39: On the left, the lower sawtooths in position in the TOFr tray, and on the right, the TOFr tray filled with 28 MRPC modules snugly positioned by all three layers of sawtooths.

gas piping was installed. The 28 modules in the TOFr tray are connected to one of two interior HV busses, A and B. The “A” bus powers the 19 best chambers (lowest noise rate and dark current), while the “B” bus powers the other 9 modules. The gas piping is  $\sim 3/8$ ” OD plastic tubing running from the end plate at the high-z end all the way to the low-z end inside the box.

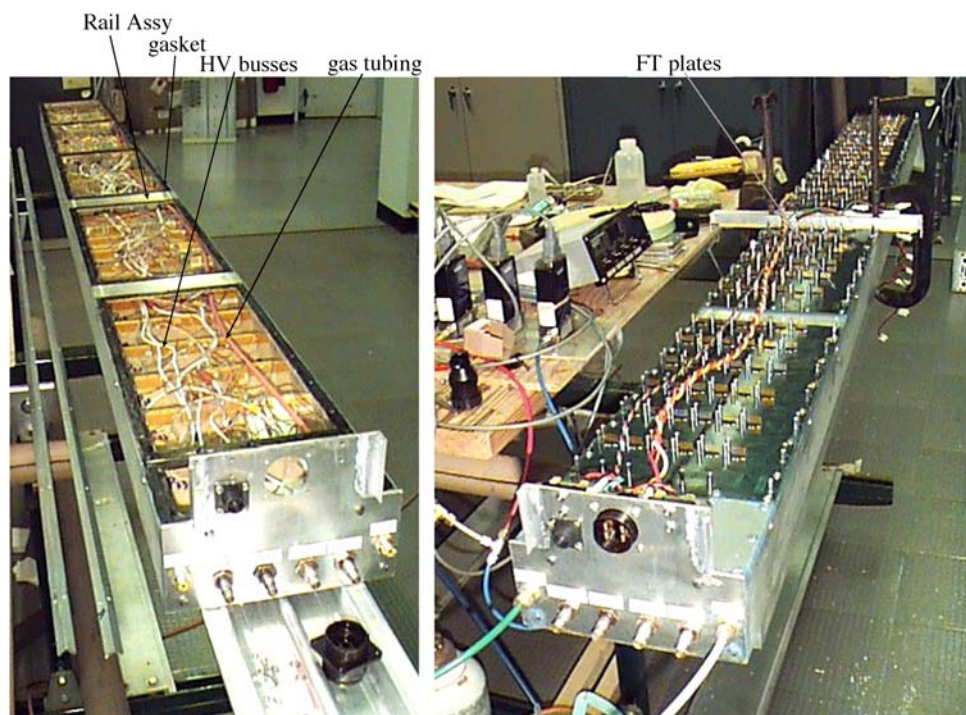


Figure 40: On the left, the TOFr tray after the completion of all interior piping and cabling and the installation of the gasketed rail assembly, and on the right, the TOFr tray with the feedthrough plates installed.



Next, the “Rail Assembly” was installed, which supports the feedthrough (FT) plates from below. The rail assembly is a single piece of aluminum, formed by butt-welding flat plates to 4 pieces of tapped 0.5” aluminum angle. The assembly as a whole fits exactly into the top opening of the box. The assembly is bolted horizontally to the tray walls with 8-32 stainless steel or brass machine screws. The FT plates bolt vertically onto the top of the rail assembly, which closes the gas volume around the detectors. These vertical bolts pass through a gasket of 1 mm-thick neoprene rubber. A view of the TOFr tray with this rail assembly installed is shown on the left side of Figure 40.

With the rail assembly installed, the 28×6 short twisted-pair cables that carry the detector signals from the modules were connected to pins on the underside of the FT plates. These plates were then bolted down to the rail assembly.

For leak checking, Freon gas was flowed through the tray. We found some leaks at the rail assembly/FT plate interface. The leaks were stopped with small amounts of RTV silicone. The leak checking was performed using a Freon sniffer with a maximum sensitivity of 0.4 l/year.

Once gas was flowing through the TOFr tray without leaks, the 28 TOFr FEE boards (see section 4.6.1) were mounted on the top of the FT plates using screw posts. Connectors on the underside of the TOFr FEE boards mount onto the same pins to which the detector signal pigtailed are connected underneath the FT plate inside the gas box. The low voltage needed by these boards is  $\pm 6.5$  V, which is distributed to the 28 FEE boards on two busses of 14 FEE cards (14 modules) each. These low voltage busses are individually fused at the high-z end of the tray. Each of the TOFr FEE boards also independently includes overvoltage protection, overcurrent protection, and input protection.

Shown in Figure 41 is the fully constructed TOFr tray under test at Rice in February 2002. The low-z end of the tray (left side of Figure 38) is closest to the observer. The feedthrough side is at the other end. One can see the individual TOFr FEE boards mounted onto the FT plates on the top of the tray. The low voltage and discriminator threshold distribution is seen above the electronics along the long side of the tray closest to the observer.

Once gas was flowing for  $\sim 24$  hours, the high and low voltage systems were powered up. Noise rate data was then collected for all 168 channels as well as the total dark current as a function of time for the A bus and the B bus and cosmic ray data in a few select channels.

Figures 42 and 43 summarize the results from these tests from the first power-up of the TOFr tray in February, 2002. In Figure 42, the total bus current for the A bus (blue & cyan) and the B bus (red & magenta) are shown. Anything below  $\sim 50$  nA on a single bus is acceptable. One observes however that, given  $\sim 24$  hours for the system to settle down once the HV was applied, the total bus current on the A(B) bus was  $< 20(30)$  nA, or  $< 1(\sim 3)$  nA/module for the 19(9) modules on this bus. The total dark current was thus as expected based on the dark current measured in single chambers.

Shown in the left panel of Figure 43 are histograms (one entry per MRPC channel)

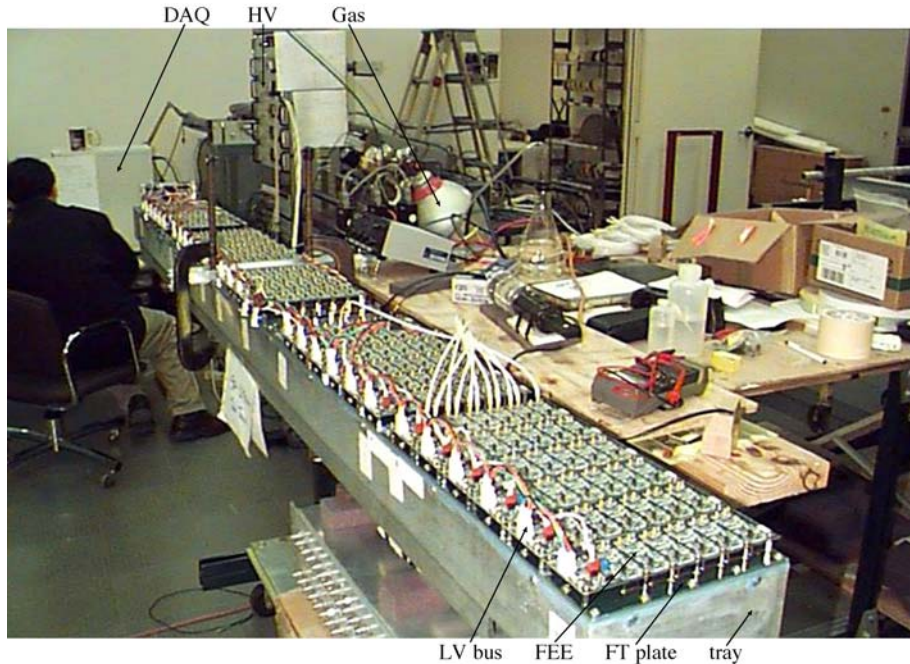


Figure 41: The completed TOFr tray, now with all FEE boards installed and gas flowing for cosmics and noise testing at Rice.

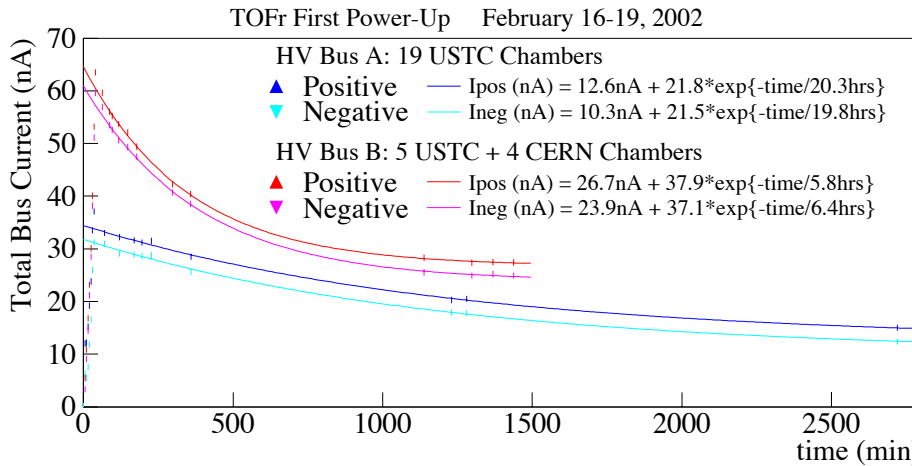


Figure 42: Results on the total HV current draw from the very first power-up of the TOFr tray.

of the noise rates from TOFr - the A bus channels are the blue histogram while the B bus channels are the red histogram. The percentages labelled in the left frame are the fractions of the total number of MRPC channels with noise rates less than the labelled rates. As expected from previous measurements, the A bus chambers are less noisy than the B bus chambers. That is, ~93% of the bus A channels have noise rates below 50 Hz, while only ~51% of the bus B channels have noise rates below this value.

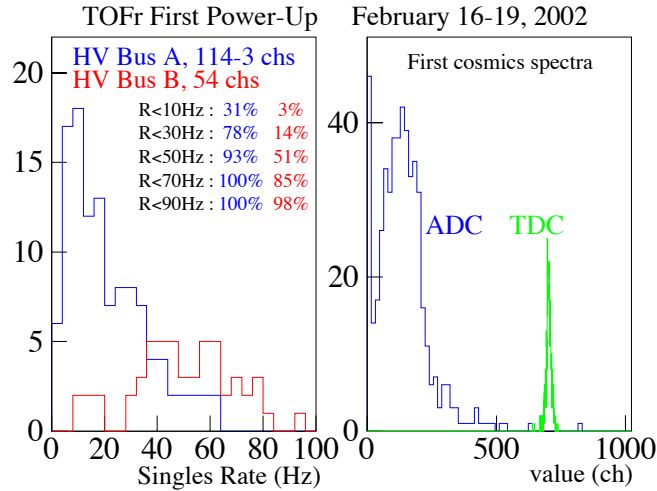


Figure 43: Results on the noise rates from the very first power-up of the TOFr tray.

We conclude that the tray environment does not significantly affect the noise rates of the chambers. On average, the B bus modules have noise rates of  $\sim 50$  Hz, larger than the 10-20 Hz noise rates for the A bus chambers. This is still acceptable for operation in STAR. The right frame of Figure 43 shows an ADC distribution (blue) and uncorrected TDC distribution (green) using small paddles above and below the tray to trigger on cosmic rays. The ADC distribution obtained is comparable to those obtained in CERN test runs, another indicator of the excellent performance the TOFr tray.

These results were from the first power-up of the TOFr tray. The system has since been transported to BNL and is now installed in STAR. The results from the testing of this tray in an AGS radiation area in the spring of 2002 are discussed in section 5.2 below.

The bench tests at Rice and the extensive testing at the AGS constitute a proof of principle for the proposed large-area TOF system. The MRPC technology is mature and the feasibility of the proposed system is not in question. The TOFr construction exercise has successfully removed most of the uncertainty from the construction of a large-scale system.

While most of the construction techniques used to build the TOFr tray are appropriate for the proposed system, there are a few aspects of the TOFr construction that can be improved for construction of 125 such trays. These areas include:

- **Sawtooths** – Constructing 96~120 sawtooths for the full system using the technique used for TOFr would be overly labor-intensive. As the detectors are positioned by the shapes of these pieces, it is important for the overall performance of the system that these pieces be made with tight tolerances. We aim to minimize the number of different sawtooth shapes required and to find a way to cut the pieces automatically.

- **Tapping** – In each rail assembly, there are approximately 200 tapped holes in the angle aluminum. We will study alternate designs that involve fewer tapped holes in the rails, and/or welds in place of machine screws in certain locations.
- **Rail Assembly** – The rail assembly for TOFr was produced in-house, and was labor-intensive even after all the holes had been tapped. The rails and cross plates must be temporarily-installed in a tray, removed as a single unit, and then welded together at many points. This procedure insured a solid custom rail assembly for TOFr, but the fabrication of many of these assemblies might best be shopped out (presumably to the same company making the trays).
- **Gasketing** – In TOFr, the gaskets were glued to the rail assembly. This was very difficult, and it was by far the most labor-intensive aspect of the TOFr construction. In the full system, the gaskets will not be glued to the rail assembly, only greased. As the gaskets are held in place all the way around their periphery by the vertical bolts through the TFEE plates, there is no concern a gasket could “squeeze-out” in such a geometry.
- **Unnecessary holes** – The trays used for the CTB and TOFp detectors include some holes in the bottom of the tray which are unnecessary for this system. Also the tray feet are riveted to the tray body, which adds  $\sim 20$  more holes in the tray, all of which must be individually sealed against gas leaks. For the proposed system, unnecessary holes will be eliminated and the tray feet will be welded to the tray body by the manufacturer. This not only removes many holes but also strengthens the feet’s connection to the tray body.

All of these areas were addressed in the design of the second full-sized prototype, called “TOFr’,” which was operated in STAR throughout RHIC Run-4. For additional details, see section 5.4 below.

## 5.2 TOFr Testing at the AGS

The TOFr tray containing 28 6-channel MRPC TOF modules was transported to BNL for testing and was set up on the floor of the AGS near Experiment 949 on March 18, 2002. The modules in this tray are identical to those we plan to use in the full TOF system. The FEE cards are nearly the same as the TFEE cards in the final design (see sections 4.6.1 and 5.1). The TOFr system contains no on-board TDCs, so the test setup at the AGS used CAMAC TDC and ADC modules to record the start and stop times and to make the various corrections.

The TOFr tray was tested in this beam for a total of ten weeks. Shown in Figure 44 is a photograph of the TOFr tray during this running.

The beam is not actually a test beam but rather a radiation area on the floor of the AGS near Experiment 949. We were able to determine that the beam contained a significant non-relativistic momentum spread by looking at the width of the time distribution in a scintillator separated 20 cm from the start scintillator and then 190

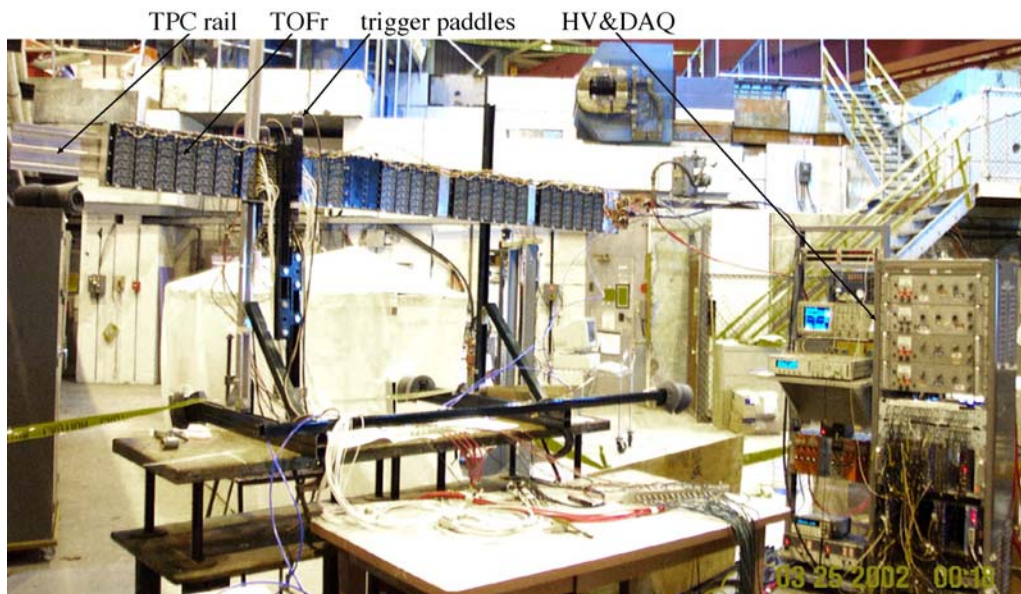


Figure 44: The TOFr tray operating in an AGS radiation area near E949.

cm from the start scintillator. There also seems to be significant radiation of the entire tray during the two-second spill. The dark current was 60 nA during the 2 s spill and dropped to 30 nA during the quiet 3 s of the cycle. The dark current was otherwise 10 nA when the AGS was not operating.

The active region of a 6-channel MRPC module is defined by the transverse dimensions of the five inner glass sheets,  $6.1 \times 20.0$  cm. The trigger defined a rectangular beam spot of  $4 \times 19$  cm so most of the active area was covered and hits could occur in any of the six channels in a module. When testing with a large-area trigger like this, one calculates a single efficiency for the module rather than an efficiency for each pad, as was possible in the CERN tests. That efficiency is just the number of triggered events with a TDC stop in any of the six channels divided by the total number of triggered events.

One of the important tests made at the AGS was to determine the optimum threshold and high voltage for operating the chambers. The previous test at CERN with earlier versions of the module and FEE design used a threshold control voltage equivalent to 2.1V in the current FEE. In these previous tests, it was observed that one can operate the modules with 95-97% efficiency at 15.0-15.5 kV. The typical noise rates for the modules tested at CERN were 60-90 Hz. The noise rate is the number of signals above the discriminator threshold (which includes actual hits from cosmics as well as the intrinsic detector noise).

The noise rates for the latest modules built in China in the prototype tray were almost a factor of 10 lower than the rates seen on previous modules. Data was collected at thresholds of 2.2V, 1.7V, and 1.2 V at operating voltages from 13-16 kV to determine the efficiency and time resolution at each threshold and high voltage setting. The results are shown in Figure 45.

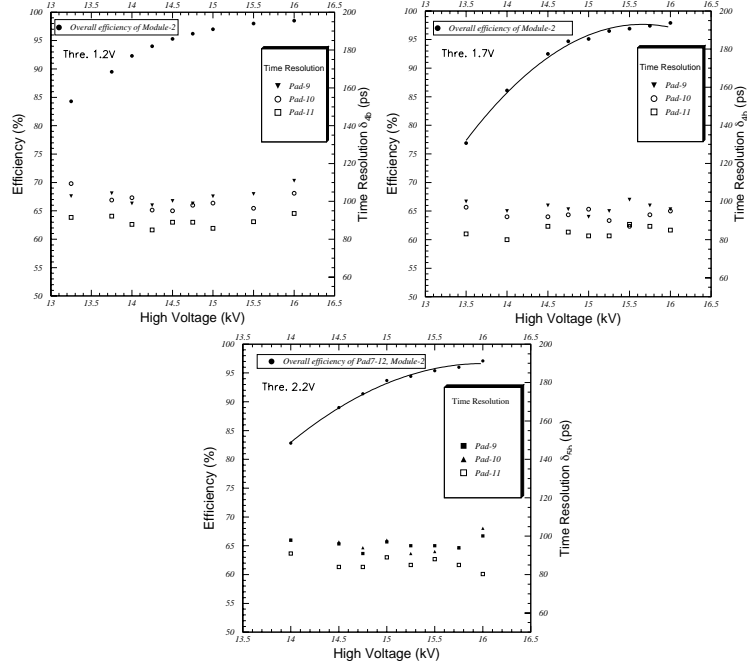


Figure 45: The efficiency (left axes) and time resolution (right axes) versus the high voltage at specific thresholds, 1.2V (upper left frame), 1.7V (upper right frame), and 2.2V (lower frame), obtained from the AGS tests of the TOFr tray.

A start-subtracted time resolution of about 80 ps was achieved. The signals propagate along the length of the 3.0cm $\times$ 6.1cm copper pick-up pads at a rate of 40 ps/cm. Since the particle firing the trigger can be distributed along any 4 cm of this pad, there is a 45 ps smearing of the stop time by the signal propagation time inside the pad. Subtracting this in quadrature from the 80 ps stop resolution indicates that a 70 ps stop resolution would be achieved if the particle position were known to a few mm as it will be in STAR. Given the beam condition at the AGS, the results are very good and fully consistent with the 60 ps result achieved in the CERN test beam runs.

Table VII: Results from the AGS tests of TOFr giving the noise rates at HV and threshold settings leading to module efficiencies of  $\geq 95\%$ .

Efficiency (%)	Threshold (V)	HV (kV)	Noise (Hz)
95.2	2.2	15.5	7.5
95.0	1.7	15.0	7.9
95.2	1.2	14.5	7.1

High voltage and threshold settings were chosen at which the module is 95%

efficient. The results are shown in Table VII. It was concluded that it is optimum to operate the modules at 14.5 kV with a 1.2V threshold. This lower operating voltage will increase the width of the plateau at which the modules operate efficiently without streamers. This should also allow the modules to be somewhat more robust to mechanical imperfections that might occur during construction.

The TOFr system was operated without SF6 for the final two weeks of testing at the AGS. The results showed that the system could be operated at a reduced voltage of 14 kV and 95% efficiency. The high voltage plateau above 95% efficiency with streamer-free operation was slightly smaller but still of order 500 V. The dark current was unchanged and the noise rates were either unchanged or only slightly larger. Although the AGS tests did not constitute a precision test of timing resolution, the preliminary indication is that the timing resolution was the same with the 2-component gas without SF6. We plan to operate the TOFr system in STAR without SF6 to confirm that this mode of operation is possible.

### 5.3 TOFr in STAR in RHIC Run-3

While the MRPC detectors performed well at the CERN test beams (section 4) and in an AGS radiation area (section 5.2), an additional important proof of principle test was to show that MRPC technology, and more importantly an integrated system with a large number of channels, could work well in the STAR environment. To test this, the TOFr prototype tray was installed in STAR and run continuously throughout RHIC Run-3. A summary of the results of this test including preliminary results on timing performance during the d+Au portion of RHIC Run-3 are presented in this section.

The specific technical goals of this test included:

- Installation and integration of an MRPC-based TOF system in a collider experiment for the first time.
- Operation of a multi-detector prototype in a quasi-steady state over the entire run to gain experience on the reliability of the system and assess possible aging effects.
- Collection of sufficient data in specific configurations (based on the choice of the gas mixture, detector high voltage, and discriminator threshold) to make statistically significant evaluations of the timing and PID performance to optimize the final design. (The choice of gas is one example. It is not clear that SF-6, a gas used during the detector development phase, is necessary. This gas is potentially detrimental to the STAR TPCs.)
- Comparison of the performance of TOFr to TOFp (see appendix B or Ref. [4]) in the same RHIC data. Both systems use exactly the same start signals from the pVPD, so the stop timing performance from the two systems can be compared directly, given consistent cuts on the sample of tracks matched to

the two systems. This provides an important apple-to-apples comparison of the well-understood conventional technology of scintillators and PMTs to the new MRPC technology.

RHIC Run-3 provided significant TOF data sets for full energy d+Au and p+p collisions. Twelve MRPC modules (72 channels total) were read out. These included the nine lowest rapidity modules, and two others at higher rapidity. The FEE were the same as those used in the TOFr AGS tests (see also section 4.6.1). The high voltage was provided by a new CAEN SY-127 unit that is also a candidate for use in the full TOF barrel system. The signal cabling was the same as that for the TOFp detector; it is based on high performance Belden 9310 signal cable, and fast, cross-talk free, line driving before digitization by Phillips Scientific 706 Discriminators. The analog(timing) signals were digitized in LeCroy 2249A ADCs(2228A TDCs). The digitization control and the interfaces to the STAR Trigger and DAQ Systems were provided by the existing components of the TOFp System.

Since the acceptance of TOFr subtends only  $\sim 1/300^{th}$  of the outer cylindrical surface of the TPC, a special STAR Level-0 trigger was set up to trigger on events with TOFr hits and a valid pVPD coincidence. The unused second outputs of the line driver PS706 discriminators were “or’ed,” leading to a single yes/no logic signal if any active channel in TOFr was struck. This signal was “and’ed” with two signals active if any channel in the pVPD East and West detectors, respectively, were struck. Also included in the logic was a simple primary vertex cut based on maximum allowable values of the timing difference of the pVPD East and West signals. This trigger enhanced the valid TOFr hits by a factor of 40 and 400 in d+Au and p+p collisions, respectively. The special trigger data sets in d+Au and p+p collisions were taken in March and May of 2003, respectively.

In the d+Au running, significant data sets were collected in two specific TOFr configurations - one in which the gas was only Freon R-134A, and the other with 95% Freon R-134A and 5% isobutane. During the period of RHIC Run-3 days 24 to 70, STAR collected approximately 25M d+Au events with minimum-bias triggers. The pVPD fired in 6.6M of these events. Approximately 700k(1.6M) total TOFr(TOFp) hits were collected without the special trigger, and 2.4M(0.6k) total TOFr(TOFp) hits were collected with the special trigger. Per detector channel, the totals were  $\sim 12k(45k)$  without the special trigger, and  $\sim 35k(20k)$  with the trigger, for TOFp(TOFr). These samples are sufficiently large to allow detailed analysis and comparison of the timing and PID performance between the different technologies and for different MRPC configurations.

In addition to providing essential data for assessing detector performance, the data acquired during these tests provided important scientific results not possible with the particle identification capability of the TPC alone. Examples include:

- Identified particle “Cronin” effect up to 3 GeV/c in transverse momentum.
- Proton/anti-proton spectra up to 3 GeV/c; dE/dx for these particles from the TPC alone extends only to transverse momenta of  $\sim 1$  GeV/c



- Distinguishing flow effects from other dynamical effects by comparison of the identified particle transverse momentum spectra for p+p, d+Au, and Au+Au collisions; distinguishing flow effects arising from the partonic versus the hadronic stage of the collision.

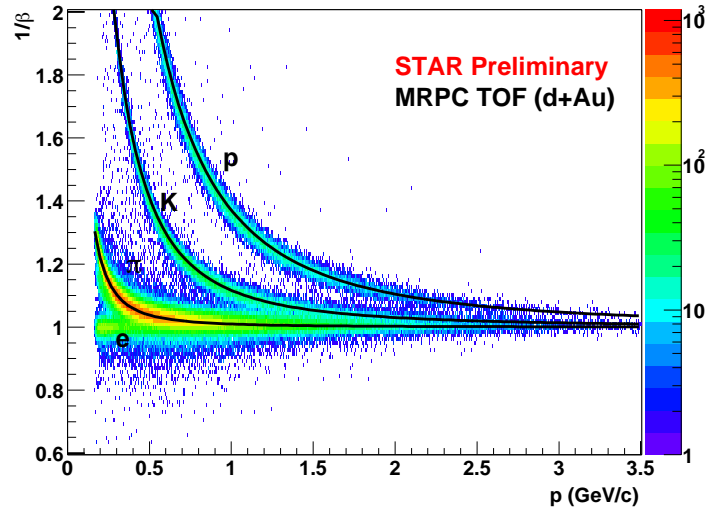


Figure 46: Inverse velocity vs momentum from 2.6 million TOFr+pVPD-triggered events in d+Au collisions.

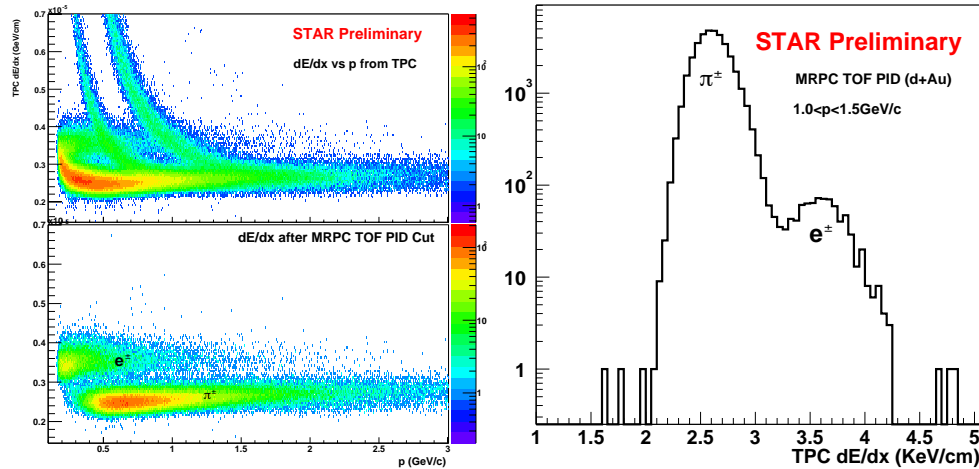


Figure 47: Left top: TPC  $dE/dx$  vs the momentum in d+Au collisions. Left bottom: TPC  $dE/dx$  vs the momentum after TOFr PID selection of  $|1 - \beta| < 0.03$ . Clean electron identification is achieved. Right:  $dE/dx$  from TPC after TOFr PID selection (left bottom panel) for  $1.0 < p < 1.5$  GeV/c.

The analyses of the Run-3 data are ongoing. Fig. 46 shows the particle identification capabilities as  $1/\beta$  from time of flight measured by TOFr versus the particle

momentum measured by the TPC tracking. A stop time resolution of  $\sim 100$ ps from the 72 TOFr channels in the d+Au data set was observed. These data supported analyses leading to the physics results described in Ref. [146]. To our knowledge, this paper is the first to describe physics results obtained with the MRPC technology.

In addition to the hadron PID capability, with the combination of TOF information and TPC  $dE/dx$  information, it is possible to cleanly identify electrons from low  $p_T$  ( $\simeq 0.2$  GeV/c), where the EMC has poor energy resolution and low electron identification capability, to very high  $p_T$  ( $\simeq 3$  GeV/c) where the EMC can do a good job. The new electron identification capability combined with large coverage of TOF and TPC will enable STAR to effectively reconstruct the  $J/\Psi$  and other vector mesons. The left top panel of Fig. 47 shows the charged particle  $dE/dx$  from the TPC as function of the momentum. At  $p < 1.5$  GeV/c, there are substantial overlaps between the electron  $dE/dx$  and the hadron (pion, kaon, and proton)  $dE/dx$ . The left bottom panel of Fig. 47 shows that an electron band can be cleanly separated in the entire momentum range by requiring  $|1 - \beta| < 0.03$  from TOFr. The  $dE/dx$  distribution after the TOFr PID selection for  $1.0 < p < 1.5$  GeV/c is shown in right panel of Fig. 47. Only pions and electrons are visible and they are well separated.

## 5.4 TOFr' in STAR in RHIC Run-4

The operation of the first prototype, TOFr, in STAR in RHIC Run-3 insured that the MRPC technology was viable for STAR. A second prototype, called TOFr', was built for Run-4 which makes improvements to the TOFr design in a number of areas. TOFr' is shown just before it was installed in STAR for Run-4 in Figure 48, and is described in this section.

Most of the MRPCs used in TOFr' were taken out of TOFr. This allows the comparison of the timing performance of the same detectors in the two different trays, and also allows the continuation of the search for any aging effects in these common MRPCs. Both TOFr and TOFr' use the sawtooth approach (see sections 4.4 and 5.1) for positioning the MRPCs inside the tray. Both TOFr and TOFr' were digitized off-detector in CAMAC via the STAR TOFp subsystem. The analysis of the data collected by TOFr' in Run-4 is in progress. The major differences between TOFr and TOFr' exist in two areas: mechanical design and electronics design.

As described in section 5.1, there are a number of aspects of the mechanical design of TOFr are not attractive for the final system. These problem areas, and the solutions for each employed in the TOFr' design, are as follows.

- The labor-intensive fabrication of the TOFr rail assembly, which involves welding aluminum angle and the tapping of some 200 holes, was replaced by a simpler and more-integrated design. The top assembly for TOFr' fits onto the tray body in a “shoe-box” design, and all mechanical fasteners are embedded PEM nuts. This fabrication was done out-of-house by the tray manufacturer.
- The unnecessary holes in the tray body, including those for the attachment of the tray feet, which must then be sealed to insure gas containment, no longer

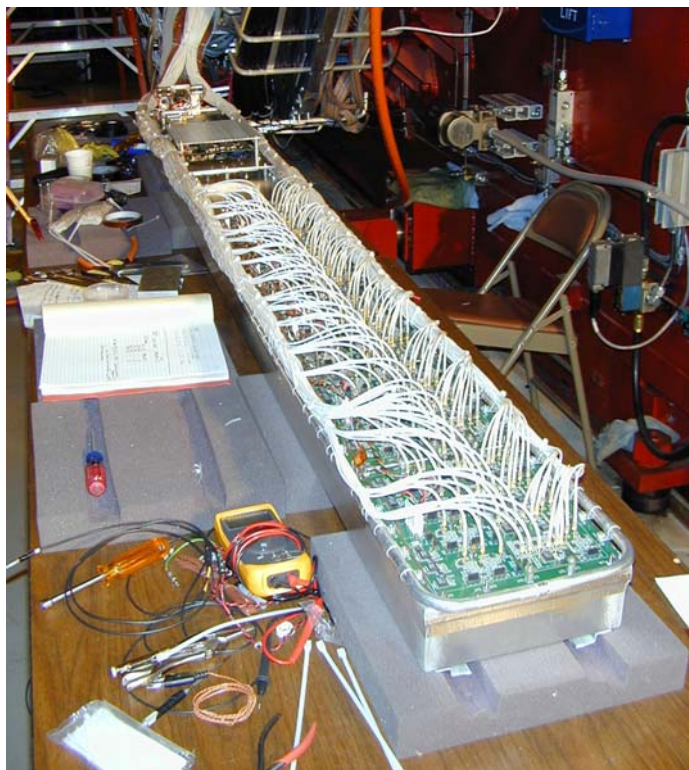


Figure 48: The TOFr' tray just before installation in STAR for operation during RHIC Run-4.

exist. The shoe-box top design removes the need for many tops near the top of the tray bottom. Also the tray feet are now welded to the tray bottom, which removes all of the holes there.

- The gasketing between the rail assembly and the TFEE boards, which was both labor-intensive to fabricate and unnecessarily complicated, no longer exists. The TFEE boards were sealed to the tray top via Dow Corning 730 Freon-resistant sealant. This resulted in an improved gas containment, and a smaller vertical distance between the tray body and the TFEE boards, which should further decrease radio-frequency interference to the (heavily-amplified) MRPC pads.

The electronics for TOFr and TOFr' are very similar in philosophy and components, but the packaging of the components onto specific boards is very different. The TOFr tray had two layers of electronics (see section 5.1) - the first, which also seals the gas box, was the "Feedthrough plates" (F/T) and the second was the TOFr FEE boards which were mounted to the F/T boards. This approach was viewed as excessive in terms of the overall height of the tray. To reduce this, in the TOFr' tray the F/T and FEE layers were merged into one layer. This is the so-called TFEE board, which seals the gas box and includes the signal feedthroughs, the preamplification, and the comparators for the discrimination.

We quickly learned however that placing so many components on the board that seals the gas box resulted in an unattractive effect. The power dissipated on the TFEE boards radiates into the gas box, which heats the gas and the MRPC detectors. This causes the MRPC noise rates and the HV current draw to increase dramatically. The total HV current draw in TOFr was  $< 1\text{nA}$  per MRPC, while in TOFr' it was several nA per MRPC, an increase of about a factor of 5. The noise rates in TOFr were typically 20Hz per pad, while in TOFr' they can exceed 100Hz.

Preliminary analyses of the Run-4 data from STAR indicate that, despite the higher internal temperature, noise rates, and HV current draw, the timing performance of TOFr' was not significantly degraded. This is seen in Figure 49, where the inverse velocity obtained after a very preliminary offline calibration is plotted versus the momentum. The timing resolution at this early stage of the analyses of the Run-4 data is already near 100ps.

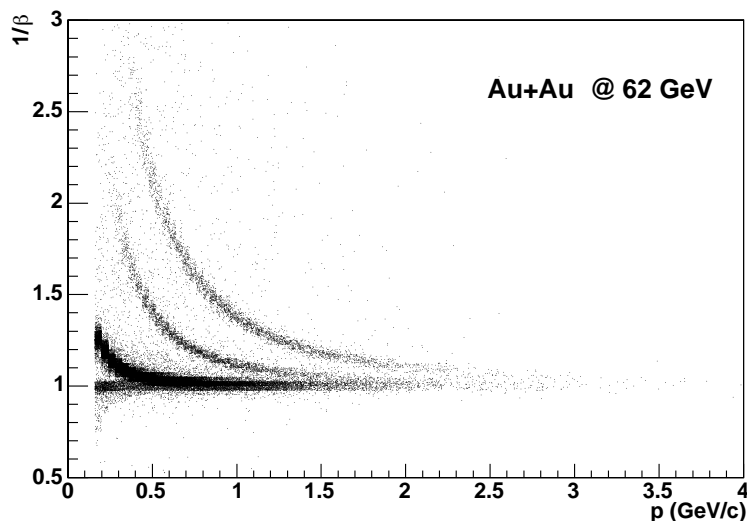


Figure 49: The PID performance of TOFr' in RHIC Run-4 after very preliminary offline calibrations.

The next full-sized prototype, “TOFr5,” is now being designed for operation in STAR in RHIC Run-5. This tray will retain all of the improvements to the mechanical design of the tray that were first implemented in TOFr'. Another very important improvement to the TOFr/TOFr' design that will be implemented in TOFr5 is the replacement of the sloppy and labor-intensive sawtooth approach for the MRPC positioning. The so-called “Inner sides” approach would simplify the tray fabrication and improve the tolerances on the MRPC positioning within the tray. See section 4.4 for additional details.

Also, in order to return the tray interior temperature back to the comfortably low values seen in TOFr, the TFEE boards will be replaced with so-called TAMP boards for Run-5. The TAMP boards likewise seal the gas box, but contain only the components for input protection and the preamplification. The discrimination and all other FEE functions are moved to TDIG in this design. This will reduce the heat

radiated into the gas volume by about a factor of 8.

Water flow is used for heat removal from the on-board electronics in both TOFp and TOFr'. Included in the design of TOFr5 is a new type of cooling water path based on 1/4" square copper tubing that makes direct thermal contact with both TAMP and TDIG via thermally conductive shims along the full length of the tray. This method is expected to more efficiently remove heat from the main power source (TDIG) than would air flow across these electronics.

## 6 Construction

The basic design of the proposed system, embodied by the TOFr prototype (section 5), is described in section 4. In this section we present details on the specific quality assurance tests to be performed during the module construction (section 6.1), the tray assembly (section 6.2), and the electronics construction (section 6.3). Also discussed below in section 6.4 are specific issues regarding the integration of the proposed system into the existing STAR apparatus.

### 6.1 Module Construction & QA

There are six Chinese groups in STAR participating in the TOF project: USTC, Tsinghua, SINR, IMP Lanzhou, IPP Wuhan, and IHEP Beijing. It is anticipated that the Chinese groups will be responsible for MRPC module production for the STAR TOF detector with financial support from the Chinese funding agencies.

The USTC group produced 26 modules in 2001, of which 24 were installed in the TOFr tray. Of the 26 modules, 20 were characterized by low dark currents and normal ADC spectra in all six channels. The other six modules had slightly higher dark currents and had abnormal ADC spectra in one or more channels. The abnormal ADC spectra have a pronounced high tail in the spectra which is due to a phenomenon known as streamers. Streamers are a class of events with abnormally large signals that can result from the glass plates approaching each other too closely, or in extreme cases, from the presence of foreign material or rough places on the glass. Devices that streamer are usable but do not provide as good timing resolution and are therefore undesirable in the system.

Research is underway at USTC and Tsinghua on how to improve the yield when assembling modules. Research is also underway to investigate methods and procedures to maintain quality while constructing thousands of modules.

There will be 32 MRPC modules in each of 120 trays, or 3840 total modules. The production yield for high quality modules, based our experience from the module production for the TOFr prototype tray, is estimated to be 70%. In order to meet the envisioned construction schedule (complete installation of a full MRPC TOF detector in two years after the approval of the project), two production facilities will be established. The Tsinghua group will lead the mass production effort. Both the Tsinghua and the USTC groups are preparing MRPC mass production facilities. Tsinghua will be responsible for 70%, and USTC for 30% of the total production. All Chinese groups will participate in the MRPC production effort by providing resources and manpower.

The Chinese STAR TOF group is responsible for testing each MRPC module during production. This will include quality tests for every module and detailed characterization for selected ( $\sim 20\%$ ) modules. The USTC group will coordinate the testing effort in China.

R&D efforts on the production technique and quality assurance procedures are underway at both USTC and Tsinghua. Significant progress has already been made

including 1) partial construction of clean space for MRPC assembly; 2) training of qualified personnel for production supervision; 3) preparation of a procedure manual for module construction; 4) establishment of quality assurance procedures; and 5) test equipment setup.

There will be sufficient manpower and technical expertise available to meet the proposed STAR TOF construction schedule once the STAR TOF project is approved by the respective funding agencies in the US and China.

The total space needed for the production at each institution is 800 m<sup>2</sup>.

We assume a 70% yield in material preparation. Approximately 30% of materials may not meet our requirements for module assembly during the preparation.

There will be a test setup for module production quality assurance at both production sites, USTC and Tsinghua. There will be two levels of testing for each MRPC module: module quality test and module characteristics test. The quality assurance effort will be led by a team of physicists including graduate students. The USTC group will be responsible for the overall coordination of MRPC production testing.

The module quality tests will be performed for each MRPC production module. This test includes:

- The leakage current for a module should be  $<10$  nA at 15 kV using the regular operating gas mixture.
- The noise rate should be  $<50$  Hz/pad with pad size 31 mm $\times$ 61 mm.
- The probability for ADC values larger than  $3\sigma$  above of the mean ADC value should be less than 10% at 14.5 kV.

The module characteristics tests will measure the amplitude response of each MRPC module from cosmic rays. We propose that only 20% of the produced modules will undergo the test of time resolution and efficiency. With a prototype testing setup at USTC, a timing resolution better than 100 ps has been achieved with cosmic rays. Relative efficiency in a standard setup can also be measured accurately. It is expected that these requirements will be determined when a final testing setup is established for mass production.

The cosmic ray test setup is built using three 22cm $\times$ 5cm $\times$ 3cm plastic scintillator counters with photo-multiplier tubes. Figure 50 shows the block diagram of the electronic readout system. A LeCroy 621 discriminator is used for signals from PMT0, PMT1 and PMT2. A constant fraction discriminator ORTEC 851 is used for the signals from PMT3 and PMT4. The coincidence signal between PMT0 and PMT4 provides the cosmic ray trigger for the ADC gate and the start time used for the MRPC digitization. The electronic start is set by the leading edge of the PMT0 pulse. All timing signals (NIM signal from the discriminators) from PMT0 through PMT4 are fed into a CAMAC TDC for digitization. The MRPC module is connected to an FEE card identical to those in use on the TOFr system. The FEE card includes a preamplifier and discriminator for the signal from each MRPC cell. The analog and digital outputs from the FEE card are connected to the ADC and TDC modules.

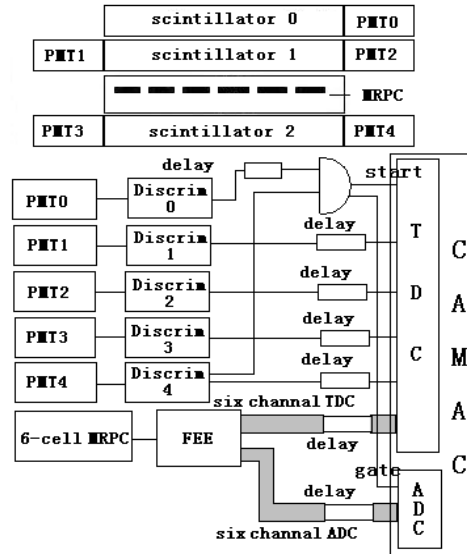


Figure 50: The block diagram of the USTC cosmic ray test apparatus.

The ADC gate signal has a width of 100 ns. The counting rate for the USTC cosmic ray test setup is approximately 7000 triggers per day covering the 6 channel MRPC module.

The USTC group has established a manual of procedure for MRPC production. This procedure will be refined and used for mass production of MRPC modules in China.

## 6.2 Tray Construction & QA

The tray which will contain the MRPC modules produced in China will be manufactured in Houston and then shipped to other participating institutions where the final assembly will be performed. A sample of the modules from each shipment from China will be retested before installation in the trays to insure there is no damage to the modules during shipping.

The following quality tests will be performed on the fully-assembled trays.

- All trays will be measured to assure uniformity. The criteria used will be similar to those used for the STAR-CTB trays.
- After tray assembly with FEE cards, gas-tightness tests will be performed with a freon sniffer and by pressurizing the tray and measuring the decay rate of the pressure versus time. The gas flow rate will be checked with bubbler at a flow rate  $< 2$  l/h.
- The leakage current at 15kV will be measured with the operating gas mixture. The current should be  $< 20$ nA.



- The noise rates should be less than 50 Hz per pad.

These tests will be performed with an electronic setup very similar to that shown in Figure 50. The TTST boards (see section 4.6.3) will be used as the interface between TFEE and the standard CAMAC electronics that will perform the digitization during full tray testing.

### 6.3 Electronics Construction & QA

Electronics design will take place in Houston. The design will include the additional markup of the bare boards necessary for the fabrication of the electronics (“stuffing”) by local industry. Experience has shown that several companies in the Houston area are capable of fabricating stuffed electronics boards appropriate for fast timing systems. The 16 boards for the TOFp system, as well as the  $\sim 40$  boards for the TOFr system, were designed at Rice and then shopped out in Houston with great success and with significant cost savings. This model will be used for the construction of the electronics for the proposed system. The specific quality assurance tests to be performed on the electronics are described below.

Once the boards are produced, the following tests will be performed to assure that the boards function adequately. These tests can be generally performed using pulsers for the input signals. For the digitization, a very high resolution oscilloscopes such as the HP Infinium (8 GS/s) used at Rice as well as CAMAC equipment can be used. The following QA tests are envisioned.

- Basic functionality will be checked.
- TFEE – Single channel pure time interval resolution at fixed input pulse height must be below 20 ps. The same test for the TOFr electronics was described above in section 4.6.1 and table VI.
- TFEE – Analog cross-talk must be below 2%, checked on 1-2 pairs of neighboring channels in a random subset of  $\sim 10\%$  of the TFEE boards.
- TFEE – Timing cross-talk must be below 20 ps, checked on 1-2 pairs of neighboring channels in a random subset of  $\sim 10\%$  of the TFEE boards.
- TDIG – The TDC values obtained locally using TFEE+TDIG must be consistent with those obtained independently using TFEE+TTST and digitization in CAMAC equipment, or obtained independently using TFEE+TTST and digitization by a high-sampling-rate oscilloscope.

Additional specific tests are envisioned and will be developed during the design phase of these electronics.

## 6.4 Integration Issues

Precise details (utility distribution, cabling, etc.) related to the integration of the barrel MRPC TOF detector will be worked out as part of the STAR review process prior to installation. An initial study of integration issues has indicated there are no obvious “show-stoppers”, and that the cost of integrating the detector should be modest. Several potential major issues have been examined including the weight of the detector, and the amount of cooling needed.

### Weight

The total weight of a Central Trigger Barrel (CTB) tray, of which there are 120 presently installed, is about 50 lbs, resulting in a total weight for the CTB of  $\sim 6000$  lbs. An MRPC TOF tray weighs approximately 70 lbs, so that 120 TOF trays would weigh  $\sim 8400$  lbs, or about 20% more. The means of support for both CTB trays and the TOF barrel trays which will replace them is the TPC. The three mechanical elements of the TPC that must carry the additional load are the rails, the support arms, and the gas vessel.

The rails are long aluminum extrusions glued onto the outer field cage of the TPC. Brackets on the bottom of each CTB or TOF tray register the tray’s position on these rails and hold them in place. The shear strength of the adhesive used for the rails is  $\sim 3000$  psi, and the tensile strength is  $\sim 4000$  psi. The peel strength is conservatively estimated to be 20 pounds per linear inch. Assuming a TPC rail behaves rigidly and the weight of the TOF tray is distributed over its entire length (160 inches or  $\sim 4$  m), given that the glue bond is  $\sim 3.5$ ” wide ( $\sim 90$  mm), the rails should be able to withstand 3200 lb of peel force (load twisting edge away from skin), 1.68 Mega-lb shear (load tangential to skin), and 2.24 Mega-lb tension (load normal to skin). The safety factor for adhesive joints is conservatively estimated to be  $\sim 3$ , so it is estimated that a TOF tray could weigh up to  $\sim 1000$  lbs (14 times more than design) without endangering the glue bond between the rails and the TPC.

The TPC support arms are two very large aluminum brackets on each end of the STAR detector that support the entire TPC from the steel of the STAR magnet. The weight that each TPC arm was engineered to hold is 25,000 lb, with a safety factor of 3-5 (Star Note 105A)(see LBL EN M7681 and 7682). The TOF detector would increase the present load on each arm by approximately 12% to 28,000 lbs. The original safety factor was 4.08 for the worst case bolt. The safety factor on the support arms including the additional weight from the TOF system is reduced slightly to 3.6, which is still felt to be conservative.

Additional work will focus on a Finite Element Analysis (based on ANSYS) of the TPC gas vessel to assess the impact of the distributed load over the “as-built” cylinder. This is not expected to present a fundamental problem.

### Cooling

Each tray dissipates approximately 250W of power when running. Hence 120 trays dissipate  $\sim 30$  kW of power. This generates heat inside the STAR detector and the

Wide Angle Hall (WAH) which must be removed.

The baseline plan is to remove the heat from the tray with circulating chilled water. The STAR chilled water system is being upgraded and the new system will have the capacity to handle 30 kW of cooling for the TOF trays and 35 kW of cooling for the low voltage power supplies on the south platform.

A backup plan is to address the additional heat load resulting from the TOF barrel is to use air flow for convective cooling of the detector electronics. There is approximately 1.5" of radial space between the present TOF integration envelope and the front face of the STAR barrel EMC. The option being examined is to extend the integration volume of TOF by  $\sim 1$ " radially, and to install a closed aluminum cover ( $\sim 30$ -40 mils thick) over each TOF tray, about 1" above the electronics, to create a confined space for channeled air flow which would enter and exit through the small ends of the tray. During tray installation, a rail fixture would be used to hold two trays at the same time in a position from which the pair could be slid into STAR as one object. This would allow one to "join" the two trays mechanically and seal together the skins of the trays where they meet end to end. With appropriate ducting near the STAR pole tips, air would be directed through these channels from one end of STAR to the other, insuring a strong and consistent flow of air over the entire length of the electronics. This plan requires the TOF system to be installed from the East side of STAR in the Assembly Building.

The warmed exit air would need to be handled by the A/C system in the Wide Angle Hall (WAH) once the STAR detector was positioned for data acquisition. It is likely that the heat dissipated by the TOF detector can be handled by the existing cooling system in the WAH.

### **Cabling**

The plan for the total number of cables, gas lines, fibers, and air cooling ducts that have to be routed from outside to inside the magnet is under development. This will need to address the limited space available for these utility penetrations.

### **Installation**

In addition to the rail fixture used to install the trays onto the TPC rails in pairs, a second fixture will also be necessary. The TPC support arms at 3 and 9 o'clock make it impossible to slide trays onto the rails behind them. A fixture is therefore needed to support the STAR TPC while installing pairs of trays on the rails behind the support arms. The cost of this fixture is estimated to be less than 75 k\$.

## List of Figures

- |   |   |    |
|---|---|----|
| 1 | Distributions of $\sqrt{n}(\langle p_T \rangle - \hat{p}_T) / \sigma_{\hat{p}_T}$ for all primary hadrons from central (top 15%) events (upper histogram) compared to two gamma distributions: reference in the absence of non-statistical fluctuations (dotted line) and with a 14% increased <i>rms</i> width (solid curve). . . . .  | 7  |
| 2 | (Left) Azimuthal anisotropy parameters $v_2$ as a function of $p_T$ for strange particles $K_S^0$ (open circle) and $\bar{\Lambda}/\Lambda$ (closed triangles) from minimum bias 200 GeV Au+Au collisions. Lines are from hydrodynamic model calculations [20] for (from top to bottom) pions, kaons, protons, and $\bar{\Lambda}/\Lambda$ . (Right) The $\langle p_T \rangle$ vs. particle mass. The lines represent the thermal results with given temperature and velocity ( $T_{fo}, \beta$ ). . . . .  | 9  |
| 3 | A schematic description of nucleus-nucleus collisions at RHIC from Ref. [12]. . . . .   | 14 |
| 4 | (Left) Measured slope parameter as a function of particle mass. Open symbols are for results from Pb+Pb central collisions at the SPS ( $\sqrt{s_{NN}} = 17.2$ GeV); filled symbols are for central Au+Au collisions at RHIC ( $\sqrt{s_{NN}} = 130$ GeV). (Right) Integrated azimuthal anisotropy parameters $v_2$ as a function of particle mass. Data points are from minimum bias Au+Au collisions at RHIC ( $\sqrt{s_{NN}} = 130$ GeV). The gray band indicates the predictions of a hydrodynamic model [20]. The expected range if there is significant partonic collectivity is indicated by the dashed band in both plots. . . . .  | 18 |
| 5 | Detection efficiencies with and without TOF PID for $\Omega$ decays. . . . .  | 19 |
| 6 | <b>Left:</b> Estimate for spectra and statistical errors from 200 GeV Au+Au top 10% central collisions. The value of $dN/dy = 0.64$ and an inverse slope parameter $T = 450$ MeV are used, for the sum of $\Omega$ and $\bar{\Omega}$ . The resulting $p_T$ spectrum, as well as what would be measured in STAR using TPC PID only, and TPC+TOF PID are indicated in left panel (a) and TPC + SVT versus TPC+SVT+TOF in the right panel (a). <b>Right:</b> An estimate of the statistical precision needed relative to the projected anisotropy $v_2$ from minimum bias Au+Au collisions at 200 GeV is shown in panel b. The reaction plane resolution is taken to be 0.75 consistent with previous STAR measurements. This level of statistical precision can be achieved with 30 million minimum bias events with the proposed TOF upgrade. Without the proposed TOF barrel, the number of events needed is 5-10 times greater, and this measurement is not feasible. . . . . | 21 |
| 7 | Mean- $p_T$ distribution for $\sqrt{s_{NN}} = 130$ GeV Au+Au central collisions with respect to $\hat{p}_T$ in units of $\sigma_{\hat{p}_T} / \sqrt{N}$ compared to a gamma distribution reference expected in the absence of non-statistical fluctuations (dotted curve) and a gamma distribution calculated with an <i>rms</i> width increased by 14% (solid curve). . . . .  | 24 |

8	Centrality dependence for Charge Independent (CI) (solid triangles) and Charge Dependent (CD) (open triangles) fluctuation measure $\Delta\sigma_{p_T}$ for 130 GeV minimum bias Au+Au events. The CD values are multiplied by 3 for clarity. The dashed lines are curve fits. Solid lines and bands reflect an extrapolation to 100% for primary charged hadrons in the detector acceptance and include a $\pm 15\%$ systematic error. . . . .	24
9	Perspective view of the two-dimensional $X(m_{t1}) \otimes X(m_{t2})$ charge independent correlations for $\sqrt{s_{NN}}=130$ GeV Au+Au collision data. . . .	26
10	Transverse-mass two-particle $X(p_{t1}) \otimes X(p_{t2})$ correlations for all charged hadrons in the top 15% most central collision events. Corresponding $p_T$ values in GeV/c are shown in the lower horizontal scale. . . . .	26
11	Relative azimuthal correlations for central Au+Au and minimum bias p+p collisions. The squares show the small-angle correlation strength, and the circles show the back-to-back correlation strength. . . . .	28
12	The expected behavior of $\Delta\sigma_{p_T}$ (CI) as a function of particle mass assuming the dominant contribution to it is due to temperature fluctuations (black circles), fluctuations in the transverse flow velocity (red triangles), or a combination of both types of fluctuations (blue squares). Without the additional PID provided by the barrel TOF detector, measurement of $\Delta\sigma_{p_T}$ as a function mass (this plot) <i>is not possible</i> over much of the $p_T$ range of interest and essential information to interpret the origin of the observed $\Delta\sigma_{p_T}$ is simply lost. . . . .	31
13	Simulated proton spectra versus transverse momentum (left) and pseudorapidity (right) for 200 GeV Au+Au central collisions for all accepted and reconstructed tracks (R - red), those identified using the TPC only (B - blue), and those identified using both TPC and full TOF (G - green).	33
14	Simulated kaon spectra versus transverse momentum (left) and pseudorapidity (right) for 200 GeV Au+Au central collisions for all accepted and reconstructed tracks (R - red), those identified using the TPC only (B - blue), and those identified using both TPC and full TOF (G - green).	33
15	Simulated pion spectra versus transverse momentum (left) and pseudorapidity (right) for 200 GeV Au+Au central collisions for all accepted and reconstructed tracks (R - red), those identified using the TPC only (B - blue), and those identified using both TPC and full TOF (G - green). . . . .	34
16	Simulated pion (left), kaon (center), and proton (right) spectra versus $X(m_T)$ for 200 GeV Au+Au central collisions for all accepted and reconstructed tracks (R - red), those identified using the TPC only (B - blue), and those identified using both TPC and full TOF (G - green).	34
17	The resulting $D^0$ peak in the reconstructed $K^- \pi^+$ invariant mass spectrum (pure decays only, no background) using all $K^-, \pi^+$ particles which survive the acceptance (including decay losses) and tracking inefficiency. . . . .	39

18	(left) Scatter plot of the total momenta of the daughter kaon versus the pion, and (right) the azimuthal angle – pseudorapidity correlation ( $\Delta\phi - \Delta\eta$ ) between the kaon and pion daughters from $D^0$ decay. . . .	39
19	The $\pi^+\pi^-$ invariant mass distribution after background subtraction from 40%-80% Au+Au (left) and p+p (right) collisions. . . . .	45
20	Left: Correlated $K+\pi$ pairs from $K^{*0}$ decay (open symbols). For $K_S^0$ (thin dot-dashed line), $\rho$ (thick dashed line), $\omega$ (thin dotted line), and $\eta$ (thin solid line), assuming of their decay pions is misidentified as a kaon. For the $\phi$ (thin dashed line), one of its decay kaons is presumed to be misidentified as a pion. For the $\Lambda$ (thin short-dashed line), the decay proton is misidentified as a kaon. These are realistic assumptions given the limitations of particle identification in the STAR TPC. The total background for $K^{*0}$ is shown as thick dot-dashed line. The $K^{*0}$ signal is shown as thick solid-line. Simple PID from specific ionization ( $dE/dx$ ) in the TPC was used for this simulation. The events are HIJING Au+Au collision at 130 GeV. Right: Correlated $K+\pi$ pairs from $K^{*0}$ after applying the PID cuts from the proposed barrel TOF detector. . . . .	47
21	Expected $\Lambda(1520)$ signal from 1.7M central Au+Au collisions with the proposed TOF detector. Without the barrel TOF detector the significance of the $\Lambda(1520)$ is only 2.1 for $p_T$ up to 1.6 GeV/c. The proposed barrel TOF upgrade increases the significance of the signal by a factor of $\sim 3.4$ , resulting in a reduction of 11.4 in the number of events required to achieve the same level of significance. With the proposed barrel TOF detector, precision measurement of the $\Lambda(1520)$ $p_T$ spectrum is possible from several million events. Without it, measurement of the $p_T$ spectrum would require approximately an order of magnitude more. . . . .	48
22	The momentum dependence of the particle mass resolution for a 100ps total resolution TOF system in the STAR environment. In regions where the lines are non-overlapping, the corresponding particle can be identified by the proposed system. . . . .	54
23	Two side views of the structure of an MRPC module. The upper(lower) view shows the long(short) edge. The two views are not shown at the same scale. . . . .	56
24	The circuit board with the copper read-out pads for the present MRPC detectors. . . . .	58
25	The raw time distribution (upper left), the time-amplitude (“slewing”) correlation (lower), and the pure stop time resolution after the slewing and start resolution corrections (upper right). . . . .	58
26	The detection efficiency (upper frame), slewing-corrected time resolution (middle frame), and time walk (lower frame), as a function of high voltage for the 6 gap MRPC. . . . .	60

27	The corrected time-of-flight distribution of pions and protons in a beam of 3 GeV/c momentum. The flight path is 2.8 m. . . . .	60
28	An end view of STAR showing the dimensions of the integration envelope allocated for this system. . . . .	62
29	A dimensioned side view of the tray indicating the detector positioning.	63
30	The integrated thickness of the tray and detectors in interaction lengths (upper two frames) and radiation lengths (lower two frames), versus the pseudorapidity and azimuthal angle, as labeled. . . . .	66
31	The schematic of the proposed gas system. . . . .	67
32	The highest-level diagram of the electronics for the proposed system.	74
33	The top level electronics diagram at the tray level. . . . .	75
34	The partitioning of electronics functions between circuit cards. . . . .	76
35	The front end electronics (TFEE) and digital sampling (TDIG) circuit cards. . . . .	81
36	The functional diagram of the construction test electronics chain TFEE to TTST to CAMAC. . . . .	82
37	The tray level CPU (TCPU) and high speed data transmit (TMIT) circuit cards. . . . .	84
38	A dimensioned side view of the TOFr tray indicating the detector positioning. . . . .	90
39	On the left, the lower sawtooths in position in the TOFr tray, and on the right, the TOFr tray filled with 28 MRPC modules snugly positioned by all three layers of sawtooths. . . . .	92
40	On the left, the TOFr tray after the completion of all interior piping and cabling and the installation of the gasketed rail assembly, and on the right, the TOFr tray with the feedthrough plates installed. . . . .	92
41	The completed TOFr tray, now with all FEE boards installed and gas flowing for cosmics and noise testing at Rice. . . . .	94
42	Results on the total HV current draw from the very first power-up of the TOFr tray. . . . .	94
43	Results on the noise rates from the very first power-up of the TOFr tray.	95
44	The TOFr tray operating in an AGS radiation area near E949. . . . .	97
45	The efficiency (left axes) and time resolution (right axes) versus the high voltage at specific thresholds, 1.2V (upper left frame), 1.7V (upper right frame), and 2.2V (lower frame), obtained from the AGS tests of the TOFr tray. . . . .	98
46	Inverse velocity vs momentum from 2.6 million TOFr+pVPD-triggered events in d+Au collisions. . . . .	101
47	Left top: TPC dE/dx vs the momentum in d+Au collisions. Left bottom: TPC dE/dx vs the momentum after TOFr PID selection of $ 1 - \beta  < 0.03$ . Clean electron identification is achieved. Right: dE/dx from TPC after TOFr PID selection (left bottom panel) for $1.0 < p < 1.5$ GeV/c. . . . .	101

48	The TOFr' tray just before installation in STAR for operation during RHIC Run-4. . . . .	103
49	The PID performance of TOFr' in RHIC Run-4 after very preliminary offline calibrations. . . . .	104
50	The block diagram of the USTC cosmic ray test apparatus. . . . .	108
51	The arrangement of the TOFp detectors and the two pVPD detectors with respect to the STAR TPC (shown in cutaway) and the RHIC beam pipe. . . . .	128
52	The components of the offline software for the STAR TOFp Systems.	130
53	TPC to TOFp match probabilities per track from central Au+Au collisions. . . . .	132
54	TPC to TOFp match ratios per track from central Au+Au collisions.	133
55	The standard deviation of the quantity $\langle 2 \rangle - \langle 4 \rangle$ in units of TDC channels (50ps/ch) versus the primary vertex location. The different point styles correspond to individual passes during the start correction procedure. . . . .	135
56	The corrected inverse velocity versus momentum from TOFp+pVPD for central Au+Au collisions from RHIC Run-2. The insets depict the projections onto the inverse velocity axis for specific momentum regions near the required limits of TOFp's reach. Prominent peaks for the various hadron species are observed in both insets. . . . .	137
57	The total time resolution versus the TOFp slat number from the RHIC Run-2 Au+Au running. The inset depicts the histogram of these values. The average total time resolution over all(the best 25) slats was 87(79) ps. . . . .	137



## List of Tables

I	Particle mass dependence of $\Delta\sigma_{p_T}$ (CI) for pions, kaons, and protons assuming random event-to-event fluctuations in temperature, transverse flow velocity, or a mixture of both types of fluctuations. Units are in MeV/c. . . . .	30
II	Statistical significance of $D$ meson signal for a variety of particle ID options as a function of $p_T$ . The last two columns are the number of events $N_{events}$ required for a $3\sigma$ signal in the invariant mass distribution for $D^0 + \bar{D}^0$ mesons under different assumptions. HIJING was used as the basis for simulating the effect of TOF PID to provide data on backgrounds and charm production. . . . .	40
III	For the $K^{*0}$ , $\phi$ , and $\Lambda(1520)$ , the ratio as a function of $p_T$ of the figure of merit $(\bar{S}/\sqrt{\bar{B}})^2$ obtained with full TOF + TPC to that for the TPC only. The inverse of these numbers equals the reduction factor in the required number of events while still achieving the same statistical significance of the signal. . . . .	46
IV	The design parameters of the gas system. . . . .	68
V	The list of fault conditions in the gas system. . . . .	71
VI	The bench test results for the TOFr FEE cards. The columns are standard deviations ( <i>i.e.</i> the resolution) in units of picoseconds. These TOFr FEE cards are very similar to cards proposed for the full system called TFEE. . . . .	80
VII	Results from the AGS tests of TOFr giving the noise rates at HV and threshold settings leading to module efficiencies of $\geq 95\%$ . . . . .	98

## References

- [1] <http://mac8.rice.edu/~WJLlope/-STAR/-TOF/TOFprop.html>; and [/TOFpatch.htm](http://mac8.rice.edu/~WJLlope/-STAR/-TOF/TOFpatch.htm);
- [2] STAR Notes 36 (1992), 49 (1992), 50 (1992), 52 (1992), 207 (1995), 208 (1995), 209 (1995), 211 (1995), 267 (1996), 326 (1998), and 416 (2000).
- [3] W.J. Llope *et al.*, <http://mac8.rice.edu/~TOF/TOFp/Documents/TOFp.pdf>
- [4] W.J. Llope *et al.*, Nucl. Inst. and Methods, Section A, **552**, 252-273, (2004).
- [5] STAR Long-Range Plan, <http://www.star.bnl.gov/STAR/smd/lrp.html>
- [6] ALICE Time-Of-Flight Proposal, <http://alice.web.cern.ch/Alice/TDR/alice-tof.ps>
- [7] Letter of Intent, A Time-of-flight System for STAR, November 1, 1999, submitted by B. E. Bonner, G. Eppley, F. Geurts, W. J. Llope, G. S. Mutchler, T. Nussbaum, E. D. Platner, J. B. Roberts and P. Yepes.
- [8] M.C.S. Williams, E. Platner, J. Roberts *et al.*, NIM A434 (1999) 362; E. Cerron Zeballos, D. Hatzifotiadou, J. Lamas Valverde, E. Platner, J. Roberts, M.C.S. Williams, A Zichichi; Micro-streamers and the Microgap RPC, document in preparation; A. Akindinov *et al.*, (E. Platner, J. Roberts) Nucl. Instr. Meth. A 456, 16 (2000), B. Bonner, G. Eppley, J. Lamas-Valverde, W. J. Llope, T. Nussbaum, E. Platner, J. Roberts, E. Cerron Zeballos, D. Hatzifotiadou, N-Y. Kim, A. Semak, M.C.S. Williams, “A Multigap Resistive Plate Chamber Prototype for TOF for the STAR Experiment at RHIC,” to be published in Procs. Of 9th Vienna Conf. On Instrumentation, Vienna, Feb. 19-23, 2001.
- [9] <http://www.er.doe.gov/production/henp/nsac/nsac.html>
- [10] TOFr Proposal, [http://mac8.rice.edu/~TOF/TOFr/Documents/TOFr\\_prop\\_11132001.pdf](http://mac8.rice.edu/~TOF/TOFr/Documents/TOFr_prop_11132001.pdf).
- [11] TOFr Proposal Update, [http://mac8.rice.edu/~TOF/TOFr/Documents/TOFr\\_prop\\_update.pdf](http://mac8.rice.edu/~TOF/TOFr/Documents/TOFr_prop_update.pdf).
- [12] S. Bass, private communication.
- [13] STAR Conceptual Design Report, LBNL Pub-5347.
- [14] M. Gyulassy and M. Plümer, Phys. Lett. B 243, 432 (1990).
- [15] X. N. Wang and M. Gyulassy, Phys. Rev. Lett. 68, 1480 (1992).
- [16] C. Adler *et al.*, nucl-ex/0210033, Phys. Rev. Lett. **90**, 082302 (2003).

- 
- [17] C. Adler *et al.*, (STAR Collaboration) Phys. Rev. Lett. **89**, 232021(2002).
- [18] K. H. Ackermann *et al.*, (STAR Collaboration), Phys. Rev. Lett. **86**, 402(2001); C. Adler *et al.*, *ibid*, **87**, 182301(2001); *ibid*, **89**, 132301(2002); *ibid* Phys. Rev. **C66**, 034904(2002).
- [19] S. Voloshin, QM02 proceedings, Nantes, France, 18-24 July 2002, nucl-ex/0210014, Nucl. Phys. A715, 379-388 (2003).
- [20] P. Huovinen, P.F. Kolb, U. Heinz, P.V. Ruuskanen, and S. Voloshin, Phys. Lett. **B503**, 58(2001).
- [21] S. Esumi *et al.*, (PHENIX Collaboration), QM02 proceedings, Nantes, France, 18-24 July 2002, nucl-exp/0210012, Nucl. Phys. A715, 599-602 (2003).
- [22] N. Xu and Z. Xu, QM02 proceedings, Nantes, France, 18-24 July 2002, Nucl. Phys., A715, 587-590 (2003).
- [23] P. Braun-Munzinger *et. al*, Phys. Lett. **B518**, 41(2001).
- [24] N. Xu and M. Kaneta, Nucl. Phys. **A698**, 306c(2002).
- [25] G. Baym and H. Heiselberg, Phys. Lett. **B469**, 7(1999).
- [26] M. Stephanov, K. Rajagopal, E. Shuryak, Phys. Rev. Lett. **81**, 4816 (1998).
- [27] J. Adams *et al.*, STAR Collaboration, “Event-by-event  $\langle p_T \rangle$  fluctuations in Au-Au collisions at  $\sqrt{s_{NN}} = 130$  GeV,” nucl-ex/0308033, Phys. Rev. Lett. (submitted).
- [28] J.G. Reid *et al.*, (STAR Collaboration), QM02 proceedings, Nantes, France, 18-24 July 2002, Nucl. Phys. A698, 611c (2002).
- [29] S. Voloshin and Y. Zhang, Z. Phys. **C70**, 665(1996).
- [30] A.M. Poskanzer and S. Voloshin, Phys. Rev. **C58**, 1671(1998).
- [31] M. Gyulassy, I. Vitev and X.N. Wang, Phys. Rev. Lett. **86**, 2537(2001).
- [32] D. Teaney, J. Lauret, and E.V. Shuryak, Phys. Rev. Lett. **86**, 4783(2001).
- [33] C. Adler *et al.* (STAR Collaboration), Phys. Rev. Lett. **89**, 132301(2002).
- [34] D. Teaney, J. Lauret, and E.V. Shuryak, LANL Preprint, nucl-th/0110037.
- [35] J.-Y. Ollitrault, Phys. Rev. **D46**, 229(1992).
- [36] S. Esumi, *et al.* (PHENIX Collaboration), Nucl. Phys. A715, 599-602 (2003).
- [37] Z. Lin and C.M. Ko, nucl-th/0207014, Phys. Rev. Lett. **89**, 202302 (2002); *ibid*, Phys. Rev. **C65**, 034904(2002).
-

- 
- [38] M. Gyulassy, I. Vitev, X.N. Wang, and P. Huovinen Phys. Lett. **B526**, 301(2002).
- [39] Yu.L. Dokshitzer, V.A. Khoze, and S.I. Troian, Phys. Rev. **D53**, 89(1996); D. Kharzeev, proceedings of “Statistical QCD”, hep-ph/0111386, Nucl. Phys. A702, 39-48 (2002).
- [40] C. Adler et al. (STAR Collaboration), submitted to Phys. Lett. **B**, (2002); e-Print Archive: nucl-ex/0206008.
- [41] C. Adler et al. (STAR Collaboration), Phys. Rev. **C65**, 04901(2002).
- [42] C. Adler et al. (STAR Collaboration), Phys. Rev. Lett. **89**, 092301(2002).
- [43] K. Adcox *et al.*, (PHENIX Collaboration), Phys. Rev. Lett. **88**, 242301(2002).
- [44] U. Heinz and P. Kolb, Nucl. Phys. **A702**, 280(2002).
- [45] E. Andersen *et al.*, (WA97 collaboration), Phys. Lett. **B433**, 209(1998).
- [46] I. Bearden *et al.*, (NA44 Collaboration), Phys. Rev. Lett. **78**, 2080(1997).
- [47] H. van Hecke, H. Sorge, and N. Xu, Phys. Rev. Lett. **81**, 5764(1998).
- [48] G. Arnison *et al.*, Phys. Lett. B 118, 173 (1982); A. Breakstone *et al.*, Z. Phys. C 23, 1 (1984).
- [49] C. Adler *et al.*, STAR Collaboration, Phys. Rev. Lett. **90**, 032301 (2003).
- [50] D.E. Jaffe *et al.*, Phys. Rev. D 38, 1016 (1988).
- [51] H. Heiselberg, Phys. Rep. **351**, 161 (2001).
- [52] L. Van Hove, Z. Phys. C **21**, 93 (1983); M. Gyulassy, Nucl. Phys. **A400**, 31c (1983).
- [53] S. J. Lindenbaum and R. S. Longacre, J. Phys. G **26**, 937 (2000).
- [54] H. Heiselberg and A. D. Jackson, eprint nucl-th/9809013, *Minneapolis 1998, Continuous Advances in QCD*, pgs. 430-439.
- [55] I. N. Mishustin, Phys. Rev. Lett. **82**, 4779 (1999).
- [56] S. Pratt, Phys. Rev. C **49**, 2722 (1994).
- [57] M. Stephanov, K. Rajagopal, E. Shuryak, Phys. Rev. Lett. **81**, 4816 (1998).
- [58] M. Stephanov, K. Rajagopal, E. Shuryak, Phys. Rev. D **60**, 114028 (1999).
- [59] B. Müller, Nucl. Phys. **A702**, 281c (2002).
- [60] G. Baym and H. Heiselberg, Phys. Lett. B **469**, 7 (1999).
-

- 
- [61] O. Scavenius, A. Dumitru and A. D. Jackson, Phys. Rev. Lett. **87**, 182302 (2001).
- [62] S. A. Bass, P. Danielewicz and S. Pratt, Phys. Rev. Lett. **85**, 2689 (2000) [nucl-th/0005044]; S. y. Jeon and S. Pratt, Phys. Rev. C **65**, 044902 (2002) [hep-ph/0110043].
- [63] J.G. Reid (STAR Collaboration), Nucl. Phys. **A698**, 611c-614c (2002).
- [64] R. L. Ray, (STAR Collaboration), “Correlations, Fluctuations and Flow Measurements from the STAR Experiment,” in the proceedings of the 16th International Conference on Ultra-Relativistic Nucleus-Nucleus Collisions - *Quark Matter-2002*, Nucl. Phys. **A715**, 45c (2003).
- [65] T. A. Trainor, “Event-by-Event Analysis and the Central Limit Theorem,” hep-ph/0001148 (2000).
- [66] E. Schnedermann, J. Sollfrank and U. Heinz, Phys. Rev. C **48**, 2462 (1993); B. Tomášik *et al.* nucl-th/9907096 (2001), Acta Phys. Hung. New Ser. Heavy Ion Phys. **17**, 105-143 (2003); Phys. Rev. C **65**, 031902(R) (2002).
- [67] M. Gyulassy and M. Plümer, Phys. Lett. B **243**, 432 (1990); X. N. Wang and M. Gyulassy, Phys. Rev. Lett. **68**, 1480 (1992); M. Gyulassy and X. N. Wang, Nucl. Phys. **B420**, 583 (1994); R. Baier, D. Schiff and B. G. Zakharov, Ann. Rev. Nucl. Part. Sci. **50**, 37 (2000).
- [68] C. Adler *et al.*, STAR Collaboration, “Disappearance of back-to-back high  $p_T$  hadron correlations in central Au+Au collisions at  $\sqrt{s_{NN}} = 200$  GeV,” Phys. Rev. Lett. **90**, 082302 (2003).
- [69] L. Bettencourt, K. Rajagopal and J. Steele, Nucl. Phys. **A693**, 825 (2001).
- [70] M. Bleicher *et al.*, Phys. Lett. B **435**, 9-12 (1998); M. Gaździcki and St. Mrówczyński, Z. Phys. C **54**, 127 (1992).
- [71] G. Wilk and Z. Włodarczyk, “Imprints of nonextensivity in multiparticle production,” eprint hep-ph/0011189 (2000).
- [72] A. Ishihara, Univ. of Texas at Austin (STAR Collaboration), Bull. Am. Phys. Soc. **46**, 29 (2001); contributed paper given at the Joint Fall 2001 Nuclear Physics Division Meeting of the APS and JPS.
- [73] J.G. Reid, T.A. Trainor, Nucl. Inst. and Meth. **A457** (2001) 378-383.
- [74] C. Adler *et al.*, STAR Collaboration, “Event-by-event  $\langle p_T \rangle$  fluctuations in Au-Au collisions at  $\sqrt{s_{NN}} = 130$  GeV,” nucl-ex/0308033.
- [75] M. J. Tannenbaum, Phys. Lett. B **498**, 29 (2001).
-

- [76] H. Appelshäuser *et al.* (NA49 Collaboration), Phys. Lett. B **459**, 679 (1999); H. Appelshäuser *et al.* (CERES Collaboration), Nucl. Phys. **A698**, 253c (2002); J. G. Reid (NA49 Collaboration), private communication.
- [77] J. Whitmore, Phys. Rep. **27**, 187-273 (1976).
- [78] B. Anderson, Cambridge Monogr. Part. Phys. Nucl. Phys. Cosmol. **7**, 1-471 (1997).
- [79] C. Adler *et al.* (STAR Collaboration), Phys. Rev. C **66**, 034904 (2002).
- [80] G. Roland (NA49 Collaboration), Nucl. Phys. **A638**, 91c (1998).
- [81] S. E. Vance, M. Gyulassy and X. N. Wang, Phys. Lett. B **443**, 45 (1998); Nucl. Phys. **A638**, 395c (1998).
- [82] D. Teaney, J. Lauret and E. V. Shuryak, eprint nucl-th/0110037 (2001).
- [83] O. Barannikova, F. Wang, (STAR Collaboration), “Mid-rapidity  $\pi^\pm$ ,  $K^\pm$ , and  $\bar{p}$  yields and spectra in Au+Au collisions at RHIC from STAR,” in the proceedings of the 16th International Conference on Ultra-Relativistic Nucleus-Nucleus Collisions - *Quark Matter-2002*, Nucl. Phys. **A715**, 458-461 (2003).
- [84] Qingjun Liu, Univ. of Washington, private communication.
- [85] C. Adler *et al.* (STAR Collaboration), “Kaon production and kaon to pion ratio in Au+Au Collisions at  $\sqrt{s_{NN}} = 130$  GeV,” nucl-ex/0206008, submitted to Phys. Rev. Lett. (2002); W. Deng, see STAR protected web are under: protected-/strange/wdeng/qm2001/support/readme.txt.
- [86] T. Ludlam *et al.*, “STAR Future Physics and Detectors – Report of the Bar Harbor Workshop,” (June 2002), see [http://www.star.bnl.gov/STAR/meetings\\_l-collab\\_l/future/summary.html](http://www.star.bnl.gov/STAR/meetings_l-collab_l/future/summary.html).
- [87] K. Adcox *et al.* (PHENIX Collaboration), Phys. Rev. C **66**, 024901 (2002).
- [88] X. N. Wang and M. Gyulassy, Phys. Rev. D **44**, 3501 (1991).
- [89] R. L. Ray and R. S. Longacre, eprint nucl-ex/0008009 (2000).
- [90] Manuel Calderon de la Barca Sanchez, “Charged Hadron Spectra in Au+Au Collisions at  $\sqrt{s_{NN}} = 130$  GeV,” Ph.D. Thesis, Yale University (2001).
- [91] C. Adler *et al.*, STAR Collaboration, Phys. Rev. Lett. **87**, 112303 (2001).
- [92] C. Adler *et al.*, STAR Collaboration, Phys. Rev. Lett. **87**, 262302 (2001).
- [93] T. Sakaguchi *et al.*, nucl-ex/0209030, Nucl. Phys. A715, 757-760 (2003).
- [94] J. L. Klay *et al.*, nucl-ex/0210026, Nucl. Phys. A715, 733-736 (2003).

- [95] D. Kharzeev and E. Levin, Phys. Lett. **B523**, 79 (2001).
- [96] X. N. Wang and B. Muller, Nucl. Phys. **A566** (1994) 555c.
- [97] E. Shuryak, Nucl. Phys. **A566** (1994) 559c.
- [98] Z. Lin and M. Gyulassy, Nucl. Phys. **A590** (1995) 495c.
- [99] H. Satz, Rept. Prog. Phys. **63** (2000) 1511.
- [100] P. Braun-Munzinger, Quark Matter 2002 Proceedings, nucl-th/0209035, Nucl. Phys. A715, 529-532 (2003).
- [101] C. Adler *et al.*, STAR Collaboration, “Centrality Dependence of High  $p_T$  Hadron Suppression in Au+Au Collisions at  $\sqrt{s_{NN}} = 130$  GeV/nucleon”, Phys. Rev. Lett. **89**, 202301 (2002).
- [102] X.N. Wang, M. Gyulassy, Phys. Rev. Lett. **68** (1992) 1480.
- [103] Y. L. Dokshitzer, D. Kharzeev, Phys. Lett. **B519** (2001) 199.
- [104] K. Adcox *et al.*, PHENIX Collaboration, nucl-ex/0202002, Phys. Rev. Lett. **88** 192303 (2002).
- [105] C. Adler *et al.*, STAR Collaboration, “ $K^*(892)^0$  production in relativistic heavy ion collisions at  $\sqrt{s_{NN}} = 130$  GeV,” Phys. Rev. C **66**, 061901(R) (2002).
- [106] C. Adler *et al.*, STAR Collaboration, Nucl. Phys. **A698** (2002) 64c.
- [107] M. C. Abreu *et al.*, NA50 Collaboration, Nucl. Phys. **A698** (2002) 127c
- [108] L. W. Alvarez, Nobel Prize Lecture, 1968.
- [109] J. Rafelski, Quark Matter 2002, Nantes, France, Nucl. Phys. A715, 98-107 (2003).
- [110] R. Rapp and J. Wambach, Adv. Nucl. Phys. **25** (2000) 1; R. Rapp, Phys. Rev. C **63** (2001) 054907.
- [111] J. Letessier, *et al.*, nucl-th/0011048, J. Phys. G **27**, 427-438 (2001); G. Torrieri, J. Rafelski, Phys. Lett. B **509** (2001) 239.
- [112] L.V. Bravina, *et al.*, hep-ph/0010172, Phys. Rev. C **63**, 064902 (2001); D. Teaney, *et al.*, nucl-th/0110037.
- [113] J. Rafelski and B. Mueller, Phys. Rev. Lett. **48** (1982) 1066; **56** (1986) 2334(E).
- [114] J. Kapusta *et al.*, Phys. Rev. C **66** 014903 (2002).

- 
- [115] P. Fachini, STAR Collaboration, “ $\rho$  and  $K^*$  measurements from STAR”, Quark Matter 2002, Nucl. Phys. A715, 462-465 (2003); P. Braun-Munzinger, E. Shuryak, private communications.
- [116] Y. J. Pei, Z. Phys. C **72**, 39 (1996), and references therein; P.V. Chliapnikov, Phys. Lett. B **470**, 263 (1999).
- [117] D.E. Groom *et al.*, Eur. Phys. J. C **15**, 1 (2000).
- [118] N. Xu and M. Kaneta, Nucl. Phys. A **698**, 306c (2002); F. Becattini, Z. Phys. C **69**, 485 (1996); F. Becattini and U. Heinz, Z. Phys. C **76** 269 (1997); P. Braun-Munzinger *et al.*, Phys. Lett. B **518** 41 (2001).
- [119] B. Zhang *et al.*, Phys. Rev. C **61** 067901 (2000).
- [120] M. Bleicher, J. Aichelin, Phys. Lett. B **530**, 81 (2002).
- [121] C. Adler *et al.*, STAR Collaboration, “Midrapidity  $\phi$  production in Au+Au collisions at  $\sqrt{s_{NN}} = 130$  GeV,” Phys. Rev. C **65**, 041901(R) (2002).
- [122] X.N. Wang, Phys. Rev. C **58**, 2321 (1998); private communication.
- [123] I. Vitev, M. Gyulassy, Quark Matter 2002, hep-ph/0208108, Nucl. Phys. A715, 779-782 (2003).
- [124] C. Adler *et al.*, STAR Collaboration, Phys. Rev. Lett. **89**, 092301 (2002).
- [125] C. Adler *et al.*, STAR Collaboration, Phys. Rev. Lett. **87**, 082301(2001).
- [126] B. Tomasik, “Simultaneous fits to spectra and HBT radii from RHIC experiments,” Talk presented at the RHIC/INT Winter Workshop, Seattle, WA., January 2002.
- [127] F. Retière for the STAR collaboration, nucl-ex/0111013
- [128] D. Teaney, J. Lauret, E.V. Shuryak, nucl-th/0110037
- [129] K. Adcox *et al.*, PHENIX Collaboration, nucl-ex/0201008, Phys. Rev. Lett. **88**, 192302 (2002).
- [130] A. Enokizono, for the PHENIX collaboration, Quark Matter 2002, nucl-ex/0209026, Nucl. Phys. A715, 595-598 (2003).
- [131] O. Barannikova, M. Kaneta, K. Schweda, and N. Xu, “Mid-rapidity proton and antiproton distributions from Au+Au collisions at  $\sqrt{s_{NN}} = 130$  GeV,” Talk presented at the STAR Physics Analysis Meeting, Nov-Dec 2001.
- [132] C. Adler *et al.*, STAR Collaboration, “Pion-kaon correlations In Au+Au collisions at  $\sqrt{s_{NN}} = 130$  GeV,” nucl-ex/0307025, Phys. Rev. Lett. (in press).
-



- 
- [133] F. Retière for the STAR collaboration, Quark Matter 2002, Nucl. Phys. A715, 591-594 (2003).
- [134] S.T. Butler and C.A. Pearson, Phys. Rev. **129**, 836 (1963).
- [135] R. Scheibl and U. Heinz, Phys. Rev. C **59**, 1585 (1999).
- [136] C. Adler *et al.*, STAR Collaboration, Phys. Rev. Lett. **87**, 262301 (2001).
- [137] A. Polleri, J.P. Bondorf, and I.N. Mishustin, Phys. Lett. B **419**, 19 (1998).
- [138] R. L. Jaffe, Phys. Rev. Lett. **38**, 195 (1977); **38**, 617(E) (1977).
- [139] J. Schaffner-Bielich, Phys. Rev. Lett. **84**, 4305 (2000); and private communications.
- [140] Z.Y. Zhang *et al.*, Phys. Rev. C **61**, 065204 (2000).
- [141] Y.W. Yu, Z.Y. Zhang and X.Q. Yuan, Commun. Theor. Phys., **31**, 1 (1999).
- [142] Q.B. Li, P.N. Shen, Z.Y. Zhang and Y.W. Yu, Nucl. Phys. A **683**, 487 (2001).
- [143] Y.W. Yu *et al.*, Phys. Rev. C **66**, 015205 (2002).
- [144] S. Pal, C.M. Ko, and Z.Y. Zhang, nucl-th/0107070.
- [145] M.C.S. Williams, Nucl. Phys. A **698**, 464 (2002).
- [146] J. Adams *et al.* (STAR Collaboration), nucl-ex/030912, Phys. Rev. Lett. (submitted).
- [147] CERN-LHCC-2003-062 ALICE TDR 010 7, January 2004, pp 136-147.

## A Appendix – Simulation Codes used in Section 3.3

All calculations and simulations presented in Section 3.3 were done using a set of standalone computer codes which produce events, simulate the inefficiencies and performances of STAR (TPC plus MRPC-TOF), and compute physics analysis quantities. This fast simulation method is an expedient way to estimate the essential performance parameters and to facilitate evaluation of the TOF system with respect to multiple physics programs. This kind of analysis of “new physics” performance lies in between a “back-of-the-envelope” estimate and a full-blown GSTAR-Reconstruction-DST-Physics analysis. Considerable care was taken to insure that the relevant performances of STAR were reproduced. The general features of the codes are described here.

**MEVSIM:** – A Monte Carlo code for producing events from a user controlled momentum space distribution model with user determined particle types. MEVSIM [89] has been used extensively in STAR for the past several years.

**FastDetecRespSim:** – [Fast Detector Response Simulator] This code applies parametrized versions of measured STAR performances to the particles in the simulated events. Included are the acceptance and decay losses, track finding efficiencies, momentum vector smearing, two-track merging, and particle identification (PID) using  $dE/dx$  in the TPC gas, kink finding for charged kaons in the TPC [85], and the proposed MRPC-TOF with varying amounts and configurations of trays. In general these quantities are  $p_T$  and  $\eta$  dependent and also depend on particle type where specific parameters for pions, kaons, protons and antiprotons were used.

The acceptance, losses due to particle decay (mainly for kaons), and track finding efficiencies were combined into an overall efficiency function which was randomly sampled using the standard rejection method to determine if a given particle will be reconstructed. The sources of information used are from the year 2000 and 2001 data analyses and include: (1) Manuel Calderon de la Barca Sanchez’s Ph.D. thesis section 8.2.1 and 8.2.2 [90], (2) QA plots for the year 2001 data, (3) results from the negative hadron spectra analysis [91], and (4) results from the antiproton spectra paper [92]. The overall efficiency was modeled as: (1) an exponential dependence on  $p_T$  representing acceptance and particle decay losses, (2) a quadratic dependence at low  $p_T$  becoming constant at higher  $p_T$  representing tracking efficiencies, and (3) constant at mid-pseudorapidity but falling off quadratically at larger  $|\eta|$  beginning at  $|\eta| = 1$ . The parameters were determined for pions, kaons and protons. At mid-rapidity and larger  $p_T$  this overall track reconstruction efficiency was assumed to be 0.80, 0.74 and 0.82 for pions, kaons and protons, respectively.

The PID performance of the TPC based on  $dE/dx$  for pions, kaons and protons was obtained from Manuel Calderon de la Barca Sanchez’s Ph.D. thesis [90] using Figures 10.2, 8.7 and 6.2 as well as results published in the antiproton spectra paper [92]. The function used here represents the *additional* loss in identified particles due to the tighter cuts which are applied to tracks selected for  $dE/dx$  PID analysis. The depen-

dence on  $p_T$  was again modeled as a quadratic at low momentum becoming constant above 0.5 GeV/c. The additional loss in identified particles varies from about 30% at 0.2 GeV/c to 4% above 0.5 GeV/c. The momentum ranges where TPC based  $dE/dx$  PID was applied are: (values are for  $p_{T,min}$  and  $P_{Total,max}$ ) (1) 0.0 - 0.75 GeV/c for pions, (2) 0.0 - 0.6 GeV/c for kaons, (3) 0.4 - 0.95 GeV/c for protons, and (4) 0.0 - 0.95 GeV/c for antiprotons. False particle identifications were not included.

The kaon identification performance based on reconstructed charge decays in the TPC was included and parameterized according to results presented by W. Deng [85]. The overall kink finding efficiency is about 1%.

Finally, the expected performance parameters of the proposed TOF detector with respect to acceptance, PID efficiency, and momentum range were used. Particle trajectory intercepts at the TOF average radius of 220 cm were computed and it was determined whether or not the particle hit an area covered by a TOF tray. For those that did the geometrical acceptance was assumed to be 90% and of those we assumed that 96% were successfully identified. This *additional* identified particle efficiency of 0.864 was randomly applied to those tracks which reach a TOF tray and which also survived the preceding acceptance, decay loss and track finding efficiency cuts. The momentum ranges where TOF based PID was applied are: (values are for  $P_{Total,min}$  and  $P_{Total,max}$ ) (1) 0.3 - 1.7 GeV/c for pions, (2) 0.3 - 1.7 GeV/c for kaons, and (3) 0.3 - 2.9 GeV/c for protons. False particle identifications were not included.

## B Appendix – The STAR TOFp and pVPD Systems

A small-area TOF system was installed in STAR in the Spring of 2001. The STAR Time Of Flight Patch (“TOFp”) [3] uses a standard CTB tray in which the two CTB slats have been replaced by 41 Bicron BC-420 plastic scintillator slats plus Hamamatsu R5946 mesh dynode PMT and Cockcroft-Walton base assemblies. Also on-detector are eleven boards of custom high-performance FEE that include a fast discrimination of the PMT signals very close to the detectors. The TOFp detectors span roughly one unit of pseudorapidity and  $1/60^{th}$  of the azimuth. Also part of the TOFp System are two smaller detectors called the pVPD’s (pseudo Vertex Position Detector’s), which are positioned very close to the beam pipe outside of STAR and provide the electronic start signals for the TOFp stops. The digitization is done on the platform in CAMAC. The goal is the measurement of the single-particle charged hadron spectra in a limited acceptance, but over many events. The system was operated for the first time during RHIC Run-2. The arrangement of the TOFp detectors and the two pVPD detectors with respect to the STAR TPC (shown in cutaway) and the RHIC beam pipe is shown in figure 51.

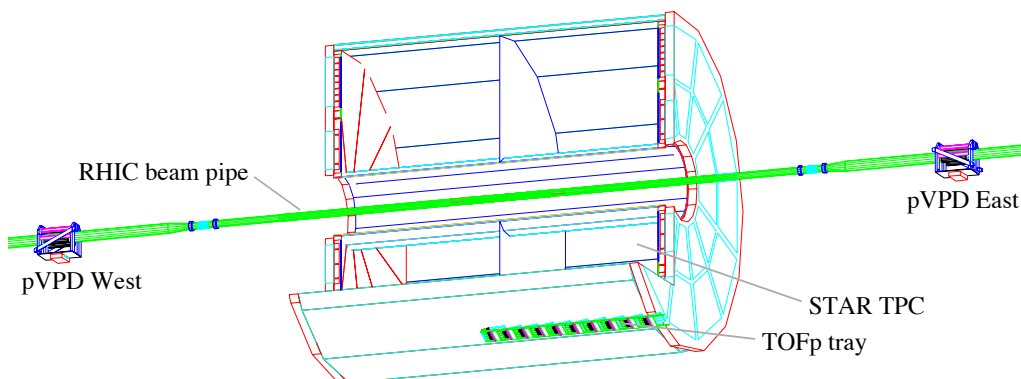


Figure 51: The arrangement of the TOFp detectors and the two pVPD detectors with respect to the STAR TPC (shown in cutaway) and the RHIC beam pipe.

While the technologies used in the TOFp system are not the same as those presently proposed for the full system, we include in this appendix comments related to the TOFp Systems for the following reasons:

- The TOFp system performed to expectations during RHIC Run-2, and provided particle identification for tracks in the TOFp acceptance up to the expected momenta. The TOFp performance is thus an experimental verification of the general expectations for the full system outlined in section 4.1.
- A considerable amount of custom software is needed for the full system to extrapolate TPC tracks and match them to the correct stop detector channels, to

calibrate the start and stop timing information, to perform the particle identification using on the calibrated information, and to evaluate the efficiencies involved via embedding simulations. The software performing these tasks for the TOFp data exists and is presently being optimized (see below for the present status). This TOFp software is directly applicable for the full system - while the technologies differ, both systems require TPC track extrapolation and matching to detector channels, and both systems exhibit similar-looking time-amplitude slewing and signal propagation velocities inside the detectors. The correction algorithms are thus effectively the same in both cases and only the parameters change. Thus, the offline software for the full system is effectively under development now, years ahead of the existence of the system itself. This means it will be possible to extract physics results from the system very quickly after the raw data is collected.

- The TOFp System was proposed, constructed, and operated by members of STAR that are also participants in the present proposal. Thus the present group has real experience operating a TOF detector system in the STAR environment, and performing TOF-based PID analyses using STAR data.

The “production” software used to perform the track-to-slat matching for the TOFp system is described in section B.1. The offline calibrations algorithms on both the start (pVPD) and stop (TOFp) sides, as well as the resulting PID performance in central Au+Au collisions at  $\sqrt{s_{NN}}=200$  GeV during the 2001 RHIC run, are described in section B.2.

## B.1 TOFp Production and Matching Software

The data flow of the TOFp detector is fully embedded in the STAR raw data production scheme. This ensures storage and handling of the TOFp data in a standardized environment requiring only a few TOFp-dedicated software modules. The production and analysis platform of STAR, STEVENT, is built on top of the ROOT package. The ROOT package is an object-oriented data analysis framework widely used in the heavy ion and high-energy community. The STEVENT classes inherit from ROOT classes which allows both batch processing and interactive use and assures the persistency of its inherited classes so they can be stored in ROOT files. The STEVENT analysis modules are called Makers. The TOFp analysis software, therefore, consists of a few Makers with some additional utility classes.

In figure 52 the essential components of the offline production are depicted. The online production, *i.e.* the STAR data acquisition, wraps the TOFp data banks in raw data files. In the offline production, the STTOFMAKER calls the DAQ Reader to check for TOFp data banks. If available, this data is then copied and formatted into an STEVENT-based TOFCOLLECTION. Collections are set up on a per-event basis and are accessible by other Makers, *e.g.* the TOFMAKER can access track or trigger-detector collections. In the offline production the collections are persistent classes and as such can be stored in ROOT files. These files tend to be sizable and a

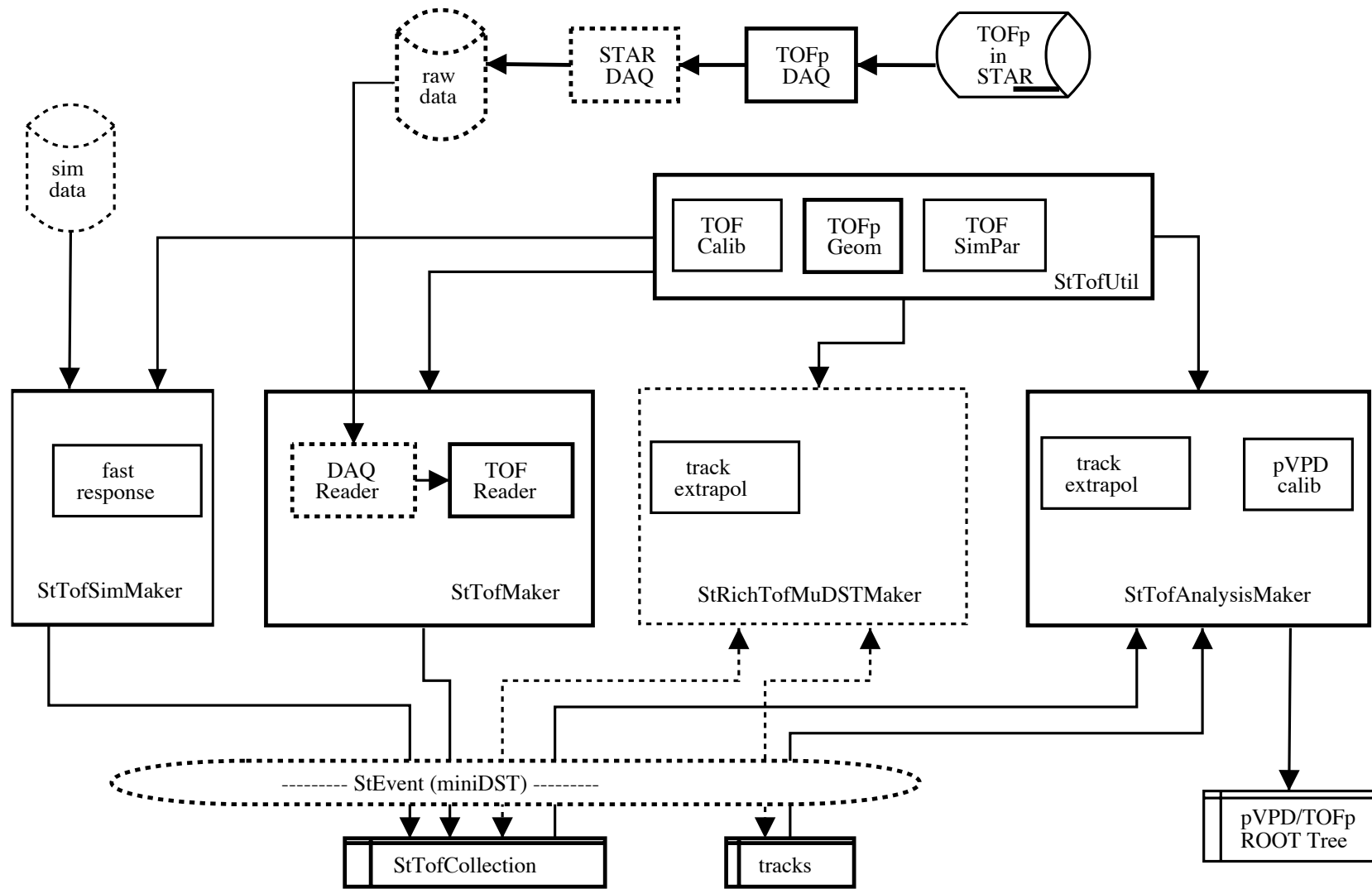


Figure 52: The components of the offline software for the STAR TOFp Systems.

Data Summary Tape (DST) Maker is used to pick out and store into smaller ROOT trees those variables that are relevant.

The first stage of the TOFp analysis focusses on the calibration of the detector. This requires both the raw TOFp data and the tracking information from the TPC. During this year's offline production, the TOFp maker only stored the raw ADC and TDC data in the TOFp collection. The TOFp detector has only limited geometrical acceptance so many of the TPC tracks do not extrapolate to one of its slats. Since the RICH detector is in similar situation and the detectors overlap in acceptance, efforts were joined in a miniDST Maker which filters out those tracks that are not close to these detectors, *i.e.* have no chance of extrapolating to either the TOFp or the RICH. Not only did this reduce the size of our data set considerably, it also sped up the analyses based on it. This TOFp miniDST contains all STAR global tracks that extrapolate into an area containing the TOFp detectors that is approximately two trays wide in azimuth ( $\sim 12$  degrees) and  $\sim 250$ cm long.

The RICH/TOF mini-DSTs remain based on the STEVENT model so prototype analysis makers can easily be fed back in future STAR-wide production runs. For the calibration analysis, the STTOFANALYSISMAKER builds a flat ROOT Tree summarizing only those slats that have tracks pointing to them (see next subsection). Besides the various TOFp makers a number of utility classes and functions have been written. Typically, they provide access to the STAR database, geometrical or timing calculations and calibration routines.

## Matching Results

Time-of-Flight based particle ID relies on accurate tracking information: apart from the obvious timing information provided by the TOFp, momentum and path length are essential ingredients for calculating the mass hypotheses. In fact, tracking information is already vital in the early calibration stage where the timing dependencies of the various track parameters are investigated. This section describes the procedure by which tracks are extrapolated and matched to TOFp slats. The length of straight line TPC tracks from the center ( $Z=0$ ) of the STAR barrel to the TOFp tray varies between  $L=2.2$ m on the  $\eta\sim 0$  side to  $L=3.2$ m at  $\eta\sim 1$ . For low momentum tracks, the STAR magnetic field curves the paths of charged particles and the straight line tracks are the limit for high momentum charged particle tracks.

Identified global tracks are usually parameterized with a helix trajectory. Such a parameterization and knowledge of the STAR magnetic field ( $B=0.5$  T maximum) allows the measurement of the track momenta, dip angles, and curvatures of the trajectories in the TPC. More sophisticated methods like the Kalman filter take energy losses along the flight paths into account. The typical momentum resolution of the TPC is about 1.3%. The track total path length,  $s$ , is given by,

$$s = \sqrt{s_T^2 + s_Z^2} \quad (7)$$

where the transverse and parallel components of the path length, respectively, are,

$$s_Z = Z_{\text{hit}} - Z_{\text{PV}} \quad \text{and} \quad s_T = (2R)\arcsin(C/2R). \quad (8)$$

Here  $Z_{\text{PV}}$  and  $Z_{\text{hit}}$  are the STAR Z positions of the primary vertex and the hit in the TOFp slat,  $R$  is the track total radius of curvature from the helix fit, and  $C$  is the straight line distance in the bend plane from the primary vertex to the hit in the slat, *i.e.*  $C = [(x_{\text{hit}} - x_{\text{PV}})^2 + (y_{\text{hit}} - y_{\text{PV}})^2]$ .

A global track which extrapolates to any one the 41 TOFp slats is called a “match.” For last year’s analysis, no requirements were set for the tracks other than having a valid helix parameterization. In future analyses, cuts will be placed on *e.g.* the number of hits and/or fit points on the track (see also the Calibrations section below). Although it is expected that slats hit by more than one track can be analyzed, currently the calibration and analysis concentrates only on singly-hit slats. All other matches are ignored for now.

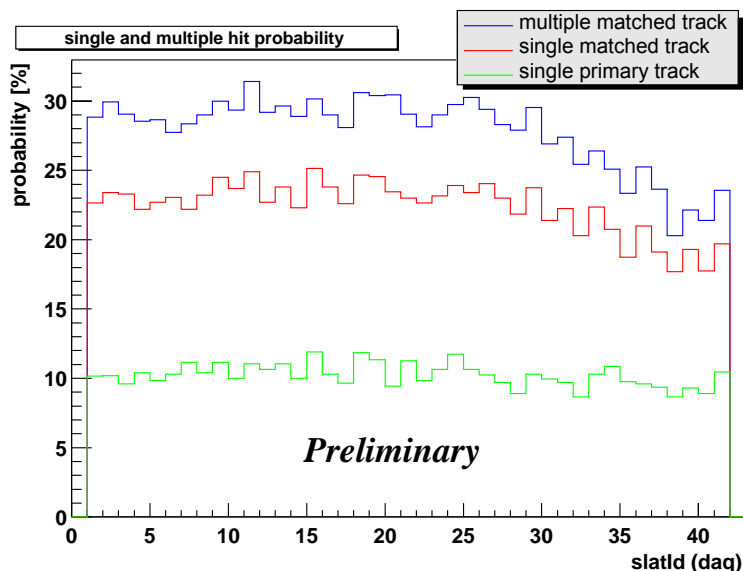


Figure 53: TPC to TOFp match probabilities per track from central Au+Au collisions.

In figure 53 the match probability in central Au+Au collisions for each of the slats is plotted. Low slat numbers start on the  $\eta \sim 0$  side and increase to the  $\eta \sim 1$  side of the tray. The (upper) blue histogram depicts the match probabilities when extrapolating all STAR global tracks in the TOFp/RICH miniDST (*i.e.* near the TOFp/RICH acceptance). The (middle) red histogram are those global track matches for which the slat matched to the track and no other tracks were matched to this slat in this event. The (lower) green histogram indicates the probability the global track matched to single-match TOFp slat is also a primary track. Primary tracks are those that originated from the event vertex while global tracks may point to secondary vertices away from the primary vertex. Our analyses are primarily aimed at charged hadron spectra so at present we are concentrating only on the primary tracks.



The matched candidates are stored in a ROOT tree together with the raw ADC and TDC value of the associated slat. Additional track information such as local hit position on the slat, angles of incidence on the slat and path length in the slat are stored as well.

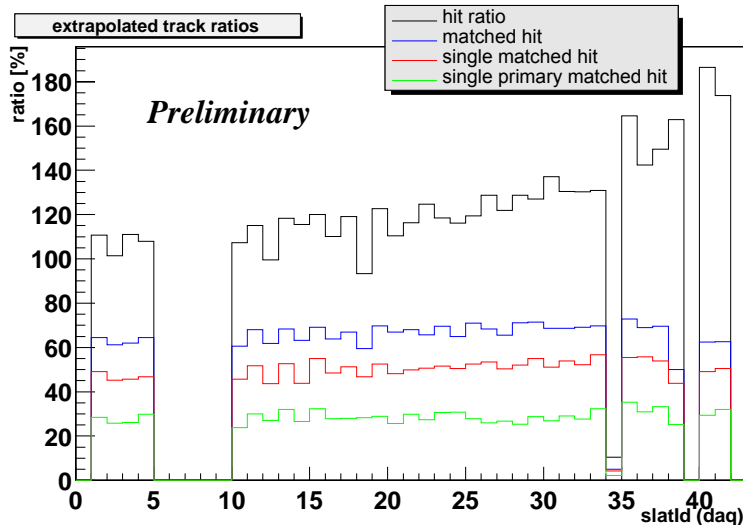


Figure 54: TPC to TOFp match ratios per track from central Au+Au collisions.

In figure 54 the hit ratios are plotted for each individual slat. The colored lines have the same meaning as Figure 53 with an additional requirement that the slat selected by the matching algorithm saw a charged particle hit (via a threshold cut on the ADC value). The (highest) black histogram indicates the ratio of the number of times a slat fired and the number of times at least one global track was matched to this slat. The (2<sup>nd</sup> highest) blue histogram then includes the requirement that the slat was struck at least once via the ADC cut. The (3<sup>rd</sup> highest) red and (lowest) green histograms are the ratios under the same conditions as in figure 53. For the global track matches (highest, black), the hit ratio is typically above 100% which means that a slat fired more often than a global track extrapolated to it. This ratio is very sensitive to the cut placed on the ADC value to locate hit slats. The other histograms show how the ratio decreases when the additional matching criteria are applied. Approximately 30% of the tracks in the TOFp/RICH miniDST are tracks that are primary and strike a singly-struck TOFp slat. The holes in the plot for slat numbers 5-8, and 9, 34 and 39 are the result of FEE board and dead HV cells, respectively.

## B.2 TOFp Systems Calibrations and Performance

The production code described in the previous section produces a ROOT N-tuple containing the event, track, and TOFp/pVPD information for all “matches”. The development of all the calibrations software needed to turn the raw TOFp/pVPD

information into time intervals, and then into particle identification information, is based on this N-tuple. This allows this development to be quickly and efficiently performed at Rice under local Linux and Mac OSX machines. The calibration code for the central full-energy Au+Au data from the 2001 run is complete. The TOFp System performed as expected in these data. Some details on the TOFp calibrations software and the observed performance of the system are described in this section.

## pVPD Calibrations

The start detector for the TOFp System is the pVPD. The information needed from this detector is the corrected average of the times measured in those channels of the pVPD that fire in a given event. In the central Au+Au data from Run-2, all six channels of the pVPD fire in every event. The average of the six raw TDC values in each event is the crudest measure of the event start time, as it is smeared by the so-called “slewing” effect intrinsic to PMTs and MRPC detectors. The first calibration necessary is thus the correction of the pVPD start times for the slewing effect.

In order to avoid bias during this correction, we compare the TDC average of one East pVPD channel and one West pVPD channel to the average of the other four pVPD TDC channels. This difference of averages, referred to as “ $\langle 2 \rangle - \langle 4 \rangle$ ”, is centered at zero by definition but has a standard deviation that is increased by the fact that all six of the times used in this average depend on the respective six ADC values for these channels. An iterative technique was employed where two channels are selected, *e.g.* East 1 and West 1, and the difference of TDC averages  $\langle 2 \rangle - \langle 4 \rangle$  is plotted versus the two ADC values for East 1 and West 1, respectively. This two-dimensional profile is then fit with a polynomial function of the two ADC values, and the fit parameters are used in later passes through the data to remove these correlations.

The next step of the iteration then involves the next pair of channels, *e.g.* East 2 and West 2. The difference of TDC averages,  $\langle 2 \rangle - \langle 4 \rangle$ , is plotted versus the ADC values for East 2 and West 2, respectively, where the  $\langle 4 \rangle$  average includes the corrected TDC values for East 1 and West 1 following the first iteration and the still uncorrected East 3 and West 3 TDC averages. This two-dimensional profile is then fit with a polynomial function of these two ADC values, and the fit parameters recorded for use in subsequent iterations. This process is continued in nine passes such that each East and West pair of pVPD TDCs is fit and corrected versus their respective pairs of ADC values three times.

The results from this process are shown in figure 55. The different point styles in this figure correspond to the different iterations performed. The black points are the raw data, indicating the resolution on the quantity  $\langle 2 \rangle - \langle 4 \rangle$  with simply the raw data is approximately 2.6 TDC channels, or  $\sim 130$ ps. The method has converged to the best possible resolution after the fourth iteration. After the procedure, the standard deviation of the quantity  $\langle 2 \rangle - \langle 4 \rangle$  is reduced to approximately 0.9 TDC channels, or  $\sim 45$ ps.

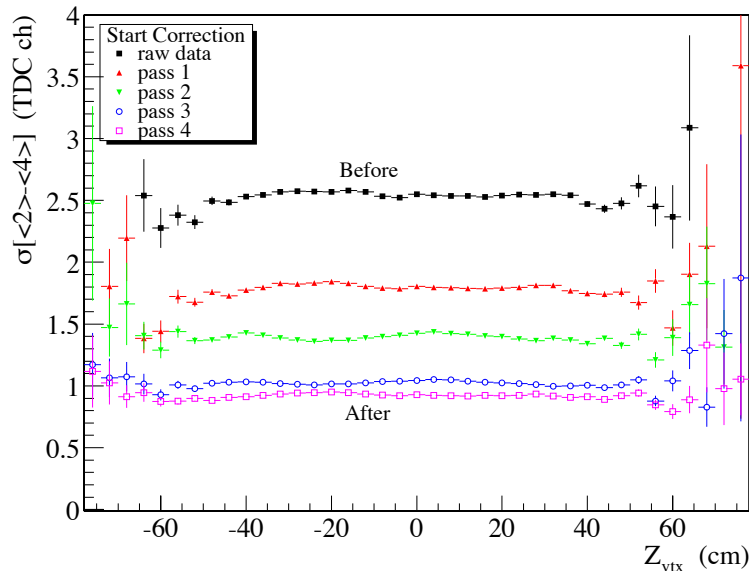


Figure 55: The standard deviation of the quantity  $\langle 2 \rangle - \langle 4 \rangle$  in units of TDC channels (50ps/ch) versus the primary vertex location. The different point styles correspond to individual passes during the start correction procedure.

The start time needed by the TOFp system is the average of all six (slew-corrected) TDCs, *i.e.* “ $\langle 6 \rangle$ ”. Assuming that all six pVPD PMTs have the same single-detector resolution, the standard deviation of the difference of averages  $\langle 2 \rangle - \langle 4 \rangle$  is related to the standard deviation of the average of all six pVPD PMTs by a factor of  $\sqrt{4/3}/\sqrt{6}$ , or 0.47. The pVPD start time resolution in the central full-energy Au+Au events is thus  $\sigma_{\langle 6 \rangle} = 24$  ps, and the equivalent single detector resolution is  $\sigma_{\langle 1 \rangle} = 58$  ps. This start-timing performance is considerably better than necessary to do efficient time-of-flight analyses in the STAR geometry. The corrections one then needs for the stop side are now described.

## TOFp Calibrations

The TOFp slats also slew causing a correlation between TOFp TDC and ADC values. Also, these slats are “single-ended,” requiring the additional correction for the time taken for the scintillation light to propagate from the location of the hit inside the slat to the PMT photocathode. This distance is referred to as  $Z_{\text{hit}}$ . This propagation time was measured on the bench using a Nitrogen laser on the TOFp slats to be linear with a slope of  $\sim 65$  ps/cm. In the case of the STAR detector, the TOFp geometry, and real events, however, these two corrections are hopelessly correlated with a large number of other variables requiring some care in the software used to correct for these effects. That is, in the case of TOFp in STAR, the slewing does not simply go like the function  $\text{const}/\sqrt{\text{ADC}}$  or  $\text{const}/\text{ADC}$ , and the scintillation

light propagation time is not simply  $\text{const} * Z_{\text{hit}}$ .

The ADC value in a TOFp slat, which is assumed to correlate directly to the pulse height that is directly related to the slewing, also depends on a number of other quantities. It depends on the momentum via Bethe-Bloch-like energy loss. Indeed the PID resolution from the ADC values in the 2cm-thick TOFp slats is not unlike that from TPC  $dE/dx$ . It depends on the location of the hit along the slat via the scintillation photon attenuation inside the wrapped scintillator. It depends on the length of the track inside the volume of the slat, as primary scintillation light is created all along this path. This length depends on the location of the slat in the TOFp tray (due to aspects of the angles of the slat positioning), the primary vertex location, and the track momentum components  $p_T$  (in the bend plane) and  $p_z$  (in the non-bend-plane). The TDC value depends on the actual time of flight of the particle in STAR, the scintillation light propagation time, and the shift from the slewing.

Thus there are numerous correlations between the TDC values and the ADC and  $Z_{\text{hit}}$  values beyond those simply related to the slewing effect and the scintillation photon propagation time. We thus use an iterative technique here as well, where polynomials in ADC or  $Z_{\text{hit}}$  are fit to the data in several steps. The quantity that is minimized in this case is the difference between the experimental and expected  $1/\beta = c\tau/s$  values for pions, where  $c$  is the speed of light and  $\tau$  is the measured TDC value minus a global offset multiplied by the time-to-digital calibration of 50 ps/ch. The quantity  $s$  is the primary track total path length calculated using the reconstructed track helix parameters and the STAR and TOFp geometry. All calibrations are defined by optimizing the pions, and these corrections are then applied to all tracks in subsequent pass through the data.

A typical plot of corrected inverse velocity versus the track momentum is shown in figure 56. The solid lines are the values expected based on the momentum and the assumption of a mass of that for a pion (lowest line), Kaon, proton, and deuteron (highest line). Strong bands for pions, kaons, and protons are seen with the expected resolution. The insets depict the projections onto the inverse velocity axis for specific momentum regions near the required limits of TOFp's reach. The insets show that TOFp met the requirements - allowing TOF-based physics analyses in STAR for the first time.

Shown in figure 57 is the total TOFp+pVPD time resolution for 0.5-1.5 GeV/c pions versus the slat number. The slats with numbers 0-4 are in the first row inside the tray near  $\eta \sim 0$ , while the slats with numbers 37-40 are in the last row near  $\eta \sim 1$ . The squares depict the resolution for all tracks passing the quality cuts listed in the figure. There is a slightly better time resolution for those matches that are not close to the PMT in a given slat. The circles depict the resolution with an additional cut that  $Z_{\text{hit}}$  is greater than 10 cm.

There are a few poorly-performing channels, and one FEE board (slats 5-8) that was off for this portion of RHIC Run-2. All of these have since been repaired. The average total time resolution of the TOFp+pVPD system over all slats was 87 ps. The average total time resolution over the best 25 slats was 79 ps.

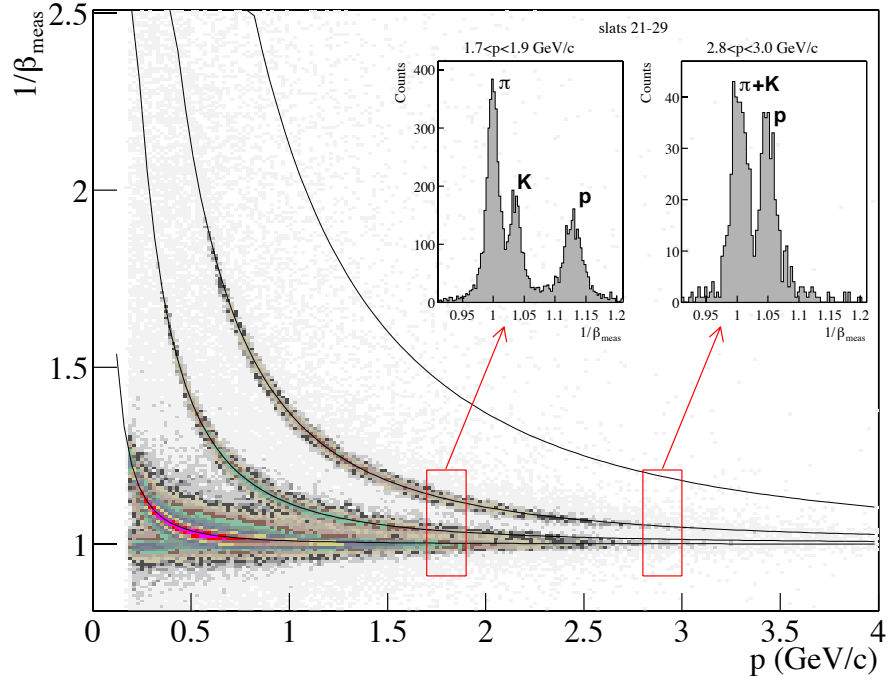


Figure 56: The corrected inverse velocity versus momentum from TOFp+pVPD for central Au+Au collisions from RHIC Run-2. The insets depict the projections onto the inverse velocity axis for specific momentum regions near the required limits of TOFp’s reach. Prominent peaks for the various hadron species are observed in both insets.

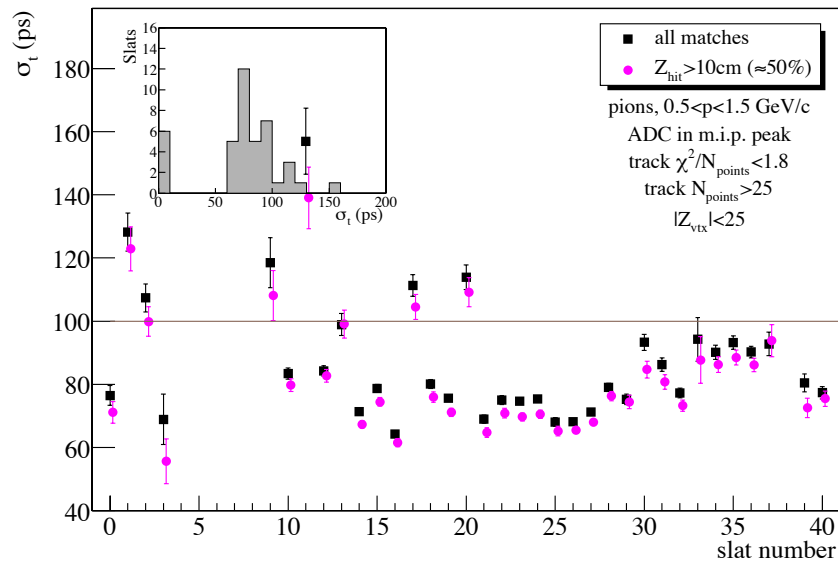


Figure 57: The total time resolution versus the TOFp slat number from the RHIC Run-2 Au+Au running. The inset depicts the histogram of these values. The average total time resolution over all(the best 25) slats was 87(79) ps.

# **Proposal for a Large-Area Time-of-Flight System for STAR**

## **Appendix C**

### **Preliminary Management Plan**

**May 21, 2004**

## 1 INTRODUCTION

This document contains major elements for a management plan to be completed on approval of the proposal.

Multi-gap resistive plate chamber (MRPC) technology is a major new detector technology developed at CERN for the ALICE experiment. STAR has been conducting successful R&D for STAR-specific MRPC detectors since 2000. The technology and test results are described in the proposal.

The parallel plate detectors are made from 7, 0.55 mm thick glass plates separated by 0.22 mm gaps. An electric potential of 14 kV is applied across the plates. The chambers operate in a highly electro-negative gas, primarily Freon r134a. Charged particles traversing the plates create avalanches in the gas gaps which are seen in 3.3 cm x 6.1 cm copper plates. The signals are amplified, discriminated, then recorded by the CERN HPTDC chip with a 25 ps least-significant-bit precision.

STAR plans to install a 23k-channel MRPC time-of-flight (TOF) system at the outer radius of the TPC, the area now occupied by the central trigger barrel (CTB). The TOF system will double STAR's particle identification reach to 95% of all charged particles within the acceptance of the TOF detector. The detector will cover the full azimuth and from  $-0.9 < \eta < 0.9$ . The new physics reach from the improved particle identification is described in the proposal. The new TOF system will allow the detailed unfolding of small scale correlations and fluctuations, significantly reduce the integrated luminosity required for key measurements such as multi-strange baryon elliptic flow, and extend the transverse momentum reach allowing accurate measurement of the mass and width of resonances up to 2 GeV.

The new detector will be realized in two parallel construction projects, one in China and one in the US. Six Chinese universities and research institutions joined the STAR collaboration in 2001 with the principal interest of participating in the TOF project. The China TOF project will manufacture and test 4000, 6-channel MRPC modules. The China TOF construction project will be funded by the China NSF. The US project will install the modules in aluminum trays, 32 per tray, build and install the read-out electronics, and test the completed detector trays. Both Chinese and US institutions will be responsible for installing and commissioning the detector in STAR.

## 2 FUNCTIONAL REQUIREMENTS

The principal functional requirement of the TOF system if it is to meet the physics goals is to provide a timing measurement with a resolution of 100 ps or better after all corrections. The requirements are described in detail in section 4.2 of the proposal.

## 3 TECHNICAL SCOPE

The STAR TOF project is divided into three major subsystem groups: (a) MRPC Modules, (b) Detector and Mechanical Systems, and (c) Electronics.

### 3.1 MRPC MODULES

The system consists of 3840, 6-channel MRPC modules housed in 120 aluminum trays. Each tray covers about 0.9 units of pseudorapidity and 1/60th of the azimuth. The production and testing of the MRPC modules is the responsibility and contribution of the Chinese collaborating institutions in STAR and the costs are not included in the cost of the US construction project. Quality assurance parameters and procedures will be established by the Chinese institutions in collaboration with the US TOF project to insure that all modules meet the design goals of the project.

### 3.2 DETECTORS AND MECHANICAL SYSTEMS

The **tray** is the mechanical support for the MRPC detectors and the electronics. It is also the gas box for the MRPCs. There are 120 trays in the system. They are roughly the same size as CTB trays and are installed in STAR in the same manner. The feet of the tray latch on to rails glued to the TPC outer field cage. An insertion fixture will be provided for safe installation of the TOF trays.

The aluminum trays will be fabricated by the same vendor that built the CTB trays. The MRPC modules will be installed in trays at the University of Texas, Austin (UT). The read-out electronics are then mounted on the tray. Quality assurance procedures and tests will be established at UT to insure that all tray assemblies are ready for successful operation in STAR when they are delivered to BNL.

The **gas system** provides a mixture of 18 parts r134a to 1 part isobutane to the detector trays. The isobutane content is analyzed and monitored to insure an accurate mixture. The isobutane content is also monitored to insure that a flammable gas mixture is not introduced into the detector and to insure the safe operation of the STAR detector. The oxygen content is monitored and maintained at less than 30 ppm. The water content is monitored and maintained at less than 10 ppm. The design and installation of the TOF gas system will be under the supervision of L. Kotchenda (MEPHI) who designed and maintains the STAR TPC gas system.



The **high-voltage system** delivers +7000V and -7000V to each tray. Each pair of high-voltage channels will serve 10 trays. The high-voltage system will be procured and fabricated at UCLA.

The **start detector** is a separate subsystem, not based on MRPC technology but similar to the existing pVPD detector in STAR. The system will consist of two detector assemblies on each side of STAR positioned very close to the beam pipe at a distance of ~5.5 meters from the center of STAR. Each detector assembly consists of a 1 X 0-thick layer of Pb, a plastic scintillator or quartz radiator, and a mesh dynode PMT. The front-end and digitization electronics are the same as that used on the stop side. These detectors will provide the start time that the MRPC (stop) system needs to do particle identification, and can provide information for a low-level (Level 0) trigger on the primary vertex location as well. The start detector will be built at Rice University.

The BNL STAR operations group will design and install appropriate **infrastructure** for the TOF system. The principal requirements are racks and cooling for the low voltage power supplies, a chilled-water delivery system to cool the TOF tray electronics, and a support structure to support the TPC during insertion of the TOF trays behind the TPC support arms.

### 3.3 ELECTRONICS

The TOF electronics system records the time of signals in the start detector and the MRPC “stop” detectors and delivers the information to the STAR DAQ system. It also interfaces with the STAR trigger system and provides multiplicity information to the Level 0 trigger, similar to the information now provided by the CTB. Prototype versions of all electronics except THUB will have been successfully operated in STAR during the R&D phase of this project, prior to the construction phase.

The following electronics cards will be produced:

TAMP. The TAMP card is the interface between the MRPC tray and the TDIG card. It amplifies the MRPC signals. Each TAMP card handles 4, 6-channel MRPC modules. There are 960 TAMP cards.

TPMT. The TPMT interfaces the start detector PMTs to the TDIG card. Each TPMT handles 24 PMT signals, provides input over-voltage protection, and splits the signals for fast z-vertex measurements. There are 4 TPMT cards.

TDIG. The TDIG card discriminates the input signals and records the signal times using HPTDC chips. Each TDIG handle 24 signal channels. There are 964 TDIG cards.

TCPU. The TCPU card concentrates the data from 8 TDIG cards and sends it to THUB. It distributes the experimental clock and the 40 MHz clock to the TDIG cards. It also sends multiplicity information to the Level 0 trigger. There are 122 TCPU cards.

THUB. The THUB card interfaces 30 or 31 TCPU cards to STAR trigger, DAQ, and the

experimental clock. It creates a low-jitter 40 MHz clock for the HPTDC chip sampling and distributes it to the TCPU card on the tray. There are 4 THUB cards, each in a chassis mounted on the magnet steel.

TMIT. TMIT is a Gigalink transmitter daughter card that resides in the THUB chassis. It transmits data from 30 trays over fiber to TOF DAQ. There are 4 TMIT cards.

TOF DAQ receiver is a linux pc with a PCI-X based optical interfaces and a Myrinet interface. There are 1 TOF DAQ receiver with 4 optical interfaces.

An overall schematic drawing showing the logical relationships of the TOF electronics and the interfaces to STAR is shown in Figure 1. Figures 33 and 34 in the proposal are partially superseded by this figure

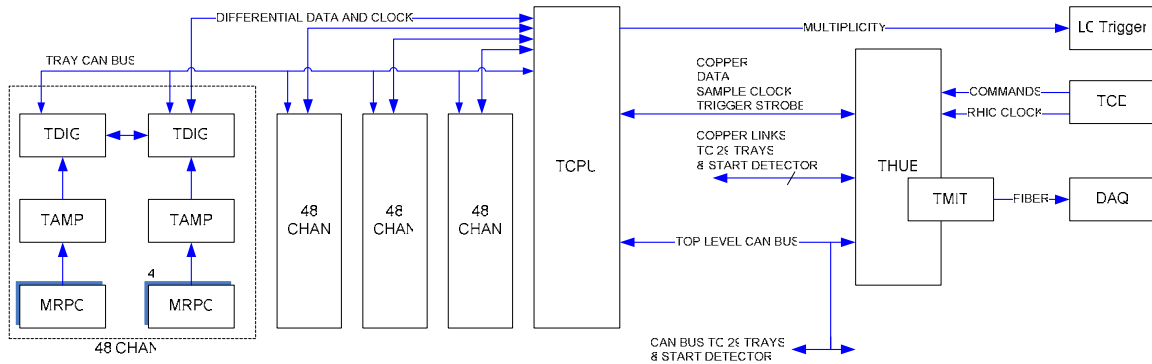


Figure 1. A schematic drawing of the TOF electronics.

The following 5 deliverables are involved in implementing the electronics subsystem:

- electronics board purchase and board testing,
- electronics integration and system testing: engineering redesign, firmware debugging and modification,
- electronics installation and commissioning,
- electronics configuration and calibration software and control software, and
- low-voltage systems.

The electronics board purchase and testing will be managed at Rice University. The low voltage system will be designed, procured, and fabricated UCLA.

The TAMP, TDIG, and TCPU cards are mounted on the detector trays as part of the assembly process at UT. The trays are then tested as complete detector units including the integral on-board read-out electronics. The trays are shipped to BNL as complete detector units including the electronics. The **installation and commissioning** at BNL will include the mechanical installation of the tray on the TPC rail and connection to the HV, gas, and cooling system. The electronics installation includes the connection to trigger, THUB,

and low voltage, and the connection from THUB to trigger and DAQ. The commissioning of the detector consists primarily of integrating the detector electronics into the STAR trigger and DAQ systems.

### 3.4 DELIVERABLES

The STAR TOF project will be complete when all deliverables have been received, tested, assembled, and installed into the STAR detector and commissioned. Table 1 shows the component deliverables for the STAR TOF project.

Table 1. Component Deliverables of TOF

Item	Number	Spares
<b>Mechanical Systems</b>		
TPC support structure	1	
Gas system	1	
Tray installation fixture	1	
<b>Detector Trays</b>		
32 modules/tray, 6 channels/module	120	6
<b>Electronics</b>		
TAMP 24-channel	960	10%
TDIG 24 channel	964	10%
TPMT	4	2
TCPU	122	10%
THUB	4	2
TMIT	8	2
TOF DAQ receiver	4	1
Low voltage supplies	121	6
High voltage supplies, 4 channel	6	2
Configuration software	1	
Electronics calibration software	1	
<b>Start Detector</b>		
Detector assemblies	2	Spare parts

### 3.5 ALTERNATIVE TECHNOLOGY

Low momentum hadronic particles are now identified by energy loss in the TPC. The most practical method of particle identification for the hadronic particles not now identified by the STAR detector is time-of-flight. RICH detectors can identify high momentum particles but there is a momentum gap in the particle identification between

RICH detectors and the TPC. The known alternative to MRPC technology for TOF is scintillator-PMT. It is not possible shield PMTs from the large magnetic field in STAR where the time-of-flight detector must be located. Therefore, it is necessary to use mesh-dynode PMTs. We have in fact built and operated a small TOF detector in STAR for the past three years using mesh-dynode PMTs and scintillator and the performance has been excellent. However, the mesh-dynode PMTs cost \$1.5k each so a large-area system is not affordable.

## **4 MANAGEMENT ORGANIZATION**

### **4.1 GENERAL**

This document provides the proposed management organization and delineates responsibilities within the project. Figure 2 shows the proposed management structure for the STAR TOF construction project.

Appendix 1 details the management structure of the China STAR TOF Project.

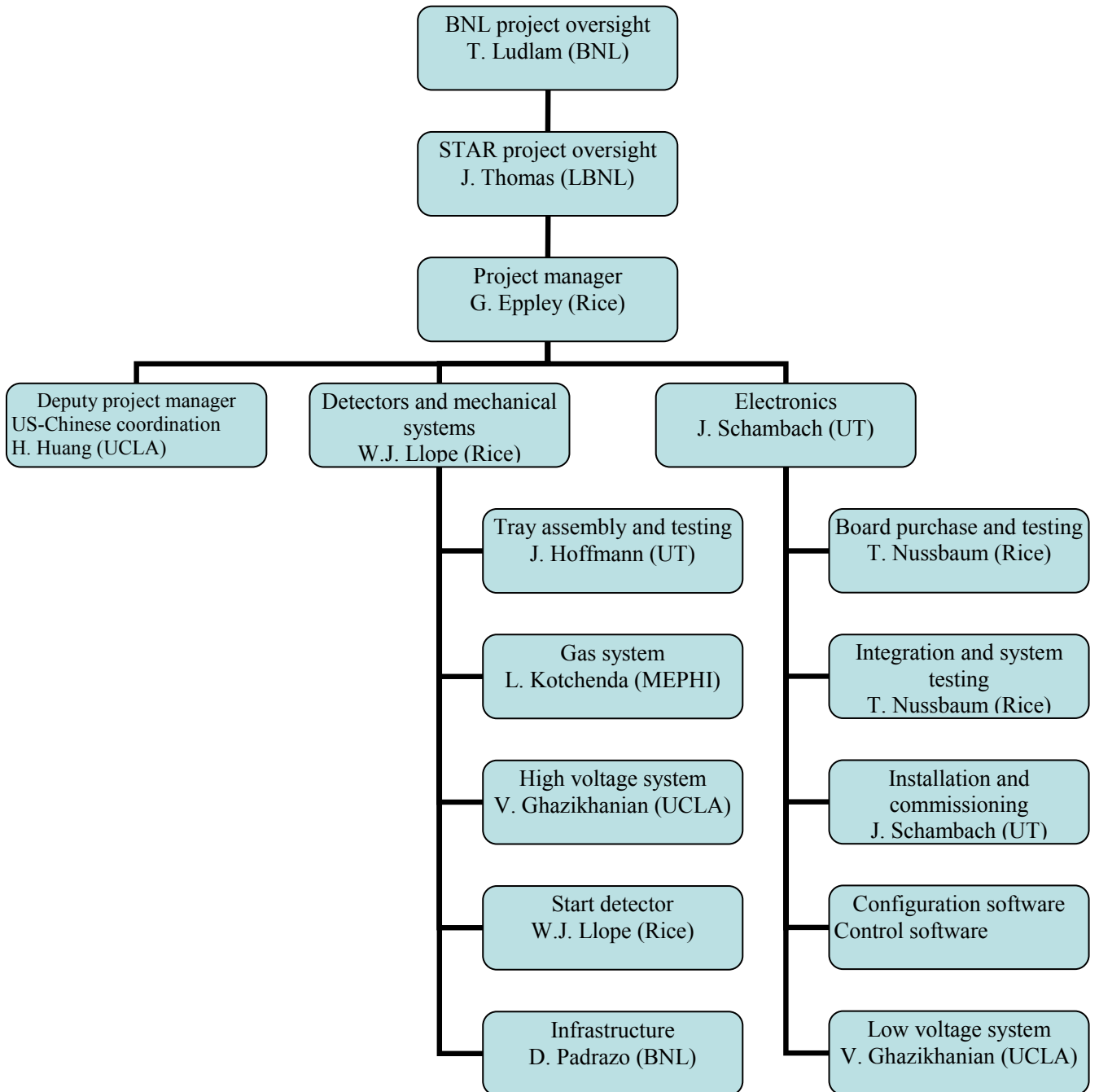


Figure 2. Management chart for the STAR TOF construction project.

## **4.2 PROJECT MANAGEMENT RESPONSIBILITIES**

### **4.2.1 BNL project oversight**

The BNL project oversight manager is T. Ludlam, BNL.

#### **Responsibilities**

The BNL project oversight manager will be administratively and fiscally responsible for the project. In particular he will:

- Provide overall management oversight for all aspects of the project.
- Approve key personnel appointments made by the project manager.
- Approve major subcontracts recommended by the project manager.
- Ensure that the project has demonstrated that it meets the functional requirements.
- Review quarterly status reports.
- Schedule and organize external reviews of the project.
- Ensure the work is performed safely and in compliance with the ISM rules.

The BNL project oversight manager will keep the BNL Detector Advisory Committee (DAC) informed about the technical goals and progress of the project and consult with the DAC to insure that the project continues to serve the long-term interests of the laboratory's research program through the related upgrades of the detectors and the RHIC collider.

### **4.2.2 STAR project oversight**

The STAR project oversight manager is J. Thomas, LBNL.

#### **Responsibilities**

The STAR project oversight manager will be administratively responsible for the project for the STAR collaboration. In particular he will:

- Provide overall management oversight for all aspects of the project for STAR.
- Approve key personnel appointments made by the project manager.
- Ensure that the project has demonstrated that it meets the functional requirements.
- Ensure that the project integrates properly into the STAR detector and with existing subsystems.
- Review quarterly status reports.
- Keep the STAR spokesperson and Advisory Board informed on the progress of the project.
- Schedule and organize STAR-internal reviews of the project.
- Ensure the work is performed safely and in compliance with the ISM rules.

The STAR project oversight manager will convene a safety review panel to insure that the project operates in a safe manner, that all official safety requirements are met, that the project does not harm the environment, and that all official environmental requirements are met.

### **4.2.3 Project manager**

The project manager is G. Eppley, Rice University.

#### **Responsibilities**

The project manager reports to the STAR upgrades manager, J. Thomas. The project manager will have the following responsibilities:

- Responsible and accountable for the successful execution of the project
- Implements performance measurement system
- Delivers project deliverables
- Identifies and ensures timely resolution of critical issues
- Allocates the contingency funds following approved procedures
- Acts as the spokesperson for the project
- Appoints subsystem managers with the approval of STAR management
- Submits quarterly status reports
- Ensures the work is performed safely and provides necessary ES&H documentation.
- Develops functional requirements with the subsystem managers
- Responsible with the subsystem managers for the technical direction of the project
- Controlling changes in the system design requirements, including interfaces between subsystems
- Responsible with the subsystem managers for providing documentation and presentations for project reviews
- Responsible with the subsystem managers for developing and maintaining project documentation meeting STAR documentation standards.

The project manager will convene a quality assurance review panel to assure that the project meets the performance and budget goals.

### **4.2.4 Subsystem managers**

Subsystem managers are responsible for each of the three major groups of subsystems: MRPC Modules, Detectors and Mechanical Systems, and Electronics. The subsystem managers are:

- H. Huang, UCLA, MRPC detector module production and liaison to the China STAR TOF project,

- W.J. Llope, Rice, Detectors and Mechanical Systems, and
- J. Schambach, UT, Electronics.

The subsystem managers report directly to the project manager and will be responsible for the design, construction, installation, and testing of their subsystem, in accordance with the performance requirements, schedule, and budget.

### **Responsibilities**

- Collaborate with the project manager to assemble the staff and resources needed to complete the subsystem
- Develop and follow the system design requirements
- Ensure that subsystems meet the system design requirements, including interfaces
- Responsible for carrying out the design, construction and assembly of the subsystem in accordance with the scope, schedule and budget
- Provide regular reports on the status of the subsystem to the project manager
- Ensure the work is performed safely and provide necessary ES&H documentation
- Responsible with the project manager for providing documentation and presentations for project reviews
- Develop and maintain project documentation.

## **5 SCHEDULE AND BUDGET**

The STAR TOF project has been organized into a work breakdown structure (WBS) for purposes of planning, managing and reporting project activities. Work elements are defined to be consistent with discrete increments of project work.

### **5.1 SCHEDULE**

Figure 3 is a Gantt chart of the project schedule, consistent with the WBS. The WBS dictionary is available in Appendix 2. The project begins in mid-FY05 and ends in early FY08. The MRPC module construction bar line, line 4, is displayed in gray rather than blue to indicate that the MRPC module construction project is a Chinese project not funded by the US construction project.

The MRPC modules are shipped to UT and assembled into trays with the onboard electronics. The completed trays are tested as complete detector units with the integral electronics before they are shipped to BNL. More than 90% of the cost of the electronics components is for components included on the trays.

A milestone that states for example, 20% of 120 trays complete, requires that the requisite modules were produced and tested in China and received at UT. It also requires that the requisite on-board electronics have been manufactured and the individual boards tested. Then the detector trays are assembled with modules and electronics and tested for ~3 weeks with cosmic rays.





### 1.1.1 Control Milestones

Table 2 shows the project management and control milestones, WBS level 1 and 2.

Table 2. Project Milestones

<b>WBS</b>	<b>Milestone Description</b>	<b>Completion Date</b>
1	Project funding approved	<b>FY05 Q1</b>
1.1	Order HPTDC chips	<b>FY05 Q1</b>
1.2	Project accounts open	<b>FY05 Q2</b>
2.1	Module production begins	<b>FY05 Q2</b>
4.1	TAMP, TDIG R&D complete	<b>FY05 Q3</b>
3.6	Tray assembly begins	<b>FY05 Q3</b>
4.2	TCPU, THUB, TMIT, TOF DAQ R&D complete	<b>FY05 Q4</b>
5.1	4-tray system installed	<b>FY05 Q4</b>
2.2	20% of 3840 modules completed and shipped	<b>FY06 Q1</b>
5.2	4-tray system commissioned	<b>FY06 Q2</b>
3.7	20% of 120 trays complete	<b>FY06 Q2</b>
2.3	40% of 3840 modules completed and shipped	<b>FY06 Q3</b>
3.8	40% of 120 trays complete	<b>FY06 Q4</b>
3.9	START detector complete	<b>FY06 Q4</b>
5.3	48-tray system installed	<b>FY06 Q4</b>
2.4	65% of 3840 modules completed and shipped	<b>FY07 Q1</b>
3.10	65% of 120 trays complete	<b>FY07 Q2</b>
5.4	48-tray system commissioned	<b>FY07 Q2</b>
2.5	3840 modules completed and shipped	<b>FY07 Q3</b>
3.11	120 trays complete	<b>FY07 Q4</b>
5.5	120-tray system installed	<b>FY07 Q4</b>
5.6	120-tray system commissioned	<b>FY08 Q2</b>
6	Project complete	<b>FY08 Q2</b>

## 1.2 BUDGET

Figure 4 shows the breakdown cost summary for the TOF project in FY04 dollars. A funding profile by year is also provided. All estimates have been inflated using escalation rates of 2% per year for material and 4% for labor, compounded.

	WBS 3/2	Contin.	Sum	FY05	FY05	FY06	FY06	FY07	FY07	FY08
<b>Detectors and Mechanical Systems</b>	Materials			Materials	Labor	Materials	Labor	Materials	Labor	Labor
<b>Tray</b>										
3.1.1	Tray aluminum structure	44100	8820	52920	52920					
3.1.2	Materials and supplies	33900	5520	39420	19710	19710				
3.1.3	Inner sides	6300	630	6930	3465	3465				
3.1.5	Gas distribution in tray	6500	650	7150	3575	3575				
3.1.6	HV distribution	23600	2360	25960	12980	12980				
3.1.10	Low voltage distribution	12600	1260	13860	6930	6930				
3.1.11	Cooling system	25000	7500	32500	16250	16250				
3.1.13	Shipping	12500	2500	15000	3000	6000		6000		
3.1	Tray	164500	29240	193740	118830	68910		6000		
3.1	Tray labor	206500	61950	268450			62638	107380		98432
<b>Gas system</b>										
3.2	Gas system	32000	6400	38400		38400				
<b>High voltage system</b>										
3.3.1	High voltage supplies	32020	3202	35222		35222				
3.3.2	Breakout boxes	13740	2748	16488	3000	13488				
3.3.3	High voltage cables	28680	2868	31548	4000	27548				
3.3.4	Shipping	1000	200	1200	200	1000				
3.3	High voltage system	75440	9018							
<b>Start detector</b>										
3.4.1	Subassembly	113700	13970	127670	19870	107800				
3.4.2	Mechanical structure	1100	220	1320	1320					
3.4.3	Electronics	20000	2400	22400	22400					
3.4	Start detector	134800	16590	151390	43590	107800				
<b>Infrastructure</b>										
3.5.2	Tray chilled water	56600	11320	67920	10000	57920				
3.5.3	LV infrastructure	69200	13840	83040		83040				
3.5.4	Tray installation fixture	15000	3000	18000	18000					
3.5.5	TPC support	35000	7000	42000				42000		
3.5	Infrastructure	175800	35160	210960	28000	140960		42000		
3.5	Infrastructure Labor	63800	19140	82940			36140		46800	
				77258						
3	Detectors and mechanical	582540	61248	678948	197620	433328		48000		
3	Det. and mech. labor	270300	81090	351390			62638	143520		145232
<b>Electronics</b>										
<b>Electronic board purchase and testing</b>										
4.3.1	TAMP	423360	127008	550368	203213	203213		143942		
4.3.2	TPMT	21550	6465	28015	28015					
4.3.3	TDIG	948640	284592	1233232	648883	326323		258026		
4.3.4	TCPU	188340	56502	244842	90403	90403		64036		
4.3.5	THUB	46200	13860	60060	20000	40060				
4.3.7	DAQ receiver	22960	6888	29848	29848					
4.3.9	Connection to trigger	49000	14700	63700	10000	53700				
4.3	Board purchase and testing	1700050	510015	2210065	1030362	713699		466004		
4.3	Labor	240500	72150	312650			57850	131300		123500
<b>System testing and integration</b>										
4.4	Labor	209250	62775	272025			42560	124610		104855
<b>Electronics installation and commissioning</b>										
4.5	Labor	204000	61200	265200			32825	73450		69550 89375
<b>Low voltage system</b>										
4.7.1	LV power supplies	231120	69336	300456	30000	270456				
4.7.2	LV power cables	26800	8040	34840	10000	24840				
4.7.3	Interlock and control	21000	6300	27300	5000	22300				
4.7	Low voltage system	278920	83676	362596	45000	317596				
4.7	Labor	13900	4170	18070			8070	10000		
4	Electronics mat.	1978970	593691	2572661	1075362	1031295		466004		
4	Electronics labor	667650	200295	867945		141305	339360		297905	89375
<b>Project Total Mat.</b>										
<b>Project Total Lab.</b>										
<b>Project Total</b>										
Inflated costs by year										
					1298442	212101	1523794	522283	545465	498469 104556
FY05 FY06 FY07 FY08										
<b>Project Total Labor and Materials by year, inflated</b>										
<b>Project Total Labor and Materials, inflated</b>										

Figure 4. The cost summary for the STAR TOF construction project and the cost profile by year. Inflated costs by year are shown in total. Amounts are in dollars.

### 1.2.1 Contingency

The project manager manages the contingency funds according to the approved procedures. Contingency is allocated under the change control procedures described in the next section.

Contingency is assigned based on the risk factors described in Table 3. The average contingency for materials is 25% and the contingency for labor is 30%. All of the labor has been assigned a contingency of 30% since the labor involves tasks with which we have no direct experience on a large-scale basis, although extensive prototyping has been done during the R&D phase of the project.

Table 3. Contingency Percentages

<b>Technical Risk Description</b>	<b>Cost Risk Description</b>	<b>Contingency Rate</b>
Direct copy of an existing, working design	Off the shelf hardware or purchased from a catalog	10%
Based on an existing design but requiring extensive modifications	Based on a vendor quote using limited conceptual design sketches	20%
New design different from established designs or existing technology	Estimate for item with little in-house experience	30%

## 2 CHANGE CONTROL

All changes to the technical, cost and schedule baselines shall be identified, controlled, and managed through a traceable, documented change control process, which will have been approved.

Changes to the technical, cost and schedule baselines will be controlled using the thresholds described in Table 4.

All changes that include or exceed Level 3 approval thresholds should first be submitted to the project manager using a Baseline Change Proposal (BCP). For changes exceeding Level 3, project manager will endorse the request (i.e., recommend approval) to higher authority or reject the request. If endorsed, the project manager will then transmit the BCP to higher authority with recommendations. All Level 3 BCPs will be reviewed and

approved by the project manager and a change control panel set up by the STAR project oversight manager.

If the change is approved, the copy of the approved BCP, together with any qualifications or further analysis or documentation generated in considering the request is returned to the requestor, and copies are sent to the official at the next higher control level. If approval is denied, a copy of the BCP, together with the reasons for denial, is returned to the requestor, and a copy is filed. The official at the next higher control level may review the granted change to ensure proper application of the procedure and consistency of the change with the goals and boundary conditions of the project.

Table 4. Summary of Baseline Change Control Thresholds

<b>Level</b>	<b>Cost</b>	<b>Schedule</b>	<b>Technical Scope</b>
Level 1 manager, DOE	Any increase in the total project cost or a cumulative allocation of more than \$500k in contingency	> 3-month delay in a Level 1 milestone date	Any deviation from technical deliverables that could affect performance specifications
Level 2 manager, DOE	A cumulative increase of more than \$250k in WBS Level 2 or cumulative allocation of more than \$250k contingency	> 1-month delay of a Level 1 milestone date or > 3-month delay of a Level 2 milestone date	Any deviation from technical deliverables that does not affect expected performance specifications
Project Manager (Level 3)	Any increase of >\$50k in the WBS Level 2 or cumulative allocation of 20% of any Level 3 contingency	> 1-month delay of a Level 3 milestone date	Technical design changes that do not impact technical deliverables

### 3 RISK

A formalized plan to identify and manage risk will be developed during the early stages of the project using the guidelines set forth in Chapter 14 of DOE Publication M 413.3-1, Project Management for the Acquisition of Capital Assets.

Risk management is an ongoing task that is accomplished using a formalized plan to identify, analyze, mitigate and monitor the risks that arise during the course of completing the project. Risk is a measure of the potential of failing to achieve overall project objectives within the defined scope, cost, schedule and technical constraints. The

purpose of this analysis is not solely to avoid risks, but to understand the risks associated with a project and devise methodologies and strategies for managing them.

The final responsibility for risk management will rest with the project manager. However, effective risk management is a multi-step process that requires continued involvement of all project members.

The risks associated with the electronics and the mechanical structure are estimated to be low due to successful R&D and the installation and successful use of prototype detectors in the STAR detector, prior to the start of construction.

The largest known source of risk to the project at the moment during the current R&D phase is the availability and successful performance of the CERN HPTDC chip. If the chip fails to perform adequately in high-resolution mode in longer term tests or in long-term equivalent testing, or if CERN is not able to produce the chips in sufficient quantity to sell chips to STAR, there would not be sufficient time between now and the scheduled start of the project to develop an alternative solution. We have acquired an alternative TDC chip (discussed in section 4.6.2 of the proposal) but the R&D required to test this chip and integrate it into the electronics would delay the start of the construction project for a year.

The second source of R&D related risk is the electronic board design and testing. If prototype electronics boards have not been tested successfully by the milestones set out in the project schedule, the project could be delayed and an additional budget and schedule for electronics R&D might need to be added to the project. Periodic evaluations of the R&D status and a review, immediately prior to the start of the construction project will minimize this risk.

A source of risk during the project will be due to the construction and testing of MRPC modules in China. This will be a Chinese contribution to STAR and not under the control of the US project. The US project management will closely monitor progress and QA in China and include the status of the Chinese construction project in reports and reviews to minimize this risk. The US project management will also make frequent visits to China to facilitate the integration of the Chinese effort into the US project.

## **4 ASSESSMENTS**

### **4.1 ENVIRONMENT, SAFETY AND HEALTH**

#### **4.1.1 Integrated Safety Management Plan**

Environment, safety and health (ES&H) will be integrated into all phases of planning and implementation through to the final design and production processes of the project.

## 1.1 QUALITY ASSURANCE

“Quality” is defined as the “fitness of an item or design for its intended use” and Quality Assurance (QA) as “the set of actions taken to avoid known hazards to quality and to detect and correct poor results.” The project manager will convene a quality assurance review panel to assure that performance and budget goals are met.

## 2 PROJECT CONTROLS AND REPORTING SYSTEMS

Technical performance will be monitored throughout the project to insure conformance to approved functional requirements. Design reviews and performance testing of the completed systems will be used to ensure that the equipment meets the functional requirements.

For each main system of the TOF project: MRPCs, trays and mechanical systems, electronics, there will be the following reviews:

- design review including detailed concept for the system, detailed cost and schedule
- pre-production review, all details settled. A small number of units will be produced and tested, and the performance reported.
- final design review, final cost and schedule, production QA and testing procedures,
- STAR and BNL safety reviews,
- STAR operations readiness review.

## 3 INSTITUTIONAL PARTICIPATION

Several institutions will participate in the TOF project. The institutions and their anticipated project responsibilities are listed in Table 5.

Table 5. Institutional Participation

<b>Institution</b>	<b>Project Responsibility</b>
Brookhaven National Laboratory	Detector infrastructure
China STAR TOF Collaboration	MRPC module production and test
Rice University	Electronics board production and test Start detector Project management
UCLA	Low voltage system High voltage system
University of Texas	Tray assembly and test

## **APPENDIX 1: CHINA TOF PROJECT MANAGEMENT RESPONSIBILITIES**

### **Project Manager**

The Chinese project manager is Yugang Ma from Shanghai Institute of Applied Physics (SINAP), Chinese Academy of Sciences

### **Responsibilities**

The Chinese Project Manager reports to the STAR TOF project manager and Advisory Board of the Chinese STAR TOF Collaboration. The Chinese Project Manager will have the following responsibilities:

- Responsible and accountable for the successful execution of the Chinese STAR project
- Delivers Chinese project deliverables
- Identifies and ensures timely resolution of critical issues in China
- Allocates the contingency funds following approved procedures
- Appoints Subsystem Managers
- Acts as the spokesperson for the Chinese STAR TOF Collaboration and maintain effective communication with the STAR management and the rest of the STAR collaboration
- Submits quarterly status reports
- Ensures the work is performed safely and provides necessary ES&H documentation.
- Develops functional requirements with the subsystem managers
- Responsible with the subsystem managers for the technical direction of the project
- Controlling changes in the system design requirements, including interfaces between subsystems
- Responsible with the subsystem managers for developing and maintaining project documentation.

### **Subsystem Managers**

Subsystem managers are responsible for each of the three major tasks of the Chinese STAR project: MRPC module production, quality assurance and control, and Chinese STAR physics analysis. The subsystem managers are:

- Jianping Cheng, Tsinghua, MRPC module production  
Yuanjing Li, Tsinghua, 70% of MRPC module production at Tsinghua facility  
Cheng Li, USTC, 30% of MRPC module production at USTC facility
- Xiaolian Wang, USTC, Quality control and assurance for MRPC production  
Yi Wang, Tsinghua, Quality control and assurance for MRPC production at Tsinghua  
Xiaolian Wang, USTC, Quality control and assurance for MRPC production at USTC  
Ming Shao, USTC, TOF off line software

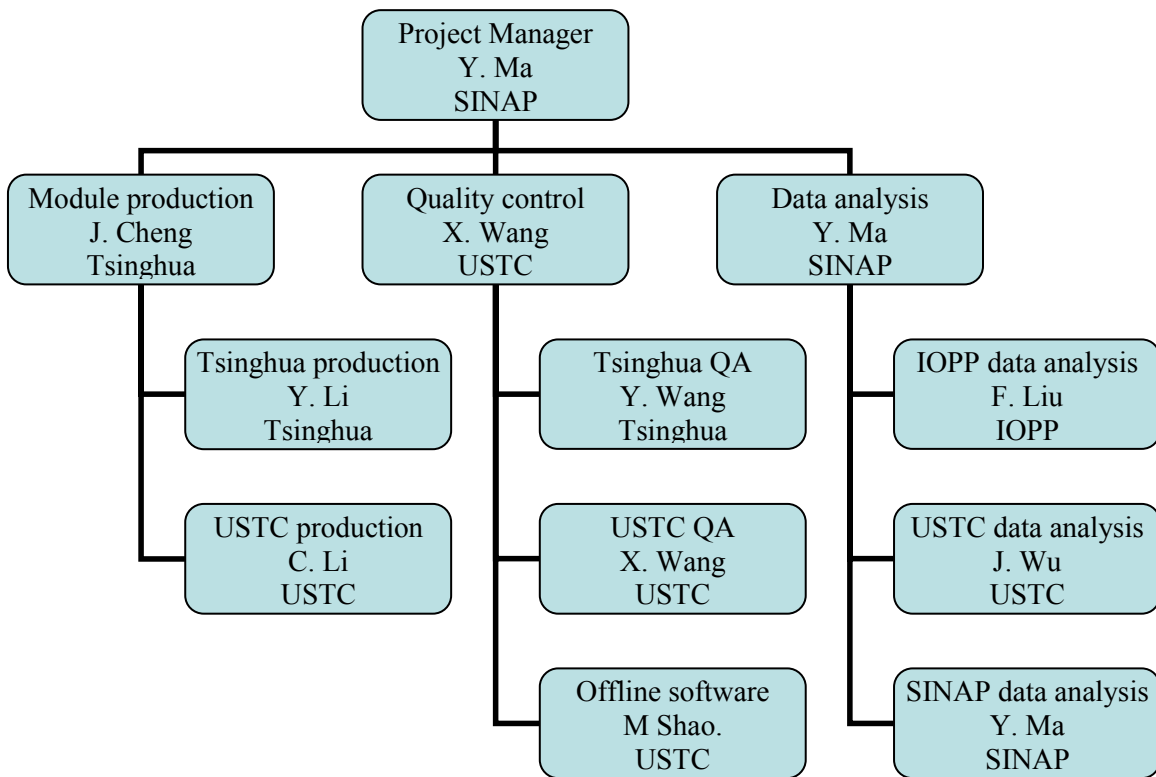


- Yugang Ma, SINAP, RHIC Physics analysis in China  
Feng Liu, IOPP, CCNU  
Jian Wu, USTC group

The subsystem managers report directly to the Chinese Project Manager and will be responsible for the design, construction, installation, and testing of their subsystem, in accordance with the performance requirements, schedule, and budget.

**Responsibilities**

- Collaborate with the Project Manager to assemble the staff and resources needed to complete the subsystem
- Develop and follow the system design requirements
- Ensure that subsystems meet the system design requirements
- Responsible for carrying out the design and construction in accordance with the scope, schedule and budget, assuming funding and resources as described in the management plan
- Provide regular reports on the status of the subsystem to the Project Manager
- Ensure the work is performed safely and provide necessary ES&H documentation
- Develop and maintain project documentation



The proposed organization structure for the China STAR TOF construction project.

## **APPENDIX 2: WBS DICTIONARY**

1 Milestone: Project approved.

1.1 Milestone: Order HPTDC chips.

1.2 Milestone: Start project. Project accounts opened for STAR TOF project.

2 MRPC Modules: The 6-channel MRPC modules are produced in China, tested, and shipped to the U.S.

2.1 Milestone: Module production begins.

2.2 Milestone: 20% of 3840 modules complete.

2.3 Milestone: 40% of 3840 modules complete.

2.4 Milestone: 65% of 3840 modules complete.

2.5 Milestone: 3840 modules complete.

3 Detectors and Mechanical Systems. The principal systems are the tray, the gas delivery system, the high-voltage power system, and detector infrastructure.

3.1 Tray. The tray is the mechanical support for the MRPC modules and the electronics, and is also the gas box for the MRPCs. There are 120 trays in the system and six spares. Each tray is roughly the same size as a CTB tray and is installed in STAR in the same manner, via feet on the tray that latch onto rails glued to the TPC outer fieldcage.

3.1.1 Tray Aluminum Structure. This includes the tray body, the tray top, and the tray cover.

3.1.1.1 Tray body. This is 5 of the 6 sides of the detector enclosure. The feet, which hold the tray onto the TPC rails, are welded onto the tray body. Fabricated out of house.

3.1.1.2 Tray top. This is the sixth side of the detector enclosure. It attaches to the tray box in a shoebox design. The TAMP boards mount onto this top via embedded PEM studs. Fabricated out of house.

3.1.1.3 Tray cover. This is a top cover that encloses the electronics layer for mechanical protection and to suppress RFI. Fabricated out of house.

3.1.1.4 Tray parts preparation. This includes degreasing of fabricated tray body, tray top, and tray cover, and applying gas sealant over welded locations.

3.1.1.5 Tray parts test. The test insures all trays meet the specifications placed on their fabrication. In addition, the tray top is fit onto a tray body and the tray cover onto a body+top assembly to insure proper fit.

### 3.1.2 Materials.

3.1.2.1 Kapton tape. One layer per tray insures there are no conductive paths between the MRPC modules inside the tray and the tray itself.

3.1.2.2 Adhesive. This is used to spot-glue the tray Inner Sides to the tray body walls. Off-the-shelf: GE RTV174.

3.1.2.3 Freon-resistent sealant. Off-the-shelf: Dow-Corning 730.

3.1.2.4 HV wire for MRPCs. Off-the shelf: Rowe R790-1522.

3.1.2.5 Connectors for MPRCs. MTA-100 connectors.

3.1.2.6 Gas for module testing. Freon and isobutane.

3.1.3 Inner sides. There are 2, ¼ inch thick acrylic sheets, ~90 inch by ~3 inch into which reveals are machined. The two inner sides are mirror images and line the inside of the two long sides of the tray body. Each pair of reveals holds a single MRPC module in three dimensions at the correct position and angle with respect to the tray body.

3.1.3.1 Acrylic sheets. 8x4 sheets, off-the-shelf.

3.1.3.2 Fabrication. Cut to outer dimensions and machine out the MRPC reveals using a Hurco machine (UT-Austin).

3.1.4 Tray interior assembly. Includes inserting 32 MRPC modules into the 2 inner sides, and placing and gluing the loaded inner sides to the tray body section.

3.1.5 Gas distribution in-tray. This allows the input of the detector gas to the tray interior at the closed end and the output of this gas at the feed-through end. This is installed following tray interior assembly and before the closing of the tray gas box.

3.1.5.1 Gas feed-through. Standard 1/4 inch compression fittings to allow gas input and output. These fittings include strain-relief. Two per tray.

3.1.5.2 Gas tubing in-tray. Standard ¼ inch polyethylene tubing that connects inside the tray body to the gas input fitting, and brings the input gas to the far end of the tray.

3.1.5.3 Fabrication. This involves installing the gas fittings in the tray feed-through end, connecting the in-tray gas tubing to one of these fittings, and affixing the other end of this tubing to the far inside wall of the tray.

3.1.6 High voltage distribution in tray. This brings +HV and -HV from the tray feed-through end to each MRPC module. Installation follows tray interior assembly and precedes closing the tray gas box.

3.1.6.1 HV feed-through. One each for +HV and -HV. Off-the-shelf: Kings 1064 or Reynolds equivalent.

3.1.6.2 HV wiring in-tray. One buss each for +HV and -HV. Off-the-shelf: Rowe R790-1522.

3.1.6.3 HV insulation in-tray. Surrounds connections between HV wiring and the HV leads on each MRPC. Off-the-shelf: Rowe GL30R67WO. ~40 per tray.

3.1.6.4 Fabrication. The in-tray wiring is soldered to the HV feed-through and run down the length of the tray. The HV leads on each MRPC are soldered to this wiring and these junctions wrapped in the HV insulation tape.

3.1.6.5 HV buss testing. This is to insure the sanity of the HV distribution inside the tray. Voltmeters can be used to insure no shorts between the HV feed-throughs and the wiring to the tray body. Also, small amounts of voltage (~1kV) can be applied to the tray without MRPC gas inside to also insure the HV cabling is correct.

3.1.7 Tray Closing. Includes installing and sealing the tray top onto the tray bottom, and installing and sealing the TAMP boards onto the tray top.

3.1.8 Tray leak testing. The tray is pressurized by an equivalent of ~1/2 inch of water above atmospheric pressure. The pressure is monitored for 2 hours and the decay rate of this overpressure, if any, is the gas leak rate and must meet specification.

3.1.9 Tray interior final testing. This involves flowing gas through the tray overnight, then powering up the HV buss and measuring the total MRPC current draw.

3.1.10 Low voltage distribution on-tray. This includes installing the on-tray fusing, the lead-wire, and the connectors that bring +LV and -LV to the local electronics boards (TAMP, TDIG, TCPU).

3.1.10.1 Low voltage buss parts. The color-coded lead wire distributes the +LV and -LV to each pair TAMP+TDIG, and to TCPU, including fusing for over-current protection.

3.1.10.2 Low voltage buss fabrication and installation. Fabrication involves wire cutting and crimping/soldering. The electronics cards, low voltage buss, and signal connections are installed on the tray.

3.1.10.3 Low voltage buss testing. This involves continuity testing to insure the proper operation.

3.1.11 Cooling System. This allows heat removal from the TDIG electronics via a direct mechanical path to water flow.

3.1.11.1 Cooling system parts. Aluminum or copper tubing and hose fittings, off-the-shelf.

3.1.11.2 Cooling system fabrication and installation on-tray. This includes bending the tubing into the required shape, welding the hose fittings onto the two open ends, and installing the cooling assembly onto the tray top assembly.

3.1.11.3 Cooling system testing. The on-tray cooling loop is water-pressurized to at least three times the STAR water skid pressure (60psi). The water path must not leak at pressures of ~200psi.

3.1.12 Tray Final Testing. This involves flowing gas through the tray overnight, powering up the HV buss and re-measuring the total MRPC current draw. Then powering the LV buss, checking detector signals in oscilloscopes and measuring detector noise rates for each channel. Trays will also be tested with cosmic rays to insure the proper functioning of all detector channels.

3.1.13 Shipping. Transport completed trays from Austin to BNL.

3.2 Gas System. The gas system delivers a mixture of 95% r134a and 5% isobutane to the MRPC detectors. Appropriate safety and monitoring systems are included.

3.2.1 Gas system design.

3.2.1.1 Milestone. Gas system design complete.

3.2.2 Gas system components.

3.2.3 Gas system installation.

3.2.3.1 Milestone. Gas system complete.

3.3 High Voltage System. The high voltage system provides +/- 7 kV to the MRPC detectors. It consists of 2 SY127 mainframes each supplying +/- 7 KV to 6 HV breakout boxes (there are a total of 12 breakout boxes, six boxes for the west end and 6 boxes for the east end of the STAR located on the iron backlegs). Each breakout box in turn distributes the +/- HV to 10 trays. Each SY127 mainframes is instrumented with three positive, and three negative 4-channel HV modules. The HV shall be monitored and

controlled remotely using CAENnet interface installed in a control PC located in the STAR control room.

### 3.3.1 High voltage supplies.

3.3.1.1 SY127. Two SY127 High Voltage mainframes will provide the +/- HV for MWPCs. One SY127 will be used to supply up to 8 channels of +/-HV for 60 trays. The reason for using two mainframes is to provide redundancy. There will be two spare HV channels per each mainframe.

3.3.1.2 A631. Each SY127 shall be instrumented with two A631N and two A631P 4-channel high voltage modules. These modules could supply up to a maximum of +/-8 KV @ 100 uA per channel.

3.3.1.3 A1303. One CAENnet-PCI interface module CAEN part number A1303 shall be used to remotely communicate with two SY127 mainframes. There will be a second backup unit.

3.3.1.4 Miscellaneous hardware. Additional hardware panels required to install the HV supplies in the crates and seal the air flow paths as well as isolate the HV ground from the chassis ground. An enclosure is provided to restrict access to the SHV connectors on the back of the supplies.

3.3.2 Breakout boxes. The design and fabrication of 12 HV breakout boxes. These have the function of distributing +/-HV supplied by a pair of outputs from A631N and A631P modules installed on SY127 mainframes to 10 trays. The boxes also have additional function of implementing current limiting and providing filtering. The isolation of the HV and HV ground between different trays will be critical since they share a single HV channel and in case of short or high noise in a single tray the HV will be dropped in the isolation resistor and will not affect other trays sharing the same HV line.

### 3.3.3 High Voltage Cables.

3.3.3.1 A631 cables. There are a total of 12 pairs of HV cables distributing HV from the mainframes to the breakout boxes. Each cable shall have an SHV female connector at the HV power supply end, and a Kings 1065-1 HV male connector mating with the breakout box. Each cable is estimated to be 100' long.

3.3.3.2 Tray cables. There are a total of 120 pairs of HV cables distributing HV from the breakout boxes to the trays. Each cable shall have a Kings 1065-1 male connector at each end. These cables are estimated to be 20' long.

3.3.4 Shipping. Cost of shipping components from UCLA to BNL after production and testing at UCLA.

3.4 Start Detector. The start detector is a separate subsystem, not based on MRPC technology but similar to the existing pVPD detector in STAR. The system will consist of two detector assemblies on each side of STAR positioned very close to the beam pipe at a distance of ~5.5 meters from the center of STAR. Each detector subassembly element consists of a 1 X 0 -thick layer of Pb, a plastic scintillator or quartz radiator, and a mesh dynode PMT. The front-end and digitization electronics are the same as that used on the stop side. These detectors will provide the start time that the MRPC (stop) system needs to do particle identification, and provide information for a low-level (Level 0) trigger on the primary vertex location as well.

3.4.1 Subassembly. Each detector subassembly consists of a 1 X 0 -thick layer of Pb, a plastic scintillator or quartz radiator, and a mesh dynode PMT.

3.4.1.1 Pb converter. This is a ¼ inch thick layer of Lead (~1X 0), which converts incident high-momentum photons into electron-positron pairs.

3.4.1.2 Optical Element. This is a ~1cm-thick layer of BC420 plastic scintillator, or quartz, and immediately follows the Pb converter. It produces the optical signal to be read-out by the following PMT.

3.4.1.3 Mesh-dynode PMT. This is the optical transducer. The first prototype start detector (for run-5) will use Hamamatsu R-5946 PMTs off-the-shelf.

3.4.1.4 Linear HV base. This distributes the applied high voltage to the dynodes of the mesh-dynode PMTs and provides the anode connection for the signal read-out.

3.4.1.5 Enclosure/electrostatic shield. This is an aluminum tube, 2 inch diameter, ~10 inch long, which contains the Pb, scintillator, PMT, and PMT base in a sealed enclosure with electromagnetic shielding.

3.4.1.6 Detector assembly. This includes joining the converter and the radiator to the PMT, inserting the PMT into the PMT base, and inserting these into the aluminum tube enclosure.

3.4.1.7 Detector testing. Each detector subassembly is tested for dark current at a fixed voltage. Cosmic ray testing will be performed to confirm proper output signals and ADC distributions, and to set default HV values for each detector to match the pulse heights for mips across the different detectors.

3.4.2 Mechanical structure. This is an aluminum clam-shell structure that holds the detector assemblies in position around the beam pipe. This mechanical structure mounts to the I-beam that supports the beam pipe (as did the pVPD). This structure also supports the local electronics boards and provides strain-relief for the power and signal cables.

3.4.2.1 Parts. ~8 square feet aluminum 6061 sheet stock, ¼ inch thick, off-the-shelf.

3.4.2.2 Fabrication. Machining of the start detector structures in Bridgeport milling machines.

3.4.2.3 Start mechanical testing. Test assembly to insure components come together as expected. Test fitting into I-beam equivalent to test installation procedure and insure stability of the structure.

3.4.3 Electronics. This includes the HV supply and cabling needed to power the PMTs, the LV supply and cabling needed to power the local electronics (TPMT, TDIG, TCPU), and the ancillary cabling for the trigger and DAQ interfaces.

3.4.3.1 High Voltage System. Design is the same as for the STAR CTB, which uses a LeCroy 1440 mainframe and 8-channel 2.5kV cards. Space is allocated in the FPD/BBC 1440 mainframe for this system, and the cards can be obtained from HEEP. This item involves only the fabrication of the cabling with SHV connectors.

3.4.3.2 Low Voltage System. Design is the same as on the stop side, as the same electronics are being powered on both start and stop sides.

3.4.3.3 Electronics chassis. Support structure for TPMT, TDIG, TCPU cards.

3.4.3.4 Ancillary cabling. Cabling for trigger interface for east and west.

3.5 Infrastructure. The required infrastructure includes racks for low voltage supplies, chilled water for tray electronics and low-voltage power supply cooling, electric power for the low-voltage supplies, a tray installation fixture and a temporary TPC support fixture.

3.5.1 Mechanical design.

3.5.1.1 Design tray chilled water delivery system.

3.5.1.2 Design low voltage infrastructure. The design provides chilled water and electric power to the low voltage supply racks.

3.5.1.3 Design TPC support structure.

3.5.2 Tray chilled water. The chilled water system will deliver chilled water to each TOF tray. It includes tubing and flow-meters.

3.5.3 Low voltage infrastructure. The low voltage infrastructure consists of racks with STAR-standard water cooling and power interlocks for the low voltage power supplies.

3.5.3.1 Install low voltage utilities. Install electric power and chilled water.

3.5.3.2 Low voltage racks. The racks include circuit breakers and heat exchangers.



3.5.4 Tray installation fixture. The installation fixture is an aluminum structure that bolts to the magnet steel. It is used to install trays in pairs from the east (2 at same azimuth) onto the existing TPC rails.

3.5.5 TPC support structure. The TPC support structure supports the TPC while one of the support arms is removed to install TOF trays behind the flange.

3.6 Milestone. Tray assembly begins.

3.7 Milestone. 20% of 120 trays complete.

3.8 Milestone. 40% of 120 trays complete.

3.9 Milestone. Start detector complete

3.10 Milestone. 65% of 120 trays complete.

3.11 Milestone. 120 trays complete.

4 Electronics. The electronics for the TOF system will digitize the stop times at the MRPC detectors with on-board circuit cards and deliver the information to the STAR DAQ system. Appropriate interfaces to the STAR trigger system are provided.

4.1 Milestone. TAMP, TDIG R&D complete.

4.2 Milestone. TCPU, THUB, TMIT, TOF DAQ R&D complete.

4.3 Electronic board purchase and testing.

4.3.1 TAMP. The TAMP card is the interface between the MRPC tray and the TDIG card. It amplifies the MRPC signals. Each TAMP card handles 4, 6-channel MRPC modules. There are 960 TAMP cards.

4.3.1.1 Amplifiers.

4.3.1.2 Other component parts.

4.3.1.3 PCB. Printed circuit boards.

4.3.1.4 Assembly.

4.3.1.5 Automated test.

4.3.1.6 Mechanical connection.

4.3.2 TPMT. The TPMT interfaces the start detector PMTs to the TDIG card. Each TPMT handles 24 PMT signals, provides input over-voltage protection, and splits the signals for fast z-vertex measurements. There are 4 TPMT cards.

4.3.2.1 Parts.

4.3.2.2 PCB.

4.3.2.3 Assembly.

4.3.2.4 Cables and mechanical connection.

4.3.3 TDIG. The TDIG card discriminates the input signal and records the signal time using the HPTDC chip. Each TDIG handle 24 signal channels. There are 964 TDIG cards.

4.3.3.1 Discriminator.

4.3.3.2 HPTDC.

4.3.3.3 PLD.

4.3.3.4 Micro-controller.

4.3.3.5 Other parts.

m4.3.3.6 PCB.

4.3.3.7 Assembly.

4.3.3.8 Automated test.

4.3.3.9 Cables and mechanical connection.

4.3.4 TCPU. The TCPU concentrates the data from 8 TDIG cards and sends it to THUB. It distributes the experimental clock and the 40 MHz clock to the TDIG cards. It also sends multiplicity information to the Level 0 trigger. There are 122 TCPU cards.

4.3.4.1 CPU.

4.3.4.2 PLD.

4.3.4.3 Other parts.

4.3.4.4 PCB.

#### 4.3.4.5 Assembly.

#### 4.3.4.6 Cables and mechanical connection.

4.3.5 THUB. The THUB card interfaces 30 or 31 TCPU cards to STAR trigger, DAQ, and the experimental clock. It creates a low-jitter 40MHz clock for the HPTDC sampling and distributes it to the TCPU card on the tray. There are 4 THUB cards, each in a chassis mounted on the magnet steel.

#### 4.3.5.1 CPU.

#### 4.3.5.2 PLD.

#### 4.3.5.3 Other parts.

#### 4.3.5.4 PCB.

#### 4.3.5.5 Assembly.

#### 4.3.5.6 Cables and mechanical connection, chassis.

4.3.6 TMIT. TMIT is an optical transceiver daughter card that resides in the THUB chassis. It transmits data from 30 trays over fiber to TOF DAQ. There are 4 TMIT cards.

#### 4.3.6.1 Optical transceiver. (commodity)

#### 4.3.6.2 Optical fiber.

4.3.7 DAQ receiver. DAQ receiver for TOF. There is 1 receiver.

#### 4.3.7.1 PC with PCIX interface.

4.3.7.2 PCIX receiver. Two, each with 2 dual optical transceivers (commodity).

#### 4.3.7.3 Mechanical connection.

#### 4.3.8 Board testing.

4.3.9 Connection to trigger. This is the cable connection for the Level 0 trigger multiplicity information and the related interface to the DSMi cards.

4.4 System testing and integration: Engineering redesign, firmware debugging and modification.

#### 4.5 Electronics installation and commissioning.

#### 4.6 Software. Configuration, calibration, and control.

4.7 Low Voltage System. The low voltage (LV) system supplies the 120 TOF trays and 2 start detector assemblies with low voltage DC power required for the operation of the on-board electronics. It also supplies the 4 THUB modules with the required DC power. In addition, this system includes the required power transmission cables, the interlock system, and the control and monitoring system.

4.7.1 LV power supplies. These are low noise, dual output, isolated, rack mounted DC power supplies located in the third floor of the STAR south electronics platform racks. These units are interlocked and remote controlled.

4.7.1.1 Tray and start detector LV supplies. 121 units.

4.7.1.2 THUB LV supplies. These units supply 4 THUB modules with approximately 4-5 amperes of DC current at about 8 volts. The electrical specifications for these units are the same as the 2.3.1.1 except only four (or two if noise is not a problem) such units will be needed for the entire system. The additional 2U space per rack is more than enough to accommodate these units. The cooling for these supplies will be through small fans installed in the 2U interface/interlock modules. The power supply for is Digi Key P/N MBB512-A-ND.

4.7.2 LV power cables. These are the DC power transmission cables to transmit DC LV power from power supplies at the racks to the trays, start detector assemblies, and THUB chassis.

4.7.2.1 Tray LV power cables. These consist of 122 multi-conductor cables at 100 feet length each.

4.7.2.2 THUB LV power cables. These supply +8 volt DC power to THUBs. There are 4 of these cables at 80' long.

4.7.3 Interlock and Remote Control/Monitoring (IRCM) Systems. Function of this unit is to supply RS485 communication between control PC and the power supply units, monitor the rack temperature, and apply interlock to the power supplies. Each rack will be equipped with one 2U module which will contain this functionality. In addition four of the 24 units will contain additional power supplies to power up the THUBs. The RS232 server on the south platform may be used to provide communication between STAR control room and the IRCMs. However, for the purpose of this document we assume a dedicated full duplex fiber optic serial link between the STAR control room and the south platform.

### 5 System installation and commissioning.

5.1 Milestone. 4-tray system installed.

5.2 Milestone. 4-tray system commissioned.

5.3 Milestone. 48-tray system installed.

5.4 Milestone. 48-tray system commissioned.

5.5 Milestone. 120-tray system installed.

5.6 Milestone. 120-tray system commissioned.

6 Milestone. Project complete.

# **Proposal for a Large-Area Time-of-Flight System for STAR**

## **Appendix D**

### **Response to the BNL Detector Advisory Committee**

**January 29, 2004**

The BNL Detector Advisory Committee (DAC) met on November 22, 2003 to review the STAR TOF project among other BNL projects. The following is our response to questions raised in the DAC report.

We reproduce below the section of the 2003 DAC report (in italics) on the STAR TOF proposal with the response from STAR.

*The development of a detailed proposal for a TOF in STAR, based on the MRPC technology, is the result of a world-wide concentrated R&D effort over the past few years. The STAR TOF group has contributed to this effort very significantly as it provided a testbed for evaluation of the detector performance under real "battle conditions", i.e. within the real RHIC background environment. Overall the STAR results are very impressive. The detector prototype has even been used for physics results. On the other hand, the committee perceived some issues to be considered by the collaboration. We list them in the following:*

*1. It is very important to analyze any problem which occurs at this very early stage. In particular, we highly recommend analyzing in every detail why 6 out of 28 modules seem to operate differently. To do this analysis, the TOF detector should be removed from STAR, take all faulty modules carefully apart, and determine that the reason for the deviation is either trivial or significant. An example of a trivial reason could be dust on the electrode surfaces, an improperly assembled unit, a wrong gap due to glass imperfections or the nylon line diameter variation, etc. An example of a significant reason for the malfunction could be: corroded glass surfaces, or development of photosensitive surface film deposits on the cathode surfaces. At first glance, it seems indeed unlikely that glass corrosion or surface chemistry can occur, given the fact that the average charge deposits are less than 2pC per track in this detector (as opposed to 1000pC in BaBar or Belle). Furthermore, one needs to stress that the Belle glass RPCs do work at this point. However, if there is an onset of multiple streamers in 6 out of 28 of the TOF detectors in STAR, the accumulated charge could be higher than 2pC/track. There was a group within the Belle collaboration, which reported buildup of a film on the cathode surface in the test chambers, which was responsible for the breakdown. For more on the film theory see: H. Sakai et al., Nucl. Instr. & Meth., A484(2002)153. In their case, the gas contained about 1000ppm of water. The paper proposes a theory that this film has a lower work function, and this causes the spontaneous emission of electrons from the cathode (for the anode such effect does not occur). This film could be easily removed by wiping it with a tissue and ammonia.*

Six modules were seen to have excess streamers in some channels in tests conducted immediately after construction. Two of these had simple mechanical defects - a small amount of solder on a glass plate and a scratched glass plate. While manufacturing defects can be addressed with tighter quality control during the module assembly process, we are allowing for a failure rate of 30% in the construction budget and schedule. This is to insure that the modules installed in STAR pass very high performance standards and will provide excellent timing resolution in all channels. The other four modules showed no apparent mechanical defects. These modules were not significantly noisier than others and were installed in TOFr for run 3 but were not read out. We would like to observe the long-term performance of these modules before performing an autopsy. Some of these modules are being read out for run 4 and we will again be able to evaluate whether the ADC distributions

continue to show excess streamers, as well as measure noise rates and timing resolution. Since the excess streamers were present in these modules at initial turn on, it is not likely to be the result of corrosion or surface deposits built up during operation but rather a construction or materials issue. We expect the next R&D goal, to produce up to four trays of MRPC TOF, will provide invaluable experience with these and other important production and QA issues. The only effect of excess streamers that we have seen in test beam data is that the timing resolution is somewhat degraded.

Concerning deterioration of efficiency and noise performance when there is water present in the gas, we note that the study of Sakai *et al.* used a single gap chamber and found that the threshold for damage was operation for several weeks to several months with  $\sim 1000$ ppm water in the gas. The STAR MRPC modules will have much smaller charge per track than typical single gap chambers. The design specification for the STAR MRPC gas system is  $<20$ ppm water in the circulating gas. The system includes both a dryer and the ability to continuously monitor the water content in the circulating gas. Experience with the STAR TPC gas system shows that this specification is achievable. The Sakai paper also indicates that the chambers damaged by wet gas can be repaired by a noninvasive technique of flowing argon plus ammonia for about a day.

There are recent reports on aging effects in glass RPC chambers presented at the RPC2003 conference. In the talk by C. Gustavino, "Aging and recovering of glass RPC,"

( <http://clrwww.in2p3.fr/RPC2003/talk/gustavino.ppt> )

no change was observed in the rate capability of single gap glass chambers exposed to  $2\text{mC}/\text{cm}^2$  in a test beam while operating the chambers at elevated temperature ( $55^\circ\text{C}$ ). In the talk by E. Scapparone, "Study of gas mixtures and ageing of the Multigap Resistive Plate Chamber used for the ALICE TOF,"

( <http://clrwww.in2p3.fr/RPC2003/talk/scapparone.ppt> )

data were presented for multi-gap chambers operated for 200 days in a test beam with an accumulated charge of  $\sim 14\text{mC}/\text{cm}^2$  – equivalent to 54 years of ALICE operation. No HF was detected in the exit gas during operation at the limit of their monitoring ( $<0.02$ ppm) and after the exposure, there was no degradation in chamber performance – no increase in dark current and no degradation of efficiency or time resolution.

In the talk by L. Linssen, "Experience with the HARP glass RPCs,"

( <http://clrwww.in2p3.fr/RPC2003/talk/linssen.ppt> ) she mentions (page 9) that the noise rates were stable over two years of operation (total flux was not mentioned but the instantaneous flux was  $\sim 0.1\text{ Hz}/\text{cm}^2$ )

*2. The composition of glass could easily vary at the ppb level. Manufacturers of simple float glass usually do not care that much about such details. Perhaps, even physicists defending this detector concept may think the same. However, there are a very few people around who understand glass in detail from the first principles. For example, about 50 DIRC PMTs corroded very rapidly in the ultra-pure water from some reason. It turns out that the corrosion of the Borosilicate glass is modulated by only 4ppb of Zn. To see such a minute level requires using ESCA surface analysis methods. In case of DIRC, the ultra-pure water, hungry for ions, removed sodium from the glass. A small amount of Zn played the important stability role from some reason, which is not understood by us, but the manufacturer ETL agrees with our conclusion. In case of the TOF MRPCs, a new variable is that the glass is subject to a very strong electric field, plasma environment and UV light. Only long-term tests or real experiments in a high multiplicity environment, such as the STAR test,*



*will prove that there is no problem. For more on the DIRC glass corrosion in water see: <http://www.slac.stanford.edu/pubs/icfa/spring01/paper3/paper3a.html>.*

We agree, long term testing is the only way to know if the glass we have been using will corrode over a long time period due to the glass composition. TOFr' (the rebuilt tray installed for RHIC Run 4) contains modules that were read out in TOFr during RHIC Run 3 (plus some new ones), so we will be able to see and track any long-term variations in the performance of our MRPCs, should these occur. We also plan to disassemble several module each year to look for long-term aging effects.

As mentioned above, there are now also direct measurements by ALICE indicating impressive stability of glass MRPCs despite large particle fluxes.

*3. Both providing and removing ~25kW of power from the experiment is non-trivial, and air-cooling seems a difficult challenge. We recommend looking seriously at both the cooling technology and total power usage. Water-cooling is likely to be a much more tractable solution than forced air cooling, and several parts of the electronics chain might benefit from additional effort to reduce total power. An obvious possibility is to replace the MAXIM preamp chip with the NINO chip, developed by Jaron's group at CERN or a similar discrete implementation. The advantages of using the NINO chip are a small power consumption (< 50mW), a truly differential input, resulting in a smaller noise, smaller cross-talk and smaller threshold voltage. The chip has ~1ns peaking time, which also gives a better timing resolution. Signal conversion and power regulation blocks probably also deserve some additional design effort.*

The TOFp tray (original scintillator TOF patch in STAR) has a water cooling-loop and the rebuilt TOFr' tray also has a water loop. We will gain experience with this in the upcoming run. Since part of the electronics (FEE) is on the sealed trays and part (digitizers) is outside, both air and water cooling may be necessary.

The most recent review of the electronics design indicates that total power will be under 20kW. A preliminary engineering calculation indicates that 24kW can be removed by an air flow of 8000 cu.ft./min. (which can be provided by one 24in. fan) and a temperature drop of 5K. There appears to be sufficient integration space in the STAR detector to provide plenums for this air flow. We would also like the plenums on each tray to provide an rf shield for the electronics.

The preamp and discriminator constitute about one-half of the power load, so using the Nino chip would provide a major reduction in system power. The differential input is also of interest since it should provide a more stable rise time, hence improved timing resolution. We are currently investigating the availability of the Nino chip.

*4. We recommend keeping a glass coupon from every TOF module. Such samples can be used for subsequent studies if some fault is found in a given detector. These coupons should be subject to ESCA surface analysis.*

Keeping a sample from each batch of glass is a good idea.

*5. We recommend to do precise charge accounting, in terms of charge per track, charge per  $cm^2$ , and as a function of time.*

We already have the software tools in place and have been monitoring the high-voltage current and the particle flux since the initial installation of TOFr. The high-voltage current is monitored continuously and the value is recorded in a log file every minute. This high-voltage current for the most part measures current through the detector glass. The logical “or” of several dozen channel’s discriminator output is monitored continuously and recorded in a permanent data base. This should provide an accurate measure of the particle flux.

*Finally, we would like to point out that a serious effort needs to be undertaken by the collaboration to develop a detailed budget for the construction project.*

The DOE has requested a detailed management plan for the project that will include a detailed budget. We plan to provide this information to the DOE on a time scale of about one month following the receipt of this proposal by the DOE.